



**HAL**  
open science

# Hybrid magnetic nanocomposites : growth, epitaxy and study of the magneto-optical properties

Thomas Tran

► **To cite this version:**

Thomas Tran. Hybrid magnetic nanocomposites : growth, epitaxy and study of the magneto-optical properties. Material chemistry. Sorbonne Université, 2023. English. NNT : 2023SORUS050 . tel-04075741

**HAL Id: tel-04075741**

**<https://theses.hal.science/tel-04075741>**

Submitted on 20 Apr 2023

**HAL** is a multi-disciplinary open access archive for the deposit and dissemination of scientific research documents, whether they are published or not. The documents may come from teaching and research institutions in France or abroad, or from public or private research centers.

L'archive ouverte pluridisciplinaire **HAL**, est destinée au dépôt et à la diffusion de documents scientifiques de niveau recherche, publiés ou non, émanant des établissements d'enseignement et de recherche français ou étrangers, des laboratoires publics ou privés.

Thèse de doctorat  
de Sorbonne Université  
École doctorale 397  
Physique et chimie des matériaux

pour obtenir  
le grade de docteur en physique

Nanocomposites magnétiques hybrides :  
Croissance, épitaxie et étude des propriétés magnéto-optiques

présentée par Thomas Tran  
et soutenue le 19 janvier 2023

devant un jury composé de

M. Pascal Andreazza	Professeur des universités Université d'Orléans, ICMN	Rapporteur
M. Yves Dumont	Professeur des universités Université de Versailles, GEMAC	Rapporteur
Mme Valérie Halté	Professeure des universités Université de Strasbourg, IPCMS	Présidente du jury
Mme Emmanuelle Jal	Chargée de recherche CNRS, LCPMR	Examinatrice
M. Franck Vidal	Professeur des universités Sorbonne Université, INSP	Directeur
M. Yunlin Zheng	Chargé de recherche CNRS, INSP	Co-directeur



---

Wierzę w rozsypanie liczb,  
w rozsypanie ich bez żalu.  
*(Je crois en la dispersion des chiffres,  
leur dispersion sans regrets.)*

Wisława Szymborska



## ABSTRACT

### *Nanocomposites magnétiques hybrides : croissance, épitaxie et étude des propriétés magnéto-optiques*

La magnétoplasmonique tire parti de l'amplification du champ électromagnétique, causée par l'excitation des plasmons à une interface ou des plasmons localisés dans un nano-objet, dans le but d'augmenter la réponse magnéto-optique d'un matériau. Cela encourage la croissance et la conception de nouveaux nanomatériaux hybrides, combinant propriétés plasmoniques et magnétiques. Dans ce contexte, ce travail a pour but la croissance et l'étude des propriétés de couches minces de nanocomposites verticalement alignés (VANs) d'Au-SrTiO<sub>3</sub> et d'Au-Co<sub>0,8</sub>Ni<sub>0,2</sub>-SrTiO<sub>3</sub>. Les échantillons ont été élaborés par dépôt laser pulsé séquentiel, en tirant parti de la séparation de phase. La morphologie des VANs et la structure des couches minces ont été étudiées par une combinaison de microscopie et spectromicroscopie électroniques, et de diffraction des rayons X par rayonnement synchrotron, validant la possibilité de concevoir des nanofils hybrides composés d'une partie d'Au et d'une partie de Co<sub>0,8</sub>Ni<sub>0,2</sub>, et entourés d'une matrice de SrTiO<sub>3</sub>. Les mesures magnétiques montrèrent que la forte déformation axiale dans le Co<sub>0,8</sub>Ni<sub>0,2</sub> cause l'amplification de l'anisotropie magnétique uniaxial via couplage magnéto-élastique. L'excitation des plasmons localisés fut démontré dans des couches minces d'Au-SrTiO<sub>3</sub> par mesures optiques. Enfin, les dynamiques photo-induites de l'aimantation furent mesurées dans des couches minces hybrides d'Au-Co<sub>0,8</sub>Ni<sub>0,2</sub>-SrTiO<sub>3</sub>, par effet Kerr magnéto-optique résolu en temps. Ce travail de thèse est une étude préliminaire des dynamiques ultrarapides de l'aimantation dans des nanocomposites hybrides, et ouvre la voie à de futures recherches sur les phénomènes magnétiques photo-induits dans ces systèmes.

### *Hybrid magnetic nanocomposites: epitaxy, growth and study of the magneto-optical properties*

Magnetoplasmonics leverages the enhancement of the electromagnetic field, caused by the excitation of plasmons at an interface or by localised plasmons in a nano-object, in order to increase the magneto-optical response of a material. This fosters the growth and design of novel hybrid nanomaterials, combining plasmonic and magnetic properties. In this context, this work aims at the growth and the study of the properties of Au-SrTiO<sub>3</sub> and Au-Co<sub>0,8</sub>Ni<sub>0,2</sub>-SrTiO<sub>3</sub> vertically aligned nanocomposite (VANs) thin films. The samples were grown by sequential pulsed laser deposition leveraging phase separation. The morphology of the VANs and the structure of the thin films were studied by a combination of electron microscopy and spectromicroscopy, and synchrotron x-ray diffraction, validating the possibility to fabricate hybrid nanowires made of two parts, Au and Co<sub>0,8</sub>Ni<sub>0,2</sub>, and embedded in SrTiO<sub>3</sub>. Magnetic measurements displayed a large axial strain in Co<sub>0,8</sub>Ni<sub>0,2</sub>, causing an enhancement of the uniaxial magnetic anisotropy through magneto-elastic coupling. The excitation of localised plasmons was demonstrated in Au-SrTiO<sub>3</sub> thin films by optical measurements. Finally, photo-induced magnetisation dynamics were measured in hybrid Au-Co<sub>0,8</sub>Ni<sub>0,2</sub>-SrTiO<sub>3</sub> thin films, using a pump-probe time-resolved magneto-optical Kerr effect set-up. This thesis work is a preliminary report of ultrafast magnetisation dynamics in hybrid nanocomposites, and paves the way for future studies of photo-induced magnetic phenomena in these systems.



## RÉSUMÉ DÉTAILLÉ

Une piste de recherche envisagée pour la densification des supports d'enregistrement magnétique est l'utilisation de matériaux à forte anisotropie. Cette anisotropie magnétique élevée garantit la stabilité de l'aimantation par rapport à l'agitation thermique et ceci pour un volume réduit, au détriment de la facilité du retournement qui est limitée par un champ coercitif trop élevé. Ce problème pourrait être résolu à l'aide du contrôle du champ coercitif par chauffage photo-induit dans des matériaux hybrides. Ces systèmes pourraient être composés d'une partie en métal de transition 3d, et d'une autre en métal noble. La partie en métal de transition est ferromagnétique, alors que celle en métal noble peut supporter des résonances de plasmons localisés. L'excitation optique des plasmons localisée produirait un chauffage localisé. Le champ coercitif serait temporairement réduit en-dessous de la valeur du champ d'écriture en chauffant le matériau avec un laser. Des systèmes hybrides seraient ainsi intéressants pour l'étude du renversement assisté par laser.

D'autres effets causés par un couplage magnéto-plasmonique ont été rapportés : amplification de l'effet magnéto-optique Kerr et Faraday, amplification de la désaimantation ultrarapide. Bien que les nanomatériaux hybrides se présentent sous différentes formes, une nouvelle classe de nanocomposés hybrides, les nanocomposés verticalement alignés (*vertically aligned nanocomposites*, VANs) pourraient offrir de nouvelles pistes de recherches dans l'étude des effets magnéto-optiques et magnétoplasmoniques.

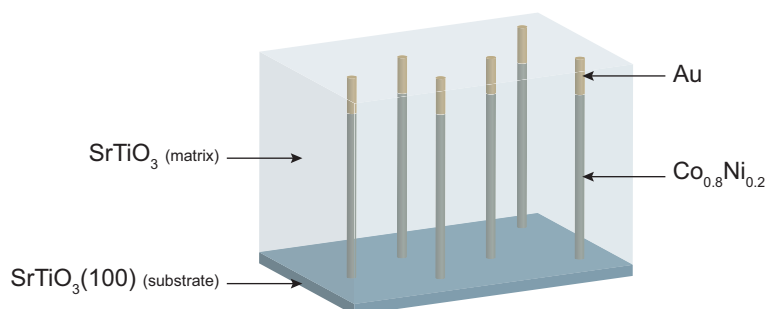


FIGURE 1 – Schéma d'une couche mince de nanocomposés verticalement alignés. Les nanofils (*nanowires*, NWs) hybrides en matrice de  $\text{SrTiO}_3$  sont composés de deux parties, un NW optique de Au supportant des résonance de plasmons localisés reposant sur un NW ferromagnétique en alliage de  $\text{Co}_{0,8}\text{Ni}_{0,2}$ .

Les VANs étudiés dans cette thèse sont des nanofils (*nanowires*, NWs) métalliques hybrides en matrice d'oxyde (Fig. 1). Les VANs sont déposés par ablation laser pulsée séquentielle sur

un substrat de SrTiO<sub>3</sub>. Les NWs sont composés d'une partie ferromagnétique en Co<sub>0.8</sub>Ni<sub>0.2</sub> et d'une partie optique en Au, cette dernière peut supporter une résonance de plasmons localisés sous excitation optique. La matrice entourant les NWs hybrides est composée de SrTiO<sub>3</sub>.

Des éléments de nanomagnétisme permettant la compréhension des mesures magnétiques de NWs sont introduits dans le **Chapitre 2**. Les différentes contributions de l'énergie magnétique sont présentées, énergie de Zeeman, énergie d'échange, énergie magnéto-statique, énergie magnéto-cristalline et énergie magnéto-élastique. Le renversement uniforme de l'aimantation dans une particule mono-domaine idéale est par la suite décrit par le modèle de Stoner-Wohlfarth. Les effets de la température sur un système magnétique sont présentés, notamment la transition superparamagnétique qui définit le renversement spontané d'une particule causé par l'énergie d'agitation thermique au-delà d'une température critique, appelée température de blocage. De plus, la dépendance en température du champ coercitif peut être décrite par une loi de puissance aux températures inférieures à la température de blocage.

Quelques éléments de plasmonique sont de plus introduits. Le cas d'une sphère conductrice dans un champ statique montre que la polarisation de la charge produit une amplification du champ proche dans la direction du champ électrique. Dans le cas d'une excitation harmonique, cette amplification est proportionnelle au facteur  $\xi$  qui dépend de l'oscillation des électrons. L'excitation des plasmons peut être quantifiée par les sections efficaces de diffusion et d'absorption,  $\sigma_{\text{sca}}$  et  $\sigma_{\text{abs}}$ , qui quantifient la capacité des nanoparticules à diffuser et absorber la lumière. Dans le cas d'un ellipsoïde, il est possible de calculer analytiquement  $\sigma_{\text{sca}}$  et  $\sigma_{\text{abs}}$  par la théorie de Gans. Les effets de la taille et de la forme d'une nanoparticule sur sa réponse optique sont enfin discutés.

Les techniques expérimentales utilisées pour préparer et étudier les échantillons sont présentées dans le **Chapitre 3**. La croissance des échantillons par ablation laser pulsée (*pulsed laser deposition*, PLD) est décrite premièrement. La PLD consiste à ablater un matériau à déposer (cible) à l'aide d'un laser pulsé. Un substrat est placé en regard de la cible à ablater, sous vide dans la chambre de croissance ( $\approx 10^{-6}$  mbar), et chauffé par une résistance chauffante (jusqu'à 700 °C). L'ablation de la cible par le laser engendre un plasma directionnel, composé de diatomes, d'atomes, d'ions et d'électrons arrachés du matériau bulk, qui se dépose sur le substrat. L'auto-assemblage des NWs de métal dans une matrice d'oxyde est induit par une ablation séquentielle de plusieurs cibles. Après ablation d'une cible métallique (par ex. CoO, NiO ou Au), les atomes diffusent sur la surface, nucléent et forment des îlots sur le substrat. La cible de SrTiO<sub>3</sub> est par la suite ablatée, et les atomes de SrTiO<sub>3</sub> enrobent les îlots métalliques. La cible métallique est ensuite réablatée, causant la croissance verticale des îlots. Répéter cette séquence  $N$  fois produit l'auto-assemblage des NWs métalliques en matrice d'oxyde. Ce mécanisme de croissance peut être vu comme une combinaison de la croissance 2D du SrTiO<sub>3</sub> et 3D du métal, causées par une différence d'énergie de surface. La séquence de base peut être écrite comme  $(n_1 \times M + n_2 \times \text{SrTiO}_3) \times N$  où  $n_1$  est le nombre de tirs sur la cible métallique,  $n_2$  est le nombre de tirs sur la cible de SrTiO<sub>3</sub> et  $N$  est le nombre de répétitions. La

---

longueur des NWs en matrice de SrTiO<sub>3</sub> est liée à  $N$ , et la forme des nanofils est liée au ratio  $\frac{n_1}{n_2}$ . Pour la croissance de nanofils en alliage binaire (par ex. Co<sub>x</sub>Ni<sub>1-x</sub>), la séquence de base est  $((n_1 \times M_1 + n_2 \times \text{SrTiO}_3) \times n_3 + (n_1 \times M_2 + n_2 \times \text{SrTiO}_3) \times n_4) \times N$  et la composition de l'alliage binaire est choisie facilement en ajustant le ratio  $\frac{n_3}{n_4}$ . Les couches minces ont été élaborées à l'*Institut des NanoSciences de Paris* (CNRS-Sorbonne Université).

Les propriétés structurales ont été mesurées par microscopie électronique et par diffraction des rayons X. Les plans atomiques des NWs ont été imagés par microscopie électronique en transmission à haute résolution (*high-resolution transmission electron microscopy*, HRTEM) en vue plane et transverse. Les images de contraste chimique ont été prises par microscopie électronique en transmission à balayage par détecteur grand angle en champ sombre (*high-angle annular dark-field scanning transmission electron microscopy*, HAADF-STEM). Les clichés de HRTEM et de HAADF-STEM ont été pris par Dominique Demaille à l'*Institut de Minéralogie, de Physique des Matériaux et de Cosmochimie* (CNRS-Sorbonne Université). Des études complémentaires par spectroscopie de rayons X à dispersion d'énergie (*energy-dispersive x-ray spectroscopy*, EDXS) ont prouvé la séparation de phase entre Au et CoNi. Les cartographies de EDXS ont été prises par Gilles Patriarche au *Centre de Nanosciences et de Nanotechnologies* (CNRS-Université Paris-Saclay). L'épitaxie des couches minces de nanocomposite a été explorée par diffraction des rayons X (*x-ray diffraction*, XRD) à l'*Institut des NanoSciences de Paris*. Des cartographies de l'espace réciproque ont de plus été mesurées par XRD avec rayonnement synchrotron sur la ligne SixS (SOLEIL) avec la collaboration de Alessandro Coati, Alina Vlad, Yves Garreau, Michèle Sauvage-Simkin et Andrea Resta.

Les propriétés magnétiques ont été mesurées par magnétométrie à échantillon vibrant à la plateforme *Mesures physiques à basse température* de Sorbonne Université. Des mesures dynamiques du magnétisme des NWs ont été conduites au *Laboratoire d'optique appliquée* (CNRS-ENSTA) à l'aide d'une expérience pompe-sonde d'effet Kerr magnéto-optique résolu en temps (*time-resolved magneto-optical Kerr effect*, TRMOKE). Ces expériences ont été réalisées avec la collaboration de Boris Vodungbo, Emmanuelle Jal, Romain Jarrier et Guillaume Lambert. Les propriétés optiques ont été sondées par ellipsométrie à l'*Institut des NanoSciences de Paris*, et les mesures ont été traitées par un modèle développé par Bruno Gallas.

Dans le **Chapitre 4**, la synthèse par PLD, la structure et les propriétés optiques des NWs de Au en matrice de SrTiO<sub>3</sub> sont présentées. Les conditions de synthèse des NWs de Au ont été étudiés dans la perspective de faire croître des NWs hybrides de Au-Co<sub>0.8</sub>Ni<sub>0.2</sub>. Pour cela, des échantillons ont été déposés à différentes températures de croissance. Les images de HRTEM prouvent la synthèse des NWs de Au en matrice de SrTiO<sub>3</sub> sur substrat de SrTiO<sub>3</sub>, un diamètre moyen de  $\approx 7$  nm est mesuré. L'épitaxie a été étudiée par XRD qui a montré que les NWs présentent moins de polycristallinité à 550 °C qu'à 650 °C. La matrice de SrTiO<sub>3</sub> possède cependant une meilleure cristallinité à 650 °C. D'autre part, une épitaxie cube-sur-cube entre Au et SrTiO<sub>3</sub> est observée dans les couches minces déposées à une température intermédiaire

de 600 °C. Une température de croissance de 600 °C est donc plus adéquate pour la croissance des NWs de Au en matrice de SrTiO<sub>3</sub>.

La section efficace des couches minces de VANs de Au-SrTiO<sub>3</sub> a été calculée par la théorie de Gans. Deux bandes d'absorption sont prédites à des longueurs d'onde visibles et proche-infrarouge. Ces bandes d'absorption sont liées aux modes de résonance des plasmons longitudinal et transverse. Des mesures des excitations des plasmons ont été conduites par spectroscopie en transmission et ellipsométrie. Une bande d'absorption dans le visible est mesurée, correspondant au mode transverse de la résonance plasmonique. Du fait de la géométrie de l'expérience, il n'est pas possible d'exciter le mode longitudinal. Les propriétés optiques ont aussi été sondées par ellipsométrie. Un modèle est utilisé pour ajuster les mesures, afin d'extraire la partie imaginaire de la permittivité  $\epsilon_2$ , liée à l'absorption. Une réponse optique anisotrope est extraite, montrant deux bandes d'absorption, attribuées aux modes transverse et longitudinal de la résonance plasmonique. Ces bandes, issues de l'ajustement des mesures d'ellipsométrie, apparaissent à des longueurs d'onde différentes des prédictions par théorie de Gans. Cet écart ne peut pas être expliqué par un couplage dipolaire entre les NWs. D'un autre côté, des nanoinclusions de Au dans la matrice sont observées sur les clichés de HRTEM, et pourraient modifier la réponse optique de la matrice. De plus, une autre explication pourrait reposer sur les constantes optiques utilisées dans les prédictions par théorie de Gans. Celles-ci sont celles du SrTiO<sub>3</sub> bulk, or la matrice n'est pas stœchiométrique, ce qui modifie les constantes optiques.

Après avoir prouvé la synthèse des couches minces de VANs de Au-SrTiO<sub>3</sub>, la croissance de NWs hybrides de Au-Co<sub>0,8</sub>Ni<sub>0,2</sub>-SrTiO<sub>3</sub>, leur structure et leurs propriétés magnétiques sont présentées dans le **Chapitre 5**. Ces échantillons ont été élaborés par PLD séquentielle en deux étapes. Un diamètre moyen de  $\approx 3$  nm est mesuré sur les images de HRTEM. La séparation de phase de Au et de Co<sub>0,8</sub>Ni<sub>0,2</sub> a été étudiée par HAADF-STEM et EDXS. Les cartographies EDXS ne montrent pas de mélange entre les NWs de Au et de Co<sub>0,8</sub>Ni<sub>0,2</sub>. Une étude statistique de ces cartographies indique de plus une nucléation préférentielle de Au au-dessus des NWs de CoNi, puisque 80 % sont recouverts et forment des NWs hybrides.

L'épitaxie des couches minces de VANs hybrides a été étudiée par cartographie de l'espace réciproque (*reciprocal space mappings*, RSM) sur la ligne SixS (SOLEIL). Les RSM montrent une texture de Au dans le plan et une épitaxie cube-sur-cube entre Co<sub>0,8</sub>Ni<sub>0,2</sub> et SrTiO<sub>3</sub>. D'autre part, une déformation axiale  $\epsilon_{zz}$  de  $\approx 5$  % est mesurée dans les NWs de Co<sub>0,8</sub>Ni<sub>0,2</sub>. Cette déformation significative est causée par l'épitaxie des NWs et de la matrice. De plus, des anneaux de diffusion ont été observés autour des réflexions de Bragg de la matrice dans les plans  $h$ - $k$ , par diffraction des rayons X à incidence rasante (*grazing incidence x-ray diffraction*, GIXRD). Ce signal diffus est dû à la présence de NWs dans la couche mince. À la condition de Bragg de la matrice, les NWs ne diffractent pas les rayons X et apparaissent comme des trous. Ils peuvent donc être modélisés par un facteur de forme. Des informations, comme l'interdistance  $D$ , sa variance  $\sigma$  et le diamètre  $d$  des nanofils, peuvent être extraites à partir du calcul de ce facteur

de forme. Les valeurs déduites des anneaux de diffusion en dehors de l'angle de Bragg sont cohérentes avec les mesures de HRTEM. La GIXRD est une mesure globale et sonde  $10^{10}$  NWs, en comparaison avec la HRTEM qui ne sonde que 25 NWs par image. Cela prouve la fiabilité des études statistiques par HRTEM, bien qu'un nombre limité de NWs soit mesuré.

Les propriétés magnétiques ont été mesurées par VSM. Les courbes d'hystérésis montrent une réponse magnétique anisotrope, avec un axe facile d'aimantation le long du long axe des NWs. Le champ coercitif de l'axe facile  $\mu_0 H_c$  atteint typiquement une valeur importante de  $\approx 1$  T à 10 K. D'autre part, les courbes  $M(H)$  sont mesurées à différentes températures, ce qui permet l'ajustement de  $\mu_0 H_c(T)$  par une loi de puissance. À partir de cet ajustement sont extraits le champ coercitif à 0 K  $\mu_0 H_c^{(0)}$  et la température de blocage  $T_b$ .  $T_b$  est compris entre 203 K et 352 K. Les longueurs d'activation  $l^*$ , correspondant au volume magnétique minimal à se renverser de façon cohérente, sont déduites des valeurs de  $T_b$ . En comparant les longueurs d'activation et les épaisseurs de paroi de domaine de Bloch, il est possible de déduire que le renversement est localisé. Le renversement débute par nucléation dans une petite portion des NWs, causant la création d'une paroi de Bloch qui se propage au travers des NWs.  $\mu_0 H_c^{(0)}$ , valeur la plus basse que peut prendre le champ d'anisotropie, est systématiquement plus élevé que le champ d'anisotropie magnétostatique  $\mu_0 H_a^{ms}$ . Cela indique une source d'anisotropie autre que l'anisotropie magnéto-statique, qui est magnéto-élastique. Cette exaltation de l'anisotropie, causée par l'anisotropie magnéto-élastique, est expliquée par une déformation axiale importante  $\epsilon_{zz} \approx 5\%$  mesurée dans les RSM, montrant un lien entre magnétisme et structure. Cependant, le champ d'anisotropie  $\mu_0 H_a^{ms+me}$  est significativement plus élevé que la valeur mesurée du champ de saturation dans l'axe difficile  $\mu_0 H_s^{IP}$ . Cela pourrait être expliqué par une inhomogénéité de déformation dans les NWs. Un modèle micromagnétique a été développé en considérant une anisotropie magnéto-élastique perturbée localement. Une inhomogénéité comprise entre 81 % et 90 % de la valeur de  $K_{me}$  est déduite du modèle micromagnétique. Cette perturbation significative de l'anisotropie magnéto-élastique est possiblement liée à une déformation axiale  $\epsilon_{zz}$  inhomogène, causée par des défauts. Ces défauts pourraient donc être la cause de la localisation et la réduction du champ coercitif dans des NWs de  $\text{Co}_{0.8}\text{Ni}_{0.2}$  fortement déformés.

Une étude préliminaire des propriétés magnéto-optiques des couches minces de nanocomposites est présentée dans le **Chapitre 6**. Deux échantillons ont été étudiés pour donner un aperçu de l'influence des NWs de Au sur les dynamiques de l'aimantation de VANs ferromagnétiques. Les propriétés optiques ont été simulées par la méthode des éléments finis. La perte ohmique simulée dans des NWs de Au de couches minces de VANs Au-CoNi-SrTiO<sub>3</sub> présente deux bandes d'absorption dans la gamme des longueurs d'onde visible et proche-infrarouge, liées aux modes transverse et longitudinal de la résonance plasmonique. L'absorption optique des NWs de CoNi a aussi été simulée, et n'indique pas d'augmentation de l'absorption induite par une excitation des plasmons avec une lumière incidente polarisée *s*. D'un autre côté, une augmentation de l'absorption optique de  $\approx 5\%$  à  $\approx 800$  nm est prédite dans des NWs hybrides

avec une lumière incidente polarisée  $p$ . Une augmentation de l'absorption est donc possible, bien qu'elle soit faible dans les systèmes présentés. La simulation de l'absorption optique pourrait être utile dans la détermination des dimensions optimales de VANs, et pourrait donc être utilisé comme guide avant la croissance de nouveaux échantillons.

Deux échantillons ont été mesurés par effet Kerr magnéto-optique (*magneto-optical Kerr effect*, MOKE) afin d'étudier l'effet des NWs de Au. L'un est une couche mince de VANs Au-CoNi-SrTiO<sub>3</sub>, alors que l'autre ne comporte que des VANs de CoNi-SrTiO<sub>3</sub>. Les courbes  $M(H)$ , mesurées par MOKE, montrent que les échantillons sont dans un état bloqué à température ambiante, avec un champ coercitif de 0.08 T et 0.16 T pour les VANs avec et sans Au respectivement. Ces mesures montrent qu'il est possible de mesurer un signal Kerr magnéto-optique dans des VANs. La dynamique de l'aimantation de ces deux couches minces a été étudiée par TRMOKE. L'aimantation chute en moins de 0.5 ps après coïncidence de la pompe et de la sonde, et recouvre partiellement sa valeur après. La chute d'aimantation  $q$  est proportionnelle à la fluence de la pompe et plus importante pour une pompe polarisée  $p$ , possiblement à cause d'une absorption optique plus importante. Les valeurs de  $q$  sont similaires pour les échantillons avec et sans NWs de Au. Le temps caractéristique de désaimantation  $\tau_{\text{demag}}$  ne varie pas par rapport à la fluence. Des valeurs de  $\tau_{\text{demag}}$  de  $190 \pm 20$  fs et  $160 \pm 20$  fs ont été mesurées dans l'échantillon de VANs hybrides pour une pompe polarisée  $p$  et  $s$  respectivement. Ces valeurs sont comparables à celles présentées dans la littérature pour des couches minces de Co et de Ni. Ainsi, la désaimantation initiale de nanocomposites pourrait être identique à celle de couches minces. Par rapport à la réaimantation, une différence remarquable est observée entre celles des échantillons avec et sans NWs de Au. Le système reviendrait à l'équilibre plus vite dans des échantillons hybrides. Une interprétation serait que l'interface Au-Co aiderait à dissiper l'énergie absorbée. Cet effet est d'autant plus prononcé que la fluence est élevée. Ces mesures de TRMOKE montrent qu'il est possible d'observer une désaimantation sub-picoseconde dans des nanocomposites avec un bon rapport signal sur bruit. Ce travail préliminaire d'étude de la dynamique de l'aimantation dans des couches minces de Au-Co<sub>0.8</sub>Ni<sub>0.2</sub>-SrTiO<sub>3</sub> ouvre la voie à de futures recherches sur la désaimantation ultrarapide dans les VANs. Par exemple, l'effet du diamètre, de la longueur, ou plus généralement de la taille des nanocomposites sur les mécanismes de désaimantation et de réaimantation pourrait être exploré.

## REMERCIEMENTS

Je remercie M. Pascal Andrezza et M. Yves Dumont pour avoir accepté d'être rapporteurs de ma thèse. Je remercie aussi Mme Valérie Halté et Mme Emmanuelle Jal pour avoir accepté d'être examinatrices.

Les résultats présentés dans cette thèse, qui a été réalisée au sein du groupe *Croissance et propriétés de systèmes hybrides en couches minces* de l'Institut des NanoSciences de Paris, n'auraient pas pu être possibles sans l'aide de nombreuses personnes.

Je tiens à remercier particulièrement mes directeurs de thèse, Franck Vidal et Yunlin Zheng, pour leur soutien pendant ces trois ans et dont les conseils et les discussions m'ont permis de mener à bien ces travaux. Un grand merci à Marcel Hennes pour toutes les discussions sur la désaimantation ultrarapide, ainsi que son aide lors des temps de faisceau au Laboratoire d'optique appliquée.

Je voudrais remercier Dominique Demaille pour avoir réalisé les clichés de microscopie électronique en transmission ainsi que pour m'avoir aidé dans l'interprétation des résultats. Il n'aurait pas été possible de montrer la séparation de phase dans les nanocomposites sans le travail de Gilles Patriarche en spectromicroscopie, que je remercie.

Merci à Nicolas Casaretto et David Hrabovsky, pour les discussions et pour m'avoir formé en diffraction des rayons X et en magnétométrie. Je remercie Bruno Gallas, dont les simulations en ellipsométrie et en méthode des différences finies ont permis de déterminer les propriétés optiques des échantillons.

Je remercie tous les chercheurs et toutes les chercheuses de la ligne SixS de SOLEIL, Alessandro Coati, Alina Vlad, Yves Garreau, Michèle Sauvage-Simkin et Andrea Resta pour leur aide lors des mesures de cartographie de l'espace réciproque.

Je voudrais remercier Boris Vodungbo, Emmanuelle Jal, Romain Jarrier et Guillaume Lambert pour les expériences d'effet magnéto-optique Kerr résolues en temps réalisées au Laboratoire d'optique appliquée. Leur collaboration et leur aide précieuse lors des mesures ont permis d'enrichir ce travail.

Merci à tous les doctorants et toutes les doctorantes pour les cafés et les mots croisés. Alicia, Patricia, Sarah, Bruno, Enrico, Jonas et John, *tusind tak for jeres omsorg, jeres venlighed og for den gode tid, vi tilbragte sammen.*



# CONTENTS

<b>ABSTRACT</b>	i
<b>RÉSUMÉ DÉTAILLÉ</b>	iii
<b>REMERCIEMENTS</b>	ix
<b>CONTENTS</b>	xi
<b>1. INTRODUCTION</b>	1
1.1 Magnetic recording . . . . .	1
1.2 Manipulation of magnetisation with light . . . . .	4
1.2.1 Ultrafast demagnetisation . . . . .	4
1.2.2 All-optical helicity-dependent switching . . . . .	7
1.3 Magneto-optical and magnetoplasmonic effects in hybrid systems . . . . .	8
1.4 Vertically aligned nanocomposites . . . . .	11
1.5 Outline . . . . .	14
<b>2. THEORY</b>	15
2.1 Introduction . . . . .	15
2.2 Nanomagnetism . . . . .	16
2.2.1 Magnetic energy . . . . .	16
2.2.2 Exchange energy and magnetic order . . . . .	17
2.2.2.1 Exchange energy . . . . .	17
2.2.2.2 Magnetic order . . . . .	18
2.2.3 Magnetic anisotropy . . . . .	19
2.2.3.1 Magnetostatic anisotropy . . . . .	19
2.2.3.2 Magnetocrystalline anisotropy . . . . .	21
2.2.3.3 Magnetoelastic anisotropy . . . . .	24
2.2.4 Stoner-Wohlfarth model . . . . .	25
2.2.5 Temperature effects . . . . .	27
2.2.5.1 Superparamagnetism . . . . .	27
2.2.5.2 Coercive field . . . . .	28
2.3 Plasmonics . . . . .	29
2.3.1 Charge polarisation . . . . .	29

2.3.1.1	Static electric field . . . . .	29
2.3.1.2	Time-harmonic electric field . . . . .	30
2.3.2	Localised plasmon resonance . . . . .	32
2.3.2.1	Optical cross sections . . . . .	32
2.3.2.2	Particle size and morphology . . . . .	33
<b>3.</b>	<b>EXPERIMENTAL TECHNIQUES</b>	<b>35</b>
3.1	Introduction . . . . .	35
3.2	Pulsed laser deposition . . . . .	36
3.2.1	Principles of pulsed laser deposition . . . . .	36
3.2.2	Growth of vertically aligned nanocomposites . . . . .	36
3.2.3	Kinetic Monte Carlo modelisation . . . . .	38
3.3	Structural properties . . . . .	41
3.3.1	Transmission electron microscopy . . . . .	41
3.3.1.1	Sample milling . . . . .	41
3.3.1.2	High-resolution transmission electron microscopy . . . . .	41
3.3.1.3	HAADF-STEM and spectromicroscopy . . . . .	42
3.3.2	X-ray diffraction . . . . .	43
3.3.2.1	Out of plane and in plane x-ray diffraction . . . . .	43
3.3.2.2	Synchrotron x-ray diffraction . . . . .	44
3.3.2.3	X-ray reflectivity . . . . .	45
3.4	Physical properties . . . . .	47
3.4.1	Vibrating sample magnetometry . . . . .	47
3.4.2	Magneto-optical Kerr effect . . . . .	47
3.4.2.1	Static magneto-optical Kerr effect . . . . .	47
3.4.2.2	Time-resolved magneto-optical Kerr effect . . . . .	49
3.4.3	Ellipsometry . . . . .	53
<b>4.</b>	<b>AU NANOWIRES</b>	<b>55</b>
4.1	Introduction . . . . .	55
4.2	Structural properties of Au NWs . . . . .	56
4.2.1	Diameter, density and epitaxy . . . . .	56
4.2.2	Influence of the growth temperature on the epitaxy . . . . .	60
4.3	Optical properties . . . . .	62
4.3.1	Gans theory simulations . . . . .	62
4.3.2	Experimental measurements . . . . .	63
4.4	Conclusion . . . . .	65
<b>5.</b>	<b>HYBRID NANOWIRES</b>	<b>67</b>
5.1	Introduction . . . . .	67

---

5.2	Structural properties of hybrid NWs . . . . .	68
5.2.1	Diameter, density . . . . .	69
5.2.2	Phase segregation . . . . .	71
5.2.3	Epitaxy of hybrid NWs . . . . .	77
5.2.4	Off-Bragg scattering . . . . .	79
5.3	Magnetic properties of hybrid NWs . . . . .	87
5.3.1	Magnetic anisotropy . . . . .	87
5.3.1.1	Magnetic anisotropy constants . . . . .	87
5.3.1.2	Magnetic anisotropy at low temperatures . . . . .	89
5.3.2	Temperature dependence of the coercivity and activation length . . . . .	92
5.3.2.1	Temperature dependence of the coercivity . . . . .	92
5.3.2.2	Activation length . . . . .	94
5.4	Discussions on the magnetic anisotropy . . . . .	95
5.4.1	Effect of large structural strain on the anisotropy . . . . .	95
5.4.2	Inhomogeneity and loss of anisotropy . . . . .	96
5.5	Conclusion . . . . .	100
<b>6.</b>	<b>MAGNETO-OPTICAL STUDY OF NANOCOMPOSITE THIN FILMS</b>	<b>103</b>
6.1	Introduction . . . . .	103
6.2	Absorption in hybrid nanocomposite thin films . . . . .	104
6.2.1	Experimental data and simulations . . . . .	104
6.2.2	Simulation of the absorption . . . . .	105
6.3	Magnetisation dynamics . . . . .	107
6.3.1	Static magneto-optical Kerr effect . . . . .	107
6.3.2	Ultrafast demagnetisation . . . . .	108
6.3.2.1	General description . . . . .	108
6.3.2.2	Initial demagnetisation . . . . .	111
6.3.2.3	Remagnetisation . . . . .	113
6.4	Conclusion . . . . .	114
<b>7.</b>	<b>CONCLUSION</b>	<b>117</b>
7.1	Conclusion . . . . .	117
7.2	Perspectives . . . . .	120
<b>BIBLIOGRAPHY</b>		<b>123</b>



# CHAPTER 1

## INTRODUCTION

1.1	Magnetic recording . . . . .	1
1.2	Manipulation of magnetisation with light . . . . .	4
1.2.1	Ultrafast demagnetisation . . . . .	4
1.2.2	All-optical helicity-dependent switching . . . . .	7
1.3	Magneto-optical and magnetoplasmonic effects in hybrid systems . . . . .	8
1.4	Vertically aligned nanocomposites . . . . .	11
1.5	Outline . . . . .	14

### 1.1 Magnetic recording

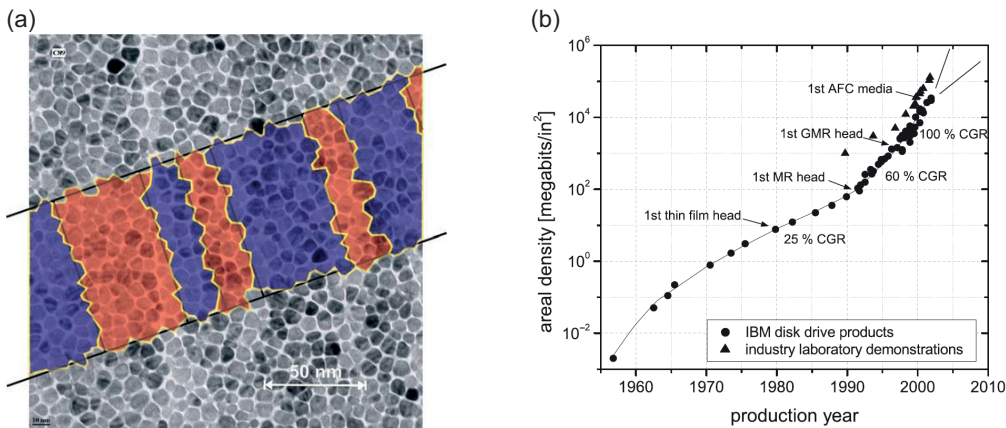


Figure 1.1 – (a) Transmission electron microscopy image of a granular magnetic medium, a track of bits with opposite polarities is sketched with red and blue colours (reproduced from [1]). (b) Evolution of the areal density, i.e. number of bits per unit area, since the production of the first hard drive disk (*IBM Ramac*, 1956) (reproduced from [2]).

The development of the hard disk drive has played a significant role in data recording. The hard disk drive (HDD) is based on the use of magnetism to write, store and read binary digital information. Fig. 1.1(a) shows a typical recording medium composed of magnetic grains. A bunch of magnetic grains forms one bit, the elementary unit of data in a computer. Data is encoded and stored in a binary fashion, thanks to the magnetisation of the bits, as sketched in Fig. 1.1(a) in red and blue colours. In 1956, IBM produced the first commercial HDD (*IBM Ramac*), featuring a total storage capacity of 5 MB at an areal density of 2 kbit in<sup>-2</sup> (Fig. 1.1(b)) [2]. It should be noted that the areal density defines the number of bits per unit area. Since 1956,

the areal density has increased 550 million-fold in modern commercial HDDs, from  $2 \text{ kbit in}^{-2}$  to  $1.1 \text{ Tbit in}^{-2}$  [3]. Modern HDDs are thus considerably smaller than their first counterparts. By comparison, an *IBM Ramac* had to be stored in a  $9 \text{ m} \times 15 \text{ m}$  room and weighted a ton.

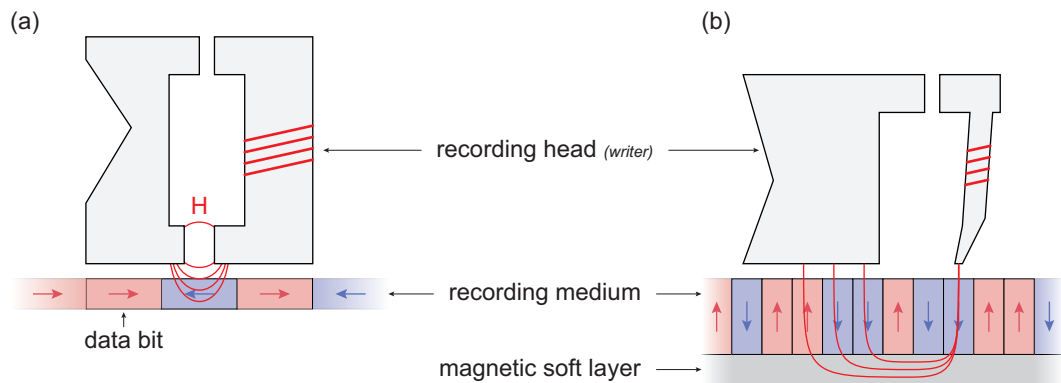


Figure 1.2 – Schematics showing the principle of (a) longitudinal magnetic recording and (b) perpendicular magnetic recording.

The quest for higher areal density is still topical and brings about significant innovations in magnetism and materials science. As proof, an areal density of  $2.27 \text{ Tbit in}^{-2}$  has been recently demonstrated [4]. One of the significant advances concerning magnetic recording media is the transition from longitudinal magnetic recording (LMR) to perpendicular magnetic recording (PMR). Longitudinal and perpendicular magnetic recordings use the same principle, a recording head passes over a magnetic medium and prints a pattern formed by the moment of the magnetic grains. The difference between LMR and PMR is in the magnetisation patterns, as sketched in Fig. 1.2. The magnetisation patterns for PMR are made of *up* and *down* moments, rather than *left* and *right* moments as for LMR. In the case of vertical bits (PMR), adjacent moments do not point at each other, contrary to the longitudinal case. Therefore, vertical bits with opposite magnetisation form surface charges, while longitudinal bits display a volume charge at the magnetic transition. For small bit sizes, demagnetising fields, opposite to the magnetisation, are thus minimised for PMR bits, in comparison to their LMR counterparts. Vertical bit alignment enables smaller bit size with superior thermal stability, consequently increasing data density [5, 6].

However, the areal density of conventional PMR is limited to  $\approx 1 \text{ Tbit in}^{-2}$  [7]. Indeed, magnetic grains are more likely to display spontaneous reversal, as their size is reduced, due to the superparamagnetic limit. This problem can be described by a trilemma (Fig. 1.3), composed of three requirements, readability, thermal stability and writability, conflicting with each other, limiting thus the areal density. As magnetic grains are randomly distributed in the medium, the magnetic transition will match the grain boundaries, based on the size and the exchange of the grains. An ensemble of tens of magnetic grains is thus required to form a bit that can be read with a sufficient signal-to-noise ratio (SNR). For the purposes of increasing the areal

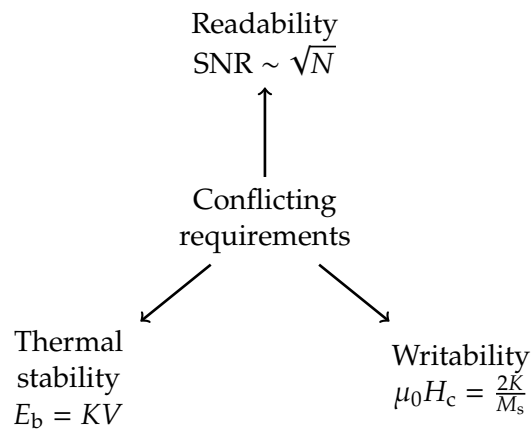


Figure 1.3 – Trilemma of magnetic recording. In order to get a high signal-to-noise ratio (SNR), the number of magnetic grain  $N$  composing a single bit must be high. The magnetic grain volume  $V$  thus should be minimised to achieve higher areal densities. As  $V$  is minimised, the magnetic grains should have a high magnetic anisotropy  $K$  for the energy barrier  $E_b$  to ensure a decent thermal stability. However, a high  $K$  will lead to a high coercive field value  $\mu_0 H_c$ , consequently increasing the switching field value.

density, in order to keep a sufficient SNR, the number of grains should not be changed and consequently the grain volume  $V$  must be reduced. As the grain size is reduced, the magnetic energy barrier  $E_b = KV$  is too low in comparison to thermal agitation  $k_B T$ , the grain is in the superparamagnetic regime and displays spontaneous thermal reversal. To solve this problem, the magnetic anisotropy  $K$  must be increased for  $E_b = KV$  to be greater than  $k_B T$ , typically  $\frac{KV}{k_B T} > 60$ . However, a high  $K$  yields a high coercive field value  $\mu_0 H_c$ , the minimal magnetic field value to encode a bit, consequently increasing the write field value. Therefore, magnetic recording medium design is restrained by readability (SNR is too low), thermal stability ( $KV$  is too small) or writability ( $K$  is too large) [8].

In other terms, the reduction of the volume of the magnetic grains, which would remain thermally stable, calls for materials with large magnetic anisotropy. For example,  $L1_0$  FePt and  $Co_5Sm$ , materials with large  $K$  value (approximately 20 times larger than that of pure Co), could form thermally stable grains with diameters as small as 2 nm to 3 nm [9], hence leading to a storage density up to 100 Tbit in<sup>-2</sup> [10]. However, a too large  $K$  value would yield a too large  $\mu_0 H_c$  value, requiring a nonrealistic write field to reverse the magnetic moment and to encode data. The areal density of conventional PMR is, therefore, limited to  $\approx 1$  Tbit in<sup>-2</sup>. As this limit, known as the superparamagnetic limit, has been reached today, new technologies are being developed in order to bypass it.

A promising line of research is heat-assisted magnetic recording (HAMR). As shown in Fig. 1.4(a), HAMR consists in temporarily reducing the coercive field value below the available write field ( $\mu_0 H_w$ ) by heating the recording material with a laser. The heated region is then

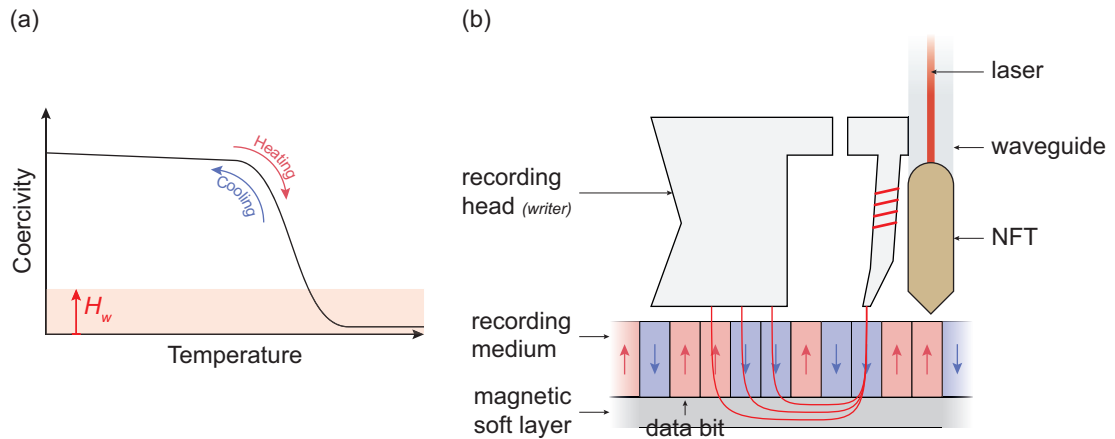


Figure 1.4 – Schematics showing the principle of (a) the heat-assisted magnetic recording (HAMR) heating and cooling processes,  $\mu_0 H_w$  is the write field value, and (b) HAMR with vertical bits and a near-field transducer (NFT).

cooled in presence of the write field, encoding the magnetic bit in function of the polarity of  $\mu_0 H_w$ . Because of the diffraction limit, the laser spot cannot be confined to a few nanometres and thus would be larger than the size of the magnetic bits. A waveguide and a near-field transducer (NFT) are therefore proposed to solve this problem and maximise the areal density. The waveguide delivers the laser to the NFT, which exalts the field by surface plasmons and point charge effect at a sub-diffraction point, heating locally the magnetic material [11, 12].

The example of HAMR shows the possibility of manipulating the magnetisation of materials with high anisotropy with the help of optical heating. HAMR is an example of technological application leveraging well known physical phenomena. Especially, light provides the energy, which heats locally the magnet. This process spans in a timescale of hundreds of nanoseconds. This is much slower than other optically mediated processes of magnetisation manipulation that are subject to intense fundamental research, as ultrafast magnetisation or all-optical switching. Sub-picosecond magneto-optical processes shall be discussed in the next section.

## 1.2 Manipulation of magnetisation with light

### 1.2.1 Ultrafast demagnetisation

Pump-probe experiments enable the measurement of magnetisation dynamics at very short timescales. A pump pulse is shone on the sample and triggers the dynamics under study. A probe pulse of lower fluence measures the sample response to the pump pulse. An adjustable delay stage placed either in the pump line or in the probe line can be used to modify the temporal delay between the pump pulse and the probe pulse. Therefore, by measuring the

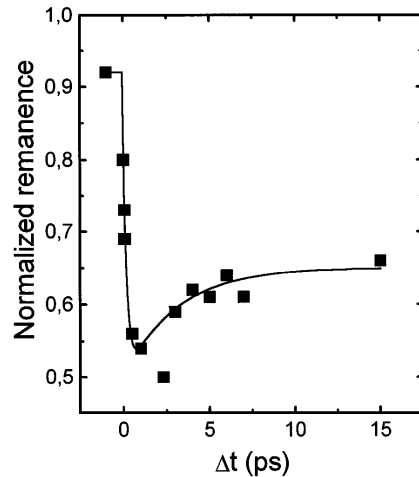


Figure 1.5 – (a) Time-resolved magneto-optical Kerr effect signal of the remanent magnetisation of a Ni thin film measured by Beaurepaire et al. The sample was excited by a 60 ps pump at a fluence of  $7 \text{ mJ cm}^{-2}$  (reproduced from [13]).

sample response for different delay values, one can monitor and reconstruct, in a stroboscopic scheme, the time evolution of the dynamics of the pumped sample.

The first evidence of ultrafast demagnetisation in a ferromagnetic material was reported in 1996 by Beaurepaire and co-workers [13]. By using a time-resolved magneto-optical Kerr effect pump-probe experiment, Beaurepaire and co-workers pumped a 20 nm thick Ni thin film with a 60 ps laser pulse at a fluence of  $7 \text{ mJ cm}^{-2}$ . They monitored the time evolution of the dynamics of the sample at remanence by measuring the hysteresis curves of the magneto-optical Kerr effect. As seen in Fig. 1.5(a), the remanent magnetisation undergoes a rapid drop of 50% in less than 2 ps, which then relaxes slowly to a long-lived plateau at two-thirds of the normalised remanence. The remanence is not full at delay  $\Delta t = 0$  ps due to heating in the course of the experiment or to slow motion of domain walls triggered by the pump pulse [14].

Apart from Ni thin films, magneto-optical contrast measured by time-resolved magneto-optical Kerr effect has been reported in other itinerant metal thin films, such as Fe [15], Co [16], ferromagnetic and ferrimagnetic alloys ( $\text{CoPt}_3$ ) [17]. Other experiments, for example time- and spin-resolved photoemission [18, 19], magnetic linear dichroism in photoemission [20], x-ray magnetic circular dichroism [21] and time-resolved small-angle x-ray scattering [22], demonstrated a sub-picosecond demagnetisation in ferromagnets.

These diverse experiments provide evidence for ultrafast demagnetisation. However, mechanisms involved in its processes are not yet fully understood. Beaurepaire and co-workers introduced a phenomenological model in their seminal work [13]. Within this model, called the three-temperature model (3TM), one considers a system composed of three interacting reservoirs in internal equilibrium: electrons, spins and lattice. Each of the reservoirs is modelled by a temperature ( $T_e$ ,  $T_s$  and  $T_l$ , respectively) and heat capacity ( $C_e$ ,  $C_s$  and  $C_l$ ). Each

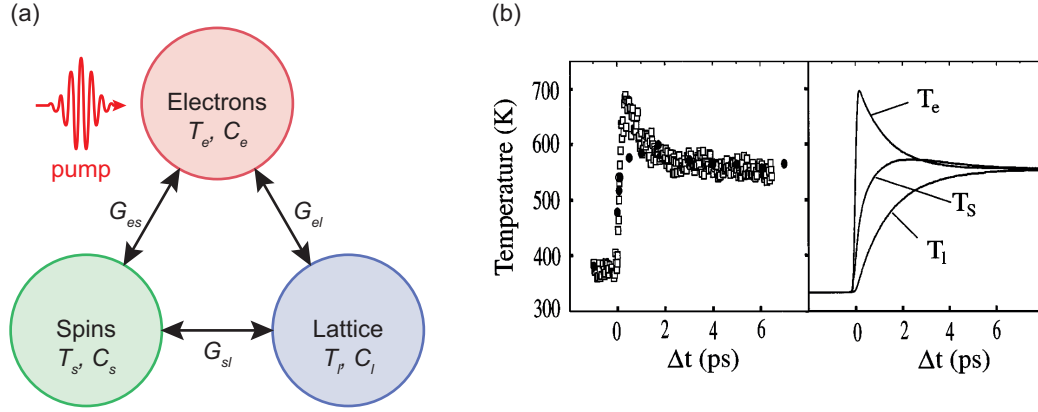


Figure 1.6 – (a) Schematics of the three-temperature model (3TM). This model takes into account three reservoirs in internal equilibrium: electrons, spins and lattice, each described by a temperature ( $T_e$ ,  $T_s$  and  $T_l$ , respectively) and a heat capacity ( $C_e$ ,  $C_s$  and  $C_l$ ). The electrons are excited by a laser pump (represented as a red arrow) and relax the energy to the spin and lattice reservoirs according to the respective coupling constants  $G_{es}$  and  $G_{el}$ . (b) Experimental (left) and calculated (right) electron ( $T_e$ ), spin ( $T_s$ ) and lattice ( $T_l$ ) temperatures with the 3TM (reproduced from [13]).

set  $(T_e, C_e)$ ,  $(T_s, C_s)$  and  $(T_l, C_l)$  interacts according to the coupling constants  $G_{es}$ ,  $G_{el}$  and  $G_{sl}$ . These coupling constants balance out any nonequilibrium between the reservoirs by energy exchange (Fig. 1.6(a)). The model was used by Beaurepaire and co-workers to calculate the time evolution of  $T_e$ ,  $T_s$  and  $T_l$  according to experimental measurements (Fig. 1.6(b)) and is often referenced in the literature. However, the 3TM only pictures a limited microscopic insight into the processes. Furthermore, the conservation of the total angular momentum  $\vec{J}$  is ignored within its framework [23].

Intensive research lead to the identification of possible processes inherent to sub-picosecond demagnetisation. Let us consider the case of a ferromagnetic thin film of a thickness larger than the optical absorption depth. Exciting the thin film causes a local repopulation of empty electronic states. The excited electrons, consequent to the laser pulse, have spin-dependent and inhomogeneous spatial distribution in the film. From this point, excited electron processes are complex, as discussed by Razdolski and co-workers [24]. After the excitation, locally excited electrons and electrons at the Fermi level interact by electron-electron scattering, equilibrating the electron thermal distribution [25]. Excited electrons also experience spin-flip scattering, often seen as the backbone of ultrafast demagnetisation, transferring angular momentum from the spin reservoir to elsewhere, possibly to the lattice [26].

On the other hand, the laser pulse triggers non-local processes. As locally excited electrons are brought to equilibrium by scattering, they also diffuse in the thin film by spin-dependent superdiffusion. Battiato et al. modelled this non-local process, considering it as a driving contribution to ultrafast demagnetisation [27]. Superdiffusive transport has a ballistic nature in

short timescales, tending to a Brownian diffusive type in long timescales. Its spin-dependent nature ensues from the splitting of the electrons in a 3d metal into spin majority and minority electrons (Stoner model of itinerant magnetism). The mean free path of these majority and minority electrons is different. When exciting the thin film, majority electrons in a 3d metal have a higher mean free path than the minority electrons. Thus, majority electrons experience higher mobility. This may trigger a depletion of majority electrons in the thin film and a transfer of magnetisation from the surface, resulting in demagnetisation.

The understanding of the mechanisms inherent to sub-picosecond demagnetisation is yet incomplete. While there are countless reports on thin films, sub-picosecond demagnetisation in nanocomposites is a *terra incognita*. However, knowledge in modelisation of this effect is progressing and countless experimental work has to be done. For example, the coupling between magnetism and structure can be studied at very short timescales. Terrier and coworkers reported on the demagnetisation of  $\text{Fe}_3\text{O}_4$  and  $\gamma\text{-Fe}_2\text{O}_3$  nanoparticles [28]. They found a faster demagnetisation in  $\gamma\text{-Fe}_2\text{O}_3$  than in  $\text{Fe}_3\text{O}_4$  caused by increased antiferromagnetic exchange interactions in  $\gamma\text{-Fe}_2\text{O}_3$ . On the other hand, Reid et al. studied magnetostriction in FePt nanoparticles by demagnetisation thanks to time-resolved soft x-ray scattering [29] and unveiled its inherent mechanisms.

### 1.2.2 All-optical helicity-dependent switching

An intense laser coupled with a magneto-optical effect can trigger different phenomena. For example, magnetisation of a thin film can be manipulated and reversed by a circularly polarised light. A possible mechanism to explain this phenomenon may lie in an inverse Faraday effect. Indeed, circularly polarised light can induce a strong magnetic field colinear to the wavevector, which is capable of manipulating the magnetisation. Furthermore, the direction of the Faraday-induced magnetic field depends on the helicity of the circularly polarised light [30]. However, no consensus has been met on this mechanism based on an inverse Faraday effect [31].



Figure 1.7 – Polarising microscope image of a GdFeCo thin film (reproduced from [32]). The sample is excited by a circularly polarised pulsed laser, which was swept on the surface at high-speed ( $50 \text{ mm s}^{-1}$ ). The colour shows the magnetisation state of the sample.

Stanciu and co-workers reported the all-optical switching of a ferrimagnetic GdFeCo thin film by inverse Faraday effect [32]. The sample was placed in a polarising microscope, in zero magnetic field and excited by a 40 fs pulsed laser. Furthermore, the pulses were swept on the surface of the thin film at high-speed ( $50 \text{ mm s}^{-1}$ ). The polarising microscope image (Fig. 1.7) shows that  $\sigma^+$  polarised pulses reversed the magnetisation in the black domain and left it intact in the white domain. An opposite situation is seen for  $\sigma^-$  polarised pulses. The reversal was explained by two mechanisms. As the optical excitation causes the magnet to heat rapidly, it is then more susceptible to the induced magnetic field by the laser pulse via inverse Faraday effect. This experiment proved the switching of the magnetic order by a circularly polarised pulsed laser, without an external magnetic field. All-optical switching thus shows exciting applications in magnetic recording.

Magnetic recording was discussed in Section 1.1. The quest for large areal density lead to hard disk drives with smaller bits. However, bit size reduction causes thermal spontaneous reversal due to the superparamagnetic limit. In order to circumvent this problem, heat-assisted magnetic recording was developed, consisting in the reversal of a high- $K$  magnet with the help of laser heating. Laser heating is a relatively slow mechanism, in comparison to magneto-optical phenomena assessed in Section 1.2. After a laser pulse, ferromagnets can experience a sub-picosecond drop of magnetisation, called ultrafast demagnetisation. Since the first report by Beaupaire and co-workers in 1996, different models were developed to describe this phenomenon. However, the description of ultrafast demagnetisation is yet incomplete. On the other hand, Stanciu and co-workers reported the all-optical switching of ferrimagnetic GdFeCo via inverse Faraday effect, without an external magnetic field. The examples of heat-assisted magnetic recording, ultrafast demagnetisation and all-optical switching raise exciting questions: Can hybrid structures, combining materials with different properties (for example magnetic and optical properties), exalt magneto-optical or magnetoplasmonic phenomena? Is it possible to envisage new lines of research with the help of these structures?

### 1.3 Magneto-optical and magnetoplasmonic effects in hybrid systems

Metals that display strong plasmonic resonances are not ferromagnetically ordered. Conversely, plasmonic resonances are strongly damped in ferromagnetic 3d metals. Thus, composite samples and materials, coupling noble (e.g. Au or Ag) and ferromagnetic metals (e.g. Co and Fe) have drawn interest.

Such hybrid systems with different shapes and compositions were reported to exalt magneto-optical (MO) Kerr and Faraday effects (Fig 1.8). MO Kerr effect is observed when a polarised light reflects on a magnetised material. The polarisation of the reflection rotates and its ellipticity changes in proportion to a component of the magnetisation of the sample, depending on the geometry of the MO Kerr effect set-up. On the other hand, the transmission of a polarised light through a magnetised material is described by the MO Faraday effect. A

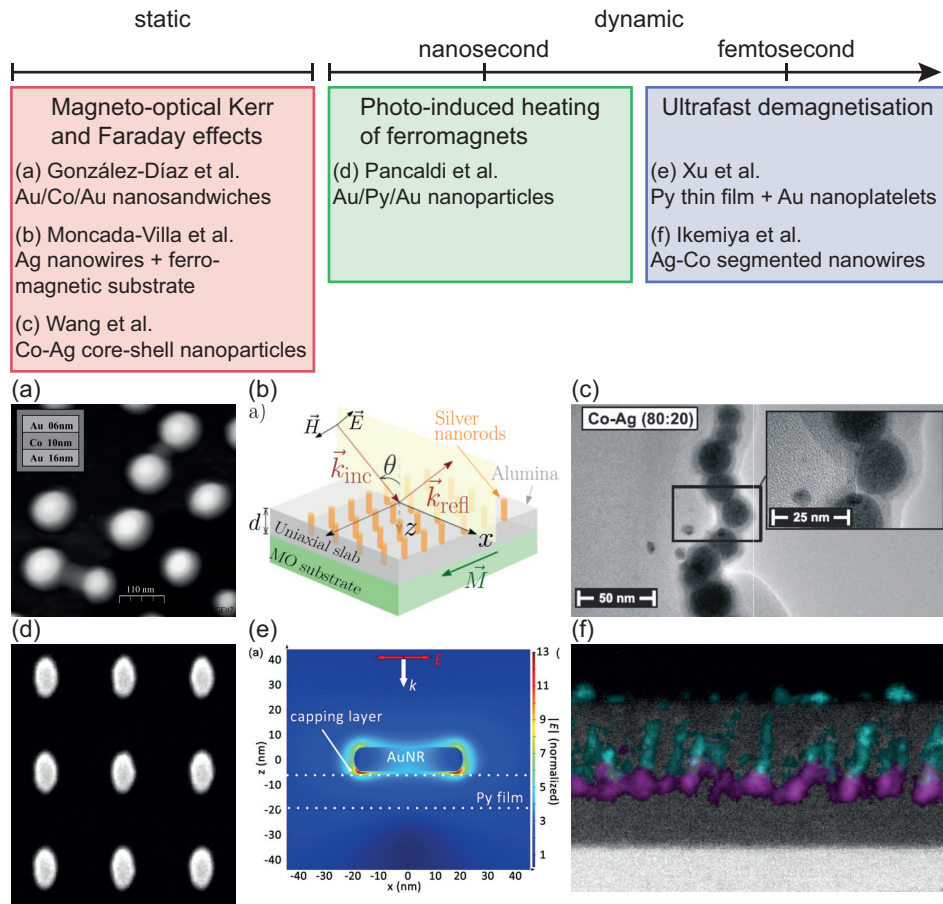


Figure 1.8 – List of reported magneto-optical and magnetoplasmonic hybrid systems. The systems presented in this figure have different shapes and compositions, and can exhibit physical effects at different timescales. (a-f) Images, sketch and simulation of the discussed hybrid systems [33–38].

strong MO Kerr effect was measured by González-Díaz and co-workers in stacks of Au/Co/Au disks (Fig. 1.8(a)) [33]. They showed that the Au/Co/Au nanodisks display simultaneous localised plasmon resonance (LPR), magnetic and magneto-optical properties. The optical and magneto-optical properties of the nanodisks are linked to the LPR, which is tuned by the shape of the particles. Furthermore, the measured enhancement of the magneto-optical properties were attributed to the LPR effect. Besides, a theoretical study by Moncada et al. [34] predicts that noble metal nanowires grown on a ferromagnetic substrate (Fig. 1.8(b)) could display an enhanced transverse MO Kerr effect. In addition, the amplitude of the MO Kerr signal could be tuned by the thickness of the nanowire thin film. Concerning the MO Faraday effect, Wang et al. carried out a study of Co-Ag core-shell nanoparticles (Fig. 1.8(c)) [35]. This study demonstrated that the electromagnetic field induced by the LPR, tunable by the thickness of the Ag shell, enhanced Faraday rotation.

While plentiful hybrid systems show an enhancement of the MO Kerr and Faraday effects, they can also present dynamic phenomena. Pancaldi et al. [36] studied the selective photo-heating of Au-permalloy (Py)-Au elliptical nanoislands (Fig. 1.8(d)). By using a laser pulse to trigger the plasmon-induced heating in the Au parts, they were able to reduce the coercive field of the ferromagnets. This coercive field was optically controlled by the power and the polarisation of the pulse. Furthermore, by packing the nanoislands in arrays of 4-vertex of two pairs of two perpendicular particles, Pancaldi et al. showed an element-selective control of the coercive field.

Ultrafast demagnetisation was also studied in hybrid nanostructures. For example, Xu and co-workers measured the time-resolved Kerr rotation of Py thin films coated by Au nanorods (Fig. 1.8(e)) [37]. They observed a  $> 50\%$  increase of the magneto-optical contrast at pump fluences on the order of  $0.1 \text{ mJ cm}^{-2}$ , compared to uncoated Py thin films. The increase of laser-induced demagnetisation was attributed to the near-field enhancement, caused by the Au nanorods LPR. Despite the low coverage of the Au nanorods (4%), this near-field enhancement contributed disproportionately to the increase of the entire demagnetisation. Ikemiya et al. also measured a plasmon-mediated enhancement of laser-induced demagnetisation by time-resolved Faraday rotation in more complex Ag-Co hybrid nanowire thin films (Fig. 1.8(f)) [38]. The concentration of Ag in the nanostructures was correlated to the increase of magneto-optical contrast. To explain it, they proposed that laser pulses trigger LPR at the Ag-Co interface, causing an increase of absorption. This LPR absorption is in addition proportional to the Ag concentration in the sample. Apart from ultrafast demagnetisation, other subpicosecond laser-induced phenomena were studied in hybrid systems. For example, Liu and coworkers studied the all-optical switching of ferrimagnetic TbFeCo thin films covered by Au nanorods [39]. By pumping the sample, they were able to locally manipulate the magnetisation. While Stanciu et al. switched an area of diameter  $10 \mu\text{m}$  GdFeCo thin films [32], Liu et al. were able to confine the switching to the nanoscale ( $\approx 50 \text{ nm}$ ), of an order comparable to that observed in HAMR. This confinement is due to the near-field enhancement, yielded by the LPR in the Au nanoantennas.

Hybrid structures presented in this section show that different MO phenomena can be studied by coupling LPR with a magnet. For example, systems combining noble and transition metals present an enhancement of MO effects linked to LPR. Besides, LPR induces photo-heating, which was used by Pancaldi et al. [36] to control the coercive field of Py nanoislands. Furthermore, the Au-Py [37] and Ag-Co [38] systems, developed by Xu et al. and Ikemiya et al. respectively, show that LPR exalts photo-induced demagnetisation. Interestingly, the amplitude of these phenomena scales as the shape of the nanoparticles, as the latter tunes the LPR. Though reported hybrid systems come in many forms, a relatively new class of nanostructures, vertically aligned nanocomposites, could provide a promising line of research for magneto-optical studies.

## 1.4 Vertically aligned nanocomposites

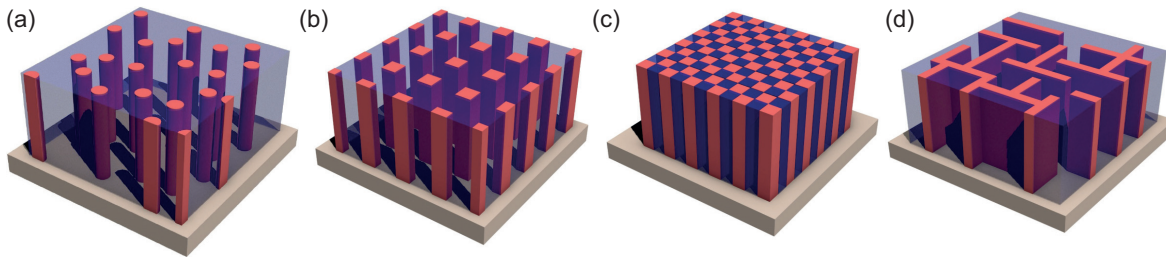


Figure 1.9 – Different examples of vertically aligned nanocomposites, (a) circular nanowires, (b) rectangular nanopillars, (c) nanochequerboard and (d) nanomaze (reproduced from [40]).

This 3-year work aims at the growth and the study of novel complex nanocomposites. In this thesis, a focus is placed on hybrid vertically aligned nanocomposites (VANs). VANs are made of two, or more, intertwined phases coupled along vertical interfaces. As sketched in Fig. 1.9, VANs exist in a wide array of embedded nanoarchitectures, such as circular nanowires [41, 42], rectangular nanopillars [43, 44], nanochequerboards [45, 46] or nanomazes [47, 48]. The variety of nanoarchitectures is even wider considering the possible combinations of host matrix-nanocomposite materials.

Because of their distinctive structures, VAN thin films present unique properties that cannot be found in conventional plain thin films. Indeed, owing to the higher area-to-volume ratios, the vertical interfaces in VANs can play a significant role in tuning the physical properties of the thin film, for example through interfacial mismatch between the VAN and the matrix leading to vertical strain in the VAN. Furthermore, with a sound selection of host matrix and nanocomposite materials, each having their own functional properties, new properties can be achieved, which would not be the case if the host matrix and the nanocomposites were not coupled across an interface. VAN thin films thus have been extensively studied, and found exciting potential applications. Ir noble metal nanopillars in  $\text{SrTiO}_3$  oxide host matrix [49, 50], for example, have photoelectrochemical properties, that are strongly enhanced due to the VAN structure, in comparison to a conventional planar thin film. Ir- $\text{SrTiO}_3$  nanocomposite thin films hence have potential application as photoelectrochemical water-splitting cells for solar-powered hydrogen generation, providing sustainable energy. Concerning oxide-oxide vertically aligned nanocomposites, multiferroic  $\text{Na}_{0.5}\text{Bi}_{0.5}\text{TiO}_3\text{-CoFe}_2\text{O}_4$  VAN thin films [51] show strong magnetoelectrical properties and an electric field-driven control of the magnetic anisotropy. This system thus could be integrated in magnetoelectric random access memory devices. Furthermore, an abundant literature on ferromagnetic nanocomposites can be found, supported by an interest in magnetic data storage. Indeed, these ferromagnetic systems could pave the way for data densification and miniaturisation, as they allow magnetic properties tuning by shape, composition and density control.

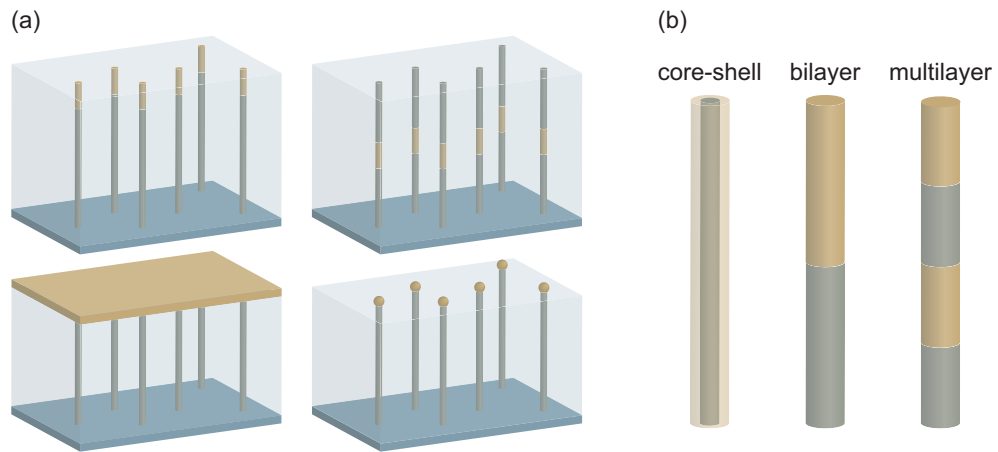


Figure 1.10 – (a) Different examples of intricate hybrid vertically aligned nanocomposites, the different parts, made of different materials, may take different shapes thanks to alternating deposition procedures. (b) Schematics of the different phase separation patterns seen in hybrid nanocomposites.

Vertically aligned nanocomposite thin films are very often grown by self-assembly, leveraging phase segregation of the materials composing the host matrix and the nanocomposites. The continuous phase separation at the growth front of the thin film may lead to the formation of vertical nanocomposites in a matrix [50]. These exciting systems, presenting novel nanoarchitectures, can be grown by bottom-up procedures, consisting in the assembly of atoms or molecules into nanostructured materials. For example, physical vapour deposition techniques, such as pulsed laser deposition or sputtering [52, 53], can be used to grow self-assembled VANs. It should be noted that ordered arrays of metallic nanowires can also be synthesised by electrochemical deposition into nanoporous anodic aluminum oxide (AAO) templates [54]. It yields perfectly ordered VANs, whose diameter and density are easily tunable. However, this technique shows some drawbacks. The matrix of an AAO templated sample is not functional and is often etched after growth. Furthermore, nanocomposites grown by electrochemical deposition are often polycrystalline and the reduction of the nanocomposite diameter is limited [55].

Self-assembly allows the growth of VANs with different nanoarchitectures, depending on the deposition conditions or the choice of materials (Fig. 1.9). Besides, more intricate hybrid VANs, composed of different parts, could be considered. One may synthesise these structures by alternating deposition procedures, consisting in growing one part at a time. These hybrid VANs are sketched in Fig. 1.10(a). For example, one may imagine nanocomposites composed of different parts, each made of different materials, or nanocomposites covered by a thin layer or nonembedded particles. Furthermore, depending on the miscibility of the materials and the surface energy, hybrid nanocomposites may display a core-shell [56, 57] or bilayer [38, 58]

phase separation pattern (Fig. 1.10(b)). Compared to the core-shell and bilayer patterns, the multilayer pattern is not energetically preferred because of the multiple interfaces.

As stressed before, the shape, composition and density of the nanocomposites, for example, are of utmost importance, as the physical properties depend on them, and consequently these parameters must be controlled. Furthermore, combining two, or more, different materials presents challenges as deposition conditions may be different. These challenges concern potential intermixing between the nanocomposites and the host matrix or oxidation of the nanocomposites and are possibly problematic for the growth of epitaxial VAN thin films. It is however possible to overcome these problems by synthesising under appropriate conditions and by a sound choice of materials [59].

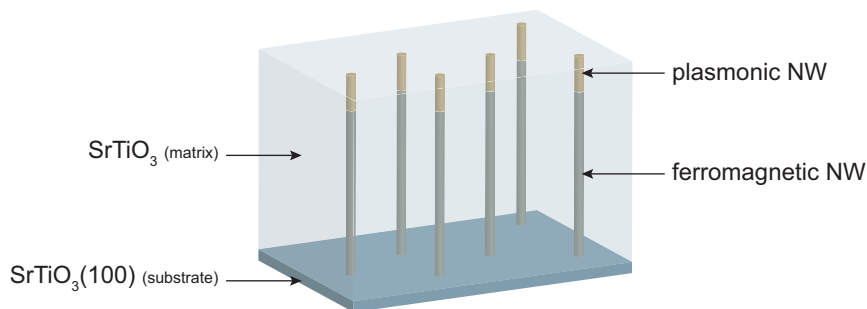


Figure 1.11 – Schematics of a hybrid nanocomposites thin film. The hybrid nanowires in  $\text{SrTiO}_3$  matrix consist of two parts, a ferromagnetic nanowire made of  $\text{Co}_{0.8}\text{Ni}_{0.2}$  alloy supporting an optical nanowire made of Au.

This thesis aims at the growth of self-assembled epitaxial hybrid nanomaterials. The structures presented in this work, sketched in Fig. 1.11, are made of ferromagnetic and plasmonic metals. They are therefore potential model systems for the study of emergent magnetoplasmonic phenomena, coupling magnetism with light. These epitaxial vertically aligned nanocomposites are grown by pulsed laser deposition and are composed of two parts, a ferromagnetic part made of  $\text{Co}_{0.8}\text{Ni}_{0.2}$  and a plasmonic part made of Au. Co and Ni can form a homogeneous alloy and grow into nanowires (NWs) in  $\text{SrTiO}_3$  matrix. An exciting feature of this alloy is the possibility of tuning the axial strain of the nanocomposite of a few per cent by increasing the Co content [60]. Thanks to the axial strain,  $\text{Co}_{0.8}\text{Ni}_{0.2}$  NWs display a hard uniaxial anisotropy, i.e. two well-defined magnetic states. Regarding the plasmonic part, Au yields localised plasmon resonances, collective oscillations of the electrons, in the visible and near-infrared range. The plasmonic NWs could act as local heat nanosources, or as near-field antennas, having an effect on the magnetic response.

## 1.5 Outline

The growth and the experimental study of hybrid magnetic nanocomposite thin films is addressed in seven chapters. Examples of photo-induced manipulation of magnetism and plasmon-mediated MO effects give reasons for magneto-optical studies with hybrid vertically aligned nanocomposites, as reviewed in **Chapter 1**. The theoretical background explaining the magnetic and the optical properties of the samples is presented in **Chapter 2**. **Chapter 3** introduces to the experimental techniques used in this work: pulsed laser deposition for the growth of the samples, transmission electron microscopy and x-ray diffraction for the structural study, vibrating sample magnetometry and (time-resolved) magneto-optical Kerr effect for the study of magnetism, and ellipsometry for the study of the optical properties.

The first step to the growth of hybrid magnetic nanocomposites vertically aligned nanocomposites is the proof of Au NWs self-assembly in SrTiO<sub>3</sub> matrix as discussed in **Chapter 4**, reporting the growth of Au-SrTiO<sub>3</sub> nanocomposite thin films. The structure and the optical properties of these thin films is furthermore presented. **Chapter 5** then presents the self-assembly by two-step pulsed laser deposition, the structure and the magnetic properties of hybrid Au-CoNi-SrTiO<sub>3</sub> nanocomposite thin films. A special focus is placed on the magnetic anisotropy and its correlation with the structure. Finally, **Chapter 6** is a preliminary study of the magneto-optical properties of hybrid nanocomposite thin films and presents pump-probe time-resolved experiments carried on these samples. A conclusion and perspectives are given to the reader in **Chapter 7**.

## CHAPTER 2

### THEORY

2.1	Introduction . . . . .	15
2.2	Nanomagnetism . . . . .	16
2.2.1	Magnetic energy . . . . .	16
2.2.2	Exchange energy and magnetic order . . . . .	17
2.2.2.1	Exchange energy . . . . .	17
2.2.2.2	Magnetic order . . . . .	18
2.2.3	Magnetic anisotropy . . . . .	19
2.2.3.1	Magnetostatic anisotropy . . . . .	19
2.2.3.2	Magnetocrystalline anisotropy . . . . .	21
2.2.3.3	Magnetoelastic anisotropy . . . . .	24
2.2.4	Stoner-Wohlfarth model . . . . .	25
2.2.5	Temperature effects . . . . .	27
2.2.5.1	Superparamagnetism . . . . .	27
2.2.5.2	Coercive field . . . . .	28
2.3	Plasmonics . . . . .	29
2.3.1	Charge polarisation . . . . .	29
2.3.1.1	Static electric field . . . . .	29
2.3.1.2	Time-harmonic electric field . . . . .	30
2.3.2	Localised plasmon resonance . . . . .	32
2.3.2.1	Optical cross sections . . . . .	32
2.3.2.2	Particle size and morphology . . . . .	33

## 2.1 Introduction

This chapter introduces the theory used for the study of ferromagnetic and optical properties of vertically aligned nanocomposites. Elements of nanomagnetism are given to the reader and a focus is placed on magnetic anisotropy, an important element for the comprehension of magnetism in elongated nanoparticles. Moreover, this chapter reviews the Stoner-Wohlfarth model, describing the uniform reversal in small magnetic particles, and the effects of temperature on thermally-activated spontaneous reversal in superparamagnetic particles and the reduction of the coercive field. Then, the second part of this chapter presents elements of plasmonics, drawing a link between optical absorption and plasmon resonances. Furthermore, effects of morphology on the plasmonic resonance wavelength are presented.

## 2.2 Nanomagnetism

### 2.2.1 Magnetic energy

The magnetisation state of a magnet results from the total magnetic free energy  $E_T$ . The total magnetic free energy  $E_T$  is defined as [61]

$$E_T = \int_V \{e_{\text{ex}} + e_{\text{ms}} + e_a + e_{\text{Zeeman}}\} dV \quad (2.1)$$

where  $e_{\text{ex}}$  is the exchange energy density,  $e_{\text{ms}}$  is the magnetostatic energy density,  $e_a$  is the anisotropy energy density and  $e_{\text{Zeeman}}$  is the Zeeman energy density. The Zeeman energy density  $e_{\text{Zeeman}} = -\mu_0 \vec{M} \cdot \vec{H}$  expresses the interaction between the magnetisation vector field  $\vec{M}$  of the specimen and the magnetic field  $\vec{H}$ .  $\mu_0$  is the magnetic constant.

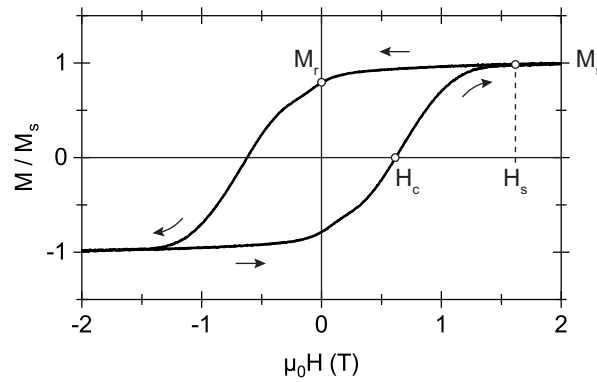


Figure 2.1 – Major  $M(H)$  curve of  $\text{Co}_{0.8}\text{Ni}_{0.2}$  nanowires.  $\mu_0 H_s$  is the saturation field,  $M_r$  is the remanence and  $\mu_0 H_c$  is the coercive field.

These different energy contributions define a nonlinear and nonlocal problem, causing the magnetic system to depend on its history (hysteresis). For simple cases, magnetisation curves  $M(H)$  can be predicted by minimising the total magnetic free energy  $E_T$  and solving the metastable magnetisation states. Fig 2.1 shows a typical major magnetisation curve  $M(H)$ , which is the variation of the magnetisation as a function of the magnetic field. The characteristic quantities  $M_s$ ,  $\mu_0 H_s$ ,  $M_r$  and  $\mu_0 H_c$  are derived from the magnetisation curve. The saturation magnetisation  $M_s$  is reached at the saturation field  $\mu_0 H_s$ , the remanence  $M_r$  is the residual magnetisation of a saturated specimen put in a null field  $\mu_0 H = 0$  and the coercive field  $\mu_0 H_c$  is the magnetic field required to attain a null magnetisation  $M = 0$ .

The shape of the magnetisation curve gives information about the magnetisation dynamics of a material. This is a result of the balance of the different energy terms in the total magnetic free energy of the system. These terms will be described further in the following sections.

## 2.2.2 Exchange energy and magnetic order

### 2.2.2.1 Exchange energy

The exchange interaction results from the Pauli exclusion principle as a consequence of the indistinguishable nature of the electrons. The effect of the Pauli principle is modelled as a spin-spin interaction by the Heisenberg hamiltonian  $H_{\text{Heis}}$

$$H_{\text{Heis}} = -2 \sum_{i>j} J_{ij} \vec{S}_i \cdot \vec{S}_j \quad (2.2)$$

where  $J_{ij}$  is the exchange integral and  $\vec{S}_i$  (respectively  $\vec{S}_j$ ) is the spin of atom  $i$  (respectively  $j$ ). The sign of the exchange integral  $J$  depends on the magnetic order of the material.  $J > 0$  for a ferromagnet and  $J < 0$  for an antiferromagnet, therefore the Heisenberg hamiltonian favours parallel spins if  $J > 0$  and antiparallel spins if  $J < 0$ .

The expectation value of the Heisenberg hamiltonian (Eq. 2.2) is

$$E_{\text{ex}} = -2 \sum_{i>j} J_{ij} S^2 \cos \theta_{ij} \quad (2.3)$$

where  $\theta_{ij}$  is the angle between the direction of a pair of adjacent spins  $\vec{S}_i$  and  $\vec{S}_j$ . This semiclassical treatment is valid for small  $\theta_{ij}$ . For this condition, one then expands  $\cos \theta_{ij}$  as  $1 - \theta_{ij}^2/2! \dots$  and writes

$$E_{\text{ex}} = JS^2 \sum_{i>j} \theta_{ij}^2 + \text{const.} \quad (2.4)$$

Eq. 2.4 shows that the exchange energy  $E_{\text{ex}}$  of a pair of adjacent spins is proportional to the square of the angle between their direction.

For a continuum treatment of the problem, the angle variation  $\theta_{ij}$  is written as  $a \partial \theta / \partial r$ , where  $a$  is the distance between spins. Eq. 2.4 is written

$$\frac{E_{\text{ex}}}{V} = A \left( \frac{\partial \theta_{ij}}{\partial r_{ij}} \right)^2 = A \left( \frac{\vec{\nabla} \cdot \vec{m}}{m} \right)^2 \quad (2.5)$$

where  $A = JS^2 n / a$  is the exchange stiffness constant in  $\text{J m}^{-1}$  and  $\vec{m}$  is the reduced magnetic moment. In the expression of  $A$ ,  $n$  is the number of atoms per unit cell ( $n = 1$  for simple cubic,  $n = 2$  for *bcc* and  $n = 4$  for *fcc*) and  $a$  is the lattice parameter. One sees from Eq. 2.5 that  $E_{\text{ex}}$  is proportional to the square of the gradient of the magnetisation. If the magnetisation of the material is uniform, i.e.  $\vec{\nabla} \cdot \vec{m} = 0$ , the exchange energy density  $E_{\text{ex}}$  is minimised and null [62]. In this case, there is a magnetic order and the magnetic moments are aligned.

## 2.2.2.2 Magnetic order

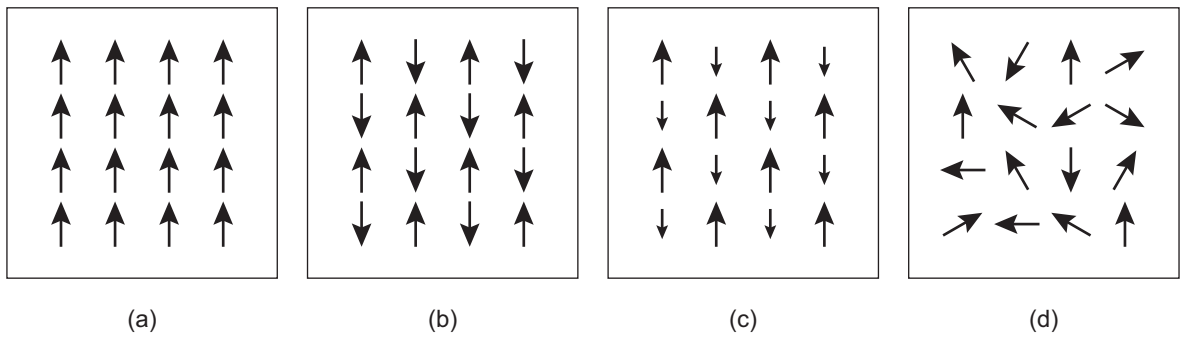


Figure 2.2 – Schematics of the three major magnetic orders, (a) ferromagnetism, (b) antiferromagnetism and (c) ferrimagnetism. (d) Noninteracting magnetic moments do not show magnetic order (paramagnetism). Each arrow represents a single atomic magnetic moment, the norm is symbolised by the length of the arrow.

The exchange interaction is responsible for the magnetic order of materials. From this interaction, three major magnetic orders are reported:

**Ferromagnetism** The exchange integral  $J$  is positive, therefore the Heisenberg hamiltonian (Eq. 2.2) is minimised for parallel spins. The magnetic moments are aligned, in a parallel fashion (Fig. 2.2(a)). The magnetisation of a ferromagnet is spontaneous, even with a null magnetic field.

**Antiferromagnetism** Antiferromagnetism is often reported from transition metal materials, in particular oxides. The exchange integral  $J$  is negative, therefore the Heisenberg hamiltonian is minimised for antiparallel spins. The magnetic moments are aligned, the magnetic structure is of two interpenetrating sublattices of contrary magnetic moments (Fig. 2.2(b)). The vector sum of the magnetic moments is zero, as the two antiparallel sublattices compensate, and the spontaneous magnetisation is null.

**Ferrimagnetism** The magnetic structure of ferrimagnetic materials, likewise to antiferromagnetism, is of two sublattices of contrary magnetic moments. The norm of these magnetic moments is, however, not equal (Fig. 2.2(c)). The vector sum of the magnetic moments is, therefore, nonzero and the spontaneous magnetisation is not null.

Thermal agitation has an effect on the magnetic order. A high thermal energy may overcome the exchange energy and rotate randomly the magnetic moments, suppressing the magnetic order. The magnetic order transition is characterised by a critical temperature, for which the thermal energy and the exchange energy compensate. This critical temperature is the Curie temperature  $\theta_C$  for ferromagnetic and ferrimagnetic materials and the Néel temperature  $\theta_N$  for antiferromagnetic materials. For  $T < \theta_C$  or  $\theta_N$ , the magnetic moments are stable and the material shows a spontaneous magnetic order. For  $T > \theta_C$  or  $\theta_N$ , the magnetic moments are noninteracting and the material does not show magnetic order, it is paramagnetic (Fig. 2.2(d)).

## 2.2.3 Magnetic anisotropy

### 2.2.3.1 Magnetostatic anisotropy

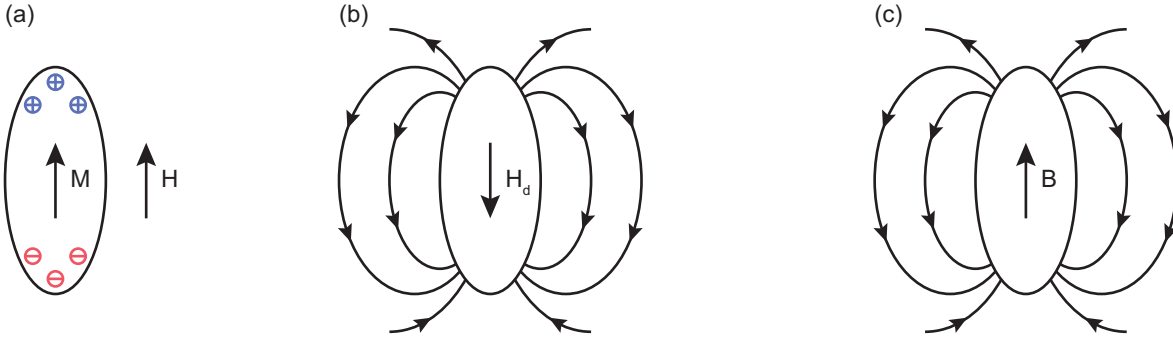


Figure 2.3 – Schematics of the magnetic fields of an ellipsoid particle. (a) The magnetisation  $\vec{M}$  goes from the minus (south) to the plus (north) magnetic pole of the particle and produces (b) a demagnetising field  $\vec{H}_d$  with an opposite direction. (c)  $\vec{B} = \mu_0(\vec{H} + \vec{M})$  is the magnetic flux field.

The magnetostatic anisotropy is a consequence of the magnetic field induced by the magnetisation  $\vec{M}$  (Fig. 2.3(a)), the demagnetising field  $\vec{H}_d$ . The demagnetising field  $\vec{H}_d$  is contrary to the magnetisation  $\vec{M}$  of the magnet and lowers it (Fig. 2.3(b)). From the definition of the magnetic flux field  $\vec{B} = \mu_0(\vec{H} + \vec{M})$  (Fig. 2.3(c)) and Maxwell's equation  $\vec{\nabla} \cdot \vec{B} = 0$ , one writes the demagnetising field  $H_d$  as

$$\vec{\nabla} \cdot \mu_0 \vec{H}_d = -\vec{\nabla} \cdot \mu_0 \vec{M} \quad (2.6)$$

The magnetostatic energy  $E_{ms}$ , expressing the interaction between the magnetisation vector field  $\vec{M}$  and the demagnetising field  $\vec{H}_d$ , is

$$E_{ms} = -\frac{1}{2} \mu_0 \int \vec{H}_d \cdot \vec{M} dV \quad (2.7)$$

where the integration is done over the volume  $V$  of the magnet and the factor  $1/2$  expresses the fact that  $E_{ms}$  is the consequence of interaction of the magnetisation with the demagnetising field it creates.

For a particle with an arbitrary shape, the demagnetising field  $\vec{H}_d$  can be computed only numerically. But, qualitatively,  $\vec{H}_d$  drives the magnetisation  $\vec{M}$  to align along the long axis of the particle. For an ellipsoidal magnet, the demagnetising field  $\vec{H}_d$  is calculated analytically by

$$\vec{H}_d = -N\vec{M} \quad (2.8)$$

where  $N$  is a demagnetisation factor and a tensor function of the magnet shape. In the case of an ellipsoid,  $N$  is a diagonal tensor and the internal field is uniform, so it has an analytical solution. The demagnetisation factor  $N$  is separated in three factors  $N_i$ , which satisfy the

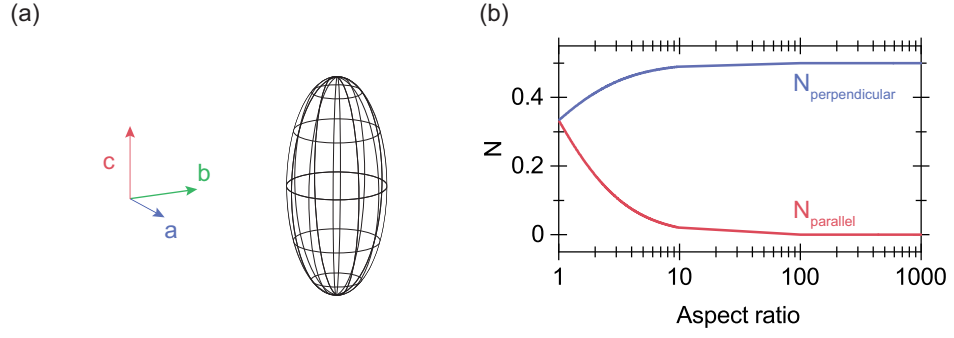


Figure 2.4 – (a) Schematics of a prolate ellipsoid. (b) Parallel  $N_{\parallel}$  and perpendicular  $N_{\perp}$  demagnetisation factors as a function of the aspect ratio of the ellipsoid.

condition  $N_a + N_b + N_c = 1$  where  $a$ ,  $b$  and  $c$  are the axes. It is possible to model a wire as a prolate ellipsoid with  $a = b \ll c$  (Fig. 2.4(a)) and define a parallel demagnetisation factor  $N_{\parallel} = N_c$  and a perpendicular demagnetisation factor  $N_{\perp} = N_{a,b}$ .  $N_{\parallel}$  is defined as [63]

$$N_{\parallel} = \frac{1}{AR^2 - 1} \left[ \frac{1}{2\sqrt{AR^2 - 1}} \ln \left( \frac{AR + \sqrt{AR^2 - 1}}{AR - \sqrt{AR^2 - 1}} \right) - 1 \right] \quad (2.9)$$

where  $AR = c/a$  is the aspect ratio of the ellipsoid. As seen on Fig. 2.4(b), in the case of a thin wire,  $AR \gg 10$  and  $N_{\parallel} \rightarrow 0$ .

From Eq. 2.7 and Eq. 2.8, the magnetostatic energy is transformed as

$$E_{ms} = \frac{\mu_0 M_s^2}{2} V (N_a \hat{m}_a^2 + N_b \hat{m}_b^2 + N_c \hat{m}_c^2) \quad (2.10)$$

where  $\hat{m}_i$  is the direction cosine of the magnetisation  $M_i$  in the axes  $a$ ,  $b$  and  $c$ . This expression of  $E_{ms}$  shows how it relies on the demagnetisation factor  $N_i$  and the shape. From the definition of the parallel and the perpendicular demagnetisation factors, one writes

$$E_{ms} = \frac{\mu_0 M_s^2}{2} V (N_{\perp} \sin^2 \theta + N_{\parallel} \cos^2 \theta) \quad (2.11)$$

where  $\theta$  is the angle between the magnetisation and the  $c$ -axis and  $N_{\parallel} = 1 - 2N_{\perp}$ . This equation is equivalent to

$$E_{ms} = \frac{\mu_0 M_s^2}{2} V N_{\parallel} + \frac{1}{4} \mu_0 M_s^2 V (1 - 3N_{\parallel}) \sin^2 \theta. \quad (2.12)$$

The first term of this equation is constant as a function of the magnetisation direction, therefore it is irrelevant in the magnetostatic anisotropy energy expression for minimising  $E_{ms}$ . Then,

the magnetostatic energy can be expressed as

$$E_{\text{ms}} = \frac{\mu_0 M_s^2}{4} V (1 - 3N_{\parallel}) \sin^2 \theta \quad (2.13)$$

In the case of a thin wire,  $N_{\parallel} \rightarrow 0$  and one writes the magnetostatic volume energy and the magnetostatic anisotropy constant  $K_{\text{ms}}$

$$\begin{aligned} \frac{E_{\text{ms}}}{V} &= \frac{\mu_0 M_s^2}{4} \sin^2 \theta \\ &= K_{\text{ms}} \sin^2 \theta \end{aligned} \quad (2.14)$$

where  $K_{\text{ms}} = \mu_0 M_s^2 / 4$ . The magnetostatic anisotropy is proportional to  $M_s^2$  and is uniaxial.  $E_{\text{ms}}/V$  is minimised for  $\theta = 0$ , that is a magnetisation  $\vec{M}$  parallel to the  $c$ -axis of the wire. Consequently, if  $E_{\text{ms}}$  is the sole source of magnetic anisotropy, a wire has an easy axis of magnetisation along its long axis [64].

### 2.2.3.2 Magnetocrystalline anisotropy

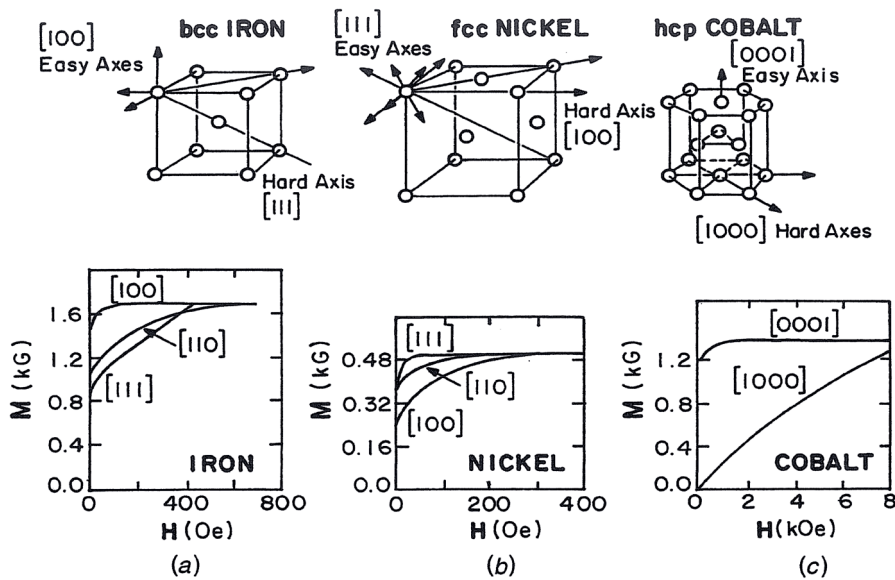


Figure 2.5 – Crystalline structure and magnetisation curves for different crystallographic directions of typical ferromagnetic single crystal materials, (a) body-centred cubic Fe, (b) face-centred cubic Ni and (c) hexagonal close-packed Co (reproduced from [62]).

The magnetocrystalline anisotropy expresses the tendency of the magnetisation to align along one or more crystallographic directions. It stems from the coupling of the spin part of the magnetic moment to the electronic orbital (spin-orbit coupling), and the chemical bonding

of the orbitals with the environment of the atoms (crystalline electric field). Due to the crystalline electric field, certain orientations of the electronic orbitals are energetically preferred. Because of the spin-orbit coupling, the anisotropy of the electronic orbitals leads to a magnetic anisotropy [65].

The consequences of the magnetocrystalline anisotropy are observed in Fig. 2.5, which shows the structure and the magnetisation curves of Fe, Ni and Co. It is readily seen that the magnetisation process depends on the direction of the magnetic field. In Fe (Fig. 2.5(a)), the [100] axis is an easy axis and the [111] axis is a hard axis of magnetisation. A contrary situation is seen in Ni (Fig. 2.5(b)). Furthermore, the  $c$ -axis of hexagonal Co (Fig. 2.5(c)) is an easy axis and its basal plane is very hard to saturate.

**Uniaxial anisotropy** In the case of hexagonal Co (Fig. 2.5(c)), the magnetisation vector  $\vec{M}$  aligns along the  $c$ -axis, in a way that minimises the energy. This magnetic anisotropy is uniaxial and is often found in hexagonal and tetragonal crystals. One can write the uniaxial anisotropy density as a power series of the form

$$\begin{aligned} \frac{E_{mc}^{\text{uni}}}{V} &= \sum_n K_n^{\text{uni}} \sin^{2n} \theta \\ &= K_0^{\text{uni}} + K_1^{\text{uni}} \sin^2 \theta + K_2^{\text{uni}} \sin^4 \theta + \dots \end{aligned} \quad (2.15)$$

where  $\theta$  is the angle between the easy axis and the magnetisation  $\vec{M}$ , and  $K_0^{\text{uni}}$ ,  $K_1^{\text{uni}}$  and  $K_2^{\text{uni}}$  are the uniaxial anisotropy constants.  $K_0^{\text{uni}}$  is meaningless for the anisotropic properties, as it is not dependent on the direction of the magnetisation  $\theta$ , and for the minimisation of  $E_{mc}^{\text{uni}}$ . For hexagonal Co,  $K_1^{\text{uni}}$  and  $K_2^{\text{uni}}$  are in the order of  $10^5 \text{ J m}^{-3}$  and  $10^4 \text{ J m}^{-3}$ , respectively [66]. If the second order of the uniaxial anisotropy constant  $K_2^{\text{uni}}$  is negligible compared to the first order, for example with hexagonal Co, Eq. 2.15 is simplified as

$$\frac{E_{mc}^{\text{uni}}}{V} = K_1^{\text{uni}} \sin^2 \theta. \quad (2.16)$$

The shape of the anisotropy energy surface is dependent on the sign of  $K_1^{\text{uni}}$ , as pictured in Fig. 2.6. After Eq. 2.16, when  $K_1^{\text{uni}} > 0$  (Fig. 2.6(a)), the magnetisation minimises the energy for  $\theta = 0$  and  $\theta = \pi$ , thus by aligning along the  $z$ -axis. The  $z$ -axis is an easy axis of magnetisation. When  $K_1^{\text{uni}} < 0$ , the minimum of energy is satisfied for  $\theta = \frac{\pi}{2}$ , thus when the magnetisation is aligned in the  $x$ - $y$  plane. The  $x$ - $y$  plane is an easy plane of magnetisation and  $z$  is a hard axis.

**Cubic anisotropy** As seen in Fig. 2.5(b-c), ferromagnetic cubic crystals, like body-centred Fe or face-centred Ni, show a cubic magnetocrystalline anisotropy. The anisotropy energy density

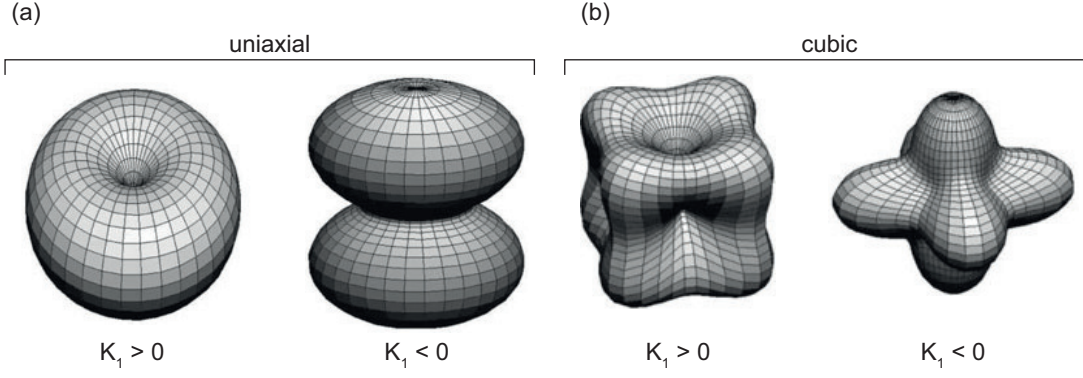


Figure 2.6 – Surfaces of the uniaxial and cubic anisotropy energies for  $K_1 > 0$  and  $K_1 < 0$ . (reproduced from [67]).

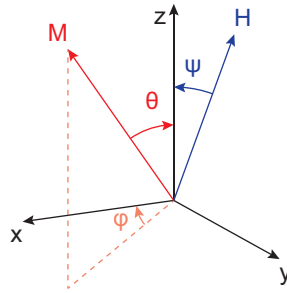


Figure 2.7 – Magnetisation  $\vec{M}$  is defined by a set of three angles ( $\psi$ ,  $\theta$ ,  $\phi$ ).  $\psi$  is the angle between  $\vec{H}$  and the easy axis,  $\theta$  is the angle between  $\vec{M}$  and the easy axis and  $\phi$  is the angle between the projection of  $\vec{M}$  in the  $x$ - $y$  plane and the  $x$ -axis.

can be written as a function of the direction cosines  $\alpha_i$  as

$$\frac{E_{mc}^{\text{cubic}}}{V} = K_0^{\text{cubic}} + K_1^{\text{cubic}} (\alpha_1^2 \alpha_2^2 + \alpha_2^2 \alpha_3^2 + \alpha_3^2 \alpha_1^2) + K_2^{\text{cubic}} (\alpha_1^2 \alpha_2 \alpha_3) + \dots \quad (2.17)$$

where  $K_0^{\text{cubic}}$ ,  $K_1^{\text{cubic}}$  and  $K_2^{\text{cubic}}$  are the cubic anisotropy constants. From the definition of the direction cosines  $\alpha_1 = \sin \theta \cos \phi$ ,  $\alpha_2 = \sin \theta \sin \phi$  and  $\alpha_3 = \cos \theta$  (Fig. 2.7), Eq. 2.17 is transformed in spherical coordinates as

$$\frac{E_{mc}^{\text{cubic}}}{V} = K_1^{\text{cubic}} \frac{\sin^4 \theta \sin^2 2\phi + \sin^2 2\theta}{4} + K_2^{\text{cubic}} \frac{\sin^2 2\theta \sin^2 2\phi \sin^2 \theta}{16}. \quad (2.18)$$

$K_0^{\text{cubic}}$  is meaningless for the anisotropic properties in Eq. 2.17 as it is not dependent on  $\alpha_i$ . At low temperatures, the second order cubic anisotropy constant  $K_2^{\text{cubic}}$  is often smaller with respect to  $K_1^{\text{cubic}}$  and can be omitted [68].

Fig. 2.6 shows the plot of cubic anisotropy energy surfaces. When  $K_1^{\text{cubic}} > 0$ , the magnetisation minimises the energy by aligning along the  $\langle 100 \rangle$  directions. This case is observed in

body-centred Fe (Fig. 2.5(c)), where  $\langle 100 \rangle$  directions are easy axes of magnetisation. When  $K_1^{\text{cubic}} < 0$ , the minimum of energy is satisfied when  $\vec{M}$  aligns along the diagonals, that is the  $\langle 111 \rangle$  directions. This situation is observed in face-centred Ni (Fig. 2.5(b)).

### 2.2.3.3 Magnetoelastic anisotropy

The magnetoelastic anisotropy is related to the magnetocrystalline anisotropy and stems from the spin-orbit coupling. Indeed, when the lattice is under a mechanical strain, the relative position of the magnetic moments is shifted, causing an energy variation and thus resulting in an additional anisotropy contribution. In the case of a strained cubic material, the anisotropy energy density  $e_a^{\text{mag}} + e_{\text{elast}}$  reads [69]

$$\begin{aligned} e_a^{\text{mag}} &= K \left( \alpha_1^2 \alpha_2^2 + \alpha_2^2 \alpha_3^2 + \alpha_3^2 \alpha_1^2 \right) \\ &\quad + B_1 \left( \alpha_1^2 \epsilon_{xx} + \alpha_2^2 \epsilon_{yy} + \alpha_3^2 \epsilon_{zz} \right) + B_2 \left( \alpha_1 \alpha_2 \epsilon_{xy} + \alpha_2 \alpha_3 \epsilon_{yz} + \alpha_3 \alpha_1 \epsilon_{zx} \right) \\ e_{\text{elast}} &= \frac{1}{2} c_{11} \left( \epsilon_{xx}^2 + \epsilon_{yy}^2 + \epsilon_{zz}^2 \right) + \frac{1}{2} c_{44} \left( \epsilon_{xy}^2 + \epsilon_{yz}^2 + \epsilon_{zx}^2 \right) + c_{12} \left( \epsilon_{yy} \epsilon_{zz} + \epsilon_{zz} \epsilon_{xx} + \epsilon_{xx} \epsilon_{yy} \right) \end{aligned} \quad (2.19)$$

where  $e_a^{\text{mag}}$  is the magnetic anisotropy energy density and  $e_{\text{elast}}$  is the pure elastic energy density.  $\alpha_i$  are the direction cosines,  $B_1$  and  $B_2$  are the magnetoelastic coupling constants,  $\epsilon_{ij}$  is the strain tensor and  $c_{ij}$  are the elastic moduli. Three types of terms are identified in Eq. 2.19. The first-type term, only depending on the direction of magnetisation  $\alpha_{ij}$ , is the magnetocrystalline anisotropy previously discussed. The second-type terms, linear in the strain components and dependent on the direction cosines, correspond to the magnetoelastic energy density. The coefficients  $B_1$  and  $B_2$  are the magnetoelastic coupling constants and express the coupling between the strain tensor  $\epsilon_{ij}$  and the direction of magnetisation  $\alpha_{ij}$ . At last, the third-type terms, quadratic in the strain components and independent of the direction cosines, represent the pure elastic energy density [62].

The magnetoelastic coupling constants  $B_1$  and  $B_2$  are related to the magnetostriction coefficients  $\lambda_{001}$  and  $\lambda_{111}$ .  $\lambda_{001}$  and  $\lambda_{111}$  are the strain measured in the  $[001]$  and  $[111]$  directions, respectively, in a magnet saturated in the same directions. They are defined as

$$\begin{aligned} \lambda_{001} &= -\frac{2}{3} \frac{B_1}{c_{11} - c_{12}} \\ \lambda_{111} &= -\frac{1}{3} \frac{B_2}{c_{44}}. \end{aligned} \quad (2.20)$$

From this definition, one may rewrite the second-type terms in Eq. 2.19, representing the magnetoelastic energy density. In the case of a nanowire distorted along the  $[001]$  direction of the cubic crystal, of which the  $[001]$  planes are homogeneously compressed (i.e.  $\epsilon_{xx} = \epsilon_{yy} = \epsilon_{zz}$ )

and the shear strains are considered to be zero, the magnetoelastic energy density reads

$$\begin{aligned}\frac{E_{me}}{V} &= \frac{3}{2} \lambda_{001} (c_{11} - c_{12}) (\epsilon_{zz} - \epsilon_{rr}) \sin^2 \theta \\ &= K_{me} \sin^2 \theta.\end{aligned}\quad (2.21)$$

This equation shows that the magnetoelastic energy density of a nanowire is uniaxial. Furthermore,  $\frac{E_{me}}{V}$  may turn an easy axis into an easy plane of magnetisation, and conversely, according to its sign (i.e. the sign of  $\lambda_{001}$  and  $(\epsilon_{zz} - \epsilon_{rr})$ ).

#### 2.2.4 Stoner-Wohlfarth model

A magnetic particle that is too small for the creation of a magnetic domain wall (i.e. an interface separating two magnetic domains) can be considered as a single magnetic domain of homogeneous magnetisation (macrospin). This situation is observed in particles containing less than  $10^4$ - $10^6$  Bohr magnetons and magnetisation rotation in this type of system is expected to be uniform [14]. The reversal of a single magnetic domain can be predicted by the Stoner-Wohlfarth model [70].

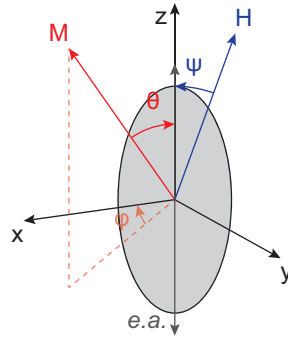


Figure 2.8 – Sketch of a Stoner-Wohlfarth particle of magnetisation  $\vec{M}$  in an external field  $\vec{H}$ .  $\psi$  is the angle between  $\vec{H}$  and the easy axis,  $\theta$  is the angle between  $\vec{M}$  and the easy axis and  $\phi$  is the angle between the projection of  $\vec{M}$  in the  $x$ - $y$  plane and the  $x$ -axis.

For the simple case of an elongated Stoner-Wohlfarth particle with an uniaxial anisotropy (Fig. 2.8), the total magnetic energy (Eq. 2.1) is the balance of the anisotropy energies and the Zeeman energy. For a Stoner-Wohlfarth particle, the exchange energy is zero because the magnetisation is homogeneous. Therefore, the magnetisation reversal is that of an assembly of noninteracting particles and modelled as the reversal of a single moment. In the following developments, the anisotropy is considered as the contribution of an uniaxial magnetocrystalline anisotropy and a magnetostatic anisotropy. The latter is due to the aspect ratio of the particle, modelled as a prolate ellipsoid. The easy axis of magnetisation (EA) is along its long axis.

Thus, the total magnetic energy is

$$E_T = \int_V \left\{ \frac{E_a}{V} - \frac{\mu_0 \vec{M} \cdot \vec{H}_d}{2} - \mu_0 \vec{M} \cdot \vec{H} \right\} dV \quad (2.22)$$

and from this equation the total magnetic energy density is further expressed as

$$\frac{E_T}{V} = \frac{E_a}{V} + \frac{\mu_0 M_s^2}{4} \sin^2 \theta - \mu_0 M_s H (\cos \theta \cos \psi + \sin \theta \sin \psi \cos \phi) \quad (2.23)$$

where  $(\theta, \phi)$  and  $\psi$  are the angles defining  $\vec{M}$  and  $\vec{H}$ , respectively (Fig. 2.8). If the problem is simplified to a planar problem ( $\phi = 0$ ) and the magnetocrystalline and magnetostatic anisotropies are enclosed in an effective anisotropy, the total energy reads

$$E_T = K_{\text{eff}} V \sin^2 \theta - \mu_0 M_s H V \cos(\theta - \psi) \quad (2.24)$$

where  $K_{\text{eff}} = K_{mc} + K_{ms}$  is the effective anisotropy constant.

For  $\vec{H}$  along the easy axis ( $\psi = 0^\circ$ ), the minimisation of Eq. 2.24 with respect to  $\theta$  gives

$$K_{\text{eff}} \sin \theta \cos \theta - \mu_0 M_s H \sin \theta = 0. \quad (2.25)$$

The switching of  $\vec{M}$  is conditioned by  $\cos \theta = \pm 1$  and the coercive field  $H_c$  is consequently defined as

$$\mu_0 H_c = \frac{2K_{\text{eff}}}{M_s}. \quad (2.26)$$

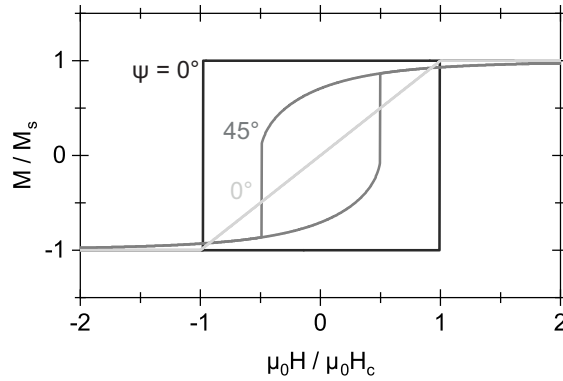


Figure 2.9 – Angular dependence of  $M(H)$  to the direction of the external field  $\vec{H}$ , according to the Stoner-Wohlfarth model. The particle is assumed to consist of a single magnetic domain (macrospin).

$M(H)$  curves are derived from the minimisation of Eq. 2.24. As plotted in Fig. 2.9, one can retrieve the angular dependence of the  $M(H)$  curves for a specified  $\psi$ . It is readily seen that

the shape of the hysteresis curves depends on the direction of  $\vec{H}$ . For a magnetic field  $\vec{H}$  along the easy axis ( $\psi = 0^\circ$ ), the  $M(H)$  curve is square.  $\vec{M}$  reverses abruptly as the magnetic field reaches the coercive field value  $H_c$ . The  $M(H)$  curve shrinks by increasing  $\psi$  from  $0^\circ$  to  $90^\circ$ . For  $\psi = 45^\circ$ , the particle switches at half the field strength needed for a reversal in the easy axis ( $\psi = 0^\circ$ ). For a magnetic field  $\vec{H}$  along the hard axis ( $\psi = 90^\circ$ ), the hysteresis curve disappears and  $\vec{M}$  aligns along  $\vec{H}$  with increasing field strength.

In the Stoner-Wohlfarth model, as the coercive field in the easy axis is the same as the saturation field needed to reverse  $\vec{M}$  in the hard axis and compensate the anisotropy, the coercive field  $H_c$  is equal to the anisotropy field  $H_a$ . However, as a rule of thumb,  $H_c$  is less than  $H_a$  in ferromagnetic nanowires [71]. This reduction of the coercive field is caused by shape or structural defects, thus real magnets depart from the ideal Stoner-Wohlfarth particles. On the other hand, defects in the material also cause localisation of the reversal [72, 73]. Because of these defects, nucleation is localised at weak points in the particle, causing a domain wall. The reversal then proceeds by propagation of the domain wall in the particle. The reversal is consequently inhomogeneous. Localisation and inhomogeneous reversal are discussed in Section 5.4.

## 2.2.5 Temperature effects

### 2.2.5.1 Superparamagnetism

A particle of magnetic volume  $V$  and anisotropy  $K$  presents two energy minima, separated by an energy barrier  $E_b = KV$ . The transition from one minimum to the other, that is the magnetisation reversal, can be thermally activated for  $T \neq 0$ . In other terms, thermal activation can surmount the anisotropy energy barrier even though  $k_B T < KV$  and spontaneously reverse the moment. The typical time between two spontaneous reversals is given by the Néel-Arrhenius law [74]

$$\tau = \tau_0 e^{\frac{KV}{k_B T}} \quad (2.27)$$

where  $\tau$  is the typical time, also known as the Néel relaxation time and  $\tau_0$  is an attempt time characteristic of the material, typically between  $10^{-12}$  s and  $10^{-9}$  s. Eq. 2.27 shows that a thermally activated system makes  $\tau_0^{-1}$  attempts per second to surmount the energy barrier, and that the probability of a spontaneous reversal is higher the larger  $k_B T$  is.

The measured magnetic state of a sample is defined by its measurement time  $t_m$ , typically a hundred seconds for a laboratory experiment. When the relaxation time is longer than the measurement time ( $\tau > t_m$ ), the particles are in the blocked regime and a nonzero magnetisation is measured. Conversely ( $\tau < t_m$ ), the spontaneous magnetisation is zero and the particles are in the superparamagnetic regime [64]. A critical volume  $V_c$  below which the particle is in superparamagnetic regime is derived from Eq. 2.27. For a typical time  $\tau = t_m = 100$  s and an

attempt time of  $10^{-9}$  s, the critical volume  $V_c$  is

$$V_c = \ln\left(\frac{\tau}{\tau_0}\right) \frac{k_B T}{K} \approx \frac{25k_B T}{K}. \quad (2.28)$$

Alternatively, a critical temperature  $T_b$ , called blocking temperature, is defined as

$$T_b = \frac{KV}{25k_B}. \quad (2.29)$$

For  $T < T_b$  the particles of volume  $V$  are in the blocked state. For  $T > T_b$ , the moments of the particles randomly flip and the sample is in the superparamagnetic regime, analogous to paramagnetism. In this situation, the magnetisation is zero when the external field is zero, and aligns with the external field when it is nonzero.

### 2.2.5.2 Coercive field

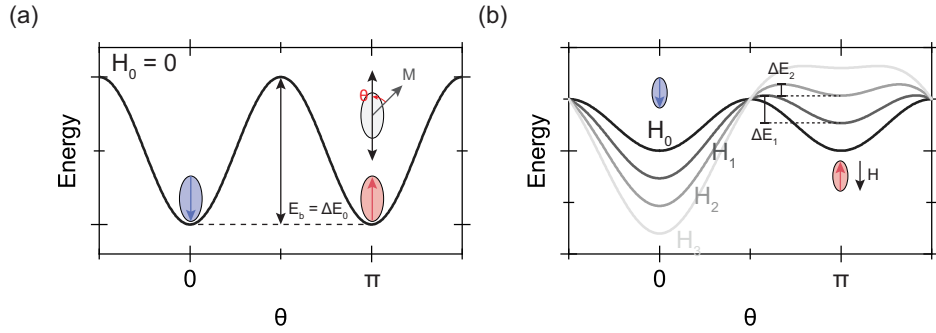


Figure 2.10 – Magnetic energy landscapes  $E(\theta)$  plotted from Eq. 2.24.  $\theta$  is the angle between  $\vec{M}$  and the easy axis. (a) For  $H = 0$ , the energy landscape shows two minima at  $\theta = 0$  and  $\theta = \pi$  and the height of the energy barrier is  $E_b = \Delta E_0$ . (b) Energy landscapes for different values of  $H$  ( $H_0 < H_1 < H_2 < H_3$ ). The increasing of  $H$  causes a decreasing of the energy barrier  $\Delta E$ .

Fig. 2.10 shows the energy landscapes plotted from Eq. 2.24 with an external field  $\vec{H}$  along the easy axis. For  $H = 0$  (Fig. 2.10(a)), the total magnetic energy is a sinusoidal function of  $\theta$  with two minima at  $\theta = 0$  and  $\theta = \pi$ . The height of the energy barrier  $E_b$  between the two minima is defined as the difference  $\Delta E_b = E_{\max} - E(\theta = 0)$  and is equal to  $KV$  for a zero external field. For  $H \neq 0$ , the height of the energy barrier is computed by minimising Eq. 2.24 (i.e.  $\partial E_T(\theta)/\partial\theta$ ), giving three solutions for  $\theta = 0$ ,  $\theta = \cos^{-1}(H/H_a)$  and  $\theta = \pi$ .  $\theta = 0$  and  $\theta = \pi$  are the previously discussed minima and  $\theta = \cos^{-1}(H/H_a)$  is the maximum, where  $\mu_0 H_a = 2K/M_s$ . The height of the energy barrier for  $H \neq 0$  is therefore

$$\Delta E_b = KV \left(1 - \frac{H}{H_a}\right)^2. \quad (2.30)$$

The temperature dependence of the coercive field can be shown by inserting the barrier energy equation (Eq. 2.30) into the Néel-Arrhenius law (Eq. 2.27). Introducing  $E_b = 25k_B T$  and identifying the magnetic field  $H$  as the coercive field yields

$$H_c = H_c^{(0)} \left( 1 - \left( \frac{25k_B T}{KV} \right)^{1/2} \right) \quad (2.31)$$

where  $H_c^{(0)} = H_a$  is the coercive field at  $T = 0$  K. For real materials, a phenomenological description of the coercive field is given by replacing the exponent in Eq. 2.31 by

$$H_c = H_c^{(0)} \left( 1 - \left( \frac{25k_B T}{KV} \right)^{1/m} \right) \quad (2.32)$$

where  $m = 2$  for Stoner-Wohlfarth particles and  $m = \frac{3}{2}$  for real magnets [75]. This equation shows the drop of the coercive field  $H_c$  according to a power law of the temperature [76].

## 2.3 Plasmonics

### 2.3.1 Charge polarisation

#### 2.3.1.1 Static electric field

Plasmons are collective oscillations of the free electrons in a metal. In a confined nanoparticle, plasmons are defined as *localised*, to distinguish them from surface plasmons, which are electronic oscillations at the interface between two materials extending over two dimensions of space.

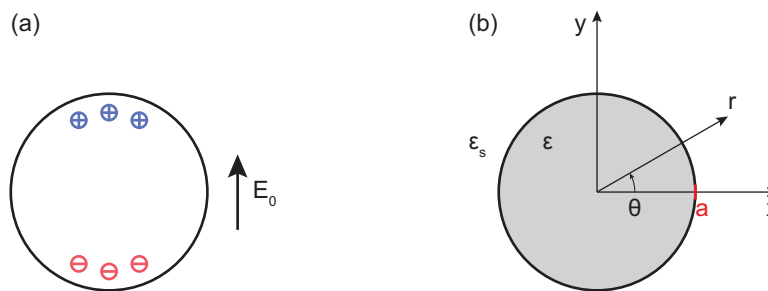


Figure 2.11 – Schematics of a spherical metal nanoparticle. (a) The charge in a metal sphere is polarised by a static and uniform external electric field  $E_0$ . (b) Spatial description of a metal sphere of permittivity  $\epsilon$  in a dielectric medium  $\epsilon_s = n_s^2$ .

The excitation of a metal nanoparticle by a static electric field forces the electrons to be displaced from equilibrium, thus leading to a charge accumulation at the boundaries of the nanoparticle (Fig. 2.11). Such displacement entails a restoring force, pushing the charges to

move back to the initial position when the perturbation is switched off. The magnitude of charge displacement is defined by the dipolar moment  $\vec{p}$ , collinear with the applied electric field  $\vec{E}_0$  and reads [77]

$$\vec{p} = \epsilon_0 \alpha \vec{E}_0 \quad (2.33)$$

where  $\alpha$  is the polarisability, linking the electric field  $\vec{E}_0$ , causing the displacement, and the dipolar moment  $\vec{p}$ , being the magnitude of charge displacement.  $\epsilon_0$  is the electric constant. For a metal sphere of radius  $a$  and permittivity  $\epsilon$  in a medium of refractive index  $n_s = \sqrt{\epsilon_s}$ , the polarisability  $\alpha$  is defined as

$$\begin{aligned} \alpha &= 4\pi\epsilon_s a^3 \\ &= 3V\epsilon_s \end{aligned} \quad (2.34)$$

Its surrounding electric potential reads  $\phi(r, \theta) = E_0 \left( r - \frac{a^3}{r^2} \right) \cos \theta$  in spherical coordinates. The radial derivative  $\partial\phi/\partial r$  shows that the normal component of the electric field at the surface of the sphere is

$$E = 3E_0. \quad (2.35)$$

It is readily seen in this equation that the electric near-field at the surface is not dependent on the refractive index of the medium  $n_s$ , nor on the radius of the sphere. The maximum electric near-field, at each pole in the direction of the applied electric field  $\vec{E}_0$ , is three times larger than  $E_0$ . Therefore, the near-field intensity is nine times larger than that of  $E_0$ . This strong enhancement of the electric near-field, linked to the charge polarisation, is a distinctive property of metal particles. A plasmonic resonance can therefore drive the near-field intensity above  $9I_0$ .

As discussed before, the displacement of the charges caused by the electric field entails a restoring force in the particle, moving back the charges to the stable position. A restoring force can yield a resonance effect if the system is excited at the proper frequency, as seen in a spring-mass system (resonator). In the case of a metal particle, its excitation with a time-harmonic electric field (light) at the proper wavelength causes a plasmonic resonance.

### 2.3.1.2 Time-harmonic electric field

Firstly, let us assume that the system discussed in this section is in a quasi-static approximation. The quasi-static approximation assumes that the phase of the time-harmonic electric field is constant in the nanoparticle, thus retardation effects due to electromagnetic interactions of distant charges in the particle are neglected. Therefore, it is only relevant for a very small particle, typically with a size inferior than the wavelength ( $ka < 1$ ), and one can consider it as a pure dipole. The (complex) polarisability  $\underline{\alpha}$  of a sphere with a permittivity  $\underline{\epsilon}(\omega)$  reads

$$\underline{\alpha} = 3V\epsilon_s \underline{\xi} \quad (2.36)$$

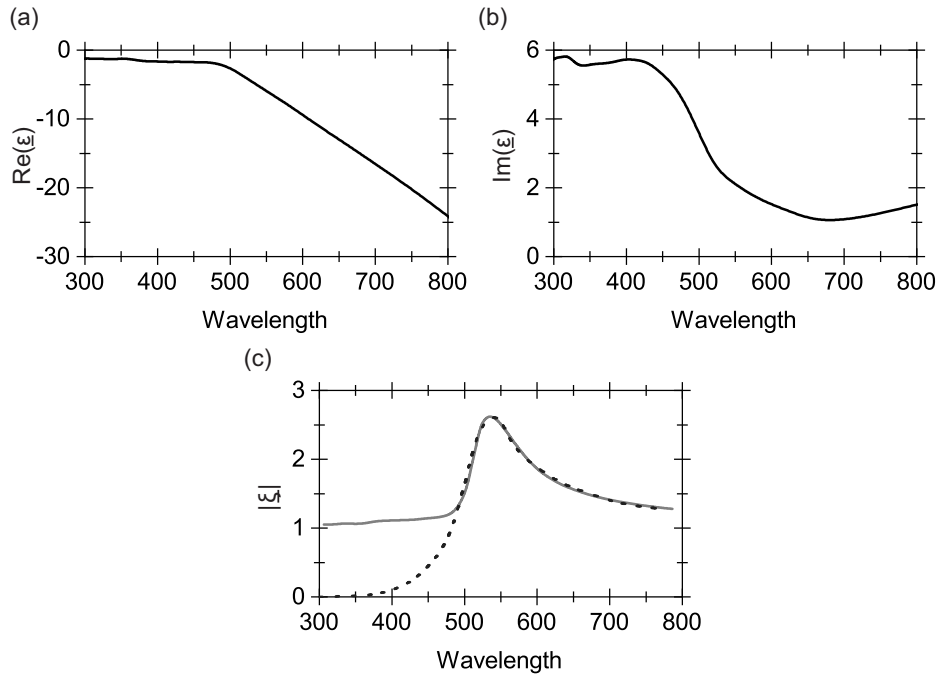


Figure 2.12 – (a) Real part and (b) imaginary part of the permittivity  $\underline{\epsilon}$  of Au, measured by Johnson and Christy [78]. (c) Norm of the enhancement factor  $|\underline{\xi}|$  of an Au nanosphere (solid line) and of a conventional resonator (dashed line) (adapted from [77]).

where  $\underline{\xi}$  is the enhancement factor defined as

$$\underline{\xi} = \frac{\underline{\epsilon}(\omega) - \epsilon_s}{\underline{\epsilon}(\omega) + 2\epsilon_s}. \quad (2.37)$$

The enhancement factor  $\underline{\xi}$  translates the charge oscillation in the nanosphere in amplitude and in phase. A plasmonic resonance occurs when the polarisability  $\underline{\alpha}$  is maximum, thus it is conditioned by a maximum  $\underline{\xi}$ . In the case of an Au nanosphere, a resonance is predicted at 530 nm, as seen in Fig. 2.12(c). This situation is observed when the denominator of  $\underline{\xi}$  is minimum, that is to say at the Fröhlich condition  $\Re(\underline{\epsilon}) = -2\epsilon_s$ . This condition can be satisfied in metals as the real part of their permittivity is negative (Fig. 2.12(a)).

At short wavelengths (or high frequencies), plasmon resonance diverges from the typical resonator case. Fig. 2.12(c) shows the response of a Au nanosphere (solid line), and that of a typical resonator (dashed line). It is readily seen that the plasmon resonance amplitude of the Au nanosphere tends to 1 and not to zero at short wavelengths. Indeed, this is caused by d electrons in the metal, which can be optically excited at short wavelengths ( $\lambda < 500$  nm) and which are able to screen the applied field.

The maximum electric field in the vicinity of a nanosphere in a time-harmonic field reads

$$E = (1 + 2\underline{\xi}) E_0. \quad (2.38)$$

This equation is developed into two terms. The first term  $E_0$  translates the applied electric field, and the second term  $2\underline{\xi}E_0$  translates the near-field yielded by the charges in the nanosphere.  $2\underline{\xi}E_0$  is cumulative to the total near-field and provides further evidence that  $\underline{\xi}$  represents the electronic oscillation.

## 2.3.2 Localised plasmon resonance

### 2.3.2.1 Optical cross sections

The polarisability  $\underline{\alpha}$  and the enhancement factor  $\underline{\xi}$  of a plasmonic nanoparticle characterise its optical response. Other quantities of interest are the optical cross sections  $\sigma_{\text{sca}}$  and  $\sigma_{\text{abs}}$ , which are linked to the polarisability.  $\sigma_{\text{sca}}$  and  $\sigma_{\text{abs}}$  define the effective surface from which the nanoparticle scatters or absorbs light. They can be calculated from the irradiance  $I$  (i.e. the radiant flux per unit area), and can be used to define scattered and absorbed energies.  $\sigma_{\text{sca}}$  and  $\sigma_{\text{abs}}$  link the scattered and absorbed powers, and the irradiance  $I$  as

$$\begin{aligned} P_{\text{sca}} &= \sigma_{\text{sca}} I \\ P_{\text{abs}} &= \sigma_{\text{abs}} I. \end{aligned} \quad (2.39)$$

The extinction cross section  $\sigma_{\text{ext}}$  is defined as

$$\sigma_{\text{ext}} = \sigma_{\text{sca}} + \sigma_{\text{abs}}. \quad (2.40)$$

Absorption and extinction cross sections can be defined for any particle interacting with light. For a dipolar sphere, cross sections are expressed as a function of the polarisability  $\underline{\alpha}$  as [79]

$$\begin{aligned} \sigma_{\text{sca}} &= \frac{k^4}{6\pi} |\underline{\alpha}^2| \\ \sigma_{\text{abs}} &= k \Im(\underline{\alpha}) \end{aligned} \quad (2.41)$$

Formulae of the optical cross sections were defined thus far for nanospheres.  $\sigma_{\text{sca}}$  and  $\sigma_{\text{abs}}$  can be nevertheless derived for elongated particles thanks to Gans theory. Gans theory is an analytical solution to Maxwell's equation for an ellipsoid in the dipole approximation. In the case of an elongated nanoparticle,  $\sigma_{\text{sca}}$  and  $\sigma_{\text{abs}}$  can be expressed as a function of its aspect

ratio and read [80]

$$\begin{aligned}\sigma_{\text{sca}} &= \frac{8\pi^3 V^2}{9\lambda^4} \epsilon_s^2 \sum_j \frac{1}{P_j} \frac{(\epsilon_1 - \epsilon_s)^2 + \epsilon_2^2}{\left(\epsilon_1 + \frac{(1-P_j)\epsilon_s}{P_j}\right)^2 + \epsilon_2^2} \\ \sigma_{\text{abs}} &= \frac{2\pi V}{3\lambda} \epsilon_s^{3/2} \sum_j \frac{1}{P_j} \frac{\epsilon_2}{\left(\epsilon_1 + \frac{(1-P_j)\epsilon_s}{P_j}\right)^2 + \epsilon_2^2}\end{aligned}\quad (2.42)$$

where  $\underline{\epsilon}(\omega) = \underline{\epsilon}_1(\omega) + i\underline{\epsilon}_2(\omega)$  and  $\epsilon_s$  are the dielectric functions of the particle and the medium, respectively and  $P_j$  is the depolarisation factor in the axes  $a$ ,  $b$  and  $c$  of the ellipsoid.  $P_j$  is defined as

$$\begin{aligned}P_c &= \frac{1-e^2}{e^2} \left[ \frac{1}{2e} \ln \left( \frac{1+e}{1-e} \right) - 1 \right] \\ P_{a,b} &= \frac{1-P_c}{2}\end{aligned}\quad (2.43)$$

where  $e = \sqrt{1 - 1/\text{AR}}$  is the eccentricity of an ellipsoid of aspect ratio AR.

### 2.3.2.2 Particle size and morphology

**Particle size** As implied in Eq. 2.36, polarisability  $\underline{\alpha}$  is proportional to the volume of the nanoparticle. An increase of the particle radius  $r$  causes an increase of the scattering and absorption cross sections, scaling in a nanosphere as  $r^6$  and  $r^3$ , respectively. For small nanoparticles, absorption dominates, however scattering is more significant as the volume increases.

As mentioned previously, the quasistatic approximation holds for small nanoparticles. If the nanoparticle is enlarged, the phase of the perturbation is nonconstant in the particle, cause inhomogeneities of the charge oscillation. Furthermore, if the particle length is longer than the plasmon wavelength (typically 50 nm in Au), retardation effects occur due to electromagnetic interactions of distant charges in the particle. Nonuniformity of the electromagnetic excitation and retardation effects lead to a red-shift of the plasmon resonance [81].

**Morphology** Increasing the volume of the nanoparticle causes a red-shift of the plasmonic resonance. However, this red-shift is limited and, in the case of Au nanoparticles, the resonance cannot be higher than 600 nm. To increase the resonance wavelength, a number of solutions exist: (1) the use of hybrid core-shell nanoparticles, (2) or of dimeric structures separated by a nanometric gap, thus leveraging the dipolar coupling between the particles, (3) the last solution is to elongate the nanoparticle.

One can tune the resonance wavelength by changing the shape of a nanoparticle into an ellipsoid, thus deviating it from a sphere. The asymmetry of the particle leads to the splitting of the plasmonic resonance into two nondegenerate modes of resonance, the transverse and longitudinal modes. The transverse mode lies in the visible range and is related to the radial charge oscillation. The longitudinal mode, of higher amplitude, is in the near-infrared range and corresponds to the charge oscillation along the long axis of the nanoparticle. By increasing the aspect ratio of the nanoparticle, the longitudinal mode of resonance shifts to higher wavelengths. In addition to being dependent to the aspect ratio, the longitudinal mode is highly sensitive to the medium dielectric constant  $\epsilon_s$  [80].

## CHAPTER 3

### EXPERIMENTAL TECHNIQUES

3.1	Introduction . . . . .	35
3.2	Pulsed laser deposition . . . . .	36
3.2.1	Principles of pulsed laser deposition . . . . .	36
3.2.2	Growth of vertically aligned nanocomposites . . . . .	36
3.2.3	Kinetic Monte Carlo modelisation . . . . .	38
3.3	Structural properties . . . . .	41
3.3.1	Transmission electron microscopy . . . . .	41
3.3.1.1	Sample milling . . . . .	41
3.3.1.2	High-resolution transmission electron microscopy . . . . .	41
3.3.1.3	HAADF-STEM and spectromicroscopy . . . . .	42
3.3.2	X-ray diffraction . . . . .	43
3.3.2.1	Out of plane and in plane x-ray diffraction . . . . .	43
3.3.2.2	Synchrotron x-ray diffraction . . . . .	44
3.3.2.3	X-ray reflectivity . . . . .	45
3.4	Physical properties . . . . .	47
3.4.1	Vibrating sample magnetometry . . . . .	47
3.4.2	Magneto-optical Kerr effect . . . . .	47
3.4.2.1	Static magneto-optical Kerr effect . . . . .	47
3.4.2.2	Time-resolved magneto-optical Kerr effect . . . . .	49
3.4.3	Ellipsometry . . . . .	53

### 3.1 Introduction

During this thesis work, several experimental techniques were used to synthesise and characterise hybrid vertically aligned nanocomposite thin films. This chapter starts with the fabrication of VANs by sequential pulsed laser deposition and the specific mechanisms underlying the growth of the nanowires are explained, including by previously studied kinetic Monte Carlo simulations. Then, different experimental techniques used to characterise the structure (x-ray diffraction and transmission electron microscopy), as well as the physical properties (vibrating sample magnetometry, magneto-optical Kerr effect, ellipsometry) of the samples are presented.

## 3.2 Pulsed laser deposition

### 3.2.1 Principles of pulsed laser deposition

Growth of epitaxial thin films using pulsed laser deposition (PLD) was intensively developed in the late eighties for the purposes of the research on CuO-based high-temperature superconductors [82]. PLD is particularly appropriate for oxide thin films growth, in comparison with molecular beam epitaxy or sputtering, as it allows growth in oxygen partial pressure. PLD is in addition discontinuous and allows specific growth dynamics that are exploited in this work.

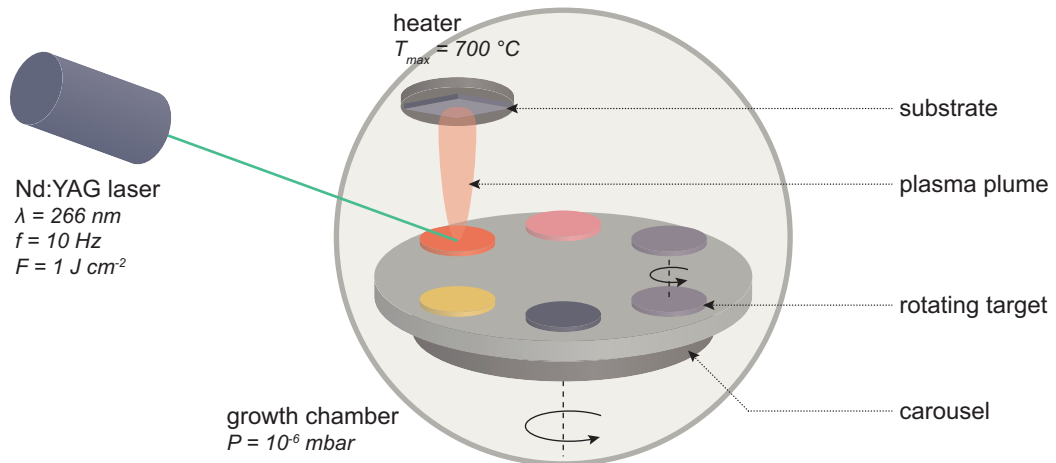


Figure 3.1 – Schematics of the pulsed laser deposition machine.

A typical PLD machine is composed of a pulsed laser and a growth chamber, in which the material targets and the substrate are kept in specific conditions of temperature and pressure (Fig. 3.1). A pulsed laser (from 100 fs to ns) allows an important instantaneous power (from MW to GW), high enough to vaporise and partially ionise the material on the target. The resulting plasma plume contains primarily diatoms, atoms, ions and electrons torn off from the material and provides the material flux for film growth. The material flux is highly directed and normal to the target surface. A too high laser energy or a rough target surface may lead to the evaporation of molecular agglomerates, which are detrimental to the crystal quality of the thin film [83].

### 3.2.2 Growth of vertically aligned nanocomposites

Hybrid nanocomposite thin films presented in this thesis were grown by sequential pulsed laser deposition at the *Institut des NanoSciences de Paris* (CNRS-Sorbonne Université). The substrate was placed 5 cm above the target, receiving matter from the plasma plume created by the laser pulse. The laser source is a quadrupled Nd:YAG laser with a wavelength of 266 nm, operating at a repetition rate of 10 Hz and at a fluence of  $\approx 1 \text{ J cm}^{-2}$ . The substrate temperature

is set by a heater able to heat up to 700 °C. It is a key parameter, as it affects the diffusion length of the adatoms on the surface and therefore has a significant effect on the quality of the crystal [84]. Chamber pressure also plays an important role during the growth, as the atmosphere in the chamber can collide with the atoms in the plasma plume, reducing the mean free path in the chamber. Furthermore, the atmosphere can also produce a chemical reaction and change the valence of the ions in the plume.

The growth of oxides is often conducted at oxygen pressure, up to  $10^{-1}$  mbar, in order to grow a stoichiometric sample [85]. Growth of hybrid nanocomposite thin films presented in this thesis was done under high vacuum, at  $\approx 10^{-6}$  mbar. This allows the reduction of the matrix, and thus preserves the metallic nanowires from oxidation. The oxide matrix is consequently nonstoichiometric and oxygen-deficient.

Before the growth, the surface of the targets were preablated by the laser to remove roughness caused by previous growths. After the preablation, the SrTiO<sub>3</sub>(001) substrate is put in the growth chamber, it is then heated at a rate of 10 °C min<sup>-1</sup> and kept at the growth temperature during 1 h for thermalisation before the growth.

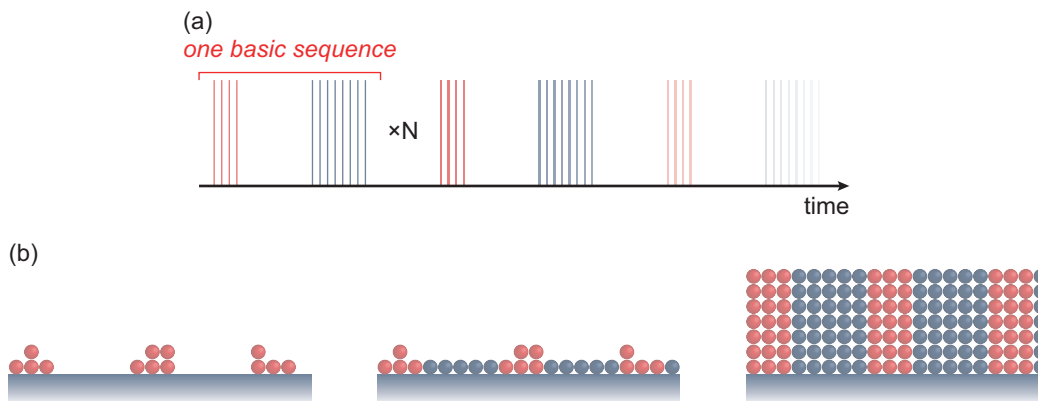


Figure 3.2 – (a) Sketch of the sequential pulsed laser deposition procedure. (b) Sketch of the mechanism underlying the self-assembly of vertically aligned nanocomposites.

A thin layer of SrTiO<sub>3</sub> of thickness 4 nm was firstly grown on the substrate. Then, the thin film of CoNi nanowires in SrTiO<sub>3</sub> was self-assembled by ablating sequentially the CoO, NiO and SrTiO<sub>3</sub> targets, as sketched in Fig. 3.2(a). The growth of Au NWs requires a lower growth temperature, in comparison to that of CoNi NWs. As it will be discussed in Chapter 4, the mobility of Au adatoms is higher than that of 3d metals. A high temperature will lead to the fabrication of large Au NWs, having a diameter not matching that of CoNi NWs. Also, Au nano-inclusions will be deposited in the matrix. Thus, the sample is cooled at a rate of 10 °C min<sup>-1</sup> and left to thermalise during 30 min after the growth of the CoNi-SrTiO<sub>3</sub> nanocomposite thin film. Finally, the Au NWs are self-assembled, using the previous sequential procedure, by ablating the Au and SrTiO<sub>3</sub> targets. After the growth, the sample is cooled at rate of 10 °C min<sup>-1</sup>. Metal oxide targets (CoO, NiO) may seem a surprising choice for the

synthesis of pure metal nanostructures. In the case of metal-oxide VAN thin film deposition by sequential PLD, the ablation of CoO and NiO targets produces pure metal NWs in oxide matrix. Indeed, as the deposition is done under high vacuum, the oxide matrix is nonstoichiometric and oxygen-deficient. This oxygen deficiency is advantageous in this situation, as the matrix will reduce the 3d metal oxides and make them purely metallic.

The mechanism underlying the self-assembly of nanowires in matrix are sketched in Fig. 3.2(b). After ablating a metal oxide or metal target (for example CoO, NiO or Au), the atoms diffuse, nucleate on the surface and create clusters on the SrTiO<sub>3</sub> substrate. The SrTiO<sub>3</sub> target is then ablated, embedding the metal clusters in an oxide matrix. After, metal targets are reablated, causing the vertical growth of the clusters. Repeating this sequence  $N$  times drives to the self-assembly of metal nanowires in oxide matrix. One can understand the growth process as a combination of 2D growth of SrTiO<sub>3</sub> and 3D growth of metals, caused by the difference of surface energies. This difference of surface energies between metal and oxide atoms causes the nucleation of initial metal clusters over the oxide substrate. During the deposition process, metal atoms diffuse horizontally and nucleate preferentially on the existing metal clusters, leading to their vertical growth.

In this thesis work, the quantity of ablated material is presented in number of shots, and not in deposition rate. It is, indeed, a convenient parameter for pulsed laser deposition, as it is possible to readily tune it. However, the same number of shots on ablating targets made of different materials does not yield the same quantity of ablated matter, the ablation rate being different from one material to another. For example, the quantity of ablated matter in one shot from a metal oxide target (CoO, NiO) is different to that of a noble metal target (Au). On the other hand, the ablation rate is close for oxide targets (SrTiO<sub>3</sub>, CoO, NiO). Thus, the deposition procedure can be described by a sequence of shots. One can write a basic sequence of growth as  $(n_1 \times M + n_2 \times \text{SrTiO}_3) \times N$ , where  $n_1$  is the number of shots on the metal  $M$  target,  $n_2$  is the number of shots on the SrTiO<sub>3</sub> targets and  $N$  is the number of repetitions. The length of the  $M$  NWs in SrTiO<sub>3</sub> matrix is related to  $N$ , and diameter and density of the nanowires are related to the ratio  $\frac{n_1}{n_2}$ . For the growth of nanowires made of binary alloy (e.g. Co <sub>$x$</sub> Ni <sub>$1-x$</sub> ), the basic sequence is  $((n_1 \times M_1 + n_2 \times \text{SrTiO}_3) \times n_3 + (n_1 \times M_2 + n_2 \times \text{SrTiO}_3) \times n_4) \times N$  and the composition of the binary alloy is readily adjusted by changing the ratio  $\frac{n_3}{n_4}$ . A single shot on the SrTiO<sub>3</sub> target typically yields an equivalent thickness of thin film of  $5 \times 10^{-3}$  nm.

### 3.2.3 Kinetic Monte Carlo modelisation

Mechanisms underlying the growth of VANs by sequential PLD were studied in the thesis work of Vivien Schuler, using kinetic Monte Carlo (KMC) modelisation [41, 86]. The vertical growth of the clusters during the deposition process is readily seen in Fig. 3.3. Ablated metal atoms diffuse and nucleate over the oxide substrate. After the rotation of the carousel and the ablation of the oxide matrix, metal clusters coalesce; the clusters are not covered by the oxide

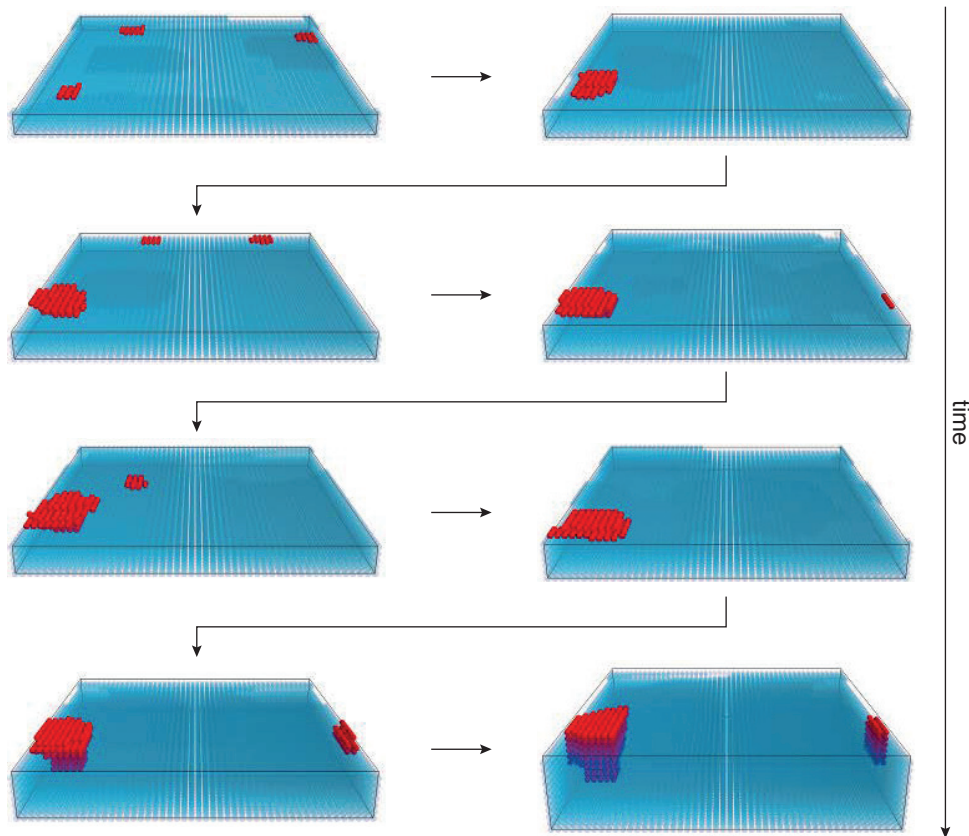


Figure 3.3 – Simulations of the growth of metal NWs in oxide matrix, showing the successive steps during the deposition process. The cell is  $50 \times 50$ , and the growth temperature is 870 K. The number of shots on the targets are  $n_{\text{metal}} = 6$  and  $n_{\text{oxide}} = 18$ . Metal and oxide atoms are respectively depicted as red and blue spheres (reproduced from [41]).

atoms as one shot on the oxide target deposits an equivalent thickness of  $0.1 \text{ \AA}$ . By ablating the metal target again, the metal atoms nucleate on preexisting clusters, making them grow vertically.

As shown by the simulations in Fig. 3.3, kinetic Monte Carlo modelisation provides an insight into the mechanisms of the self-assembly of VANs. KMC simulations can also predict the influence of different growth parameters. For instance, Fig. 3.4 shows the influence of the growth temperature, the number of shots and the laser repetition rate, on the morphology of the NWs.

At low growth temperature, the sequential deposition process yields metal clusters in oxide matrix; whereas at high temperature, metal NWs in oxide matrix, extending from the substrate to the thin film surface, are expected. This is due to the mobility of the atoms, which scales as the temperature of the substrate. In the case of the lowest temperature seen in Fig. 3.4, the temperature is not high enough to activate the diffusion of the metal atoms and the coalescence

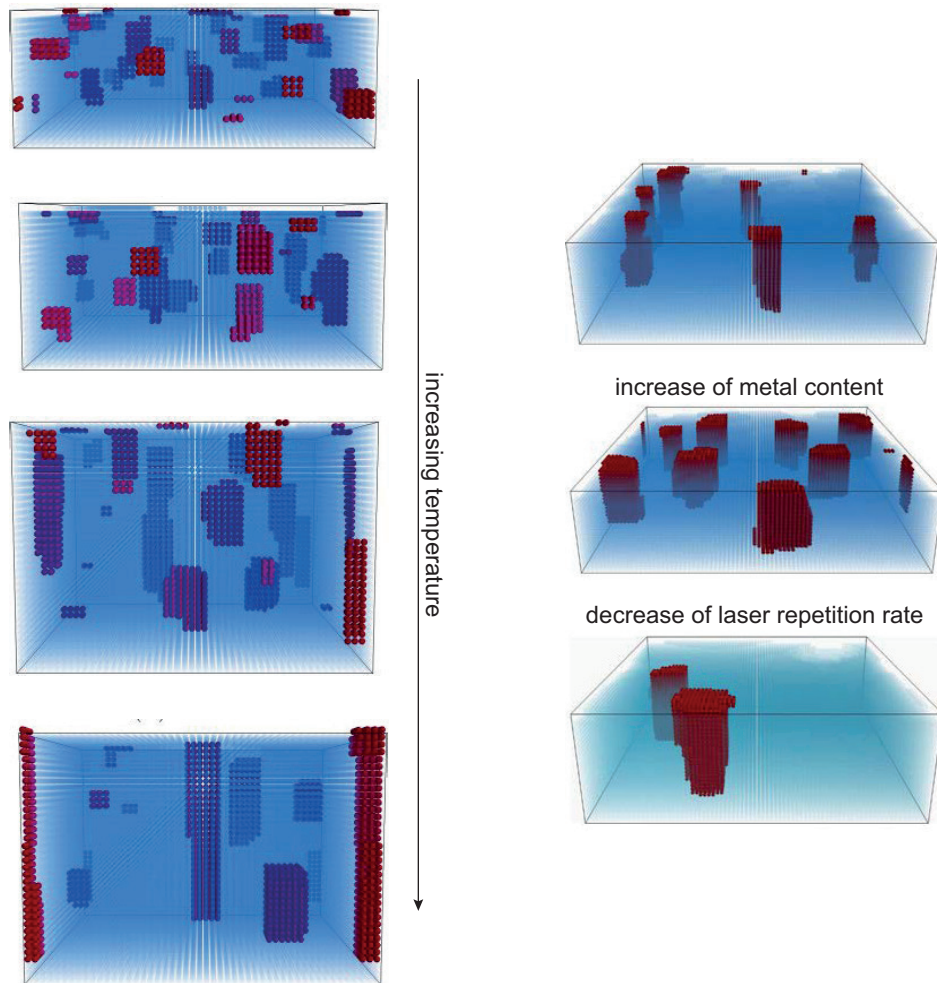


Figure 3.4 – Simulations of the growth of metal NWs in oxide matrix, showing influence of the (a) growth temperature, the (b) number of shots on the metal target, and the laser repetition rate. The cell is  $50 \times 50$ . Metal and oxide atoms are respectively depicted as red and blue spheres (reproduced from [41]).

of the clusters. At high temperature, the mean free path of the metal atoms is longer, which is preferable for their diffusion, thus yielding the vertical growth of the clusters.

Kinetic Monte Carlo simulations show that the shape of the NWs is tuned by the number of shots on the metal target. Indeed, an increase of  $n_{\text{metal}}$  for the same number of shots on the oxide target leads to an increase of the NWs average diameter and of their density. In addition, the laser repetition rate plays also a role in the morphology of the nanocomposites. For a lower laser repetition rate, using the same deposition basic sequence, the NWs are larger and their density is lower. This is due to the waiting time between each pulse; as the repetition rate is lower, metal atoms have more time to diffuse and nucleate before the deposition of the oxide atoms.

### 3.3 Structural properties

#### 3.3.1 Transmission electron microscopy

Transmission electron microscopy (TEM) allows the morphological, structural and chemical description of nanocomposites [87, 88]. High-resolution transmission electron microscopy (HRTEM) micrographs were recorded using a *JEOL JEM 2100F* microscope equipped with a Schottky emitter and a *Gatan GIF 2001* EELS spectrometer at the *Institut de Minéralogie, de Physique des Matériaux et de Cosmochimie* (CNRS-Sorbonne Université).

The structure of the samples was studied by HRTEM in plan, cross section and tilt view. The chemical composition was studied by scanning transmission electron microscopy (STEM) with a high-angle annular dark-field detector (HAADF) and energy-dispersive x-ray (EDX) spectroscopy.

Additional scanning transmission electron microscopy micrographs and chemical mappings were recorded using a *Thermo Fischer Titan Themis 200* microscope equipped with a *ChemiSTEM Super-X* EDX detector at the *Centre de Nanosciences et de Nanotechnologies* (CNRS-Université Paris-Saclay).

##### 3.3.1.1 Sample milling

Transmission electron microscopy experiments require a specimen thickness inferior to 50 nm. Samples were observed in plan view (from the top) and cross section view (from the side).

For plan view milling, the back of the sample is thinned down mechanically to 40  $\mu\text{m}$ , then by Ar ion milling using a *Gatan Precision Ion Polishing System II* machine until the first appearance of a hole in the centre. For cross section view milling, two samples are glued *layer to layer*, then thinned down following the previous procedure.

##### 3.3.1.2 High-resolution transmission electron microscopy

High-resolution transmission electron microscopy (HRTEM) plan ([001] zone axis) and cross section view ([100]) images (Fig. 3.5(a)(c)) show the metal NWs in oxide matrix as disks and ribbons, respectively, allowing the estimation of the characteristic quantities (diameter, density and length) of the NWs. HRTEM tilt view images (Fig. 3.5(d)) show the projected long axis of the NWs and give complementary information on the shape of the NWs, which appear as matchstick-like structures. Indeed, the top layer in thin zones of a specimen thinned for cross section view is damaged by the ion milling, whereas it cannot be viewed in detail in thick zones. Thus, tilt view allows to distinguish the top layer.

The fast Fourier transform (FFT) of a region of interest centred on a specific NW (Fig. 3.5(b)) allows one to define the epitaxial relations of this structure and the oxide matrix. The moiré patterns seen on plan and cross section view HRTEM micrographs (Fig. 3.5(a)(c)) stem from

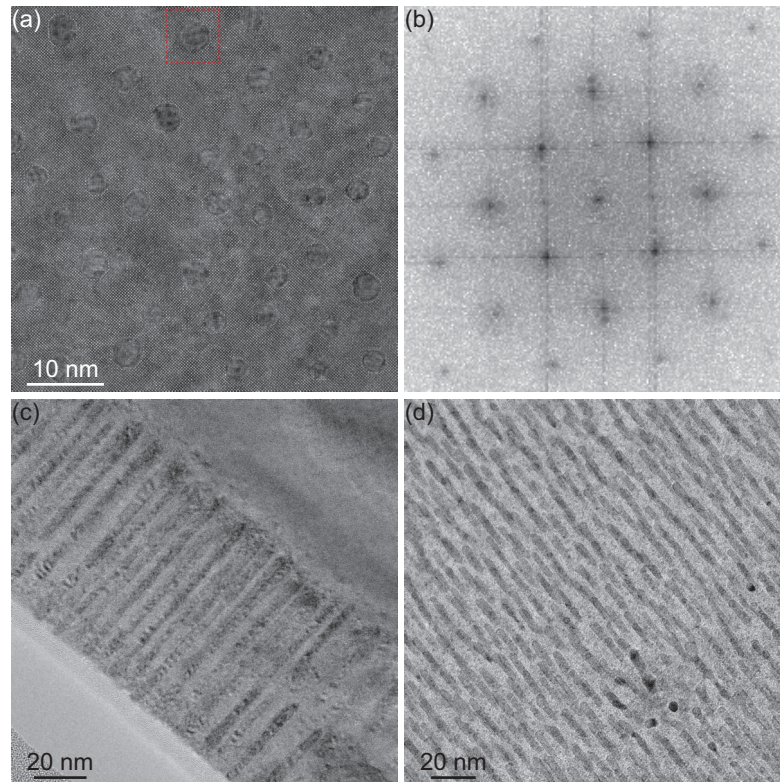


Figure 3.5 – High-resolution transmission electron microscopy micrographs of metal nanowires in oxide matrix. (a) Plan view image and (b) fast Fourier transform of the red zone. (c) Cross section view image. (d) Tilt view image.

the multiple diffraction of two intertwined lattices [89] and show the hybrid (in plan view) or epitaxial (in plan and cross section view) nature of the nanocomposites.

### 3.3.1.3 HAADF-STEM and spectromicroscopy

High-angle annular dark-field scanning transmission electron microscopy (HAADF-STEM) is a compositional ( $Z$ -)contrast imaging technique, which consists in the measurement of electrons undergoing high angle scattering. A part of the incident electron beam is scattered by the nuclei of the specimen (Rutherford scattering) at high angles. The electrons are then collected by a high-angle annular detector with an angle proportional to the square of the atomic number  $Z^2$ . Fig. 3.6(a) is a HAADF-STEM image in cross section view of a hybrid vertically aligned nanocomposite thin film. The top of the layer is brighter than the bottom, revealing a difference in atomic composition.

Energy-dispersive x-ray spectroscopy (EDXS) mapping analysis is an element-selective imaging technique, which consists in the measurement of the x-ray emissions of an excited specimen. An electron beam excites the atoms and ionises the electrons, creating electron holes. An electron of an orbital of higher energy recombines with the electron hole, producing an

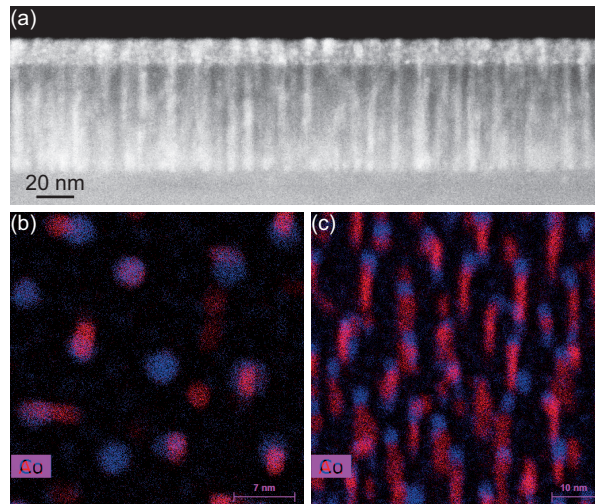


Figure 3.6 – Compositional contrast micrographs of metal nanowires in oxide matrix. (a) High-angle annular dark-field scanning transmission electron microscopy image in cross section view. Energy-dispersive x-ray spectroscopy mappings in (b) plan view and (c) tilt view.

x-ray emission whose energy corresponds to an electronic transition specific to the atomic species. Fig. 3.6(b)(c) shows EDXS mappings in plan and tilt view, distinguishing two atomic species, Co (in red) and Au (in blue).

### 3.3.2 X-ray diffraction

X-ray diffraction (XRD) allows the structural study of nanocomposite thin films by recording the reciprocal space. Specular  $\theta$ - $2\theta$  and grazing incidence in plane  $\phi$ - $2\theta_\chi$  scans, and reciprocal space mappings (RSM) reveal the epitaxy and the strain defining the nanocomposites [90].

Specular  $\theta$ - $2\theta$  scans (Fig. 3.7(a)) and vertical  $\phi$ - $2\theta_\chi$  scans (Fig. 3.7(b)) were recorded using a laboratory *Rigaku SmartLab* five-circle diffractometer with a Cu  $K\alpha_1$  radiation ( $\lambda = 1.5406 \text{ \AA}$ ). Complementary studies of the reciprocal space using synchrotron x-ray were carried out at the SixS beamline at the synchrotron SOLEIL (Fig. 3.8).

#### 3.3.2.1 Out of plane and in plane x-ray diffraction

Laboratory x-ray studies were carried out using a *Rigaku SmartLab* five-circle diffractometer with a Cu rotating anode and a Ge(220) $\times$ 2 channel-cut monochromator, which selects Cu  $K\alpha_1$  radiation ( $\lambda = 1.5406 \text{ \AA}$ ). The laboratory x-ray diffractometer allows five degrees of freedom: the specimen rotates by the three Euler angles ( $\omega$ ,  $\phi$ ,  $\chi$ ) and the detector rotates by two angles ( $2\theta$ ,  $2\theta_\chi$ ).

The two x-ray diffraction geometries used in this work, out of plane  $\theta$ - $2\theta$  specular scan and in plane  $\phi$ - $2\theta_\chi$  scan, are shown in Fig. 3.7.  $\theta$ - $2\theta$  scan allows the study of horizontal planes

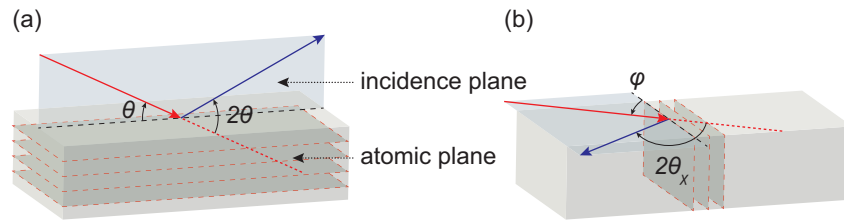


Figure 3.7 – Schematics of x-ray diffraction geometries in (a) specular  $\theta$ - $2\theta$  scan and (b) in plane  $\phi$ - $2\theta_\chi$  scan. Incident and diffracted x-ray are coloured in red and blue, respectively.

(Fig. 3.7(a)). The detector rotates by an angle  $2\theta$ , synchronously with the angle of incidence of the incident x-ray  $\omega = \theta$ .

Vertical planes cannot be probed by specular scan. In comparison to a typical four-circle diffractometer, the  $2\theta_\chi$  angle allows the detector to quit the plane of incidence defined by the incident x-ray and the normal to the specimen surface. With a grazing angle of incidence ( $\omega = 0.5^\circ$ ),  $\phi$ - $2\theta_\chi$  scan allows the study of vertical planes (Fig. 3.7(b)), similarly to a  $\theta$ - $2\theta$  specular scan.

Major limitations of laboratory x-ray diffraction are the quality of the x-ray source and the instrumental resolution. The resolution of the interreticular distance is related to the intrinsic spectral width of Cu  $K\alpha_1$  radiation ( $\Delta\lambda/\lambda \approx 10^{-4}$ ) and reaches a minimal value of  $\Delta d/d \approx 10^{-4}$  for out of plane scans. The divergence of the diffracted x-ray is mitigated by the addition of slits or collimators. Furthermore, the radius of the Ewald sphere, defining the accessible reciprocal space, is inversely proportional to the wavelength of the incident x-ray; the higher is  $\lambda$ , the smaller is the radius of the Ewald sphere.

### 3.3.2.2 Synchrotron x-ray diffraction

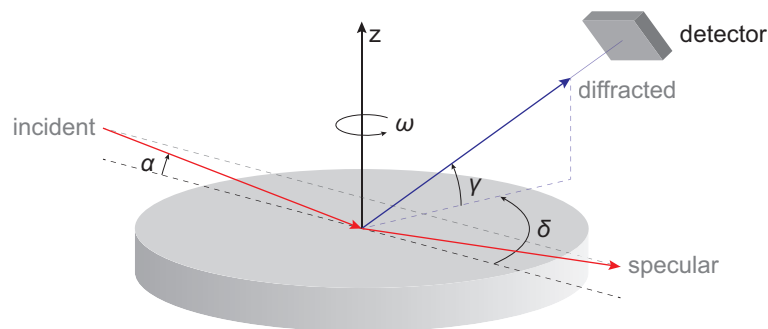


Figure 3.8 – Schematics of the x-ray diffraction z-axis geometry at the SixS beamline (SOLEIL).  $\alpha$  is the incident angle and the specimen rotates by  $\omega$  to set the (nonspecular) planes at Bragg position. The detector rotates with two degrees of freedom by  $\delta$  and  $\gamma$ .

Synchrotron radiation alleviates the aforementioned limitations and allows high intensity radiations and high instrumental resolution, in comparison to laboratory x-rays. Regarding thin layers study, in order to make x-ray diffraction surface-sensitive, the penetration of the x-rays in the specimen thickness is limited by a grazing angle of incidence from  $0.1^\circ$  to  $0.3^\circ$ , close to the critical angle of total internal reflection. The x-ray diffraction z-axis geometry at the SixS beamline (SOLEIL) allows a constant grazing angle of incidence  $\alpha$ , meanwhile the specimen rotates around its normal by an angle  $\omega$  (Fig. 3.8). The detector rotates with two degrees of freedom by  $\delta$  and  $\gamma$ , which enables it to cover an half-sphere above the specimen and to intercept any diffracted x-ray [91]. Such XRD geometry allows the study of vertical and inclined planes and the mapping of the in plane and part of the out of plane reciprocal spaces (Fig. 3.9). Furthermore, synchrotron XRD at the SixS beamline can be carried out in Euler geometry, similarly to laboratory five-circle XRD, to probe the out of plane reciprocal spaces.

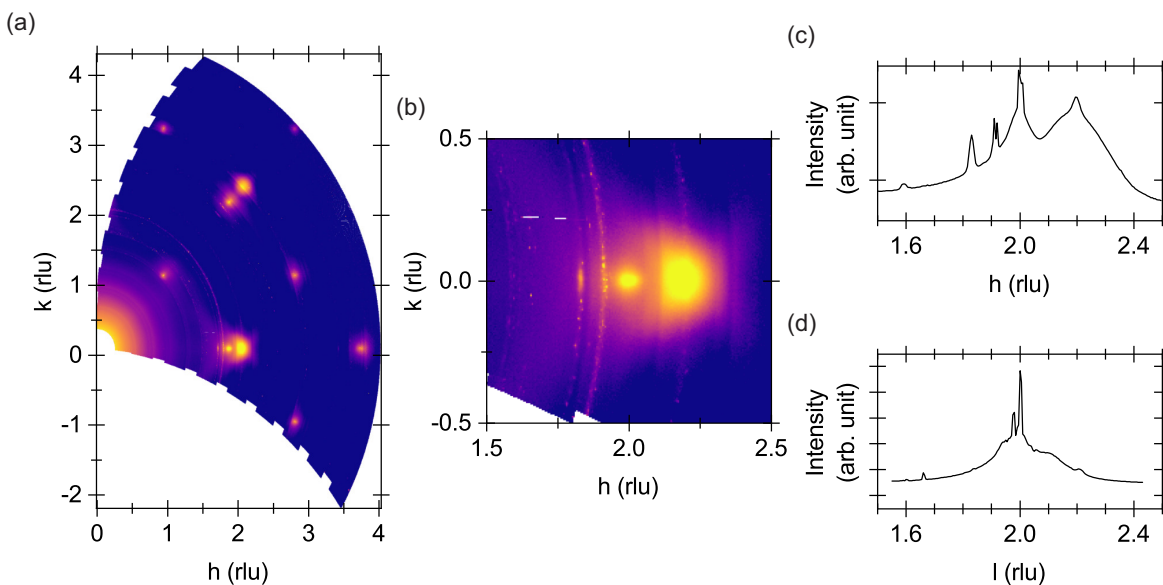


Figure 3.9 – Structural synchrotron x-ray study of metal nanowires in oxide matrix. (a) In plane reciprocal space mapping and (b) reciprocal space near the matrix 200 reflection. (c) In plane profile of Fig. 3.9(b) and (d)  $\theta$ - $2\theta$  scan. Coordinates are expressed in bulk  $\text{SrTiO}_3$  reciprocal lattice unit (rlu). Data were recorded at the SixS beamline (SOLEIL).

### 3.3.2.3 X-ray reflectivity

X-ray reflectivity is a thickness determination technique based on the interference of totally reflected x-rays from the top and the bottom interfaces of a layer of finite electron density, bracketed by layers of different electron density (Fig. 3.10(a)), and consists in the measure of reflected x-ray intensity as a function of the angle of incidence close to the critical angle  $\theta_c$ .

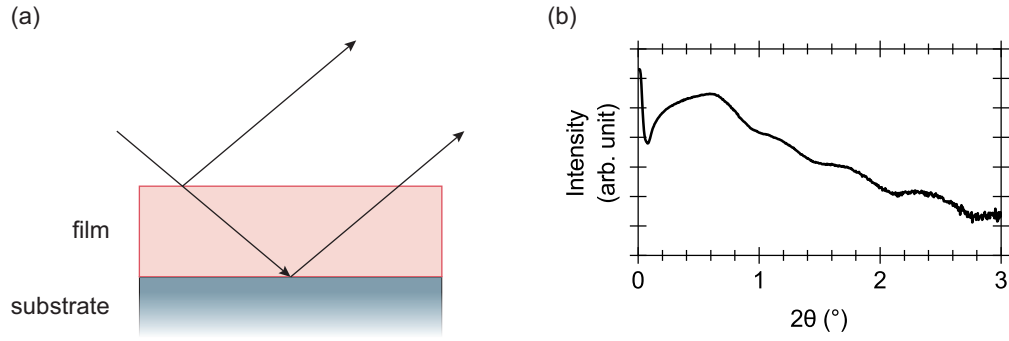


Figure 3.10 – (a) Sketch of the x-ray reflectivity geometry. (b) Typical x-ray reflectivity scan from  $2\theta = 0^\circ$  to  $3^\circ$  of a hybrid Au-Co<sub>0.8</sub>Ni<sub>0.2</sub>-SrTiO<sub>3</sub> vertically aligned nanocomposite thin film (log<sub>10</sub> scale).

Maxima of reflection are seen for angles of incidence equal to  $\theta_m$ , for which the path difference of the reflected waves from the top and the bottom interfaces of the layer are an integer multiple  $m$  of the x-ray wavelength  $\lambda$ . Thus, the thickness  $t$  is [92]

$$t = \frac{m\lambda}{2\sqrt{\sin^2 \theta_m - \sin^2 \theta_c}}. \quad (3.1)$$

For small angles, this equation is simplified as

$$t = \frac{m\lambda}{2\sqrt{\theta_m^2 - \theta_c^2}}. \quad (3.2)$$

Fig. 3.10(b) shows a typical x-ray reflectivity scan from  $2\theta = 0^\circ$  to  $3^\circ$  of a hybrid Au-Co<sub>0.8</sub>Ni<sub>0.2</sub>-SrTiO<sub>3</sub> vertically aligned nanocomposite thin film. X-ray reflectivity scans in this thesis work were measured using a Cu  $K\alpha_1$  radiation ( $\Delta\lambda/\lambda \approx 10^{-4}$ ). The critical angle  $\theta_c$ , defined as the inflexion point of the curve, is at  $2\theta_c = 0.6^\circ$  in this example, and a thickness of 11 nm is deduced from the maxima of reflection with a precision of 10 %.

Furthermore, the surface roughness, the density of the film and its electronic density, can also be extracted [93]. Indeed, the higher is the surface roughness, the faster is the decay. Then, the amplitude of the oscillations is related to the density contrast, i.e. the difference of density between the film and the substrate. The larger is the density contrast, the higher is the amplitude. As the value of the critical angle  $\theta_c$  is linked to the refractive index, it is thus also related to the electronic density of the film. Therefore, the larger is the electronic density, i.e. the higher is the atomic number  $Z$ , the larger is the critical angle.

## 3.4 Physical properties

### 3.4.1 Vibrating sample magnetometry

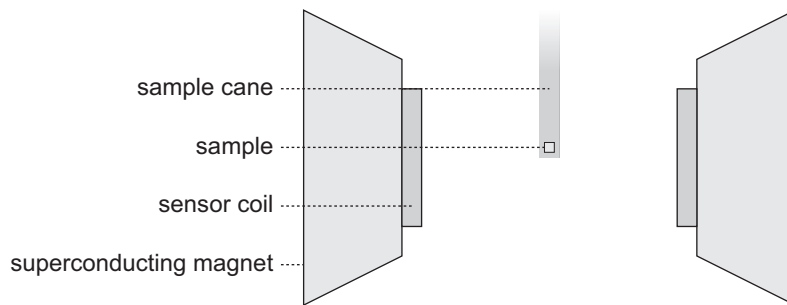


Figure 3.11 – Sketch of a vibrating sample magnetometry module in a *Physical Property Measurement System*. It operates from 1.8 K to 400 K and the magnetic field can reach up to 9 T.

Magnetic properties of hybrid nanocomposite thin films were measured by a vibrating sample magnetometry (VSM) module in a *Physical Property Measurement System (Quantum Design PPMS 9T)* at the *Mesures physiques à basse température* platform (Sorbonne Université). It operates at a wide range of temperature (from 1.8 K to 400 K) and of magnetic field (up to 9 T). The sample can be measured parallelly (in plane) or perpendicularly (out of plane) to the magnetic field.

The magnetic field is created by a superconducting magnet placed in liquid He. As sketched in Fig. 3.11, the magnetisation  $M$  of the sample is measured by its vibration at 40 Hz between two coils, creating a magnetic flux. The voltage induced in the coils is proportional to  $M$ . VSM gives a fast quantitative measure of the magnetic properties and its root mean square is of  $\approx 10^{-6} \text{ emu s}^{-1}$ .

Fig. 3.12(a)(c) show raw  $M(H)$  curves measured by vibrating sample magnetometry in solid red line. These curves are the sum of the ferromagnetic and the diamagnetic responses from the sample and the sample holder, respectively. The contribution of the sample holder, plotted in blue in Fig. 3.12(a)(c), is extracted by fitting the raw curves at high magnetic field values and subtracted from the measurements. The sign of the sample holder diamagnetic contribution depends on the geometry of the measurement. It is positive for the out of plane geometry, and negative for the in plane geometry. Fig. 3.12(b)(d) show nonnormalised treated  $M(H)$  curves.

### 3.4.2 Magneto-optical Kerr effect

#### 3.4.2.1 Static magneto-optical Kerr effect

Static magneto-optical Kerr effect measurements were conducted at the *Institut des NanoSciences de Paris* (CNRS-Sorbonne Université). Magneto-optical Kerr effect is the result of the interaction between a polarised light and a magnet. When a linear light is shone on a magnetised ( $M \neq 0$ ) surface, the reflection polarisation becomes elliptical. This reflection can be defined by two

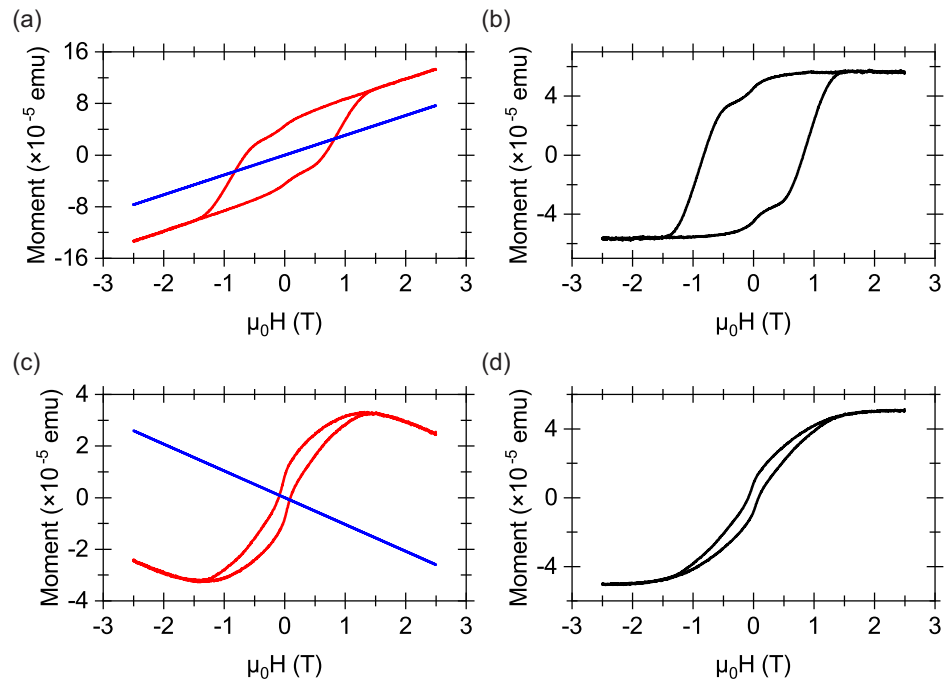


Figure 3.12 – Out of plane  $M(H)$  curves (a) before and (b) after data treatment. In plane  $M(H)$  curves (c) before and (d) after data treatment. Raw measured curves (red) were treated by subtracting the diamagnetic signal of the sample holder (blue).

angles,  $\theta_K$  (Kerr rotation) and  $\epsilon_K$  (Kerr ellipticity).  $\theta_K$  and  $\epsilon_K$  are proportional to a component of the magnetisation of the sample. Therefore,  $M(H)$  curves can be extracted by measuring  $\theta_K$  and  $\epsilon_K$  as a function of the external field.

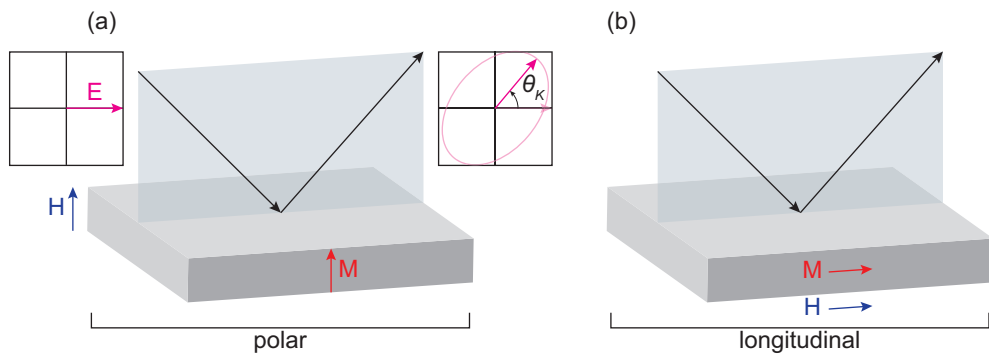


Figure 3.13 – Sketches of the magneto-optical Kerr effect in (a) polar and (b) longitudinal geometries. The plane of incidence is coloured in blue. The quadrants show the polarisation vector before and after reflection on the magnetised material.  $\vec{M}$  is the magnetisation of the material and  $\vec{H}$  is the external field.

Fig. 3.13 depicts different geometries of magneto-optical Kerr effect. The magneto-optical Kerr effect is polar (Fig. 3.13(a)) or longitudinal (Fig. 3.13(b)) depending on the direction of the

magnetisation vector  $\vec{M}$  of the material to the plane of incidence. Polar magneto-optical Kerr effect probes the out of plane component  $\vec{M}$ , whereas in longitudinal geometry the in plane component is measured.

### 3.4.2.2 Time-resolved magneto-optical Kerr effect

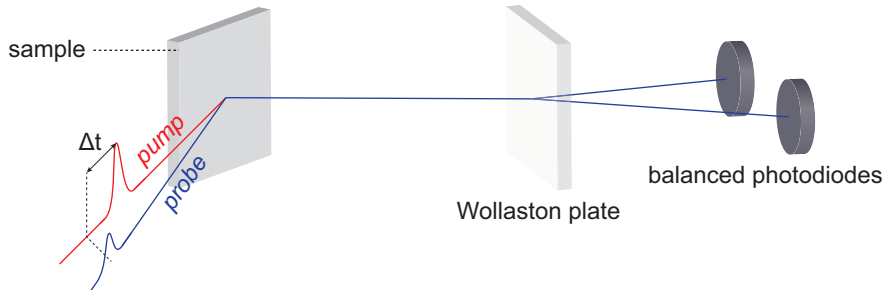


Figure 3.14 – Sketch of a pump-probe magneto-optical Kerr effect polarising beam splitter-based set-up. The probe is splitted by a Wollaston plate between its  $s$  and  $p$  components. A balanced photodetector measures the difference of intensity between the  $s$  and  $p$  components caused by the magneto-optical Kerr effect.

Magneto-optical Kerr effect can be measured in pump-probe experiments to study the magnetisation dynamics at very short timescales. The basic principle of a pump-probe experiment is sketched in Fig. 3.14. A pump pulse is shone on the sample, causing an ultrafast demagnetisation. A probe pulse, at a lower fluence, measures the sample response to the pump. One can monitor its evolution in time by varying the temporal delay between the pump pulse and the probe pulse and reconstruct, in a stroboscopic scheme, the dynamics of the pumped sample.

**Experimental set-up** Time-resolved magneto-optical Kerr effect (TRMOKE) experiments were conducted at *Laboratoire d'optique appliquée* (CNRS-ENSTA) thanks to a pump-probe polarising beam splitter-based set-up. Légaré and coworkers discussed the pertinence of analyser-based and polarising beam splitter-based magneto-optical Kerr effect set-ups thanks to Jones formalism [94]. It was shown that polarising beam splitter-based set-ups improve the signal intensity by a factor of two. The experimental set-up uses a femtosecond *Coherent Legend Elite Duo* Ti:Al<sub>2</sub>O<sub>3</sub> laser, delivering 2 mJ pulses at 800 nm. The repetition rate is 5 kHz and the temporal resolution of the pulse is  $\approx 35$  fs. The laser is used by two experiments and four-fifths of the pulses are allocated to the TRMOKE set-up. The sample is magnetised by a permanent magnet ( $\mu_0 H \approx 0.6$  T).

The experimental set-up is sketched in Fig. 3.15. A set of lenses is used to collimate and change the size of the spot. The beam is frequency doubled by a BBO plate to get a pump pulse at 800 nm and a probe pulse at 400 nm. The beam is then splitted and a delay stage placed on the pump line is used to change the time delay between the pump pulse and the probe pulse.

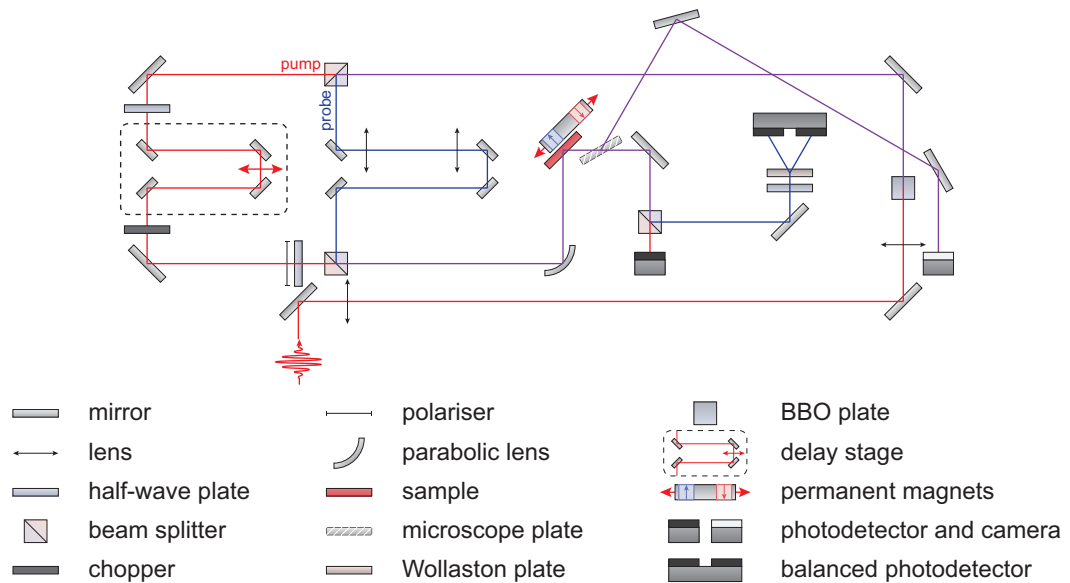


Figure 3.15 – Optical schematics of the pump-probe time-resolved magneto-optical Kerr effect at *Laboratoire d'optique appliquée* (CNRS-ENSTA). The  $\text{Ti:Al}_2\text{O}_3$  laser shoots 2 mJ pulses at 800 nm. The repetition rate is 5 kHz and the temporal resolution of the pulse is  $\approx 35$  fs.

A half-wave plate placed before the delay stage is used to tune the pump fluence. To reduce the noise, a chopper synchronised with the laser chops the pump pulse at a frequency of 2.5 kHz so that a static signal is measured throughout the measurement. The polarisation of the pump pulse is changed thanks to a polariser. Both pump and probe pulses are focused on the sample by a parabolic lens. The polarity of the sample magnetisation is changed easily by translating the permanent magnets.

The probe pulse is splitted by a Wollaston plate between its  $s$  and  $p$  components. A balanced photodetector (*PDB220A2/M Thorlabs*) measures the  $s$  and  $p$  components separately. The Kerr rotation is deduced from the difference of intensity between the  $s$  and  $p$  components. A digitizer (*PicoScope 6424E*) is used to record four waveforms, namely the intensity of the  $s$  and  $p$  splitted probe pulse in each photodetector ( $I_s$  and  $I_p$ ), the amplified difference of these intensities (RF signal), and the intensity of the pump pulse.

A camera is used to image the pump and the probe spots (Fig. 3.16). The diameters of the spots are extracted by a fit using a gaussian function. The resolution of the images is  $1024 \text{ px} \times 768 \text{ px}$  and the conversion factor is  $1.38 \text{ px } \mu\text{m}^{-1}$ . Full width at half maximum (FWHM) diameters of  $98 \mu\text{m}$  and  $58 \mu\text{m}$  are measured for the pump and the pulse respectively.

**Protocols** In this paragraph, protocols used for data measurement and treatment are presented. As discussed previously, two permanent magnets, of opposed polarity, are placed behind the sample. The polarity of the sample magnetisation is changed by translating the magnets. One measurement consists in 20 scans of alternating polarities. For example, after one scan is

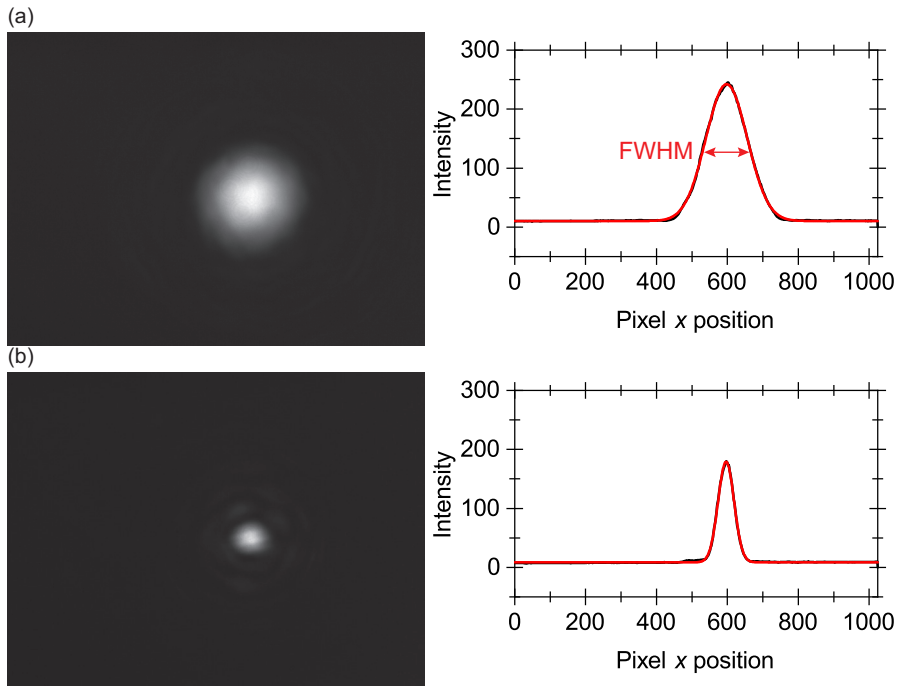


Figure 3.16 – Images of the (a) pump and (b) the probe spots. Profiles of the spots (black) were fitted by a gaussian function (red). The resolution of the images is 1024 px  $\times$  768 px.

done in magnetic field  $+H$ , the sample is probed again in an opposing field  $-H$  and so on. As the laser-induced transient change in reflectivity is not sensitive to the magnetic field, purely optical contributions are removed by subtracting  $+H$  and  $-H$  scans. Averaging over 10 scans, for each field polarity, furthermore reduces the noise of the measurement.

Time evolution of the magnetisation is reconstructed in a stroboscopic scheme by measuring Kerr rotation  $\theta_K$  for different time delay  $t$  values.  $t$  varies by translating the mirrors on the delay stage and ranges from  $-3000$  fs to  $20\,000$  fs with variable steps. A step sequence of  $\Delta t = 200$  fs from  $-3000$  fs to  $-500$  fs,  $\Delta t = 20$  fs from  $-500$  fs to  $2000$  fs,  $\Delta t = 100$  fs from  $2000$  fs to  $10\,000$  fs and  $\Delta t = 500$  fs from  $10\,000$  fs to  $20\,000$  fs was used. Two-hundred fifty one  $t$  values are thus measured in one scan.

The power of the pump is measured in front of the sample before changing the pump fluence. The incident fluence values are deduced from the FWHM diameter of the pump corrected by a factor of  $\sqrt{2}$ , to take account of the  $45^\circ$  incidence angle, and a repetition rate of 4 kHz. Demagnetisation curves presented in this thesis were measured with incident fluences ranging from  $1.7$  mJ cm $^{-2}$  to  $19.8$  mJ cm $^{-2}$ .

The digitizer measures four time traces: the intensities of the probe in each photodetector, the RF signal and the intensity of the pump pulse. An example of time traces is plotted in Fig. 3.17. The time base of the time trace is 3.2 ns and 500 points are stored. Recording of time traces is repeated a 100 times for a single time delay, and four hundred time traces of 500 points

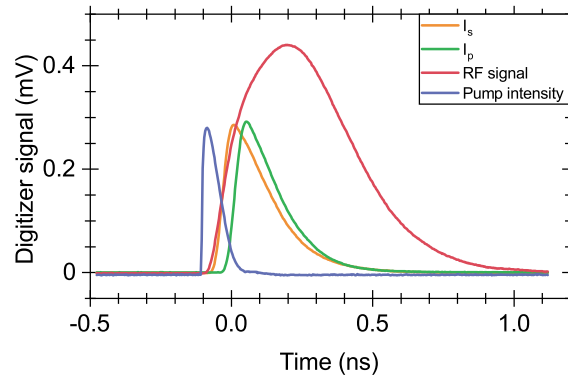


Figure 3.17 – Four time traces measured by the digitizer: intensities of the probe in each photodetector  $I_s$  and  $I_p$ , the amplified difference of  $I_s$  and  $I_p$  (RF signal) and the intensity of the pump pulse. The time traces are averaged over 100 recordings.

are thus measured in one time delay  $t$ . Kerr signal is recovered by integrating in time the RF signal, and the pump intensity is used to see if the chopper has cut the pump. A data set of dimension  $20 \times 251 \times 4 \times 100 \times 500$  is recorded for one measurement, so for a single fluence value. The data analysis was performed with the help of a Python program.

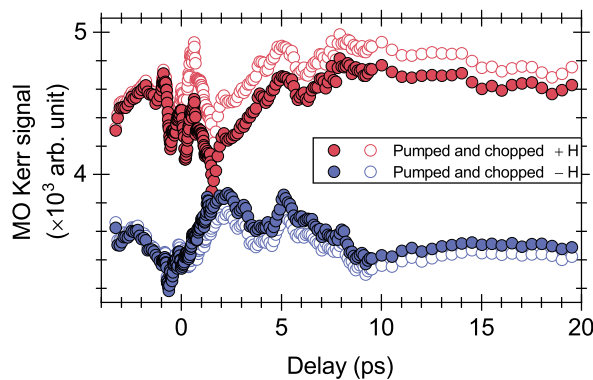


Figure 3.18 – Magneto-optical Kerr signals after sorting between pumped and chopped signal values. Two measurements with different magnetic fields ( $+H$  and  $-H$ ) are presented in the figure. Pumped signal values  $I_p$  are plotted in solid colours, and chopped  $I_s$  in white.

RF signal time traces are integrated in time to recover the Kerr signal, there are thus 100 signal values per time delay  $t$ . The repetition rate of the laser is 5 kHz and the chopper rotates at a frequency of 2.5 kHz, consequently half of the data (50 values per time delay) are sample signal without pump perturbation. Data are therefore sorted between pumped and chopped signal values, noted  $I_p$  and  $I_s$  respectively, using the measured intensity of the pump pulse. That is to say,  $I_p$  is the Kerr rotation signal after pump perturbation, and  $I_s$  is the static Kerr rotation signal.  $I_p$  and  $I_s$  are plotted in Fig. 3.18 for  $+H$  and  $-H$  magnetic fields.

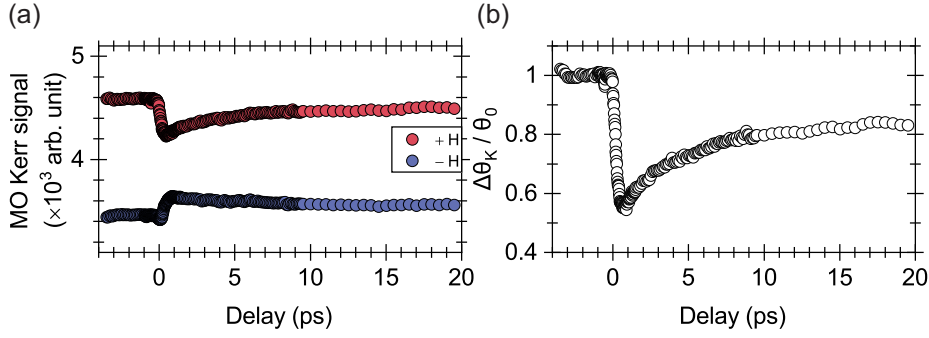


Figure 3.19 – (a) Normalised magneto-optical Kerr signals after normalisation of pumped signal values  $I_p$  by static  $I_s$ .  $\langle I_s \rangle I_p(t) / I_s(t)$  is plotted for  $+H$  and  $-H$  magnetic fields. (b) Demagnetisation curve retrieved from Eq. 3.3.

By measuring the sample with magnetic fields  $+H$  and  $-H$ , the normalised variation of Kerr rotation is then retrieved by

$$\frac{\Delta\theta_K}{\theta_0}(t) = \frac{\langle I_s^+ \rangle I_p^+(t) / I_s^+(t) - \langle I_s^- \rangle I_p^-(t) / I_s^-(t)}{\langle I_s^+ \rangle - \langle I_s^- \rangle} \quad (3.3)$$

where  $\Delta\theta_K$  is variation of the Kerr rotation and  $\theta_0$  is the Kerr rotation signal before pump-probe coincidence.  $\langle I_s^+ \rangle$  and  $\langle I_s^- \rangle$  are the mean static Kerr rotation signal and superscripts + and - denote measurements with magnetic fields  $+H$  and  $-H$  respectively. To reduce noise, magnetisation dynamics curves presented in this thesis are plotted from the averaging of 10 pairs of  $+H$  and  $-H$  measurements. The normalised magneto-optical Kerr signal  $\langle I_s \rangle I_p(t) / I_s(t)$  is plotted in Fig. 3.19(a). Fig. 3.19(b) shows an example of demagnetisation curve retrieved from Eq. 3.3.

### 3.4.3 Ellipsometry

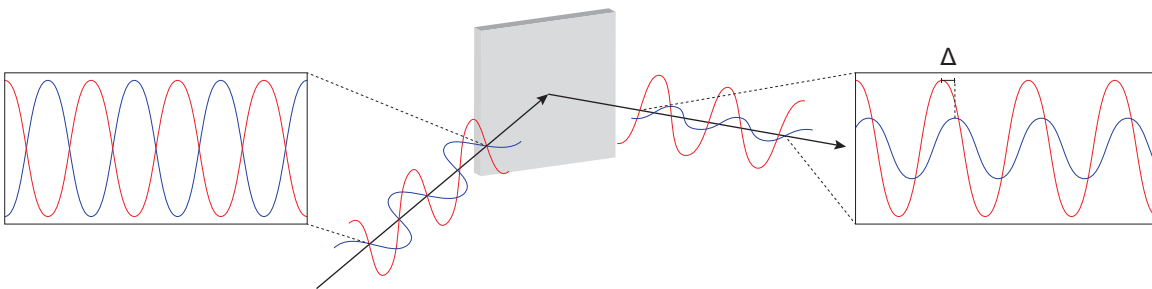


Figure 3.20 – Sketch of a reflectometer. Ellipsometry is based on the change in state of polarisation after specular reflection. The reflectance is measured as a function of the wavelength, at various angles of incidence close to the Brewster's angle.

Optical properties were measured by ellipsometry at Institut des NanoSciences de Paris (CNRS-Sorbonne Université). Dielectric constants of a material can be defined by ellipsometry. It is based on the change in state of polarisation after specular reflection. Thus, the reflectance of the sample is measured as a function of the wavelength, at various angles of incidence close to the Brewster's angle. Reflectances of the  $p$  and  $s$  components of the light,  $r_p$  and  $r_s$ , are tied to the angles  $\Psi$  and  $\Delta$  as

$$\frac{r_p}{r_s} = \tan \Psi e^{i\Delta} \quad (3.4)$$

where the angles  $\tan \Psi$  and  $\Delta$  are the ratio of amplitude and the phase difference of the  $p$  and  $s$  components.

Optical properties cannot be deduced readily from the angles  $\Psi$  and  $\Delta$ . A model, based on the structure of the sample (thickness, particle size, volume fraction), must be firstly built. In the case of elongated particles, the anisotropy is modelled by adding a depolarisation factor. One can deduce, thanks to the model, the optical indices  $n$  and  $k$  from  $\Psi$  and  $\Delta$ , through the permittivity tensor  $\underline{\epsilon}$ . Indeed, the complex permittivity  $\underline{\epsilon} = \epsilon_1 + i\epsilon_2$  is related to  $n$  and  $k$  by

$$\begin{aligned} \epsilon_1 &= n^2 - k^2 \\ \epsilon_2 &= 2nk. \end{aligned} \quad (3.5)$$

## CHAPTER 4

### AU NANOWIRES

4.1	Introduction . . . . .	55
4.2	Structural properties of Au NWs . . . . .	56
4.2.1	Diameter, density and epitaxy . . . . .	56
4.2.2	Influence of the growth temperature on the epitaxy . . . . .	60
4.3	Optical properties . . . . .	62
4.3.1	Gans theory simulations . . . . .	62
4.3.2	Experimental measurements . . . . .	63
4.4	Conclusion . . . . .	65

#### 4.1 Introduction

Ferromagnetic nanocomposite thin films were synthesised and extensively studied in the thesis work of Xiaorong Weng [95, 96]. Thus, a first step before the growth of hybrid ferromagnetic and plasmonic vertically aligned nanocomposite thin films is the growth of Au NWs in SrTiO<sub>3</sub> matrix. Indeed, the growth of these thin films requires the knowledge and comprehension of each constituent of the hybrid nanocomposites. The influence of the growth conditions, for instance the growth temperature or the metal-oxide ratio in the basic sequence, has to be identified to grow noble metal NWs with the suitable epitaxy and shape, the latter influencing optical properties (absorption cross section, plasmonic resonance position).

Au is, in this case, a good material choice for different reasons. Firstly, the Au-Co couple is known to be immiscible [97]. Furthermore, Hennes and coworkers have proved that phase separation is present in hybrid Au-Co NWs in SrTiO<sub>3</sub> matrix grown by sequential pulsed laser deposition [58]. Then, as discussed in the previous paragraph, the shape of the particles modifies the absorption cross section and the plasmonic resonance position. Au is particularly interesting due to the possibility to shift the plasmonic resonance positions from the visible to the near-infrared according to the aspect ratio of the particle. This feature is convenient if one wants to conduct optical or magneto-optical experiments at these wavelengths. Lastly, Au and SrTiO<sub>3</sub> have both a face-centred cubic structure, making it possible to envisage epitaxial growth.

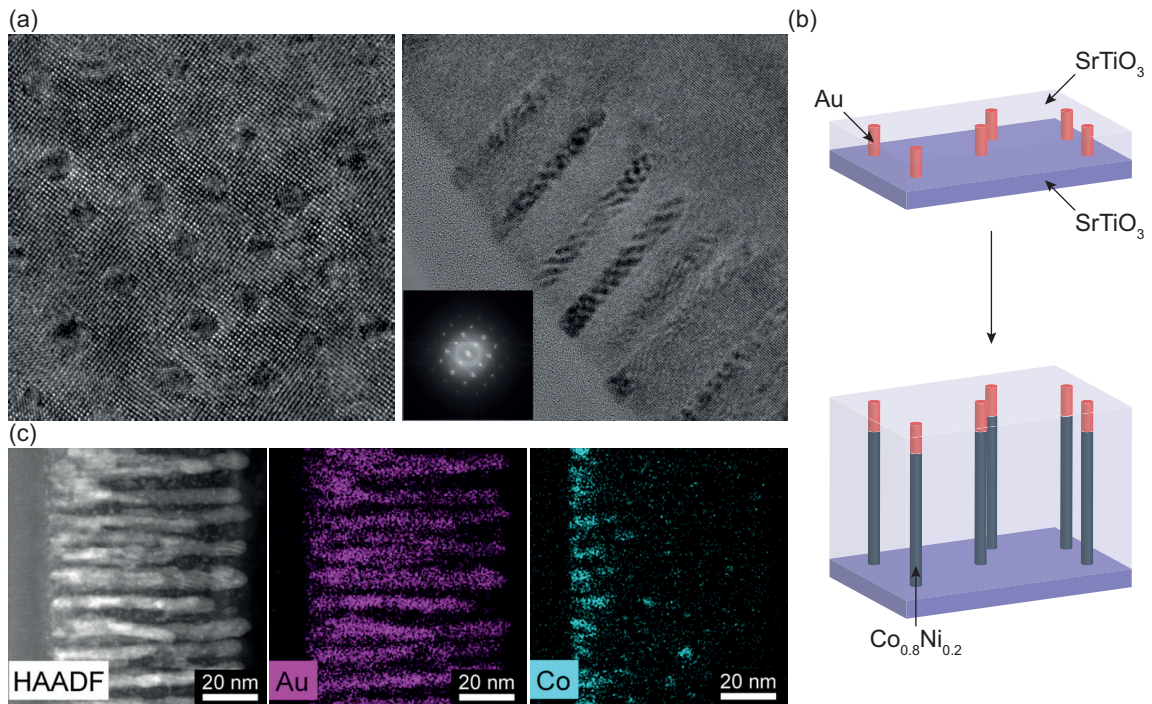


Figure 4.1 – (a) High-resolution transmission electron microscopy images in plan (left) and transverse (right) views of ferromagnetic  $\text{Co}_x\text{Ni}_{1-x}$  vertically aligned nanocomposites (VANs) in  $\text{SrTiO}_3$  matrix grown by sequential pulsed laser deposition (reproduced from [95, 96]). (b) Schematics of basic (top) and hybrid (bottom) VAN thin films. (c) Transverse scanning transmission electron microscopy images showing chemical contrast of Au-Co nanocomposites in  $\text{SrTiO}_3$  matrix (reproduced from [58]).

## 4.2 Structural properties of Au NWs

Three Au- $\text{SrTiO}_3$  samples were grown with varying growth temperature  $T_{\text{growth}}$  from 550 °C to 650 °C to demonstrate its influence on the structure of the matrix and the nanowires. A low temperature should have adverse effects on the crystal quality of the oxide matrix [98], whereas a high temperature should induce a high mobility of the Au adatoms [99], unfavourable to nucleation. The number of basic sequence repetition  $N$  was varied as well, to study the influence of the aspect ratio on the optical properties. The specifics related to the growth procedure of these samples are listed in Table 4.1.

### 4.2.1 Diameter, density and epitaxy

In this section, the structural properties of Au- $\text{SrTiO}_3$  nanocomposite thin film samples were investigated by transmission electron microscopy and x-ray diffraction. The diameter of the nanowires was measured by a statistical study of a set of plan view transmission electron microscopy images and the thickness by cross section view transmission electron microscopy

Table 4.1 – List of the Au-SrTiO<sub>3</sub> nanocomposite thin film samples. The growth process follows a basic ablation sequence  $[n_{\text{SrTiO}_3} + n_{\text{Au}}] \times N$ , where  $n_{\text{SrTiO}_3}$  and  $n_{\text{Au}}$  are the number of shots on the SrTiO<sub>3</sub> and Au targets, respectively and  $N$  is the number of repetition.  $T_{\text{growth}}$  is the growth temperature.

Sample	$n_{\text{SrTiO}_3}$	$n_{\text{Au}}$	$N$	$T_{\text{growth}}$ (°C)
<i>n1</i>	18	6	375	550
<i>n2</i>	18	6	180	600
<i>n3</i>	18	6	375	650

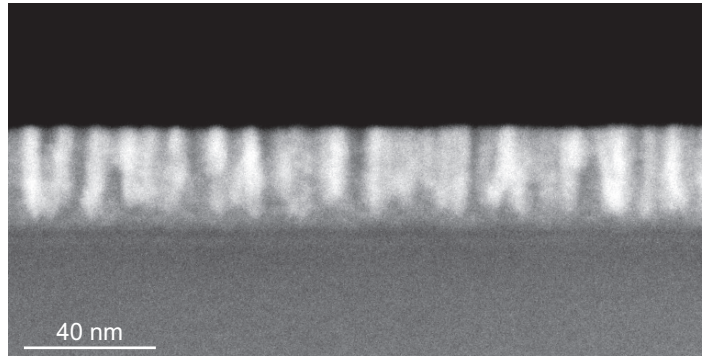


Figure 4.2 – High-angle annular dark-field scanning transmission electron microscopy cross section view image in the [100] zone axis of sample *n1*.

and x-ray reflectivity. The epitaxy of the nanowires and the oxide matrix was locally studied by transmission electron microscopy, whereas the general distribution of each epitaxy variant is deduced by x-ray diffraction.

High-angle annular dark-field scanning transmission electron microscopy is a compositional contrast imaging technique. The atomic number  $Z$  of Au ( $Z_{\text{Au}} = 79$ ) is higher than that of Sr, Ti and O ( $Z_{\text{Sr}} = 38$ ,  $Z_{\text{Ti}} = 22$  and  $Z_{\text{O}} = 8$ ), therefore the intensity of the Au NWs should be higher than that of the oxide matrix. Fig. 4.2 shows a HAADF-STEM cross section view image in the [100] zone axis of sample *n1*, showing a significant contrast between a grey volume, the SrTiO<sub>3</sub> matrix and light ribbons, the Au NWs. The Au NWs stretch from the top to the bottom of the SrTiO<sub>3</sub> matrix, normal to the substrate, in consequence the measure of the thickness of the epilayer gives the length of the NWs. A length of the NWs of 30 nm is deduced from Fig. 4.2.

Fig. 4.3 shows high-resolution transmission electron microscopy images of Au NWs in SrTiO<sub>3</sub> matrix in the [001] zone axis. The plan view (Fig. 4.3(a)(b)) shows dark disks on a light surface, corresponding to the section of Au NWs and the SrTiO<sub>3</sub> matrix, respectively. As Fig. 4.2 and Fig. 4.3 show elongated ribbons in cross section view and circular sections in plan view, respectively, high-resolution transmission electron microscopy images prove the self-assembly of the ablated Au-SrTiO<sub>3</sub> matter into Au NWs in oxide matrix.

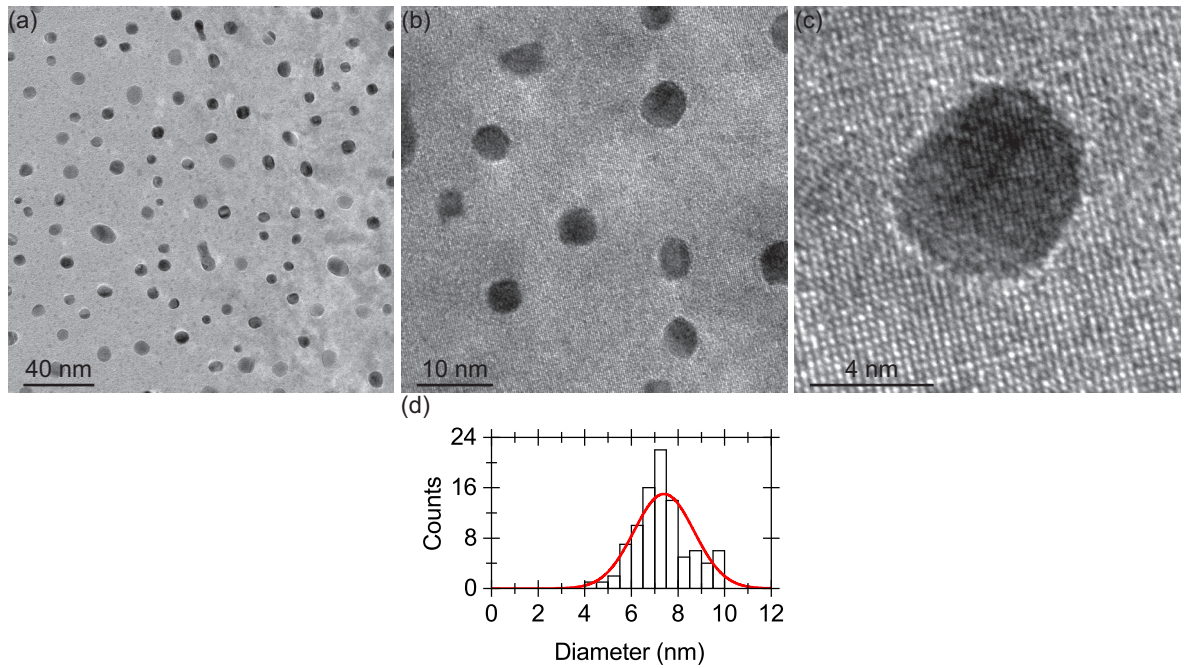


Figure 4.3 – Transmission electron microscopy study of Au-SrTiO<sub>3</sub> nanocomposite thin film *n1*. (a) Low-resolution transmission electron microscopy plan view image in the [001] zone axis. (b) High-resolution transmission electron microscopy plan view image in the [001] zone axis. (c) Enlargement of Fig. 4.3(b) showing the circular section of a Au nanowire in SrTiO<sub>3</sub> matrix. (d) Diameter distribution of Au NWs in nanocomposite thin film *n1*, extracted from a low-resolution transmission electron microscopy plan view image.

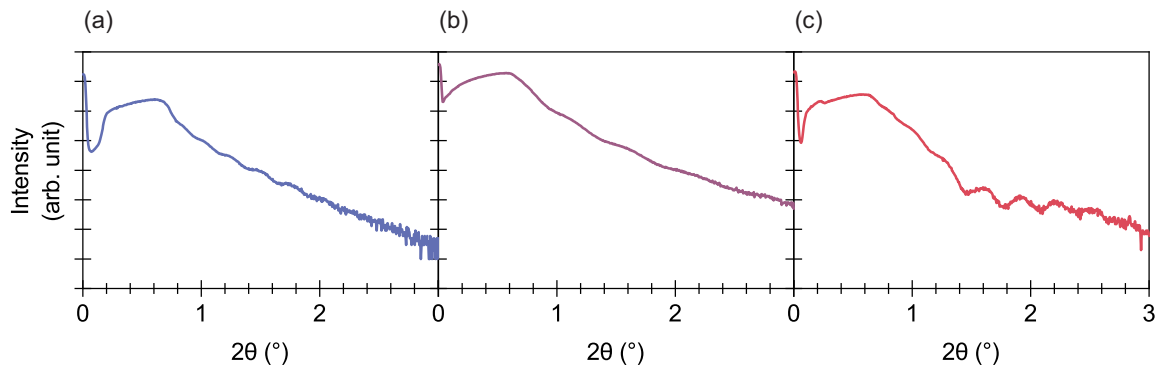


Figure 4.4 – X-ray reflectivity scans of Au-SrTiO<sub>3</sub> nanocomposite thin films, (a) *n1*, (b) *n2* and (c) *n3* (log<sub>10</sub> scale).

Other than cross section view electron microscopy, the thickness of the epilayer can be deduced by x-ray reflectivity. Fig. 4.4 shows the reflectivity scans of Au-SrTiO<sub>3</sub> nanocomposite thin films from  $2\theta = 0^\circ$  to  $6^\circ$ . An inflexion at  $2\theta = 0.6^\circ$  is observed in every scan and corresponds to the critical angle  $2\theta_c$ . Fringes are seen on the reflectivity scans for  $2\theta > 2\theta_c$ . These fringes are caused by the interference of totally reflected x-rays from the top and bottom interfaces of the layer, and their spacing is used to deduce the thickness of the layer. Eq. 3.2 gives a thickness of epilayer  $t = 32$  nm for *n1* (Fig. 4.4(a)). The thickness of epilayer of sample *n1* deduced by HAADF-STEM (Fig. 4.2) is close to that deduced by x-ray reflectivity, the value of  $t$  found by x-ray reflectivity is consistent.

The mean diameter  $\langle d \rangle$ , its distribution, and the density  $\rho$  of the NWs are measured from the statistical study of transmission electron microscopy images Fig. 4.3(a)(b). Fig. 4.3(c) shows the diameter distribution of NWs, a mean diameter of  $7.4 \pm 1.3$  nm and a density of  $0.21 \times 10^{-2} \text{ nm}^{-2}$  are extracted. The thickness is deduced from x-ray reflectivity (Fig. 4.4). These structural characteristic values of Au NWs in SrTiO<sub>3</sub> matrix, grown at different growth temperatures, are listed in Table 4.2.

Table 4.2 – Structural characteristic values deduced by high-resolution transmission electron microscopy and x-ray reflectivity of Au nanowires.  $\langle d \rangle$  is the mean diameter of the nanowires,  $\rho$  is the in plane density of nanowires,  $t$  is the epilayer thickness and  $T_{\text{growth}}$  is the growth temperature.  $\langle d \rangle$  and  $\rho$  were measured by transmission electron microscopy and  $t$  was deduced by x-ray reflectivity.

Sample	$\langle d \rangle$ (nm)	$\rho$ ( $10^{-2} \text{ nm}^{-2}$ )	$t$ (nm)	$T_{\text{growth}}$ ( $^\circ\text{C}$ )
<i>n1</i>	$7.4 \pm 1.3$	0.21	32	550
<i>n2</i>	$6.5 \pm 1.2$	0.29	13	600
<i>n3</i>	-	-	25	650

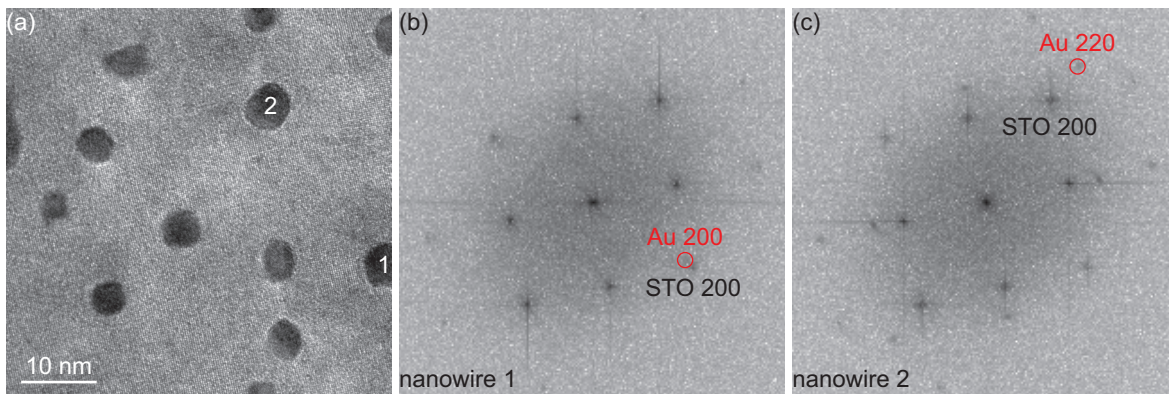


Figure 4.5 – High-resolution transmission electron microscopy (HRTEM) study of the epitaxy of sample *n1*. (a) HRTEM plan view image in the [001] zone axis. Fast Fourier transform of (b) nanowire 1 and (c) nanowire 2.

Fast Fourier transform were done on high-resolution transmission electron microscopy plan view images, giving an insight of the epitaxy. Fig. 4.3(c) shows the enlargement of nanowire 1 (Fig. 4.5(a)) and the lattice planes of Au and SrTiO<sub>3</sub>. The fast Fourier transform of nanowire 1 (Fig. 4.5(b)) shows diffraction spots, attributed to Au 200 and STO 200 planes. The alignment of the Au 200 and STO 200 diffraction spots shows that the (100) planes of Au and SrTiO<sub>3</sub> are parallel, thus an epitaxial relationship Au(001)/STO(001), Au[100] || STO[100] is defined. This epitaxial relationship is related to that of a cube-on-cube structure. The fast Fourier transform of nanowire 2 (Fig. 4.5(c)) also shows diffraction spots. These diffraction spots are attributed to Au220 and STO200 planes and define a different epitaxial relationship Au(001)/STO(001), Au[110] || STO[100]. This epitaxial relationship indicates an in plane 45° rotation of the Au lattice, with respect to the SrTiO<sub>3</sub> lattice.

The study of the nanocomposites by fast Fourier transform shows that variants of epitaxy exist, Au NWs either have an in plane 45° rotation or a cube-on-cube structure. A sound amount of each variant cannot be measured by transmission electron microscopy because of the limited statistics.

#### 4.2.2 Influence of the growth temperature on the epitaxy

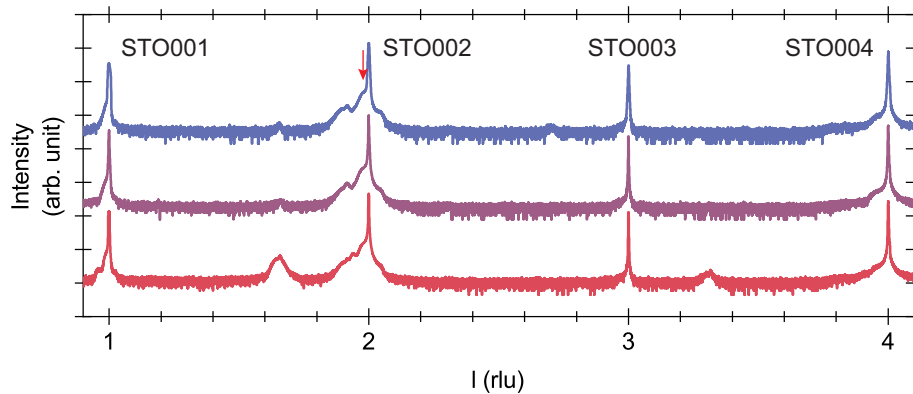


Figure 4.6 –  $\theta$ - $2\theta$  x-ray diffraction scans from  $2\theta = 20^\circ$  to  $120^\circ$  of samples  $n1$  ( $T_{\text{growth}} = 550^\circ\text{C}$ , blue line),  $n2$  ( $T_{\text{growth}} = 600^\circ\text{C}$ , purple line) and  $n3$  ( $T_{\text{growth}} = 650^\circ\text{C}$ , red line) ( $\log_{10}$  scale). The horizontal axis is expressed in bulk SrTiO<sub>3</sub> reciprocal lattice unit (rlu). The matrix reflection is marked by a red arrow.

$\theta$ - $2\theta$  x-ray diffraction scans were measured on three samples with varying growth temperatures  $T_{\text{growth}}$  from  $550^\circ\text{C}$  to  $650^\circ\text{C}$  to study the influence of  $T_{\text{growth}}$  on the epitaxy of Au NWs and the SrTiO<sub>3</sub> matrix.  $\theta$ - $2\theta$  measures the diffracted intensity of the planes parallel to the substrate, that is the epitaxy in the [001]  $l$ -axis.

Fig. 4.6 shows the  $\theta$ - $2\theta$  x-ray diffraction scans from  $2\theta = 20^\circ$  to  $120^\circ$ . Four main peaks are measured at  $l = 1$  rlu,  $l = 2$  rlu,  $l = 3$  rlu and  $l = 4$  rlu, and attributed to the {001} planes of the

SrTiO<sub>3</sub> substrate. A shoulder, marked by an arrow in Fig. 4.7, is seen, and corresponds to the (002) planes of the SrTiO<sub>3</sub> matrix. The shoulder shows a shift from the bulk position, attributed to the out of plane distortion of the SrTiO<sub>3</sub> matrix, a consequence of the nonstoichiometry of SrTiO<sub>3</sub> caused by the oxygen-free growth, often reported in the literature [100–102]. The SrTiO<sub>3</sub> substrate and matrix peaks are seen on every sample.

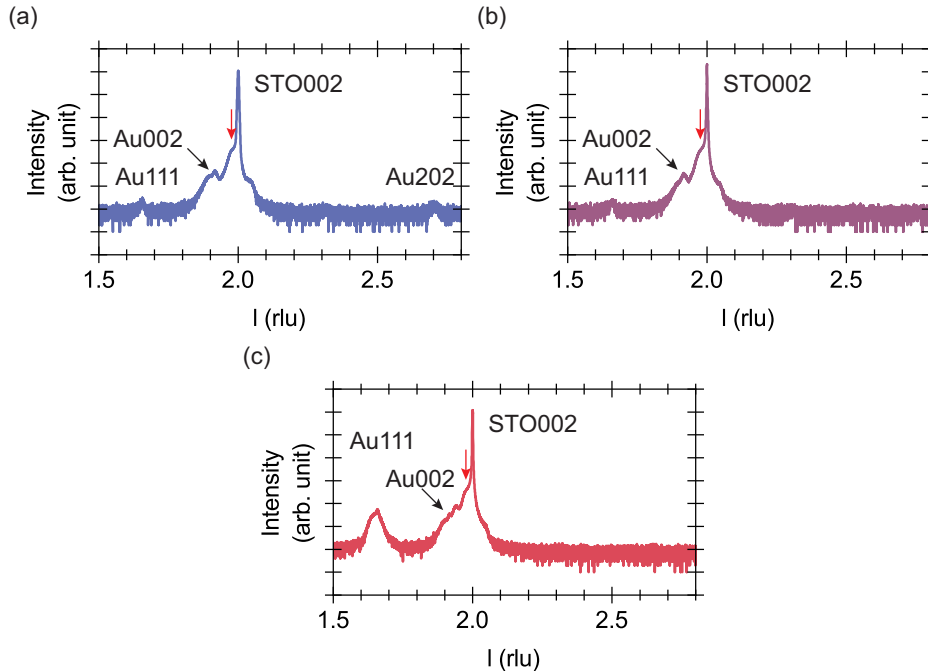


Figure 4.7 –  $\theta$ - $2\theta$  x-ray diffraction scans near the 002 Bragg reflection of the SrTiO<sub>3</sub> substrate of (a)  $n1$ , (b)  $n2$ , (c)  $n3$  (log<sub>10</sub> scale). The horizontal axis is expressed in bulk SrTiO<sub>3</sub> reciprocal lattice unit (rlu). The matrix reflection is marked by a red arrow.

Fig. 4.7 shows the enlargement of Fig. 4.6 from 1.5 rlu to 2.8 rlu, near 002 Bragg reflection of the SrTiO<sub>3</sub> substrate. The  $\theta$ - $2\theta$  scan of sample  $n1$  (Fig. 4.7(a)) shows the reflection of Au111, Au002 and Au202 at  $l_{\text{Au111}} = 1.66$  rlu,  $l_{\text{Au002}} = 1.91$  rlu and  $l_{\text{Au202}} = 2.70$  rlu, respectively. The structure factors of Au111, Au002 and Au202 have close values, therefore the higher intensity of Au002 infers that Au(001)  $\parallel$  STO(001) is preferential. The  $\theta$ - $2\theta$  scan of sample  $n2$  (Fig. 4.7(b)) is close to that of sample  $n1$ , showing the reflection of Au111 and Au002. Au202 does not appear. The intensity of Au002 is higher than that of Au111, Au(001)  $\parallel$  STO(001) is also favoured for this sample. For  $n3$ , the  $\theta$ - $2\theta$  scan shows fringes near the Bragg peak of the oxide matrix, indicating its high crystallinity. Au111 and Au002 are seen, however their intensities are equal, therefore no orientation is favoured.

$\theta$ - $2\theta$  scans of samples  $n1$  ( $T_{\text{growth}} = 550$  °C) and  $n2$  ( $T_{\text{growth}} = 600$  °C) show that Au grows with (001) planes parallel to (001) planes of SrTiO<sub>3</sub>. For sample  $n2$ , in addition, the reflection of Au202 does not appear. For a higher  $T_{\text{growth}}$  (sample  $n3$ ), the matrix is of high crystal order, but

Au does not have a preferential orientation. As a consequence, a temperature of 600 °C is more suitable for the growth of Au NWs and the oxide matrix.

## 4.3 Optical properties

### 4.3.1 Gans theory simulations

A localised plasmon is a collective mode of oscillation of the free electrons of a metal nanoparticle. The electric field of a light wave can excite the electrons and induce a polarisation of the electron cloud. At resonance, for a frequency of the light wave close to the plasmon eigenfrequency, the absorption and the electric near-field of the particle are amplified. The resonance amplitude and frequency is related to the shape and the composition of the nanocomposite and its dielectric medium.

After a light wave hits a nanoparticle, photons can be absorbed by the material and the energy transferred in heat or luminescence, or they can be scattered. These two processes are quantified by the absorption and scattering cross sections,  $\sigma_{abs}$  and  $\sigma_{sca}$ , respectively. The absorption and scattering cross sections define the effective surface from which the nanoparticle absorbs or scatters light. At plasmonic resonance,  $\sigma_{abs}$  and  $\sigma_{sca}$  can be larger than the physical size of the particle.

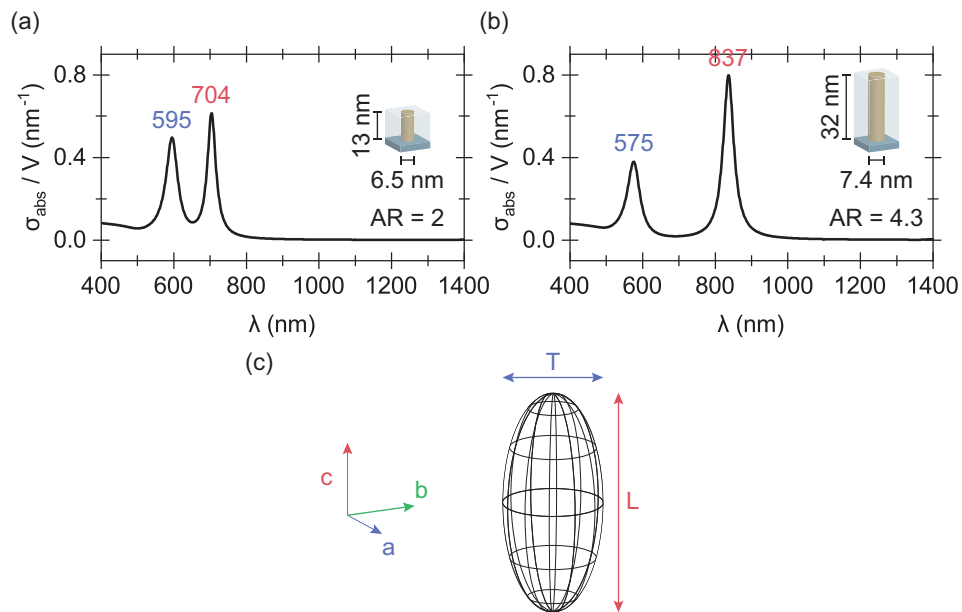


Figure 4.8 – Absorption cross section  $\sigma_{abs}$  calculated by Gans theory of Au particles modelled as ellipsoids in  $\text{SrTiO}_3$  medium for (a)  $n_2$  ( $\langle d \rangle = 6.5$  nm,  $t = 13$  nm) and (b)  $n_1$  ( $\langle d \rangle = 7.4$  nm,  $t = 25$  nm). (c) Schematics of a prolate ellipsoid.

Fig. 4.8 shows the absorption cross section  $\sigma_{abs}$  calculated by Gans theory (Eq. 2.42) of Au particles modelled as ellipsoids in  $\text{SrTiO}_3$  medium for  $n_2$  (Fig. 4.8(a)) and  $n_1$  (Fig. 4.8(b)). The

diameter  $\langle d \rangle$  and the length  $t$  of sample  $n2$  and  $n1$  used to calculate  $\sigma_{abs}$  were measured by transmission electron microscopy and x-ray reflectivity (Table 4.2). The permittivity of Au  $\epsilon(\omega) = \epsilon_1(\omega) + i\epsilon_2(\omega)$  was measured by Arwin [103] (Fig 4.9). A permittivity of SrTiO<sub>3</sub> of  $\epsilon_s = 5.71 \text{ F m}^{-1}$  was used to calculate  $\sigma_{abs}$ .

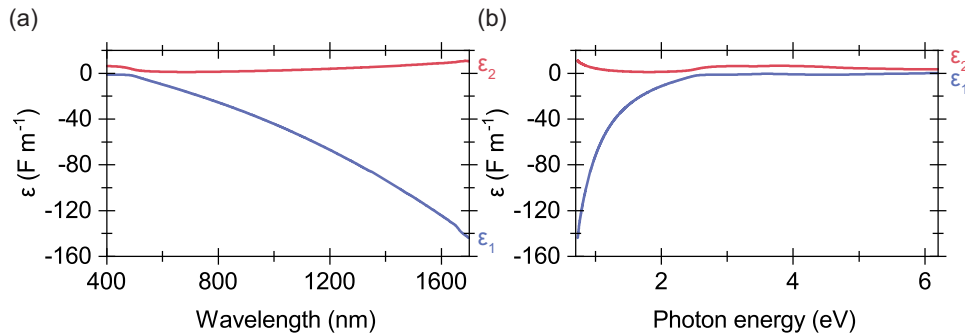


Figure 4.9 – Dielectric function of Au as a function of the (a) wavelength ( $\lambda$ ) and (b) photon energy ( $h\nu$ ) (adapted from [103]).

Two absorption bands in the visible and the near-infrared range are seen in Fig. 4.8(a)(b), attributed to the two nondegenerate plasmonic resonance modes, i.e. transverse and longitudinal modes, respectively. The transverse mode is related to the free electron polarisation in the normal to the nanowire, the lower in energy longitudinal mode is stronger and related to the free electron oscillation in the long axis of the nanowire (Fig. 4.8(c)). The transverse mode of resonance is at 595 nm and 581 nm for  $n2$  and  $n1$ , respectively and that of the longitudinal is at 704 nm and 787 nm for  $n2$  and  $n1$ , respectively.  $n2$  (AR = 2) and  $n1$  (AR = 4.3) are of different shapes, Fig. 4.8(a)(b) shows that a higher AR shifts the longitudinal mode to higher wavelengths.

### 4.3.2 Experimental measurements

Plasmonic resonance in Au-SrTiO<sub>3</sub> nanocomposite thin films was studied by transmission spectrometry and ellipsometry. Fig. 4.10 shows the  $1 - T$  spectra of sample  $n2$  (in solid line) and of a SrTiO<sub>3</sub> substrate (in dashed line). Below 400 nm, light is totally absorbed for both samples, due to the band gap of SrTiO<sub>3</sub> (from 3.22 eV to 3.5 eV [104]). An absorption band at 566 nm is seen in the spectrum of sample  $n2$ . Simulation of the absorption cross sections (Fig. 4.8(a)) show a transverse band at 595 nm, thus the absorption band seen in the spectrum is related to the transverse mode of the plasmonic resonance in the Au NWs. The small difference in plasmonic resonance wavelength between the Gans theory simulation and the spectrometry measurement can be explained by the optical constants used to simulate the absorption cross sections. Indeed, the optical constants of the matrix are those of bulk SrTiO<sub>3</sub>, whereas the matrix is nonstoichiometric and its constants are thus different. Furthermore, transmission

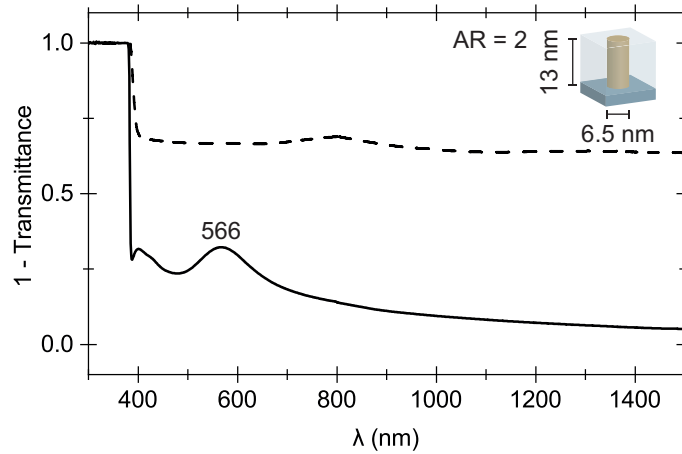


Figure 4.10 – 1 -  $T$  spectra of Au-SrTiO<sub>3</sub> nanocomposite thin film  $n2$  (solid line) and of a SrTiO<sub>3</sub> substrate (dashed line). Below 400 nm, light is totally absorbed because of the band gap of SrTiO<sub>3</sub> (from 3.22 eV to 3.5 eV [104]).

electron microscopy images show nanoinclusions of Au in the matrix, changing the optical response of the matrix. The longitudinal mode of the plasmonic resonance is not measured in Fig. 4.10 and cannot be probed. Because of the normal incidence in the spectrometer, the polarisation vector is not parallel with the long axis of the nanowires and longitudinal plasmons cannot be excited.

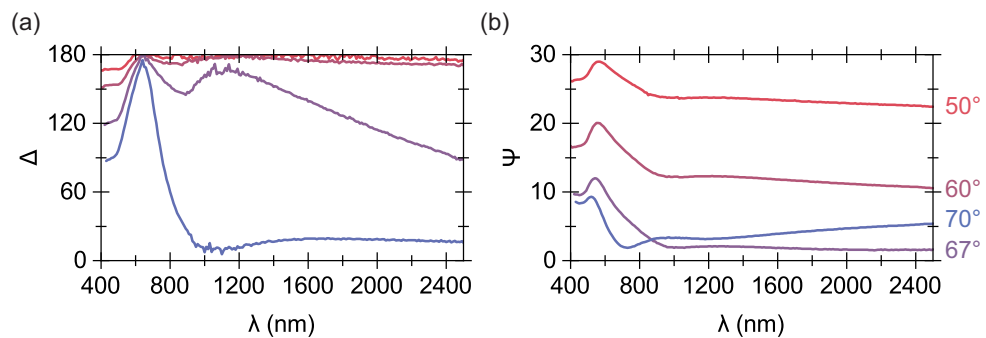


Figure 4.11 – (a) Angles  $\Delta$  and (b)  $\Psi$  of sample  $n1$ , measured by ellipsometry.  $\tan \Psi$  and  $\Delta$  are related to the ratio of amplitude and the phase difference of the  $p$  and  $s$  components by the equation  $\frac{r_p}{r_s} = \tan \Psi e^{i\Delta}$ .

Sample  $n1$  was measured by ellipsometry. Fig. 4.11(a) shows the phase difference  $\Delta$  and Fig. 4.11(b) shows the angle related to the ratio of amplitude  $\Psi$ , as a function of the wavelength  $\lambda$  and the angle of incidence. As discussed previously, optical constants cannot be readily deduced from the measured angles  $\Psi$  and  $\Delta$ . Thus, a model of sample  $n1$  is used to fit  $\Psi$  and  $\Delta$  according to the Kramers-Krönig relations.

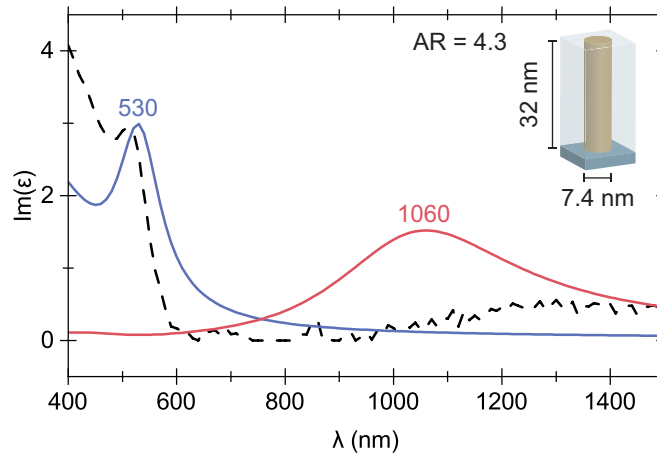


Figure 4.12 – Imaginary part of the permittivity  $\underline{\epsilon}$  of sample  $n1$ , deduced from angles  $\Delta$  and  $\Psi$  (Fig. 4.11). The imaginary part of the permittivity of an Au NW, modelled as an ellipsoid with  $AR = 4.3$ , is plotted in blue (transverse mode) and red (longitudinal mode). The dashed line shows the optical response of an Au-SrTiO<sub>3</sub> nanocomposite thin film.

Optical constants were first deduced using an isotropic homogeneous film model, as plotted in Fig. 4.12 in dashed line. The imaginary part of the permittivity  $\epsilon_2$  was then refined using a multilayer model of Au ellipsoids in a SrTiO<sub>3</sub> matrix on a SrTiO<sub>3</sub> substrate, as shown in Fig. 4.12 in solid lines. Some approximations were made to model this film: (1) Au NWs were modelled as ellipsoids by changing the depolarisation factor, (2) the Au NWs distribution is considered to be isotropic and homogeneous. These models were built using thickness, aspect ratio and volume fraction measured by transmission electron microscopy and x-ray reflectivity.

The effective imaginary part of the permittivity  $\underline{\epsilon}$  of sample  $n1$  is plotted in Fig. 4.12 in dashed line and shows two absorption bands.  $\epsilon_2$  is refined by a multilayer model (Fig. 4.12 in solid lines). The absorption bands at 530 nm and 1060 nm correspond to the transverse and longitudinal modes of the plasmonic resonance, respectively. As expected by Gans theory calculations, two bands are measured in the visible and near-infrared ranges, and the optical response is anisotropic. There is however a difference of 8% between the simulation and the ellipsometry measurement for the transverse mode. This difference reaches 25% for the longitudinal mode. This discrepancy is unlikely caused by a dipolar coupling between the nanowires. Indeed, dipolar coupling is seen when the distance between the nanoparticles is comparable to their size [105].

## 4.4 Conclusion

This chapter discussed the growth of Au-SrTiO<sub>3</sub> nanocomposite thin films by sequential pulsed laser deposition, and reported structure and optical properties of thin films. To study

the influence of growth temperature on the crystal quality, samples were deposited at different temperatures. High-angle annular dark-field scanning transmission electron microscopy and high-resolution transmission electron microscopy proved the growth of Au NWs in SrTiO<sub>3</sub> matrix on SrTiO<sub>3</sub> substrate. A mean diameter of the Au NWs of  $\approx 7$  nm was measured in electron microscopy images. HAADF-STEM measurements and x-ray reflectivity were used to measure the length of the nanocomposites.

Epitaxy of the samples was studied by x-ray diffraction. Three samples were deposited at different temperatures  $T_{\text{growth}}$  of 550 °C, 600 °C and 650 °C. X-ray diffraction showed less polycrystallinity of Au NWs at 550 °C, than at 650 °C. On the other hand, crystallinity of the SrTiO<sub>3</sub> matrix is higher at 650 °C. Diffraction study of the sample deposited at an intermediate  $T_{\text{growth}}$  of 600 °C showed that a preferential cube-on-cube epitaxy between Au and SrTiO<sub>3</sub>. A temperature of 600 °C is thus more suitable for the growth of Au NWs and the SrTiO<sub>3</sub> matrix.

Optical properties of Au-SrTiO<sub>3</sub> nanocomposite thin films were then reported. Absorption cross section of samples *n2* and *n1* was calculated by Gans theory. In the two samples, two absorption bands were predicted at visible and near-infrared wavelengths. These absorption bands are related to the transverse and longitudinal plasmonic resonance modes. An experimental study of the excitation of plasmons in Au-SrTiO<sub>3</sub> nanocomposite thin films was conducted by transmission spectroscopy and ellipsometry measurements. An absorption band at 566 nm is measured by spectroscopy in sample *n2*, corresponding to the transverse mode of the plasmonic resonance. Due to the geometry of the set-up, it is not possible to excite the longitudinal mode. Optical properties were also measured in sample *n1* by ellipsometry. A model was used to fit angles  $\Delta$  and  $\Psi$ , to extract the imaginary part of the permittivity  $\epsilon_2$ , related to absorption. An anisotropic optical response is extracted, showing two absorption bands at 530 nm and 1060 nm, which correspond to the transverse and longitudinal modes of the plasmonic resonance respectively. However, these experimental values stray from the Gans theory predictions. An explanation of this discrepancy cannot be a dipolar coupling between the nanowires, due to their size and interdistance. On the other hand, nanoinclusions of Au in the matrix were seen in transmission electron microscopy, changing the optical response of the matrix. An explanation, which cannot be ruled out, could lie in the optical constants used in Gans theory. Bulk SrTiO<sub>3</sub> optical constants were used, and the matrix is nonstoichiometric and oxygen-deficient, leading to a change in optical constants.

## CHAPTER 5

### HYBRID NANOWIRES

5.1	Introduction . . . . .	67
5.2	Structural properties of hybrid NWs . . . . .	68
5.2.1	Diameter, density . . . . .	69
5.2.2	Phase segregation . . . . .	71
5.2.3	Epitaxy of hybrid NWs . . . . .	77
5.2.4	Off-Bragg scattering . . . . .	79
5.3	Magnetic properties of hybrid NWs . . . . .	87
5.3.1	Magnetic anisotropy . . . . .	87
5.3.1.1	Magnetic anisotropy constants . . . . .	87
5.3.1.2	Magnetic anisotropy at low temperatures . . . . .	89
5.3.2	Temperature dependence of the coercivity and activation length . . . . .	92
5.3.2.1	Temperature dependence of the coercivity . . . . .	92
5.3.2.2	Activation length . . . . .	94
5.4	Discussions on the magnetic anisotropy . . . . .	95
5.4.1	Effect of large structural strain on the anisotropy . . . . .	95
5.4.2	Inhomogeneity and loss of anisotropy . . . . .	96
5.5	Conclusion . . . . .	100

#### 5.1 Introduction

Co and Au, compounds with low miscibility, are a typical material choice for the growth of hybrid magnetoplasmonic nanocomposites. A previous work by Hennes et al. proved the growth of hybrid Au-Co nanowires in SrTiO<sub>3</sub> matrix by pulsed laser deposition [58]. However, at room temperature pure Co has a hexagonal close-packed (hcp) structure [106], which is detrimental to the uniaxial anisotropy of the nanowires as the *c*-axis of hexagonal Co is not parallel to the long axis of the NWs, and thus would not achieve a bistable magnetic system [107]. A previous work by Bonilla et al. [108] showed that Co and Ni can form a homogeneous alloy and grow into epitaxial CoNi nanowires in CeO<sub>2</sub> matrix, with an axial strain smaller than 1%. The growth of CoNi nanowires was further demonstrated in SrTiO<sub>3</sub> matrix in a compositional study of the CoNi alloy [42, 60]. By increasing the Co content from 20% to 80%, the axial strain has been increased from 2.4% to 4.2%. In spite of the high concentration of Co, the nanowires retained a face-centred cubic (fcc) phase at room temperature. It should be

noted that the fcc/hcp phase transition at room temperature of bulk CoNi binary alloy occurs at Co content superior to 65 % [109].

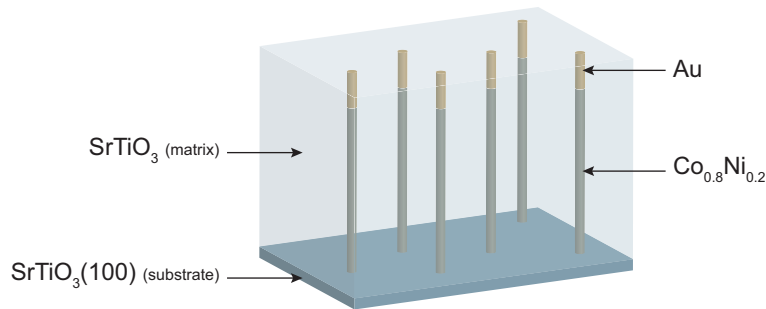


Figure 5.1 – Schematics of a hybrid nanocomposites thin film. The hybrid nanowires in SrTiO<sub>3</sub> matrix consist of two parts, a ferromagnetic nanowire made of Co<sub>0.8</sub>Ni<sub>0.2</sub> alloy supporting an optical nanowire made of Au.

From these previous works, epitaxial hybrid nanocomposite thin films were grown by pulsed laser deposition. Fig. 5.1 sketches the hybrid nanowires in oxide matrix. The ferromagnetic nanowires are made of CoNi alloy. A Co content of 80 % was chosen to retain a hard uniaxial anisotropy with the face-centred cubic phase. The optical nanowires are made of Au. Given that CoNi and Au require different growth conditions, the ideal growth temperature being higher for CoNi ( $\approx 700^\circ\text{C}$ ) than that for Au ( $600^\circ\text{C}$ ) according to previous procedures, the deposition consists in a two-step process. CoNi nanowires are first deposited at a temperature of  $\approx 700^\circ\text{C}$  following the basic ablation sequence  $[[n_{\text{SrTiO}_3} + n_{\text{NiO}}] + [n_{\text{SrTiO}_3} + n_{\text{CoO}}] \times 4] \times N$ . Au nanowires are thereafter grown at a lower temperature ( $600^\circ\text{C}$ ) following the basic ablation sequence  $[n_{\text{SrTiO}_3} + n_{\text{Au}}] \times N$ . Co and Ni contents were checked by energy-dispersive spectroscopy, using a scanning electron microscope. The specifics related to the growth procedure of these samples are listed in Table 5.1.

In this chapter, the structure and magnetic properties of epitaxial hybrid nanocomposite thin films are presented. The structure was investigated by transmission electron microscopy and x-ray diffraction using synchrotron radiation, proving the self-assembly of hybrid nanowires and unveiling an important axial strain. The magnetic properties were measured by vibrating sample magnetometry, demonstrating an important magnetic anisotropy correlated with the structure.

## 5.2 Structural properties of hybrid NWs

The growth of Au-SrTiO<sub>3</sub> nanocomposite thin films by sequential pulsed laser deposition has been proven in the previous chapter. Thus, the growth of Au NWs and Co<sub>0.8</sub>Ni<sub>0.2</sub> NWs in the same SrTiO<sub>3</sub> matrix should be possible. The mean diameter of the Au NWs and Co<sub>0.8</sub>Ni<sub>0.2</sub> NWs [60, 110] are of the same order, hinting that the stacking of Au NWs and Co<sub>0.8</sub>Ni<sub>0.2</sub> NWs is

Table 5.1 – List of the (Au-)CoNi-SrTiO<sub>3</sub> nanocomposite thin film samples. The two-step growth process follows a first basic ablation sequence  $[[n_{\text{SrTiO}_3} + n_{\text{NiO}}] + [n_{\text{SrTiO}_3} + n_{\text{CoO}}] \times 4] \times N$  and ends with a second basic ablation sequence  $[n_{\text{SrTiO}_3} + n_{\text{Au}}] \times N$ , where  $n_{\text{SrTiO}_3}$  and  $n_{\text{NiO,CoO,Au}}$  are the number of shots on the SrTiO<sub>3</sub> and NiO, CoO or Au targets, respectively and  $N$  is the number of repetition.  $T_{\text{growth}}$  is the growth temperature.

Sample	First step				Second step			
	$n_{\text{SrTiO}_3}$	$n_{\text{NiO,CoO}}$	$N$	$T_{\text{growth}}$ (°C)	$n_{\text{SrTiO}_3}$	$n_{\text{Au}}$	$N$	$T_{\text{growth}}$ (°C)
<i>s1</i>	18	6	150	700	18	9	160	600
<i>s2</i>	18	6	150	700	18	6	160	600
<i>s3</i>	18	9	150	680	18	6	160	600
<i>s4</i>	18	9	150	680	18	6	90	600
<i>s5</i>	18	9	150	680	18	6	90	600
<i>s6</i>	18	9	150	680	18	18	20	600
<i>s7</i>	18	6	150	700	-	300	1	600
<i>t1</i>	18	9	150	700	-	-	-	-
<i>t2</i>	18	9	150	680	-	-	-	-
<i>t3</i>	18	9	150	680	-	-	-	-

possible. It should be noted that the growth of Au NWs at the top of CoNi NWs can change the structure or the magnetic properties of the hybrid NWs, in comparison to pure nanowires. In this section, the study of the structure by electron microscopy and x-ray diffraction proves the growth of Au-Co<sub>0.8</sub>Ni<sub>0.2</sub>-SrTiO<sub>3</sub> epitaxial hybrid nanocomposite thin films with Au-Co<sub>0.8</sub>Ni<sub>0.2</sub> segregation. The structural properties of two sets of selected samples are presented in this section, samples from *s1* to *s3*, whose structural properties are studied extensively, and samples in the series *s4* to *s7* and *t1* to *t3*, whose structure is correlated with the magnetic properties. Furthermore, *t*-series samples, made of Co<sub>0.8</sub>Ni<sub>0.2</sub> VANs, were compared to *s*-series samples to study the physical properties of simple and hybrid vertically aligned nanocomposite thin films.

### 5.2.1 Diameter, density

Fig. 5.2(a)(b) shows transmission electron microscopy images of hybrid Au-Co<sub>0.8</sub>Ni<sub>0.2</sub> nanowires in SrTiO<sub>3</sub> matrix. The plan view (Fig. 5.2(a)) shows the circular section of hybrid NWs and Fig. 5.2(c) the diameter distribution of NWs from a low-resolution transmission electron microscopy plan view image. A mean diameter  $\langle d \rangle = 6.3 \pm 1.5$  nm and density  $\rho = 0.37 \times 10^{-2}$  nm<sup>-2</sup> are measured from the statistical study of transmission electron microscopy images of sample *s1*. The mean diameter and the density values measured in plan view should be regarded with caution as each part of the NW may have different  $\langle d \rangle$  and  $\rho$ . Complementary energy-dispersive x-ray spectroscopy imaging and tilt view transmission electron microscopy allow to measure  $\langle d_{\text{CoNi}} \rangle$  and  $\langle d_{\text{Au}} \rangle$ , the diameter of the CoNi NWs and Au NWs, respectively.  $\langle d \rangle$  and  $\rho$  values of other samples are reported in Table 5.2. The cross section view (Fig. 5.2(b)) shows elongated ribbons and an interface separating the Au-SrTiO<sub>3</sub> and the Co<sub>0.8</sub>Ni<sub>0.2</sub>-SrTiO<sub>3</sub>

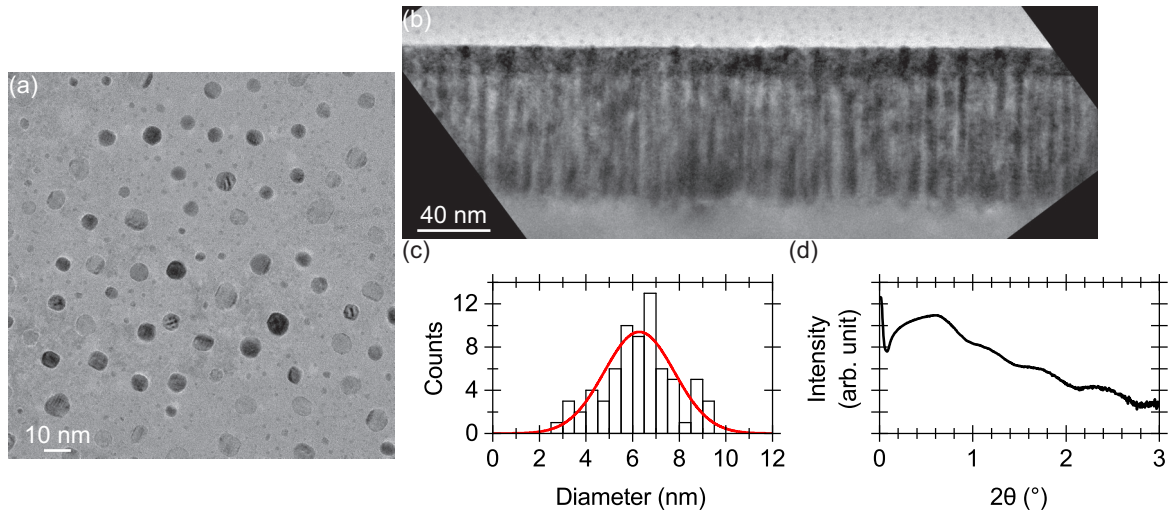


Figure 5.2 – Transmission electron microscopy and x-ray reflectivity study of Au-Co<sub>0.8</sub>Ni<sub>0.2</sub>-SrTiO<sub>3</sub> hybrid nanocomposite thin film *s1*. (a) Transmission electron microscopy plan view image in the [001] zone axis. (b) Transmission electron microscopy cross section view image in the [100] zone axis of a thick specimen. (c) Diameter distribution of NWs in hybrid nanocomposite thin film *s1*, extracted from a low-resolution transmission electron microscopy plan view image. (d) X-ray reflectivity scan from  $2\theta = 0^\circ$  to  $3^\circ$  (log<sub>10</sub> scale).

layers. Fig. 5.2(a)(b) prove the self-assembly of the ablated Au-Co<sub>0.8</sub>Ni<sub>0.2</sub>-SrTiO<sub>3</sub> matter into NWs in oxide matrix.

Fig. 5.2(b) is an image of a thick specimen, the hybrid nanowires stretch from the bottom to the top of the thin layer. A length of the hybrid NWs of 81 nm and of the Au NWs of 14 nm is deduced from Fig. 5.2(b). A x-ray reflectivity scan (Fig. 5.2(d)) was measured from  $2\theta = 0^\circ$  to  $3^\circ$  and a thickness of 11 nm is deduced from Eq. 3.2. This value is attributed to the thickness of Au-STO epilayer, as the resolution of the laboratory diffractometer is not high enough to discern the fringes of the CoNi-STO layer. The values of the length of the hybrid NWs and of the Au NWs of other samples are reported in Table 5.2.

To study the influence of the ratio of shots on the oxide and the metal targets on the diameter of the nanowires, samples *s1* and *s5* are compared. Samples *s1* and *s5* were grown by a two-step procedure following the basic sequences  $[[n_{\text{SrTiO}_3} + n_{\text{NiO}}] + [n_{\text{SrTiO}_3} + n_{\text{CoO}}] \times 4] \times N$  and  $[n_{\text{SrTiO}_3} + n_{\text{Au}}] \times N$ . As tabulated in Table 5.3, the number of shots on the metal targets is different in the two samples.  $n_{\text{NiO,CoO}}$  is indeed higher and  $n_{\text{Au}}$  lower in sample *s5* than in sample *s1*.

Fig. 5.3 shows transmission electron microscopy tilt view images of samples *s1* and *s5*. Hybrid nanocomposites in sample *s1* look like matchsticks, whereas those in sample *s5* have the shape of elongated cylinders. It thus appears that the shape of the nanowires can be tuned by the basic sequence used during deposition. It seems furthermore that the shape of each

Table 5.2 – Structural characteristic values deduced by high-resolution transmission electron microscopy, energy-dispersive x-ray spectroscopy imaging, and x-ray reflectivity of hybrid Au-Co<sub>0.8</sub>Ni<sub>0.2</sub> nanowires.  $\langle d \rangle_{\text{CoNi}}$  and  $\langle d \rangle_{\text{Au}}$  are the mean diameter of the CoNi NWs and Au NWs,  $\rho_{\text{CoNi}}$  and  $\langle \rho \rangle_{\text{Au}}$  are the in plane density of the CoNi NWs and the Au NWs.  $t$  is the total length of the hybrid NWs,  $t_{\text{CoNi}}$  and  $t_{\text{Au}}$  are the length of the CoNi NWs and Au NWs.

Sample	$\langle d \rangle_{\text{CoNi}}$ (nm)	$\langle d \rangle_{\text{Au}}$ (nm)	$\rho_{\text{CoNi}}$ ( $10^{-2} \text{ nm}^{-2}$ )	$\rho_{\text{Au}}$ ( $10^{-2} \text{ nm}^{-2}$ )	$t_{\text{CoNi}}$ (nm)	$t_{\text{Au}}$ (nm)	$t$ (nm)
<i>s1</i>	3.4	$6.3 \pm 1.5$	-	0.37	70	11	81
<i>s2</i>	3.1	$3.3 \pm 0.4$	1.2	1.0	-	13	-
<i>s3</i>	-	-	-	-	67	12	79
<i>s4</i>	-	-	-	-	68	6	74
<i>s5</i>	3.0	$3.0 \pm 0.2$	-	1.5	68	7	75
<i>s6</i>	3.2	$3.2 \pm 0.4$	-	1.3	59	5	64

Table 5.3 – Growth parameters of samples *s1* and *s5*.  $n_{\text{SrTiO}_3}$  and  $n_{\text{NiO,CoO,Au}}$  are the number of shots on the SrTiO<sub>3</sub> and NiO, CoO or Au targets, respectively and  $N$  is the number of repetition.  $T_{\text{growth}}$  is the growth temperature.

Sample	First step				Second step			
	$n_{\text{SrTiO}_3}$	$n_{\text{NiO,CoO}}$	$N$	$T_{\text{growth}}$ (°C)	$n_{\text{SrTiO}_3}$	$n_{\text{Au}}$	$N$	$T_{\text{growth}}$ (°C)
<i>s1</i>	18	6	150	700	18	9	160	600
<i>s5</i>	18	9	150	680	18	6	90	600

nanowire of the hybrid nanocomposites can be tuned differentially. The tuneability of the shape is rather interesting, as some magnetic and optical properties are modified by the aspect ratio of the nanoparticles, as discussed in the next subsection. By changing the basic sequence, these properties could therefore be tuned.

### 5.2.2 Phase segregation

Co and Au are typical materials with low miscibility. The Co-Au mixture shows a tendency to form structures with phase segregation [97] and theoretical work confirms that, at equilibrium, the mixture retains its low miscibility even when downsizing the system to a few hundred atoms [111]. The Ni-Au alloy is characterised by a miscibility gap in the solid state spanning through the entire concentration range at room temperature [112]. The miscibility gap is however significantly reduced for nanoparticles, the component mutual solubility increases as the size of particle decreases [113]. The phase separation of two Au-CoNi-SrTiO<sub>3</sub> nanocomposite thin films (*s1* and *s2*) was extensively studied by transmission electron microscopy and compositional microscopy (HAADF-STEM and EDXS).

The tilt view image of sample *s1* (Fig. 5.4) shows particles with the shape of a matchstick. This implies a segmented structure with elongated NWs covered by a spherical particle, however the chemical composition of each part cannot be guessed and the segregation of

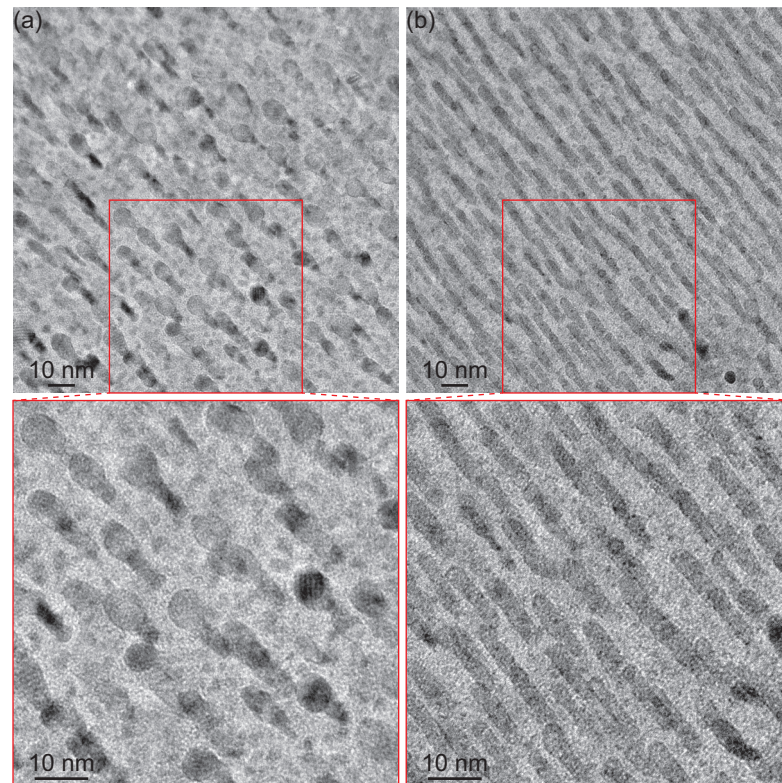


Figure 5.3 – Transmission electron microscopy tilt view images of samples (a) *s1* and (b) *s5*. The close-ups show that nanowires in samples *s1* and *s5* have different shapes.

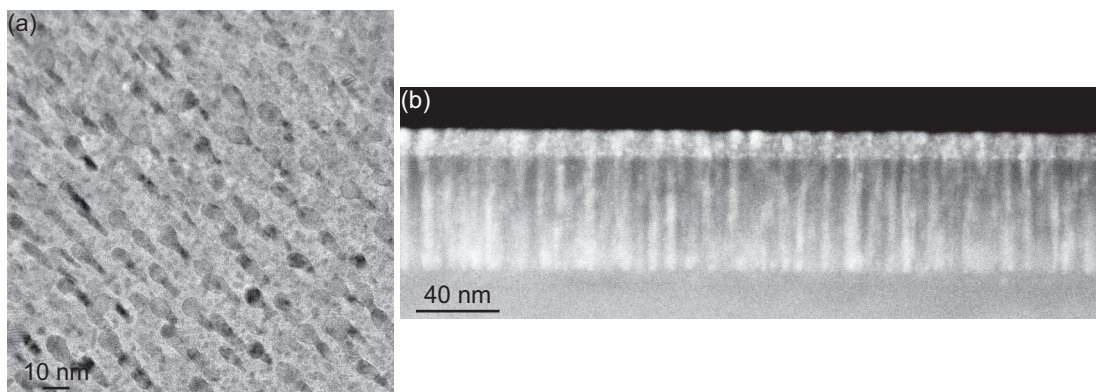


Figure 5.4 – Transmission electron microscopy images of sample *s1*. (a) Transmission electron microscopy tilt view image. (b) High-angle annular dark-field scanning transmission electron microscopy cross section view image in the [100] zone axis.

CoNi and Au cannot be confirmed by Fig. 5.4. Cross section view images (Fig. 5.4(b), Fig. 5.5) were taken by HAADF-STEM, a compositional contrast imaging technique, and transmission electron microscopy to confirm the segregation of CoNi and Au in a hybrid nanocomposite in SrTiO<sub>3</sub> matrix.

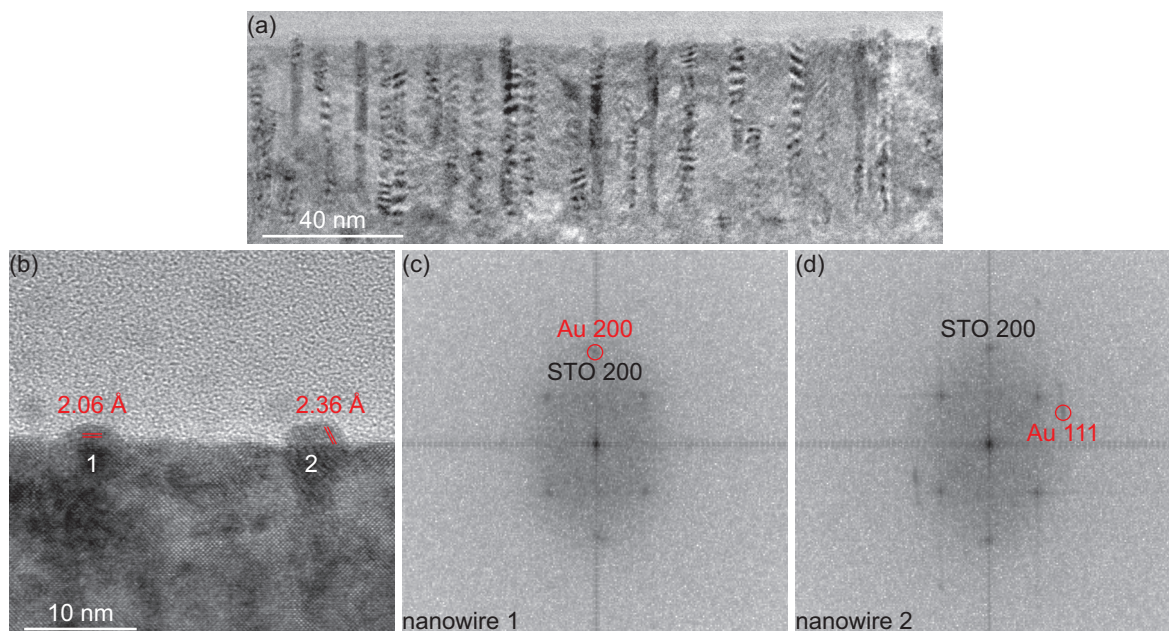


Figure 5.5 – High-resolution transmission electron microscopy images in cross section view of sample *s1* of (a) the total thin film and (b) the glue-thin film interface in the [100] zone axis. Fast Fourier transform of (c) nanowire 1 and (d) nanowire 2.

Fig. 5.4(b) shows the HAADF-STEM cross section view image of sample *s1*. The contrast gradient seen in one single layer is due to a thickness gradient caused by the ion milling, as HAADF-STEM is also sensitive to the quantity of matter. The nanowires stretch from the bottom to the top of the thin film and an interface is seen between two layers with different contrast, therefore these layers have different chemical compositions. Au-CoNi segregation is further shown by high-resolution transmission electron microscopy cross section view images (Fig. 5.5(a)(b)).

The nanowires are seen in the cross section view of the total thin film (Fig. 5.5(b)) with moiré fringes parallel to the substrate caused by the multiple diffraction from the superposition of the STO and CoNi lattices. These moiré fringes consequently prove that the bottom of the thin film is made of CoNi NWs in SrTiO<sub>3</sub> matrix. Fig. 5.5(a) is an image of the glue-thin film interface, spherical particles stick out from the oxide matrix. The fast Fourier transform of nanowire 1 (Fig. 5.5(c)) shows diffraction spots, attributed to Au(200) and STO(200) planes. The FFT of nanowire 2 (Fig. 5.5(d)) also shows diffraction spots, in this case attributed to Au(111) and STO(200) planes. These diffraction spots, found on the FFT of the image at the glue-thin

film interface, are the result of only Au and SrTiO<sub>3</sub> lattices and show no trace of CoNi, therefore only Au and SrTiO<sub>3</sub> are present at the top of the thin film.

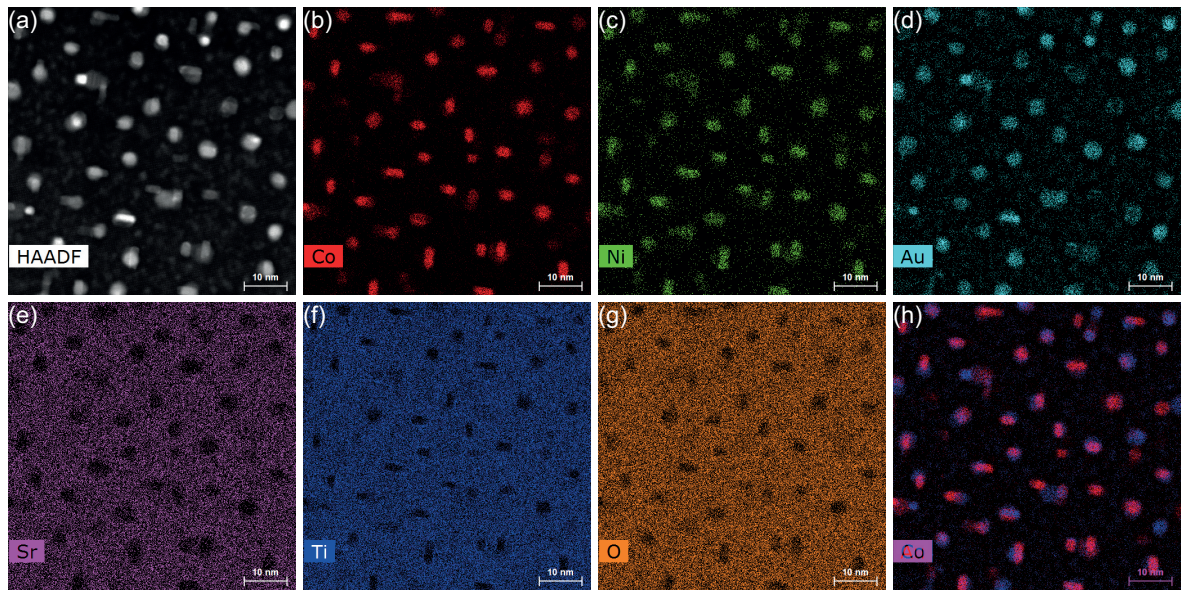


Figure 5.6 – Energy-dispersive x-ray spectroscopy (EDXS) analysis of hybrid NWs (sample *s2*) in plan view. (a) HAADF-STEM image. (b-g) Elemental spectromicroscopy mappings of (b) Co, (c) Ni, (d) Au, (e) Sr, (f) Ti, (g) O. (h) Superposition of the Co (Fig. 5.6(b)) and Au (Fig. 5.6(d)) EDXS mappings.

Energy-dispersive x-ray spectroscopy (EDXS) imaging was conducted on hybrid NWs (sample *s2*) to complement the transmission electron microscopy study. Fig. 5.6(b-g) shows the EDXS mappings of the constituent elements of the NWs (Fig. 5.6(b-d)) and the oxide matrix (Fig. 5.6(e-g)) in plan view. The position of the NWs is correlated with the high concentration of Co, Ni and Au metal and the absence of oxide in Fig. 5.6(e-g). CoNi NWs and Au NWs are easily distinguished from each other in the EDXS mappings, in comparison to HAADF-STEM (Fig. 5.6(a)).

The shape and the mean diameter of the CoNi NWs and Au NWs are not identical. CoNi NWs have an oblong shape, whereas Au NWs are circular with a bigger diameter in plan view. The statistical study of the EDXS mappings gives a value  $\langle d \rangle_{\text{CoNi}} = 3.1$  nm and  $\langle d \rangle_{\text{Au}} = 3.3$  nm for CoNi NWs and Au NWs, respectively, for *s2*. 80 % of the CoNi NWs are covered by an Au NW, indicating a preferential nucleation of Au at the top of the CoNi NWs. The Sr, Ti and O chemical mappings show negatives of nanowires with different shapes. The negatives of nanowires seen in the Sr and O mappings are circular and those in the Ti mapping are oblong and have a shape similar to the CoNi NWs. This difference of shape gives an information on the vertical interface of the CoNi NWs with the SrTiO<sub>3</sub> matrix.

A previous work by Radtke et al. [114] described the vertical interface of Ni NWs in a SrTiO<sub>3</sub> matrix. Fig. 5.7 shows the chemical profiles of Ni, Ti and O, measured by electron

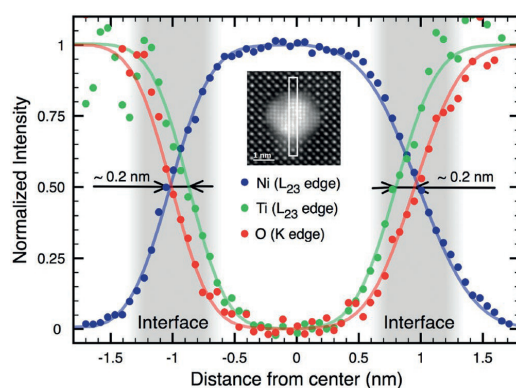


Figure 5.7 – Ni, Ti and O chemical profiles from the integrated EELS signal of a region of interest crossing a Ni NW in SrTiO<sub>3</sub> matrix (inset) (reproduced from [114]).

energy loss spectroscopy. A difference of 0.4 nm (0.2 nm per interface) between the widths of the chemical profiles of Ti and O is measured at the vertical interface. This indicates that the interface between Ni NWs and a SrTiO<sub>3</sub> matrix is rich in Ti and deficient in O. Fig. 5.6(f) is consistent with this result and shows that, similarly to Ni NWs, the vertical interface of CoNi NWs with the SrTiO<sub>3</sub> matrix is rich in Ti and deficient in O.

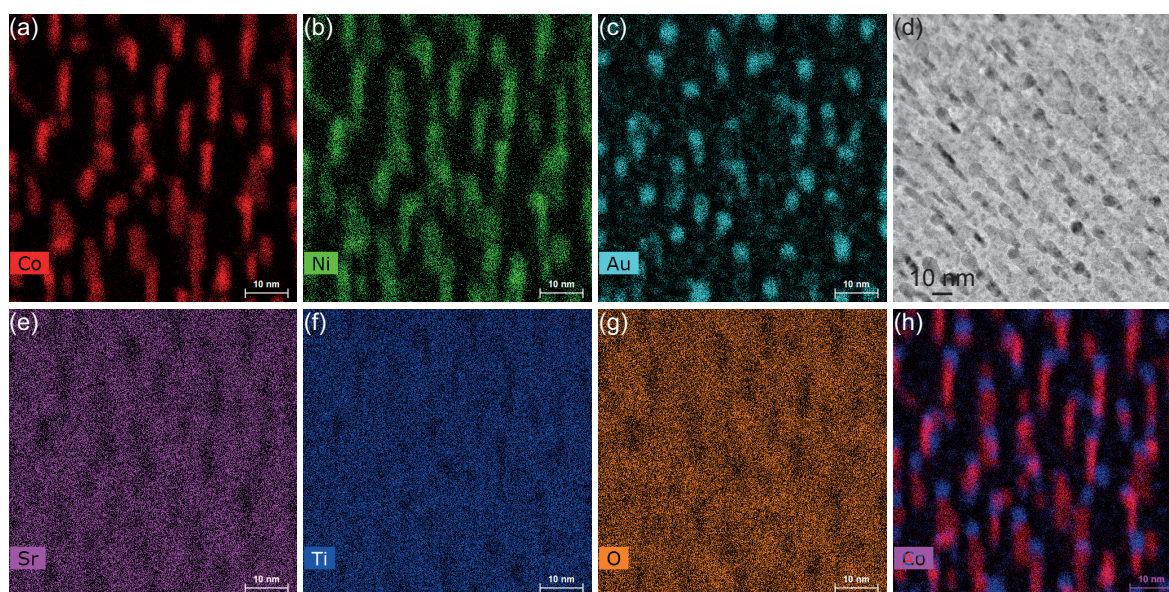


Figure 5.8 – Energy-dispersive x-ray spectroscopy (EDXS) analysis of hybrid NWs (sample *s2*) in tilt view. (a-c)(e-g) Elemental spectromicroscopy mappings of (a) Co, (b) Ni, (c) Au, (e) Sr, (f) Ti, (g) O. (d) High-resolution transmission electron microscopy image in tilt view of sample *s1*, given as a comparison. (h) Superposition of the Co (in red) and Au (in blue) EDXS mappings.

Sample *s2* was also studied by EDXS in tilt view to confirm the vertical segregation of Au and Co<sub>0.8</sub>Ni<sub>0.2</sub> in hybrid NWs suggested by transmission electron microscopy (Fig. 5.8(d)).

Fig. 5.8(a-c) shows the EDXS mappings of Co, Ni and Au. The signal of Co and Ni are superposed and no separate phase is seen in the chemical mappings, implying that CoNi NWs are of homogeneous alloy. CoNi NWs have the shape of elongated cylinders in the Co and Ni mappings, whereas Au NWs show as spherical particles. Fig. 5.8(h) shows the superposition of Co (in red) and Au (in blue) chemical mappings. The particles are made of two parts and have a similar shape to those seen in Fig. 5.8(d). Energy-dispersive x-ray spectroscopy analysis, nevertheless, gives additional information about the composition of each part. The bottom part, in the shape of an elongated cylinder, is made of  $\text{Co}_{0.8}\text{Ni}_{0.2}$ , whereas the top part, in the shape of a spherical particle, is made of Au. Fig. 5.8(h) thus proves the phase segregation of Au and  $\text{Co}_{0.8}\text{Ni}_{0.2}$  in Au- $\text{Co}_{0.8}\text{Ni}_{0.2}$ - $\text{SrTiO}_3$  hybrid nanocomposite thin films grown by sequential pulsed laser deposition.

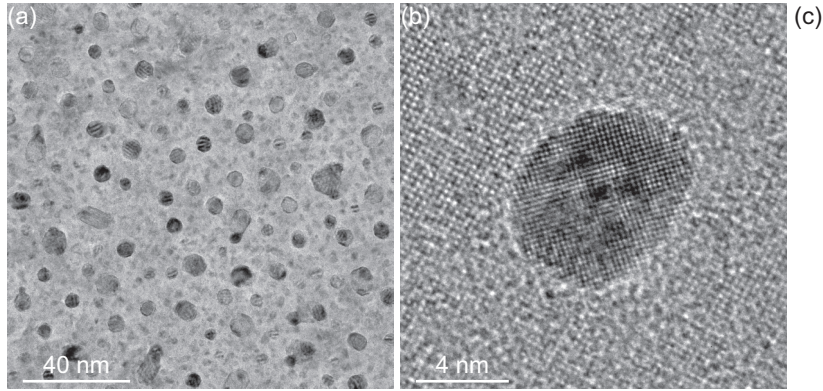


Figure 5.9 – Moiré fringes in transmission electron microscopy images of Au- $\text{Co}_{0.8}\text{Ni}_{0.2}$ - $\text{SrTiO}_3$  nanocomposite thin film *sl*. (a) Low-resolution transmission electron microscopy plan view image. (b) Enlargement of Fig. 5.9(a) showing the moiré fringes in a hybrid Au- $\text{Co}_{0.8}\text{Ni}_{0.2}$  NW in  $\text{SrTiO}_3$  matrix. (c) Schematics of moiré fringes.

Fig. 5.9(a) shows a low-resolution transmission electron microscopy image in plan view. A lot of NWs have moiré fringes. These moiré fringes, drawn in Fig. 5.9(c), are caused by the multiple diffraction from the superposition of CoNi and Au lattices. A general formula for the moiré fringes spacing  $D$  is [89]

$$D = \frac{d_a d_b}{\sqrt{d_a^2 + d_b^2 - 2d_a d_b \cos \alpha}} \quad (5.1)$$

where  $d_a$  and  $d_b$  are the interplanar spacings of two lattices  $a$  and  $b$ , and  $\alpha$  is the angle between the  $a$  and  $b$  lattices. In the case of two parallel lattices, for instance in a cube-on-cube epitaxy,  $\alpha = 0$  and Eq. 5.1 reduces to

$$D = \frac{d_a d_b}{d_a - d_b}. \quad (5.2)$$

With  $d_{\text{CoNi}200} = 0.177$  nm and  $d_{\text{Au}200} = 0.204$  nm, a value  $D_{th} = 1.3$  nm is calculated, related to moiré fringes caused by CoNi and Au 200 planes. A moiré fringes spacing of 1.4 nm is deduced from Fig. 5.9(b). This value is close to  $D_{th}$ . This indicates that the NW is made of two epitaxial parts, with different materials. Moiré fringes, seen in important number in Fig. 5.9(a), thus prove the hybrid and epitaxial nature of the NWs.

### 5.2.3 Epitaxy of hybrid NWs

The structure of Au-Co<sub>0.8</sub>Ni<sub>0.2</sub>-SrTiO<sub>3</sub> nanocomposite thin films was studied by laboratory x-ray diffraction. Complementary studies of the reciprocal space by synchrotron x-ray were carried out at the SixS beamline of the synchrotron SOLEIL. Reciprocal space coordinates are expressed in bulk SrTiO<sub>3</sub> reciprocal lattice unit (rlu). For example, a spot at  $l_{\text{CoNi}200} = 2.21$  rlu corresponds to an interplanar distance  $d_{\text{CoNi}200} = \frac{a_{\text{SrTiO}_3}}{l_{\text{CoNi}200}} = 1.77$  nm.

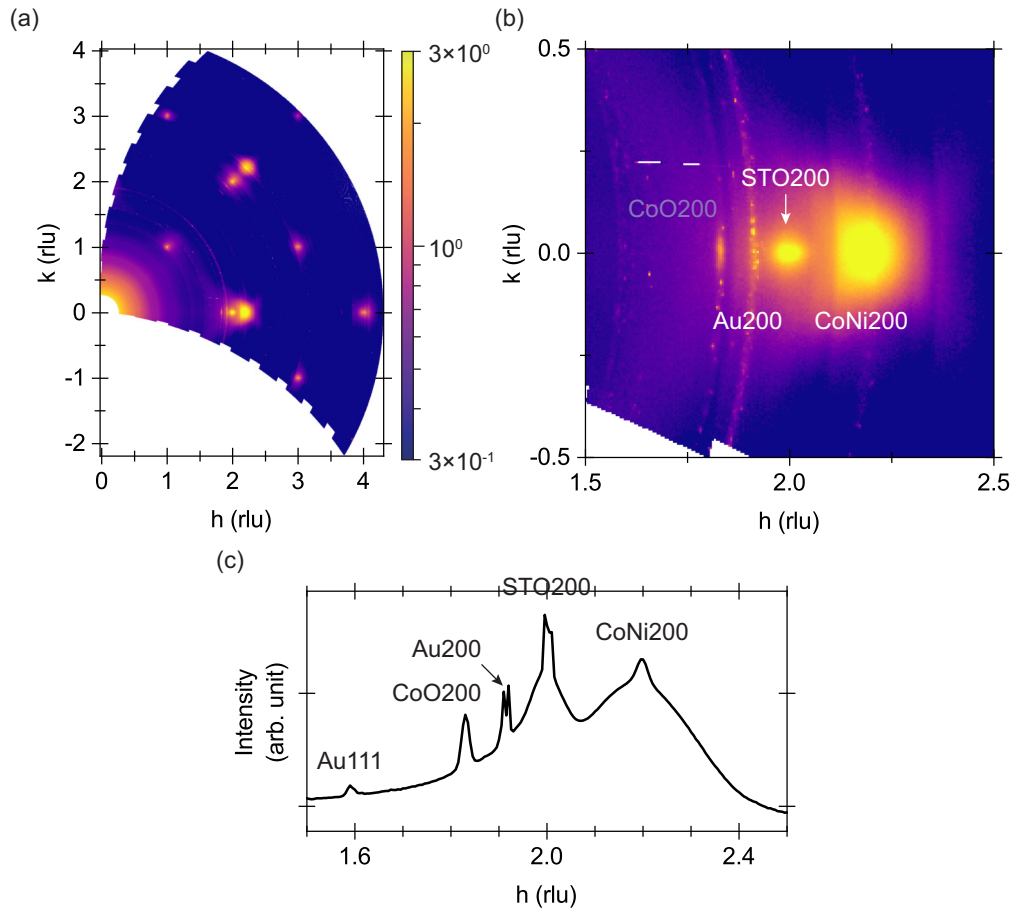


Figure 5.10 – Synchrotron x-ray reciprocal space mapping of hybrid Au-Co<sub>0.8</sub>Ni<sub>0.2</sub> nanowires in SrTiO<sub>3</sub> matrix *s3*. (a) In plane reciprocal space mapping and (b) reciprocal space near the matrix 200 reflection. (c) In plane profile of Fig. 5.10(b) (log<sub>10</sub> scale). Coordinates are expressed in bulk SrTiO<sub>3</sub> reciprocal lattice unit (rlu). Data were recorded at the SixS beamline (SOLEIL).

Fig. 5.10 shows a typical in plane ( $l = 0$ ) reciprocal space mapping (RSM) of hybrid Au-Co<sub>0.8</sub>Ni<sub>0.2</sub> in SrTiO<sub>3</sub> matrix by synchrotron x-ray diffraction. The reciprocal space near the 200 coordinate (Fig. 5.10(b)) and the corresponding profile (Fig. 5.10(c)) show the reflections of STO200 and CoNi200 at  $h = 2.00$  rlu and  $h = 2.21$  rlu, respectively. This infers an epitaxial relationship CoNi[100] || STO[100]. The radial strain of the Co<sub>0.8</sub>Ni<sub>0.2</sub> lattice is negligible. An arc is measured in Fig. 5.10(a)(b) with a radius of 1.92 rlu corresponding to the reflection of Au200, this indicates an in plane rotation of Au. A lattice constant of Au of 4.07 Å is deduced from the radius. This value is close to the bulk lattice constant, indicating that the Au lattice is relaxed.

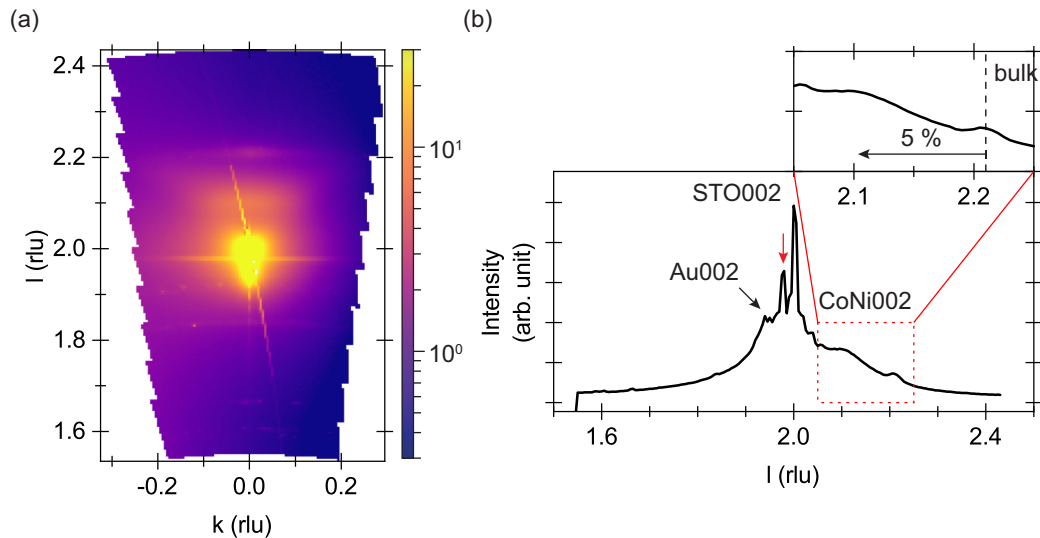


Figure 5.11 – Synchrotron x-ray reciprocal space mapping of hybrid Au-Co<sub>0.8</sub>Ni<sub>0.2</sub> nanowires in SrTiO<sub>3</sub> matrix *s3*. (a) Out of plane reciprocal space mapping near the matrix 002 reflection and (b) the corresponding profile (log<sub>10</sub> scale). The matrix reflection is marked by a red arrow. Coordinates are expressed in bulk SrTiO<sub>3</sub> reciprocal lattice unit (rlu). Data were recorded at the SixS beamline (SOLEIL).

The specular profile Fig. 5.11(b), measured in a typical out of plane reciprocal space mapping Fig. 5.11(a) shows the STO002 reflections. The matrix peak ( $l = 1.98$  rlu) is shifted from the one of the substrate ( $l = 2.00$  rlu), indicating a vertical strain of the SrTiO<sub>3</sub> thin film of 1.0%. The pseudomorphism of the matrix is related to the nonstoichiometry of SrTiO<sub>3</sub> caused by the oxygen-free growth. Fig. 5.11(b) also shows the reflections of Au002 and CoNi002 at  $l_{\text{Au}} = 1.91$  rlu and  $l_{\text{CoNi}} = 2.10$  rlu, respectively. The vertical strain state of the Au lattice is null and the out of plane mapping shows the Au002 reflection as a spot, indicating that the Au horizontal planes are parallel. Au thus shows an in plane texture.

Fig. 5.11(a) shows the out of plane reciprocal space mapping. The matrix spot is under the substrate spot, indicating the out of plane lattice expansion of the matrix. This spot degenerates into a horizontal diffuse line, reflecting the presence of vertical objects in the matrix. The

alignment of the CoNi002 and the STO002 spots defines an epitaxial relationship CoNi(001) || STO(001). If one adds the in plane epitaxial relationship, the general epitaxial relationship of the Co<sub>0.8</sub>Ni<sub>0.2</sub> and SrTiO<sub>3</sub> lattices is CoNi[100] || STO[100], CoNi(001) || STO(001), corresponding to a cube-on-cube structure. The lattice parameter of bulk fcc Co<sub>x</sub>Ni<sub>1-x</sub> ranges from 0.3545 nm (bulk fcc Co) [106] to 0.3524 nm (bulk fcc Ni) [115] and varies with a linear function of the content following Vegard's law [116, 117]. The lattice parameter of bulk fcc Co<sub>0.8</sub>Ni<sub>0.2</sub> is approximately 0.3540 nm. The out of plane Co<sub>0.8</sub>Ni<sub>0.2</sub> peak is shifted from the bulk value and a lattice parameter of 0.37 nm is measured. The shift of the Co<sub>0.8</sub>Ni<sub>0.2</sub> reflection corresponds to a mean axial strain of  $\langle \epsilon_{zz} \rangle = 5.3\%$ . A smaller Co<sub>0.8</sub>Ni<sub>0.2</sub> peak is seen at the value of bulk fcc Co<sub>0.8</sub>Ni<sub>0.2</sub> ( $l = 2.21$  rlu), besides the strained Co<sub>0.8</sub>Ni<sub>0.2</sub> peak, indicating a relaxed state. This shows that the highly strained Co<sub>0.8</sub>Ni<sub>0.2</sub> NWs may be partially relaxed. Furthermore, a comparison of the axial strain of the Co<sub>0.8</sub>Ni<sub>0.2</sub> NWs in simple and hybrid thin films shows that Au NWs do not affect the strain. Table 5.4 lists the mean axial strain of the CoNi nanowires and the matrix deduced by x-ray diffraction.

Table 5.4 – Structural characteristic values deduced by transmission electron microscopy and x-ray diffraction of hybrid Au-Co<sub>0.8</sub>Ni<sub>0.2</sub> nanowires.  $\langle d \rangle_{\text{CoNi}}$  is the mean diameter of the CoNi nanowires,  $\langle \epsilon_{zz} \rangle$  and  $\langle \epsilon_{zz} \rangle_{\text{matrix}}$  are the mean axial strain of the CoNi nanowires and the matrix, respectively.

Sample	$\langle d \rangle_{\text{CoNi}}$ (nm)	$\langle \epsilon_{zz} \rangle$	$\langle \epsilon_{zz} \rangle_{\text{matrix}}$
s3	-	5.3	1.1
s4	-	5.3	1.3
s5	$3.0 \pm 0.2$	5.3	1.5
s6	$3.2 \pm 0.4$	5.1	1.4
s7	$3.3 \pm 0.4$	4.4	1.8
t1	$3.4 \pm 0.5$	5.2	1.4
t2	3.3	4.9	1.9
t3	3.3	5.3	1.5

#### 5.2.4 Off-Bragg scattering

Table 5.5 – List of the nanocomposite thin film samples studied by diffuse scattering.  $a_{\text{matrix,OP}}$  is the out of plane matrix lattice parameter,  $t$  is the film thickness,  $\rho$  is the in plane density of nanowires and  $\langle d \rangle$  is the mean diameter of the nanowires.  $a_{\text{matrix,OP}}$  was deduced by x-ray diffraction,  $t$  was deduced by x-ray diffraction and transmission electron microscopy,  $\rho$  and  $\langle d \rangle$  were measured by transmission electron microscopy.

Sample	NWs chem. comp.	$a_{\text{matrix,OP}}$ (nm)	$t$ (nm)	$\rho$ ( $10^{-2} \text{ nm}^{-2}$ )	$\langle d \rangle$ (nm)
t4	Ni	0.3942	51	0.41	5.7
t5	Ni	0.3931	231	1.8	4.1
s6	Au-Co <sub>0.8</sub> Ni <sub>0.2</sub>	0.3957	59	1.3	3.2

Complex nanomaterials, for example comprising inclusions, require investigation tools complementing local means of observation which are often destructive. Small-angle x-ray scattering (SAXS) is a powerful technique for the investigation of nanocomposites standing on or embedded in a soft matter layer [118]. In the case of a conventional substrate, SAXS requires nondamaging techniques for the removal of the substrate in order to obtain an ultrathin specimen of the material [119–121]. Grazing-incidence small-angle x-ray scattering allows to probe buried objects [122], however the scattering signal of the latter is fainter than that of the surface or the matrix and its analysis is complex [123], even nearly impossible if the objects and the matrix have the same mass density or if the layer of interest is buried under other structures. From the off-Bragg scattering of the host matrix by x-ray diffraction, structural information of embedded nanocomposites is retrieved, independently on the crystal order, the strain state or the presence of defects of the latter [124]. In this subsection, three samples of nanocomposite thin films measured by x-ray diffraction using synchrotron radiation are presented (Table 5.5). It should be noted that samples *t4* and *t5* were synthesised by Xiaorong Weng.

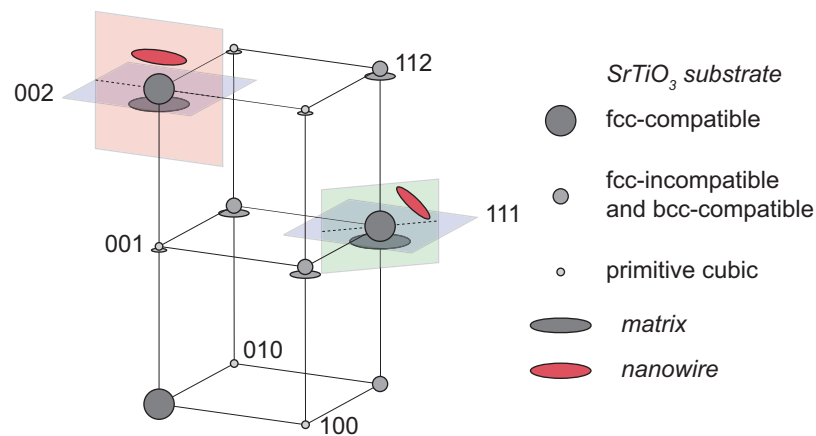


Figure 5.12 – Schematics of the reciprocal space. The  $\text{SrTiO}_3$  reflections are classified into three types, each symbolised by the circle size. An out of plane (OP) mapping corresponds to a vertical cut (red rectangle) or a radial cut (green rectangle). An in plane (IP) mapping corresponds to a horizontal cut (blue rectangle) at the matrix spot position.

Fig. 5.12 is a schematics of the position of the diffraction spots of the nanowires, the matrix and the substrate in the reciprocal space. The spots of the epitaxial face-centred cubic Ni and CoNi NWs are located near the strong reflections of  $\text{SrTiO}_3$ . These strong reflections of the matrix and the substrate are fcc-compatible and their structure factor adds the in phase contributions of Sr and O, at least ( $F_{hkl} = f_{\text{Sr}} \pm f_{\text{Ti}} + 3f_{\text{O}}$  with + or – for even or odd  $hkl$  combinations, respectively). The medium reflections, for example 112, involve the in phase contributions of Sr and Ti and the antiphase contribution of O ( $F_{hkl} = f_{\text{Sr}} + f_{\text{Ti}} - f_{\text{O}}$ ). Whereas for weak reflections, the contributions of Ti and O are in antiphase with Sr ( $F_{hkl} = f_{\text{Sr}} - f_{\text{Ti}} - f_{\text{O}}$ ).

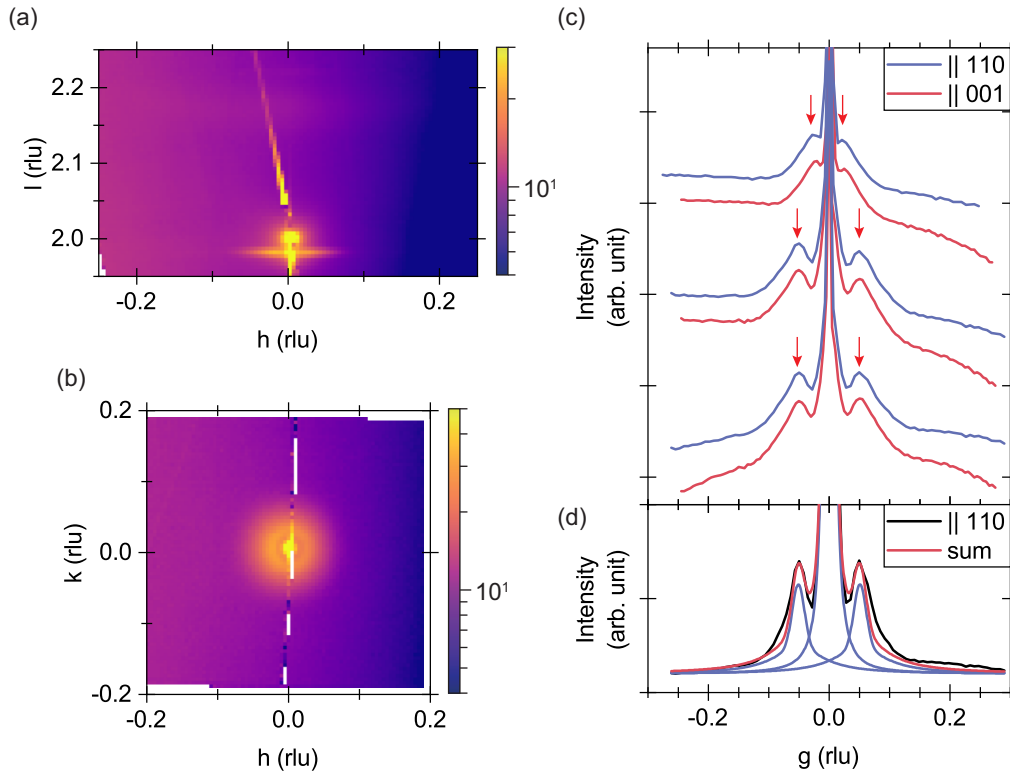


Figure 5.13 – Reciprocal space mappings and profiles of the 002 SrTiO<sub>3</sub> spot. (a) Out of plane and (b) in plane reciprocal space mappings of sample *t4*. (c) In plane profiles of sample *t4* (raw) and *t5* (raw and corrected) in the [110] (blue) and [100] (red) directions (log<sub>10</sub> scale). The scattering ring is marked by an arrow. The background slope of the *t5* in plane profile, resulting from nonconstant irradiated area during the specular scan, is corrected by normalisation of the intensity by the footprint of the incident beam. *g*-coordinates are relative to the centre of the spot. (d) Decomposition of the [110] corrected profile of sample *t5* in one central peak and two secondary peaks (blue), and the resulting sum of the peaks (red) (linear scale).

The examination of the in plane reciprocal space mapping (Fig. 5.13(b)), measured by specular scan, reveals a scattering ring. This feature is clearly seen in the in plane profiles (Fig. 5.13(c)) of multiple samples. In the profiles, *g*-coordinates, in bulk SrTiO<sub>3</sub> reciprocal lattice unit, are relative to the centre of the spot. A background slope is seen in the mappings and the in plane profiles, from negative to positive values of *h*, resulting from the nonconstant area of irradiation of the specimen during the specular scan. This slope is corrected by normalisation of the intensity by the footprint of the incident beam (Fig. 5.13(d)).

The radii of the scattering rings  $g_1$  are 0.023 rlu and 0.051 rlu and correspond to lengths of 17.0 nm and 7.7 nm, for *t4* and *t5* respectively. As seen in Table 5.5, these lengths are not corresponding to the diameter of the nanowires (5.7 nm and 4.1 nm, for *t4* and *t5* respectively). If one assumes a hexagonal arrangement of the nanowires, the mean interdistance  $\langle D \rangle$  between two nanowires can be estimated from the density of the nanowires  $\rho$ . A mean interdistance

$\langle D \rangle$  of 16.8 nm and 8.0 nm is calculated from transmission electron microscopy  $\rho$  values, for  $t4$  and  $t5$  respectively. These values hint at a link between the interdistance  $\langle D \rangle$  and the radius of the scattering rings  $g_1$ . It should be noted that the intensity beyond the scattering ring does not drop under noise level, indicating that additional information is contained in the diffuse signal.

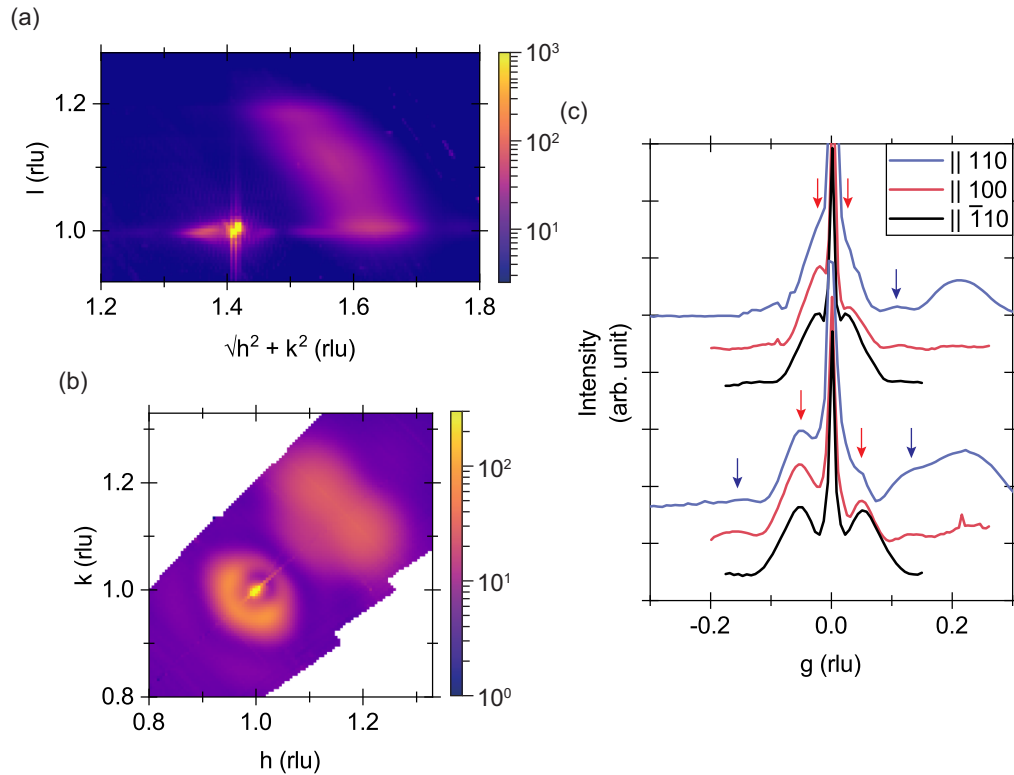


Figure 5.14 – Reciprocal space mappings and profiles of the 111 SrTiO<sub>3</sub> spot. (a) Out of plane and (b) in plane reciprocal space mappings of sample  $t5$ . (c) In plane profiles of sample  $t4$  and  $t5$  in the  $[110]$  (blue),  $[100]$  (red) and  $[\bar{1}10]$  (black) directions ( $\log_{10}$  scale). The first and second scattering rings are marked by a red and a blue arrow, respectively.

Nonspecular reciprocal space mappings were recorded by grazing incidence x-ray diffraction (GIXRD) with a constant grazing angle of incidence of  $0.3^\circ$ , approximately twice the critical angle of SrTiO<sub>3</sub>. This ensures a large constant area of irradiation of the specimen during the measurement and increases the sensitivity of the epilayer. As seen in the 111 reciprocal space mappings (Fig. 5.14), the scattering of the matrix appears in the horizontal plane as a ring, similar to that seen in the 002 specular RSM. However, the scattering intensity is asymmetric in the radial  $[110]$  direction due to the proximity of the substrate spot. As a similar scattering ring is observed on different Bragg spots, this diffuse signal does not reflect a texture of the matrix but constitutes a satellite of the Bragg reflection of the matrix, which results from a convolution in the reciprocal space similar to that of a form factor.

A faint second ring is observed, overlapped by the broad spot of the nanowires in the radial direction. The radii of the second scattering rings  $g_2$  are 0.109 rlu and 0.135 rlu, that is the inverse of 3.6 nm and 2.9 nm, for  $t_4$  and  $t_5$  respectively. These lengths are not corresponding to the distance, nor the interdistance of the nanowires. The second ring cannot be explained neither as a harmonic of the first ring, as the radius ratios of sample  $t_4$  and  $t_5$ , respectively of 4.7 and 2.6, do not agree with the harmonicity of a cylindrical symmetry problem, often associated with Bessel functions.

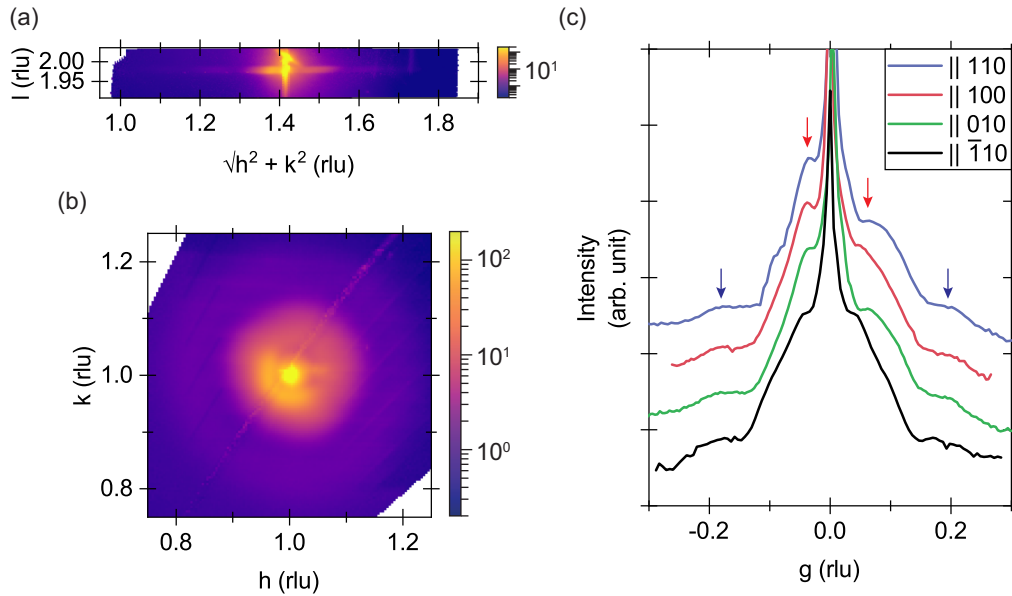


Figure 5.15 – Reciprocal space mappings and profiles of the 112 SrTiO<sub>3</sub> spot of sample  $s_6$ . (a) Out of plane and (b) in plane reciprocal space mappings. (c) In plane profiles in the [110] (blue), [100] (red), [010] (green) and  $[\bar{1}10]$  (black) directions ( $\log_{10}$  scale). The first and second scattering rings are marked by a red and a blue arrow, respectively.

The scan of the medium reflection of STO112, forbidden for fcc systems, removed the contribution of the nanowires and enhanced the diffuse signal of the matrix as seen on the mappings of sample  $s_6$  (Fig. 5.15). The radius of the first ring is 0.040 rlu (inverse of 9.8 nm) and could be linked to the interdistance of sample  $s_6$  ( $\langle D \rangle = 9.4$  nm). The radius of the second ring is 4.9 times larger than that of the first. A similar radial asymmetry of the scattering ring is observed. The complementary measurement of the 301 medium reflection shows that the intensity asymmetry is radial and not related in particular to the [110] direction as seen in the 111 and 112 reflections.

Structural information can be extracted from the scattering rings if one considers the nanocomposite thin film as a porous thin film. Indeed, when the incident beam is at Bragg condition of the host matrix, the nanowires do not contribute to the reflection. In this case, nanowires thus appear as holes (Fig. 5.16) and x-ray diffraction measurements are comparable

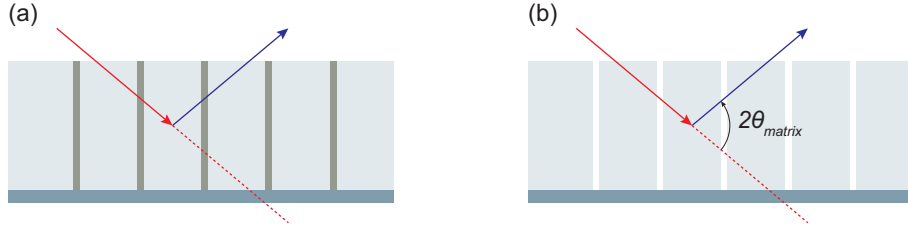


Figure 5.16 – (a) Schematics of a nanocomposite thin film. (b) When the incident beam is at Bragg condition of the host matrix, it is diffracted by the host matrix only and nanowires thus appear as holes. Incident and diffracted x-ray are coloured in red and blue, respectively.

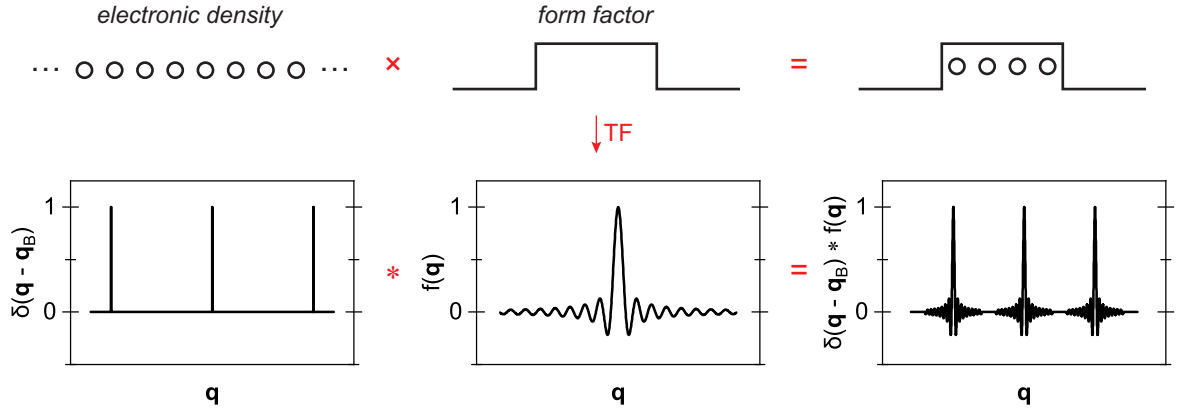


Figure 5.17 – Schematics of the Fourier transform of the electronic density of a 1D finite crystal. (top) The electronic density of a finite crystal is equal to the product of the electronic density of an infinite crystal by a form factor. (bottom) The Fourier transform of the electronic density of a finite crystal shows a nonzero intensity near Bragg conditions.

to those of porous materials [125, 126]. It is possible to modelise the nanocomposite thin film with a general form function  $f(\vec{r})$ , where  $f(\vec{r}) = 1$  inside a nanowire (or hole) and  $f(\vec{r}) = 0$  elsewhere. The electronic density  $\rho(\vec{r})$  of the host matrix is  $\rho(\vec{r}) = \rho_{\text{film}}(\vec{r}) - \rho_{\text{film}}(\vec{r}) \times f(\vec{r})$ , where  $\rho_{\text{film}}$  is the electronic density of a constant thin film (Fig. 5.17). The Fourier transform of  $\rho(\vec{r})$  is the diffracted amplitude  $A(\vec{q})$

$$A(\vec{q}) = \rho_{\text{film}}(\vec{q}) - \rho_{\text{film}}(\vec{q}) * f(\vec{q}) \quad (5.3)$$

where  $\vec{q}$  is the scattering vector near the Bragg scattering vector  $\vec{q}_B$ . For a narrow Bragg reflection of the host matrix, the scattering intensity  $I(\vec{q} \neq \vec{q}_B)$  is nonzero and equals

$$I(\vec{q} \neq \vec{q}_B) = |F_{hkl}|^2 |f(\vec{q} - \vec{q}_B)|^2 \quad (5.4)$$

implying that the off-Bragg scattering intensity is only related to the last term of  $A(\vec{q})$ , i.e. the form function. The off-Bragg scattering from a pattern of holes in a host crystal matrix is, in

consequence, equivalent to its negative, a pattern of nanocomposites made of the host matrix material in vacuum. Off-Bragg scattering is hence analogous to optical experiments relying on Babinet's principle.

The form function  $f(\vec{r})$  is simplified in the ideal homogeneous case as a convolution of the form function of an individual hole  $f_h(\vec{r})$  with the position of the holes  $f_p(\vec{r})$ , in other terms  $f(\vec{r}) = f_h(\vec{r}) * f_p(\vec{r})$ . The scattering intensity is then given by the product of the squared modulus of the Fourier transform of the form function of an individual hole  $|f_h(\vec{q})|^2$ , i.e. the Airy pattern, and that of the position of the holes  $|f_p(\vec{q})|^2$ , i.e. the Fourier transform of the position autocorrelation. The position autocorrelation  $f_p(\vec{r}) * f_p(\vec{r})$  can be normalised and expressed as a function of the position pair function  $p(\vec{r})$  as  $\delta(\vec{r}) + np(\vec{r})$ , where  $n$  is the hole density. The intensity  $I_p(\vec{q}) = |f_p(\vec{q})|^2$  is thus related to the position pair function  $p(\vec{q})$  by  $I_p(\vec{q}) \propto 1 + np(\vec{q})$ .

Pair functions are used to describe short, mean or long range order in matter [127, 128]. From the concept of paracrystal by Hosemann and Bagchi [129], the short range order of a 1D or 2D system can be described by the nearest neighbour distance  $D$  and its variance  $\sigma^2$ ,  $\sigma^2$  being cumulative for next neighbours. In 1D,  $I_p(\vec{q})$  is defined as

$$I_p(\vec{q}) = \frac{1 - G^2(\vec{q})}{1 - 2 \cos(\vec{q}D)G(\vec{q}) + G^2(\vec{q})} \quad (5.5)$$

where  $G(\vec{q}) = e^{-q^2\sigma^2/2}$  is the Fourier transform of the gaussian distribution of the first neighbours.

Table 5.6 – Structural characteristic values of the nanowires deduced by the calculation of the scattering rings.  $g_1$  is the radius of the first ring,  $\Gamma_1$  is its standard deviation,  $g_2$  is the radius of the second ring,  $D$  is the interdistance between the nanowires,  $\sigma$  is its deviation and  $d$  is the diameter of the nanowires.  $g_1$ ,  $\Gamma_1$  and  $g_2$  were measured in the reciprocal space mappings and  $D$ ,  $\sigma$  and  $d$  were calculated.

Sample	$g_1$ (rlu)	$\Gamma_1$ (rlu)	$g_2$ (rlu)	$D$ (nm)	$\sigma$ (nm)	$d$ (nm)
<i>t4</i>	0.023	0.008	0.109	16.2	5.9	5.9
<i>t5</i>	0.051	0.010	0.135	7.5	1.8	4.7
<i>s6</i>	0.040	0.012	0.194	9.7	3.0	3.3

The qualitative reproduction of the scattering ring positions (Fig. 5.18(a)) is possible from the generalisation of Eq. 5.5 in 2D [130] with a hole form factor of diameter  $d$ , and agrees with the reciprocal space measurements. A more realistic representation should implement a cut-off distance ( $< d$ ) to avoid hole superposition. This can be done by considering a hexagonal lattice of nonsuperposed holes (Fig. 5.18(c)), the first neighbours being disordered by a log-normal distribution, the next with increasing disorder. The total intensity of this model is seen in Fig. 5.18(b). The calculated values of the interdistance  $D$ , its deviation  $\sigma$  and the nanowire diameter  $d$  are listed in Table 5.6. The first scattering ring is related to the nanowire interdistance  $D$ . The value of  $D$  is slightly different from the inverse of  $g_1$  because of the slope of the Airy

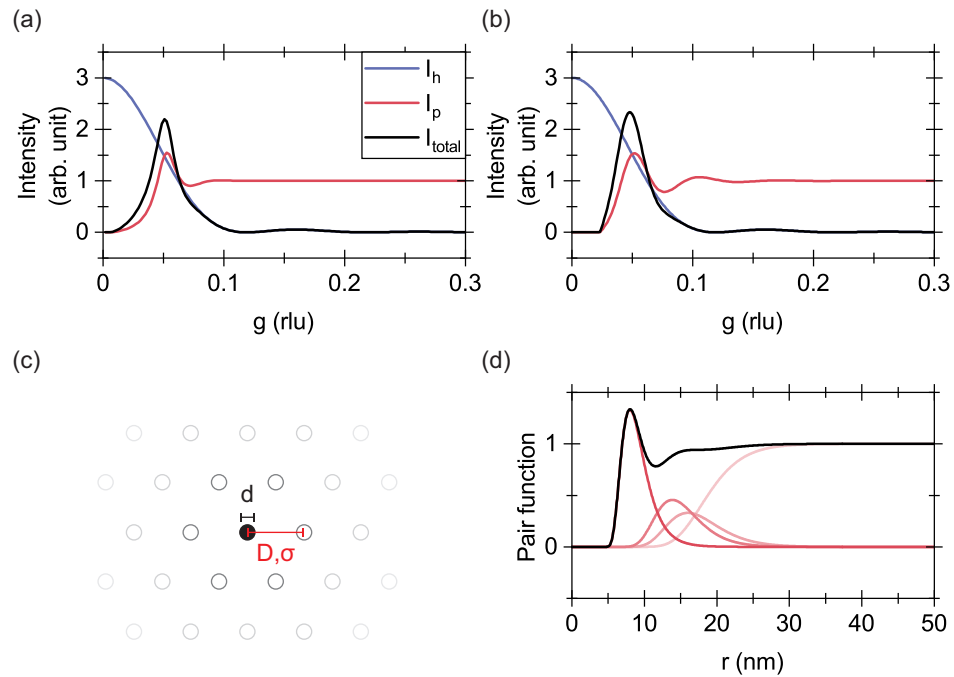


Figure 5.18 – Scattering profiles calculated with  $D = 8$  nm,  $\sigma = 2$  nm and  $d = 4$  nm by considering (a) a paracrystal order of neighbours and (b) an asymmetric distribution of neighbours. The total intensity  $I_{\text{total}}$  (black) is the product of the intensities caused by the form factor  $I_h$  (blue) and the position correlation  $I_p$  (red). (c) Schematics of a hexagonal lattice of holes. (d) Pair function (black) of an asymmetric distribution and contributions of the three first and next neighbours (red).

pattern, i.e. the individual hole form factor. The relative deviation of first neighbour position  $\frac{\sigma}{D}$  is calculated to be 30%. The second scattering ring is seen in Fig. 5.18, caused by the first ring of the Airy pattern at  $g_2 = \frac{1.635}{d}$ . The calculated diameter of the nanowires (Table 5.6) are consistent with transmission electron microscopy measurements (Table 5.5).

Scattering rings are observed near the matrix spot in specular 002 and nonspecular 111 and 112 reflections. This diffuse signal stems from the presence of nanocomposites in the thin film, modelled by a form factor. From the calculation of the form factor, structural information, such as the interdistance  $D$ , its variance  $\sigma$  and the diameter  $d$  of the nanowires, are extracted. GIXRD probes an area in the order of the square millimetre, measuring  $10^{10}$  nanowires. Because of the considerable number of nanocomposites, the structural characteristic values  $D$ ,  $\sigma$  and  $d$  calculated from the scattering intensity in the reciprocal space mappings are reliable. A statistical study by transmission electron microscopy, in comparison, is local, measuring roughly 25 nanowires per image. However, nonspecular reflections cannot be measured in laboratory and require large scale facility. Structural information extracted by GIXRD are consistent with transmission electron microscopy data, proving the reliability of statistical study by TEM even if a limited number of nanowires are probed.

## 5.3 Magnetic properties of hybrid NWs

### 5.3.1 Magnetic anisotropy

#### 5.3.1.1 Magnetic anisotropy constants

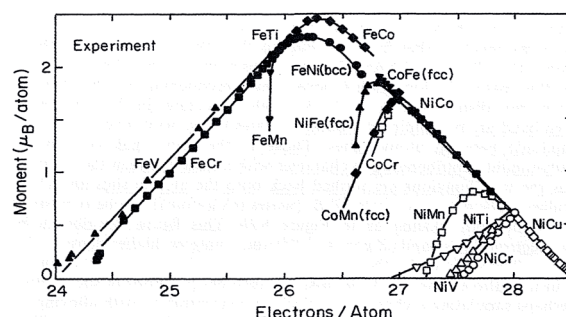


Figure 5.19 – Slater-Pauling curve for 3d transition metals (reproduced from [62]).

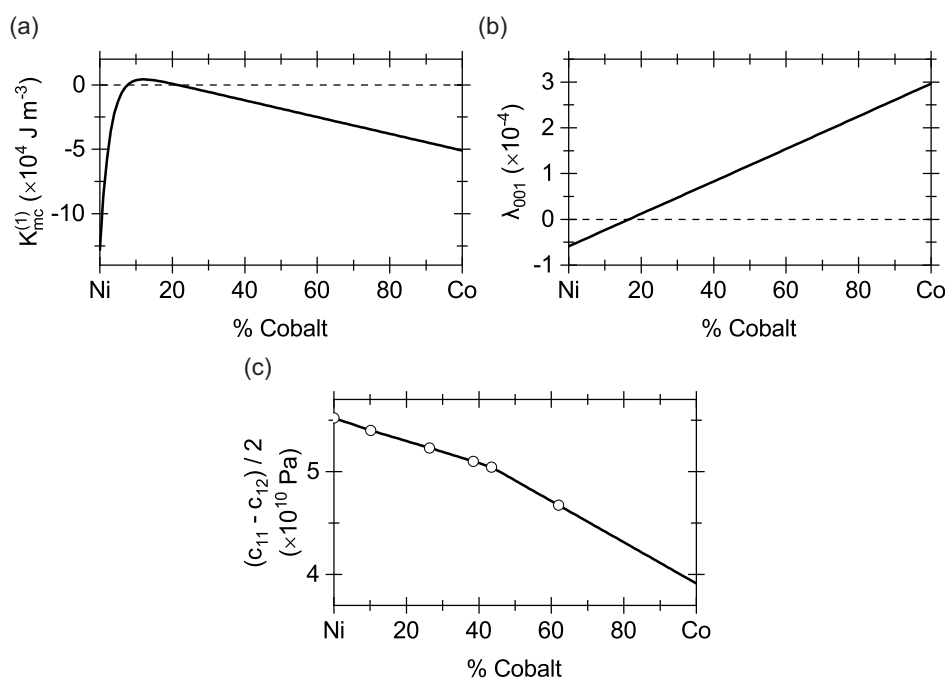


Figure 5.20 – Magnetic anisotropy constants of the face-centred cubic  $\text{Co}_x\text{Ni}_{1-x}$  binary alloy. (a) Magnetocrystalline anisotropy  $K_{\text{mc}}^{(1)}$  (measured at  $T = 77 \text{ K}$  and adapted from [131]). Magnetostrictive anisotropy constants, (b) [001] magnetostriction coefficient  $\lambda_{001}$  (measured at room temperature and adapted from [132]) and (c) shear stiffness  $\frac{c_{11}-c_{12}}{2}$  (extrapolated at  $T = 0 \text{ K}$  and adapted from [133]).

The magnetic properties of hybrid nanowires are defined by the magnetic anisotropy constants. These constants are the magnetostatic  $K_{ms}$ , magnetocrystalline  $K_{mc}$  and magnetoelastic  $K_{me}$  anisotropy constants, and they are reviewed in the following paragraph.

The magnetostatic anisotropy is uniaxial because of the important form factor of the nanoparticles and  $K_{ms} = \mu_0 M_s^2 / 4$ . For the  $\text{Co}_x\text{Ni}_{1-x}$  binary alloy, the saturation magnetisation  $M_s$  increases linearly with  $x$  (Fig. 5.19), that is the magnetostatic anisotropy  $K_{ms}$  increases as the content of Co. All the  $\text{Co}_{0.8}\text{Ni}_{0.2}$  nanowires in this work have a face-centred cubic structure, the cubic magnetocrystalline anisotropy is approximated by its first term,  $K_{mc}^{(1)}$  (Fig. 5.20(a)). It should be noted that the magnetocrystalline anisotropy constants are temperature-dependent. Kadowaki and Takahashi measured the magnetocrystalline anisotropy constants of the bulk  $\text{Co}_x\text{Ni}_{1-x}$  alloy from 77 K to 700 K and found an expression of  $K_{mc}^{(1)}$  as a function of the content of Co  $x$  at 0 K:  $K_{mc}^{(1)} = 14.0 - 0.65x - 142e^{-0.36x}$  [131]. As shown in Fig. 5.20(a), the magnetocrystalline anisotropy  $K_{mc}^{(1)}$  is negative for concentrations of Co  $x < 0.08$  and  $x > 0.21$ . The uniaxial magnetoelastic anisotropy  $K_{me} = \frac{3}{2}\lambda_{001}(c_{11} - c_{12})(\epsilon_{zz} - \epsilon_{rr})$  is defined by the [001] magnetostriction coefficient  $\lambda_{001}$  (Fig. 5.20(b)) and the elastic constants  $c_{ij}$  (Fig. 5.20(c)). The magnetostriction coefficient  $\lambda_{001}$  increases linearly as a function of the content of Co and is positive for  $x > 0.17$  [132]; the shear stiffness  $\frac{c_{11}-c_{12}}{2}$  decreases as a function of the content of Co, by 22 % for  $x = 0.8$ , and is strictly positive [133].

Table 5.7 – Calculated magnetic anisotropy constants for bulk face-centred cubic Co,  $\text{Co}_{0.17}\text{Ni}_{0.83}$ ,  $\text{Co}_{0.8}\text{Ni}_{0.2}$  and Ni.  $M_s$  is the saturation magnetisation,  $K_{ms} = \mu_0 M_s^2 / 4$  is the magnetostatic anisotropy,  $K_{mc}^{(1)}$  is the magnetocrystalline anisotropy (measured at  $T = 77$  K and adapted from [131]),  $\lambda_{001}$  is the [001] magnetostriction coefficient (measured at room temperature and adapted from [132]),  $c_{ij}$  are the elastic constants (extrapolated at  $T = 0$  K and adapted from [133]),  $\langle \epsilon_{zz} \rangle$  is the mean axial strain (from [60]) and  $K_{me} = \frac{3}{2}\lambda_{001}(c_{11} - c_{12})(\epsilon_{zz} - \epsilon_{rr})$  is the magnetoelastic anisotropy.

	Magnetostatic		Magnetocrystalline		Magnetoelastic		
	$M_s$ ( $10^5 \text{ A m}^{-1}$ )	$K_{ms}$ ( $10^4 \text{ J m}^{-3}$ )	$K_{mc}^{(1)}$ ( $10^4 \text{ J m}^{-3}$ )	$\lambda_{001}$ ( $10^{-4}$ )	$\frac{c_{11}-c_{12}}{2}$ ( $10^{10} \text{ Pa}$ )	$\langle \epsilon_{zz} \rangle$ (%)	$K_{me}$ ( $10^4 \text{ J m}^{-3}$ )
Ni	5.07	8.08	-12.8	-0.59	5.52	2.4	-23.45
$\text{Co}_{0.18}\text{Ni}_{0.82}$	6.74	14.27	0.21	0.05	5.32	2.8	2.23
$\text{Co}_{0.57}\text{Ni}_{0.43}$	10.35	33.65	-2.31	1.43	4.77	3.1	63.44
$\text{Co}_{0.78}\text{Ni}_{0.22}$	12.30	47.53	-3.67	2.18	4.35	4.2	119.49
Co	14.34	64.60	-5.10	2.97	3.91	-	-

Table 5.7 shows the calculated magnetic anisotropy constants of  $\text{Co}_x\text{Ni}_{1-x}$  NWs for different concentrations of Co ( $x = 0$ ,  $x = 0.18$ ,  $x = 0.57$ ,  $x = 0.78$  and  $x = 1$ ). For an alloy ratio of  $x > 0.18$ , the magnetostatic term  $K_{ms}$  and the magnetoelastic term  $K_{me}$  are at least 10 times superior to the magnetocrystalline term  $K_{mc}$ .  $K_{mc}$  is thus neglected in further discussions. The stoichiometry of the  $\text{Co}_x\text{Ni}_{1-x}$  binary alloy affects the effective magnetic anisotropy:

- at a very low concentration of Co ( $x < 0.17$ ),  $\lambda_{001} < 0$  and  $K_{me}$  is negative; if the NW is under a sufficient strain  $\langle \epsilon_{zz} \rangle$ , the sum  $K_{ms} + K_{me}$  is negative and the axis of the NWs is a hard axis of magnetisation;
- at a low concentration of Co ( $x \approx 0.17$ ),  $\lambda_{001} = 0$  thus the magnetoelastic anisotropy is null and the magnetostatic anisotropy is predominant;
- at a high concentration of Co ( $x > 0.78$ ), the magnetoelastic term is greater than the magnetostatic term; the effect of magnetostriction is predominant and exalts the effective magnetic anisotropy all the more so that its amplitude is high.

The magnetic properties of Ni NWs in oxide matrix were extensively studied by Weng *et al.* [134]. The uniaxial magnetic anisotropy  $K$  stems from the competition of the magnetostatic and magnetoelastic terms:  $K = K_{ms} + K_{me}$ . The [001] magnetostrictive constant  $\lambda_{001}$  of Ni is negative thus  $K_{me} < 0$ . If an important strain is exerted on the NWs, the amplitude of the magnetoelastic term is superior to that of the magnetostatic term and the uniaxial anisotropy is negative, implying that the axis of the NWs is a hard axis of magnetisation and the plane of the NWs is an easy plane of magnetisation.

For bulk  $\text{Co}_x\text{Ni}_{1-x}$  binary alloy, the magnetostrictive constant  $\lambda_{001}$  varies as a function of the stoichiometry of the alloy. As the concentration of Co  $x$  increases,  $\lambda_{001}$  increases and is positive for  $x > 0.17$  thus  $K_{me}$  is positive. As the magnetostatic term  $K_{ms}$  and the magnetoelastic term  $K_{me}$  are of the same sign,  $K_{me}$  reinforces the uniaxial anisotropy all the more so that the strain is important. Hence, with a composition  $x > 0.2$  and an important strain the enhancement of the uniaxial magnetic anisotropy might be possible.

### 5.3.1.2 Magnetic anisotropy at low temperatures

Magnetic hystereses were measured at low temperature by applying an external field parallelly (out of plane) and perpendicularly to the axis of the NWs (in plane). Fig. 5.21 shows the typical  $M(H)$  curves of  $\text{Co}_{0.8}\text{Ni}_{0.2}$  NWs in oxide matrix at 10 K. Sample *t1* is made of pure  $\text{Co}_{0.8}\text{Ni}_{0.2}$  NWs and sample *s7* of pure  $\text{Co}_{0.8}\text{Ni}_{0.2}$  NWs coated by sputtered Au particles (Fig. 5.21(c)).

Out of plane  $M(H)$  curves show a much more pronounced squareness than the in plane  $M(H)$  curves; and the NWs saturate at a lower magnetic field value in the out of plane direction than in the in plane direction, indicating an easy axis of magnetisation along the axis of the NWs (Fig. 5.21(a)(b)). The out of plane coercive field  $\mu_0 H_c$  reaches a significant value of  $\approx 1$  T and the reduced remanent magnetisation  $m_r = \frac{M_r}{M_s}$  exceeds 0.96. The characteristic values of the  $M(H)$  curves are tabulated in Table 5.8.

Fig. 5.22 shows the typical  $M(H)$  curves of hybrid Au- $\text{Co}_{0.8}\text{Ni}_{0.2}$ - $\text{SrTiO}_3$  thin films at 5 K. Hybrid NWs in oxide matrix are schematised in Fig. 5.22(c). As for samples *t1* and *s7*, hybrid NWs show an anisotropic magnetic response; the out of plane curves display an important squareness in comparison to the in plane curves and the easy axis of magnetisation is in the out of plane direction. The out of plane coercive field  $\mu_0 H_c$  and the reduced remanent

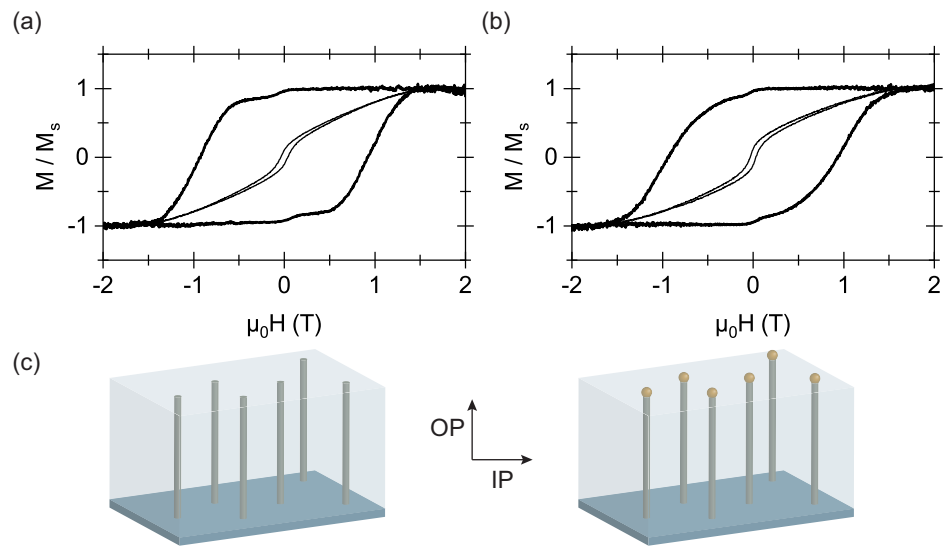


Figure 5.21 – Out of plane (bold) and in plane (thin) normalised  $M(H)$  curves measured by vibrating sample magnetometry at 10 K of samples (a) *t1* and (b) *s7*. (c) Schematics of samples *t1* (left) and *s7* (right).

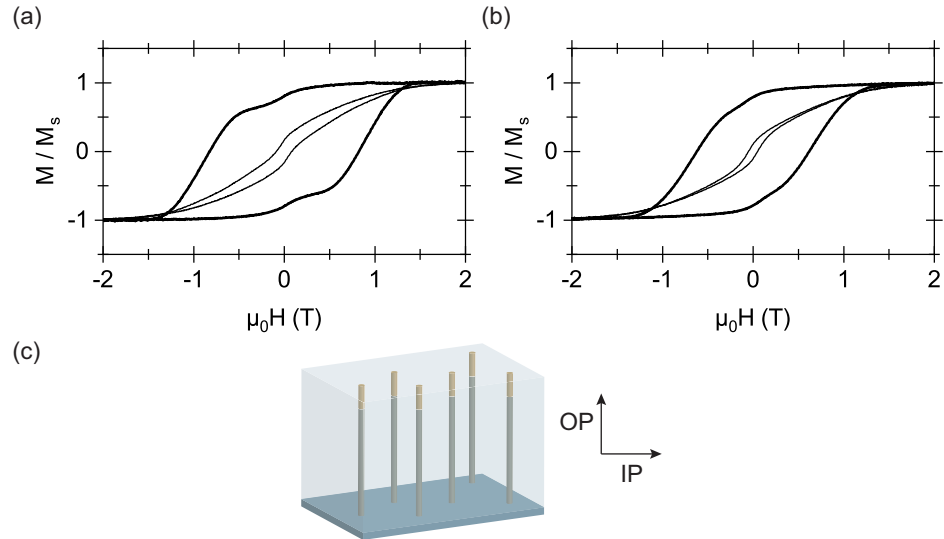


Figure 5.22 – Out of plane (bold) and in plane (thin) normalised  $M(H)$  curves measured by vibrating sample magnetometry at 5 K of samples (a) *s5* and (b) *s4*. (c) Schematics of samples *s5* and *s4*.

magnetisation  $m_r$  of hybrid nanocomposite thin films are however lower than those of samples not containing Au NWS (samples  $t1$  and  $s7$ ). The characteristic values of the  $M(H)$  curves are tabulated in Table 5.8.

Table 5.8 – Out of plane (OP) and in plane (IP) characteristic values of  $M(H)$  curves of hybrid (Au-)Co<sub>0.8</sub>Ni<sub>0.2</sub>-SrTiO<sub>3</sub> nanowires measured at 5 K (<sup>†</sup> at 10 K) by VSM.  $\mu_0H_c$  is the coercive field,  $\mu_0H_s$  is the saturation field and  $m_r = \frac{M_r}{M_s}$  is the reduced remanent magnetisation. Co<sub>0.8</sub>Ni<sub>0.2</sub>-SrTiO<sub>3</sub> nanowires samples are marked with ‡.  $\mu_0H_c$  uncertainty is less than  $\pm 0.01$  T.  $\mu_0H_s$  uncertainty is  $\pm 0.02$  T.

Sample	OP			IP		
	$\mu_0H_c$ (T)	$\mu_0H_s$ (T)	$m_r$	$\mu_0H_c$ (T)	$\mu_0H_s$ (T)	$m_r$
$s4$	0.63	1.53	0.79	0.05	1.81	0.12
$s5$	0.82	1.59	0.81	0.09	1.80	0.17
$s6$	0.41	1.39	0.69	0.04	1.54	0.12
$s7^\dagger$	0.92	1.79	0.96	0.03	1.93	0.11
$t1^{\dagger\ddagger}$	0.94	1.50	0.96	0.04	1.92	0.09
$t2^\ddagger$	0.75	1.79	0.76	0.05	2.17	0.07
$t3^\ddagger$	0.87	1.57	0.90	0.04	2.17	0.07

The presented magnetisation curves depart from the ideal Stoner-Wohlfarth particle. The shape of an ideal easy axis  $M(H)$  curve is a perfect square and that of an hard axis is linear, whereas the measured hysteresis curves are rhomboid in the easy axis and slightly opened in the hard axis. The shape of the easy axis  $M(H)$  curves is caused by a distribution of nanowire diameter, the misalignment of the nanoparticles, dipolar interactions between the nanowires, or structural or anisotropy inhomogeneities. In real systems, magnetisation is not seen to reverse coherently at  $H_c$ , but progressively according to a distribution of switching field  $\mu_0H_{sw}$ . The mean switching field  $\mu_0H_{sw}$  and the size of its distribution  $\mu_0\Delta H_{sw}$  is deduced from the first derivative  $\frac{dM}{d\mu_0H}$  by a gaussian fit of the distribution. The switching field values are listed in Table 5.9.

Table 5.9 – Switching field distribution of hybrid (Au-)Co<sub>0.8</sub>Ni<sub>0.2</sub>-SrTiO<sub>3</sub> nanowires measured at 5 K (<sup>†</sup> at 10 K) by vibrating sample magnetometry.  $\mu_0H_c$  is the coercive field,  $\mu_0H_{sw}$  is the switching field and  $\mu_0\Delta H_{sw}$  is the size of its distribution. Co<sub>0.8</sub>Ni<sub>0.2</sub>-SrTiO<sub>3</sub> nanowires samples are marked with ‡.

Sample	$\mu_0H_c$ (T)	$\mu_0H_{sw}$ (T)	$\mu_0\Delta H_{sw}$ (T)
$s4$	0.63	0.68	0.64
$s5$	0.82	0.90	0.56
$s6$	0.41	0.44	0.74
$s7^\dagger$	0.92	0.97	0.67
$t1^{\dagger\ddagger}$	0.94	0.95	0.53
$t2^\ddagger$	0.75	0.91	1.02
$t3^\ddagger$	0.87	0.92	0.58

### 5.3.2 Temperature dependence of the coercivity and activation length

#### 5.3.2.1 Temperature dependence of the coercivity

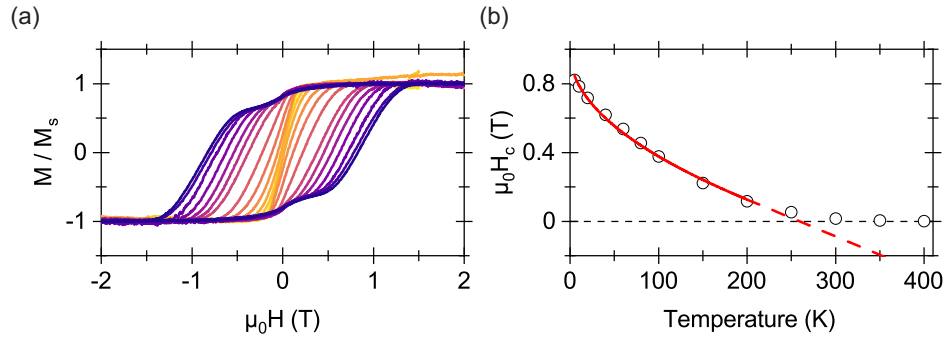


Figure 5.23 – Temperature dependence of magnetic properties of Au-Co<sub>0.8</sub>Ni<sub>0.2</sub>-SrTiO<sub>3</sub> nanowires. (a) Out of plane  $M(H)$  curves measured by vibrating sample magnetometry from 5 K to 400 K of sample s5. (b) The out of plane coercive field  $H_c$  is measured for each temperature (open circles) and the  $H_c(T)$  curve fitted with Sharrock's thermal reduction law (solid red line).

$M(H)$  curves were measured by VSM at different temperatures, from 5 K to 400 K (Fig 5.23(a)), typically. Fig 5.23(b) shows the out of plane coercive field  $\mu_0 H_c$  as a function of the temperature, which decays according to Sharrock's thermal reduction law  $H_c = H_c^{(0)}(1 - (T/T_b)^{1/2})$  where  $\mu_0 H_c^{(0)}$  is the coercive field at 0 K and  $T_b$  is the superparamagnetic blocking temperature. The superparamagnetic blocking temperature  $T_b$  is the minimal temperature required to equal the anisotropy barrier energy and for the magnetic moment to reverse spontaneously itself.

Table 5.10 – Temperature dependence of magnetic properties of (Au-)Co<sub>0.8</sub>Ni<sub>0.2</sub>-SrTiO<sub>3</sub> nanowires.  $\langle d \rangle$  is the diameter of the nanowires,  $\mu_0 H_c^{(0)}$  is the out of plane coercive field and  $T_b$  is the blocking temperature.  $\mu_0 H_c^{(0)}$  and  $T_b$  were deduced from Sharrock's thermal reduction law. Co<sub>0.8</sub>Ni<sub>0.2</sub>-SrTiO<sub>3</sub> nanowires samples are marked with ‡.

Sample	$\langle d \rangle$ (nm)	$\mu_0 H_c^{(0)}$ (T)	$T_b$ (K)
s4	-	0.75	203
s5	3.0	0.98	263
s6	3.2	0.49	300
s7	3.3	1.19	255
t1‡	3.4	1.08	352
t2‡	3.3	0.90	265
t3‡	3.3	1.05	250

The out of plane coercive field  $\mu_0 H_c^{(0)}$  and the superparamagnetic blocking temperature  $T_b$  which were deduced from Sharrock's thermal reduction law are tabulated in Table 5.10, with the diameter of the NWs  $\langle d \rangle$ .

The blocking temperature  $T_b$  is related to the effective magnetic anisotropy  $K$  and the activation volume  $V^*$  by  $25k_B T_b = KV^*$ . For cylindrical nanowires, the activation volume equals  $V^* = \pi(\langle d \rangle / 2)^2 l^*$ , where  $l^*$  is the activation length. Thus, if the effective magnetic anisotropy  $K$  and the activation length  $l^*$  are constant,  $T_b$  scales as  $\langle d \rangle^2$ . Such trend cannot be seen on Table 5.10. The variation of the diameter  $\langle d \rangle$ , limited in the 3 nm range, cannot explain by itself the variation of  $T_b$ .

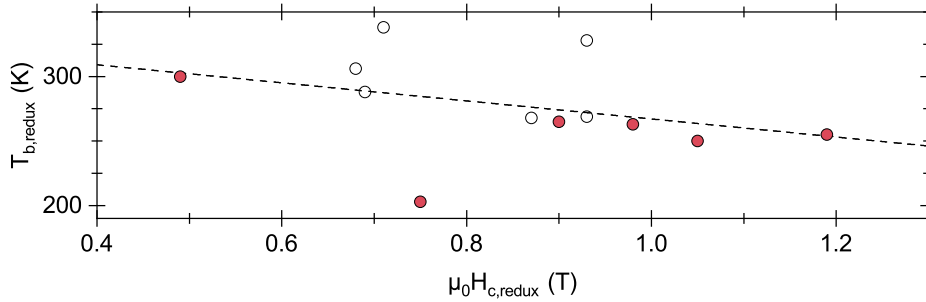


Figure 5.24 –  $T_b$  as a function of  $H_c^{(0)}$ . Each circle represents a sample (red circles for samples in Table 5.10); the blocking temperature  $T_b$  and the coercive field  $H_{c,redux}$  were deduced from Sharrock's thermal reduction law, the dashed line is a guide to the eye.

The out of plane anisotropy field  $\mu_0 H_a \propto \mu_0 H_c^{(0)}$  and the blocking temperature  $T_b$  are equal to  $\mu_0 H_a = 2K/M_s$  and  $T_b = K\pi(\langle d \rangle / 2)^2 l^*$ , respectively. If the effective magnetic anisotropy  $K$  increases,  $\mu_0 H_c^{(0)}$  and  $T_b$  should increase too. Data in Table 5.10 show an inverse proportion trend, on the contrary. A high out of plane coercive field  $\mu_0 H_c^{(0)}$  is correlated to a low blocking temperature  $T_b$ . This contrary trend is also seen on Fig. 5.24. Fig. 5.24 shows  $T_b$  as a function of the  $\mu_0 H_c^{(0)}$  of a set of samples of (Au-)Co<sub>0.8</sub>Ni<sub>0.2</sub>-SrTiO<sub>3</sub> NWs, samples listed in Table 5.10 are represented by a red circle.

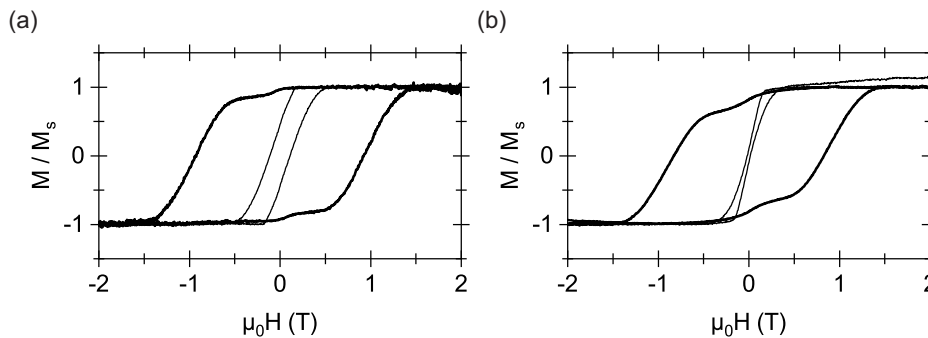


Figure 5.25 – Out of plane normalised  $M(H)$  curves measured by vibrating sample magnetometry (a) at 10 K (bold) and 300 K (thin) of sample  $t1$  and (b) at 5 K (bold) and 300 K (thin) of sample  $s5$ .

### 5.3.2.2 Activation length

Table 5.11 – Magnetic scales of (Au-)Co<sub>0.8</sub>Ni<sub>0.2</sub>-SrTiO<sub>3</sub> nanowires.  $\mu_0 H_c^{(0)}$  is the out of plane coercive field,  $T_b$  is the blocking temperature,  $E_b = 25k_B T_b$  is the barrier energy,  $l^*$  is the activation length and  $\delta = \pi\sqrt{A/K}$  is the Bloch domain wall width.  $\mu_0 H_c^{(0)}$  and  $T_b$  were deduced from Sharrock's thermal reduction law. Co<sub>0.8</sub>Ni<sub>0.2</sub>-SrTiO<sub>3</sub> nanowires samples are marked with ‡.

Sample	$\mu_0 H_c^{(0)}$ (T)	$T_b$ (K)	$E_b$ (10 <sup>-20</sup> J)	$l^*$ (nm)	$\delta$ (nm)
s4	0.75	203	7.00	-	21
s5	0.98	263	9.07	21	18
s6	0.49	300	10.35	42	26
s7	1.19	255	8.80	14	17
t1‡	1.08	352	12.14	20	17
t2‡	0.90	265	9.14	19	19
t3‡	1.05	250	8.63	15	18

The spontaneous reversal criterion  $KV^* = 25k_B T_b$  links the effective anisotropy  $K$  and the activation volume  $V^*$ . The effective anisotropy  $K = \mu_0 H_c M_s / 2$  is estimated at  $3.06\text{-}7.43 \times 10^5 \text{ J m}^{-3}$  based on  $H_c^{(0)}$  values deduced by Sharrock's thermal reduction law (Table 5.10). From the estimation of  $K$ , an activation volume  $V^*$  of  $118\text{-}338 \text{ nm}^3$  is deduced. The activation volume is the smallest volume of material reversing coherently in an event [135]. In the case of nanowires, the activation length  $l^*$  is expressed from  $V^*$  by considering  $V^* = \pi(\langle d \rangle / 2)^2 l^*$ , allowing to deduce lengths of 15-42 nm. These values can be compared to the Bloch domain wall width  $\delta = \pi\sqrt{A/K}$ , where  $A$  is the stiffness exchange constant.

As seen in Table 5.11, the activation length  $l^*$  is  $\approx 4$  times shorter than the physical length of the nanowires, suggesting a localised magnetisation reversal mechanism in the presented samples. Indeed, as reported in Table 5.8, the coercive field  $\mu_0 H_c$  is smaller than the anisotropy field  $\mu_0 H_a$ , the latter approximately equal to the hard axis saturation field  $\mu_0 H_s^{\text{IP}}$ , which would therefore be contrary to a coherent Stoner-Wohlfarth reversal [70]. It should be noted that magnetisation tends to reverse via the energetically most favourable mechanism, determining the lowest coercive field value. Furthermore,  $l^*$  is close to the Bloch domain wall width  $\delta$  (Table 5.11), implying that the reversal initiates with the formation of a Bloch domain wall.

Localised magnetisation reversal mechanism in nanomaterials is often reported in the literature [136–138], the reversal starts in a portion of a nanowire and propagates through it. Fig. 5.26 sketches the reversal mechanism observed in a nanowire under an external field. The reversal is first localised in a small region of the nanowire, typically the volume of  $V^*$ , creating a domain wall. The reason for the localisation are shape, structural or anisotropy inhomogeneities [71, 73, 107]. After nucleation, the reversal proceeds by propagation of the domain wall through the nanowire.

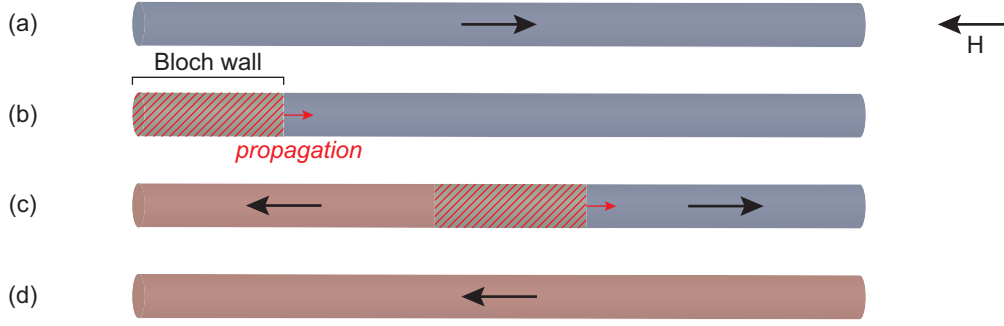


Figure 5.26 – (a) Initial magnetisation state of a nanowire. (b) The reversal is initiated by the creation of a domain wall, (c) propagating through the nanowire and reversing the magnetisation. (d) Final magnetisation state.

## 5.4 Discussions on the magnetic anisotropy

### 5.4.1 Effect of large structural strain on the anisotropy

The coercive field of the (Au-)Co<sub>0.8</sub>Ni<sub>0.2</sub>-SrTiO<sub>3</sub> nanocomposite thin films presented in this work reaches a value of  $\approx 1$  T. This significant value, in comparison to other references in the literature [110, 139], reveals an important magnetic anisotropy.

Table 5.12 – Magnetic anisotropy constants of (Au-)Co<sub>0.8</sub>Ni<sub>0.2</sub>-SrTiO<sub>3</sub> nanocomposite thin films.  $M_s$  is the saturation magnetisation,  $K_{ms} = \mu_0 M_s^2 / 4$  is the magnetostatic anisotropy,  $\langle \epsilon_{zz} \rangle$  is the mean axial strain measured by x-ray diffraction and  $K_{me} = \frac{3}{2} \lambda_{001} (c_{11} - c_{12}) (\epsilon_{zz} - \epsilon_{rr})$  is the magnetoelastic anisotropy. Co<sub>0.8</sub>Ni<sub>0.2</sub>-SrTiO<sub>3</sub> nanowires samples are marked with ‡.

Sample	Magnetostatic		Magnetoelastic	
	$M_s$ ( $10^5$ A m <sup>-1</sup> )	$K_{ms}$ ( $10^4$ J m <sup>-3</sup> )	$\langle \epsilon_{zz} \rangle$	$K_{me}$ ( $10^4$ J m <sup>-3</sup> )
s4			5.28	153.81
s5			5.25	152.94
s6			5.11	148.86
s7	12.49	49.01	4.37	127.30
t1‡			5.24	152.65
t2‡			4.93	143.62
t3‡			5.33	155.27

Magnetic anisotropy constants  $K_{ms} = \mu_0 M_s^2 / 4$  and  $K_{me} = \frac{3}{2} \lambda_{001} (c_{11} - c_{12}) (\epsilon_{zz} - \epsilon_{rr})$  are listed in Table 5.12. The magnetostatic  $K_{ms}$  and magnetoelastic  $K_{me}$  anisotropies were deduced from tabulated bulk Co<sub>0.8</sub>Ni<sub>0.2</sub>  $M_s$  values. The axial strain  $\epsilon_{zz}$ , used in the calculation of  $K_{me}$ , was measured by x-ray diffraction. From  $K_{ms}$  and  $K_{me}$ , the associated anisotropy field  $\mu_0 H_a$  is straightforwardly obtained thanks to  $\mu_0 H_a = 2K / M_s$ . Table 5.13 lists the values of  $\mu_0 H_a^{ms}$ , deduced from the magnetostatic anisotropy only, and  $\mu_0 H_a^{ms+me}$ , deduced from  $K = K_{ms} + K_{me}$ . These values are compared to the out of plane coercive field  $\mu_0 H_c^{(0)}$ , retrieved by Sharrock's

Table 5.13 – Characteristic magnetic fields of (Au-)Co<sub>0.8</sub>Ni<sub>0.2</sub>-SrTiO<sub>3</sub> nanocomposite thin films.  $\mu_0H_c^{(0)}$  and  $\mu_0H_s^{IP}$  are the out of plane coercive field and the in plane saturation field,  $\mu_0H_a^{ms}$  and  $\mu_0H_a^{ms+me}$  are the calculated anisotropy fields, deduced from  $K = K_{ms}$  and  $K = K_{ms} + K_{me}$ , respectively. Co<sub>0.8</sub>Ni<sub>0.2</sub>-SrTiO<sub>3</sub> nanowires samples are marked with ‡.

Sample	$\mu_0H_c^{(0)}$ (T)	$\mu_0H_s^{IP}$ (T)	$\mu_0H_a^{ms}$ (T)	$\mu_0H_a^{ms+me}$ (T)
s4	0.75	1.81		3.25
s5	0.98	1.80		3.23
s6	0.49	1.54		3.17
s7	1.19	1.93	0.78	2.82
t1‡	1.08	1.92		3.23
t2‡	0.90	2.17		3.08
t3‡	1.05	2.17		3.27

thermal reduction law, and the in plane hard axis saturation field  $\mu_0H_s^{IP}$ , which provides a good estimation of the total anisotropy field  $\mu_0H_a$ .

$\mu_0H_c^{(0)}$  and  $\mu_0H_s^{IP}$  are systematically higher than  $\mu_0H_a^{ms}$ . As  $\mu_0H_a^{ms}$  only depends on the shape of the nanowires, this fact implies an enhancement of the magnetic anisotropy caused by a different source of anisotropy, that is the magnetoelastic anisotropy. As mentioned previously, an important strain exerted on the nanowires should lead to an important uniaxial anisotropy for Co-rich systems, furthermore the magnetic anisotropy is reinforced all the more so that the strain is important. By using the relation linking the anisotropy field and the total magnetic anisotropy  $\mu_0H_a = 2K/M_s$  and the total magnetic anisotropy field, estimated by  $\mu_0H_s^{IP}$ , it is possible to deduce the additional anisotropy  $K_{add} = \mu_0H_s^{IP}M_s/2 - K_{ms}$  related to the anisotropy enhancement. A highest ratio of  $\frac{K_{add}}{K_{ms}} = 1.77$  is obtained for t2 and t3, the lowest ratio is higher than 0.96, proving the magnetoelastic enhancement of the anisotropy.

However, the anisotropy field  $\mu_0H_a^{ms+me}$ , calculated with tabulated values of magnetostriction coefficient and elastic constants, is significantly higher than the experimental  $\mu_0H_s^{IP}$ . This discrepancy could stem from the  $\lambda_{001}$  and  $c_{11} - c_{12}$  bulk values used in the calculation of  $K_{me}$ , straying from those of a nanoparticle, and more plausibly from the inhomogeneity of the strain within the nanowires, as observed in reciprocal space mappings, leading to a distribution of anisotropy.

#### 5.4.2 Inhomogeneity and loss of anisotropy

The micromagnetic model, presented in the following paragraph, intends to simulate the contribution of the distribution of anisotropy caused by the inhomogeneity of the strain and its influence on the localisation of the reversal in the nanowire.

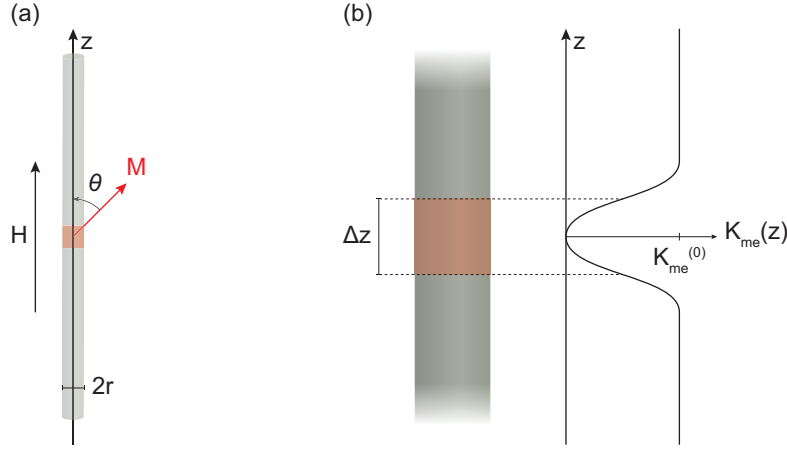


Figure 5.27 – (a) Schematics of a nanowire of radius  $r$ ,  $\theta$  is the angle between the magnetisation  $\vec{M}$  and the  $c$ -axis of the nanowire. (b) Schematics of the micromagnetic model, the magnetoelastic anisotropy  $K_{me}$  is perturbed in a  $\Delta z$  length, the inhomogeneity of  $K_{me}$  is modelled by a gaussian.

The variation of total magnetic free energy  $\Delta E$  of a NW of radius  $r$  with its magnetisation depending only on the  $z$ -coordinate is

$$\Delta E = \pi r^2 \int \left\{ A \left( \frac{\partial \theta}{\partial z} \right)^2 + K_{ms} \sin^2 \theta + K_{me}(z) \sin^2 \theta + \mu_0 M_s H \cos \theta \right\} dz \quad (5.6)$$

where  $A$  is the exchange stiffness constant and  $\theta$  is the angle between the magnetisation and the  $c$ -axis of the NW. The micromagnetic equation Eq 5.6 is minimised by solving Euler's equation [140, 141]

$$\frac{\partial \mathcal{L}(z, \theta, \dot{\theta})}{\partial \theta} - \frac{d}{dz} \frac{\partial \mathcal{L}(z, \theta, \dot{\theta})}{\partial \dot{\theta}} = 0 \quad (5.7)$$

where  $\dot{\theta} = \frac{\partial \theta}{\partial z}$  and the Lagrangian  $\mathcal{L}(z, \theta, \dot{\theta})$  is

$$\mathcal{L}(z, \theta, \dot{\theta}) = A \left( \frac{\partial \theta}{\partial z} \right)^2 + K_{ms} \sin^2 \theta + K_{me}(z) \sin^2 \theta + \mu_0 M_s H \cos \theta. \quad (5.8)$$

If one assumes the variation of  $\theta$  is small, the micromagnetic equation is

$$2A\ddot{\theta} - 2(K_{ms} + K_{me}(z))\theta + \mu_0 M_s H \theta = 0. \quad (5.9)$$

The inhomogeneity of the magnetoelastic anisotropy constant is modelled by a gaussian, representing the gradient of strain in a  $\Delta z$  length of the NW and one writes  $K_{me}(z) = K_{me}^{(0)} - \Delta K_{me} e^{-z^2/\Delta z^2} = K_{me}^{(0)} - \Delta K_{me}(1 - z^2)/\Delta z^2$  where the gaussian has been developed into

Taylor series. From this expression of  $K_{me}(z)$ , Eq. 5.9 is expressed in reduced units

$$\frac{d^2\theta}{d\zeta^2} + [\kappa^2 - \zeta^2] \theta = 0 \quad (5.10)$$

where a change of variables is done with these variables

$$\zeta^2 = z^2 \frac{\sqrt{\Delta K_{me}/A}}{\Delta z} \quad \text{and} \quad \kappa^2 = \frac{\Delta z}{\sqrt{\Delta K_{me}/A}} \left[ -K_{ms} - K_{me}^{(0)} + \Delta K_{me} + \frac{\mu_0 M_s H}{2} \right] \quad (5.11)$$

Eq. 5.10 is the harmonic oscillator equation and has a general solution with  $\kappa^2 = 1$ . Therefore, the smallest nucleation field  $H_n$ , that is the minimal external field required to create a magnetic nucleus in the nanowire, is written as

$$\mu_0 H_n = \frac{2(K_{ms} + K_{me})}{M_s} - \frac{2\Delta K_{me}}{M_s} + \frac{2\Delta K_{me}}{M_s} \sqrt{\frac{A}{\Delta K_{me}}} \frac{1}{\Delta z} \quad (5.12)$$

where the first term translates the anisotropy field of a homogeneous nanowire, and the next the reduction of the nucleation field caused by the strain inhomogeneity. The last term recalls the Bloch domain wall width  $\delta = \pi \sqrt{A/\Delta K_{me}}$ , therefore it denotes the additional cost to create a Bloch wall at the border of the magnetic nucleus.

To compute the nucleation field  $\mu_0 H_n$ , the anisotropy constants  $K_{ms}$  and  $K_{me}$  must be chosen soundly. The value of  $K_{ms}$  referenced in Table 5.12 is deduced from the tabulated value of  $M_s$  of bulk  $\text{Co}_{0.8}\text{Ni}_{0.2}$ . For high density nanocomposite systems, the porosity of the assembly, i.e. the volume ratio of particles on the surface, must be taken into account in the determination of  $K_{ms}$ . Indeed, the higher is the density, the stronger is the dipolar coupling between the nanowires. The effective magnetostatic anisotropy constant, assuming a dipolar coupling, is expressed as  $K_{ms}^{\text{eff}} = K_{ms}(1 - 3P)$ , where  $P$  is the porosity of the material [142]. A porosity of nanowires  $P \approx 10\%$ , a typical value measured by transmission electron microscopy in the presented samples, gives a magnetostatic anisotropy constant of  $K_{ms}^{\text{eff}} = 34.31 \times 10^4 \text{ J m}^{-3}$ . This estimation of  $K_{ms}^{\text{eff}}$  is valid in the system presented in this work, according to previous mean field calculations [107]. As the only two sources of anisotropy are  $K_{ms}$  and  $K_{me}$ , the magnetoelastic anisotropy  $K_{me}$  is deduced from the anisotropy field, estimated by  $\mu_0 H_s^{\text{IP}}$ .  $K_{me} = \mu_0 H_s^{\text{IP}} M_s / 2 - K_{ms}^{\text{eff}}$  yields a value of  $85.50 \times 10^4 \text{ J m}^{-3}$  for  $s7$ .

Fig. 5.28(a) shows the contour map of the nucleation field  $\mu_0 H_n$  as a function of the length of the inhomogeneity  $\Delta z$  and its ratio  $\frac{\Delta K_{me}}{K_{me}}$ . The length of the inhomogeneity  $\Delta z$  should be of the same order as the activation length  $l^*$ , as the reversal is localised and related to inhomogeneities in the nanowire. Furthermore, the nucleation field  $\mu_0 H_n(l^*, \frac{\Delta K_{me}}{K_{me}})$  should be compared to the coercive field  $\mu_0 H_c$ . Indeed, according to the Stoner-Wohlfarth,  $H_c = H_a$  for an independent magnet. A more realistic model should include the anisotropy inhomogeneity in the nanowire. In the presented micromagnetic model, taking into account the inhomogeneity,  $H_c$  is reduced,

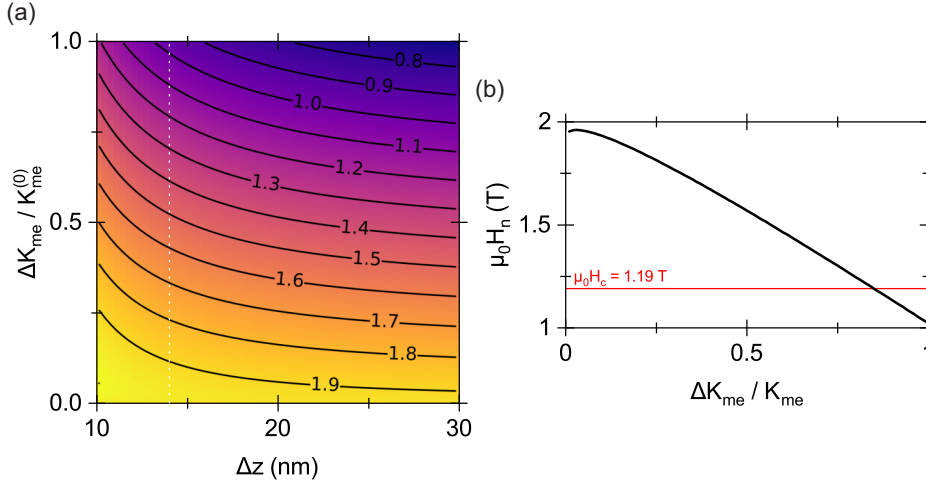


Figure 5.28 – (a) Contour map of the nucleation field  $\mu_0 H_n$  as a function of the length of the inhomogeneity  $\Delta z$  and its ratio  $\frac{\Delta K_{me}}{K_{me}}$ , the white dotted line is  $\Delta z = l^*$ . (b)  $\mu_0 H_n(\frac{\Delta K_{me}}{K_{me}})$  profile for  $\Delta z = l^*$ .  $K_{ms}$  and  $K_{me}$  values of sample  $s7$  were used to compute these figures.

hence  $H_c \neq H_a$  and  $H_c = H_n$ . It should be reminded that the activation length  $l^*$  and the coercive field  $\mu_0 H_c^{(0)}$  have, respectively, a value of 14 nm and 1.19 T, deduced previously and tabulated in Table 5.11. The  $\mu_0 H_n(\frac{\Delta K_{me}}{K_{me}})$  profile for  $\Delta z = l^*$ , represented by a white dotted line in Fig. 5.28(a), is shown in Fig. 5.28(b). Assuming  $\mu_0 H_n = \mu_0 H_c^{(0)}$ , an anisotropy inhomogeneity in the nanowire of  $\frac{\Delta K_{me}}{K_{me}} \approx 81\%$  is deduced.  $\mu_0 H_n$  is computed for the samples listed in Table 5.13. Under the hypothesis that there is a correlation between the inhomogeneity length  $\Delta z$  and the activation length  $l^*$  and that  $\Delta z = l^*$ , an inhomogeneity ranging from 81% to 90% of the value of  $K_{me}$  is deduced.

The micromagnetic model is able to simulate the localised reversal, for simple cases for which the sources of anisotropy are restricted to  $K_{ms}$  and  $K_{me}$  and assuming  $\Delta z = l^*$ . Thus, within this framework, the local loss of anisotropy in a length of  $l^*$  is the main cause of the localisation of the reversal and the reduction of the coercive field. The significative perturbation of the anisotropy ( $\frac{\Delta K_{me}}{K_{me}} > 81\%$ ) could be related to an inhomogeneity of vertical strain  $\epsilon_{zz}$ , as borne out by x-ray diffraction. As shown in Fig. 5.11, the 002 Bragg peak of  $\text{Co}_{0.8}\text{Ni}_{0.2}$  is wide, implying a short structural coherence length or a distribution of vertical strain. Thus, structural defects in the nanowires plausibly cause this inhomogeneity of the anisotropy. As reported in Ref. [60], Ni nanowires are composed of rotated domains spreading out over a length of 15 nm, matching with the activation length  $l^*$  previously retrieved. A rotation mechanism is also found in highly strained  $\text{Co}_x\text{Ni}_{1-x}$  nanowires. It is linked to the relaxation of the  $\text{Co}_x\text{Ni}_{1-x}$  lattice, leading to a rotation of the (111) planes to match the matrix and the creation of stacking faults. Therefore, this rotation mechanism is a possible cause of the anisotropy inhomogeneity, and thus to the localisation of the reversal and the loss of coercive field.

However, samples with important loss of coercive field, for example *s6*, cannot be modelled by the presented micromagnetic simulation. Indeed, the smallest calculated nucleation field  $\mu_0 H_n$  is higher than the coercive field  $\mu_0 H_c^{(0)}$ . Possible explanations can be found and show the limits of the micromagnetic simulation. For example, Table 5.9 shows that some samples have a small switching field  $\mu_0 H_{sw}$  and they cannot be modelled by the simulation. As pointed by Fig. 5.24, the blocking temperature  $T_b$  seems to decrease as the coercive field, so the anisotropy, increases. This could imply that localisation is much stronger than predicted in samples with high anisotropy.  $\lambda_{001}$  and  $c_{11} - c_{12}$  bulk values, taken in the micromagnetic simulation, stray from those of a nanoparticle, thus this simple model should be taken with caution. Further work on a more complex model is needed to solve these issues and to shed light on the correlation between structure and the loss of anisotropy.

## 5.5 Conclusion

This chapter discussed the growth of hybrid Au-Co<sub>0.8</sub>Ni<sub>0.2</sub>-SrTiO<sub>3</sub> nanocomposite thin films by sequential pulsed laser deposition using a two-step procedure, and reported structure and magnetic properties of thin films. Transmission electron microscopy images proved the growth of hybrid nanocomposite thin films. A mean diameter of the hybrid nanocomposites of  $\approx 3$  nm was measured in microscopy images. Phase separation of Au and Co<sub>0.8</sub>Ni<sub>0.2</sub> was extensively studied by high-angle annular dark-field scanning transmission electron microscopy and energy-dispersive x-ray spectroscopy. Elemental spectromicroscopy proved the phase separation of Au and Co<sub>0.8</sub>Ni<sub>0.2</sub> in hybrid nanocomposite thin films. Statistical study of these images point to a preferential nucleation of Au at the top of the Co<sub>0.8</sub>Ni<sub>0.2</sub> NWs (80 % of hybrid nanocomposites).

Epitaxy of hybrid nanocomposite thin films was studied by reciprocal space mapping, at the SixS beamline of the synchrotron SOLEIL. Reciprocal space mappings showed that Au has an in plane texture and a cube-on-cube epitaxy between Co<sub>0.8</sub>Ni<sub>0.2</sub> and SrTiO<sub>3</sub>. Besides, an axial strain  $\epsilon_{zz}$  of  $\approx 5$  % is measured in Co<sub>0.8</sub>Ni<sub>0.2</sub> NWs. This significative strain is caused by the epitaxy of Co<sub>0.8</sub>Ni<sub>0.2</sub> NWs and the SrTiO<sub>3</sub> matrix. Scattering rings were observed in the  $h$ - $k$  plane, around the matrix Bragg reflection, by grazing incidence x-ray diffraction. This diffuse signal stems from the presence of nanocomposites in the thin film, modelled by a form factor. Information, such as the interdistance  $D$ , its variance  $\sigma$  and the diameter  $d$  of the nanowires, were deduced from this form factor. Values deduced from the off-Bragg scattering rings are consistent with transmission electron microscopy.

Magnetic properties were measured by VSM. Magnetic hystereses showed an anisotropic magnetic response, the easy axis of magnetisation being along the long axis of the nanowires. Coercive field in the easy axis  $\mu_0 H_c$  reaches a huge typical value of  $\approx 1$  T at 10 K. Besides, temperature dependence of  $\mu_0 H_c$  was reported.  $\mu_0 H_c(T)$  curves were fitted by Sharrock's thermal reduction law to extract the coercive field at 0 K  $\mu_0 H_c^{(0)}$ , and the blocking temperature

$T_b$ .  $T_b$  values range from 203 K to 352 K. Activation lengths  $l^*$ , corresponding to the smallest volume to reverse coherently in an event, were deduced from  $T_b$  values. Comparison of activation lengths and Bloch domain wall widths shows that reversal is localised. Reversal starts by nucleation in a small region of the nanowire, and proceeds by propagation of a domain wall through the nanowire.

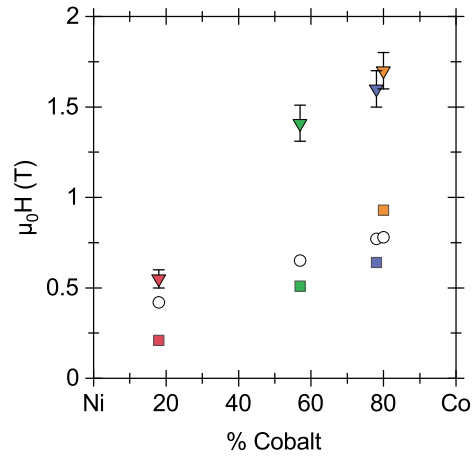


Figure 5.29 – Comparison between the out of plane coercive field  $\mu_0 H_c^{(0)}$  (squares), the in plane saturation field  $\mu_0 H_s^{IP}$  (triangles) and the magnetostatic anisotropy field  $\mu_0 H_a^{ms}$  (circles) as a function of the content of Co (reproduced from [96]).

$\mu_0 H_c^{(0)}$  values, being the lowest anisotropy field value, were systematically higher than the magnetostatic anisotropy field  $\mu_0 H_a^{ms}$ . This fact points to another contributing source of anisotropy, that is the magnetoelastic anisotropy.  $\mu_0 H_c^{(0)}$  and  $\mu_0 H_a^{ms}$  are plotted in Fig. 5.29, indicating a predominant magnetoelastic anisotropy for Co contents above 80%. This shows possible strain engineering in  $\text{Co}_{0.8}\text{Ni}_{0.2}$  NWs. A contributing magnetoelastic anisotropy was explained by the large axial strain of  $\epsilon_{zz} \approx 5\%$ , measured in reciprocal space mappings, showing the link between magnetism and strain. However, the anisotropy field  $\mu_0 H_a^{ms+me}$  is significantly higher than the experimental  $\mu_0 H_s^{IP}$ . A possible explanation lies in strain inhomogeneity in the nanowires, as discussed by the micromagnetic model. A micromagnetic equation was computed considering a locally perturbed anisotropy. An inhomogeneity ranging from 81% to 90% of the value of  $K_{me}$  is deduced from the micromagnetic model. This significant perturbation of the magnetoelastic anisotropy is possibly related to an inhomogeneity of axial strain  $\epsilon_{zz}$ , caused by defects. Thus, defects could cause localisation and reduction of the coercive field in highly strained  $\text{Co}_{0.8}\text{Ni}_{0.2}$  NWs.



## MAGNETO-OPTICAL STUDY OF NANOCOMPOSITE THIN FILMS

6.1	Introduction . . . . .	103
6.2	Absorption in hybrid nanocomposite thin films . . . . .	104
6.2.1	Experimental data and simulations . . . . .	104
6.2.2	Simulation of the absorption . . . . .	105
6.3	Magnetisation dynamics . . . . .	107
6.3.1	Static magneto-optical Kerr effect . . . . .	107
6.3.2	Ultrafast demagnetisation . . . . .	108
6.3.2.1	General description . . . . .	108
6.3.2.2	Initial demagnetisation . . . . .	111
6.3.2.3	Remagnetisation . . . . .	113
6.4	Conclusion . . . . .	114

## 6.1 Introduction

Hybrid Au-CoNi-SrTiO<sub>3</sub> nanocomposite thin films, of which the properties were reported in the previous chapter, are potential model systems for the study of magnetoplasmonic phenomena, coupling magnetism with light. Co<sub>0.8</sub>Ni<sub>0.2</sub> NWs show a hard uniaxial anisotropy, i.e. two well-defined magnetic states. Au NWs sustain plasmonic resonances, and thus could have an effect on magneto-optical properties. As discussed in Section 1.3, novel magneto-optical effects were reported in hybrid systems, as the enhancement of the magneto-optical Faraday and Kerr effects, the photo-induced heating of ferromagnets or the amplification of sub-picosecond demagnetisation.

This chapter reports the preliminary study of magneto-optical properties in two nanocomposite thin film samples. Sample *s5* is a hybrid Au-Co<sub>0.8</sub>Ni<sub>0.2</sub>-SrTiO<sub>3</sub> nanocomposite thin film, and sample *t2* a Co<sub>0.8</sub>Ni<sub>0.2</sub>-SrTiO<sub>3</sub> nanocomposite thin film. Studying coated and uncoated samples could provide an insight into the effects of Au NWs on the magnetisation dynamics of ferromagnetic nanocomposites. Firstly, optical properties simulated by finite-difference time-domain method of nanocomposite thin films are reported. A presentation of the model used to simulate the optical absorption is given. The reliability of the model is tested by comparing simulation and experimental data, measured by ellipsometry. Optical absorption of coated and uncoated ferromagnetic nanocomposites was deduced from the simulation. After assessing the optical properties, time-resolved magneto-optical Kerr effect measurements are presented and discussed.

## 6.2 Absorption in hybrid nanocomposite thin films

### 6.2.1 Experimental data and simulations

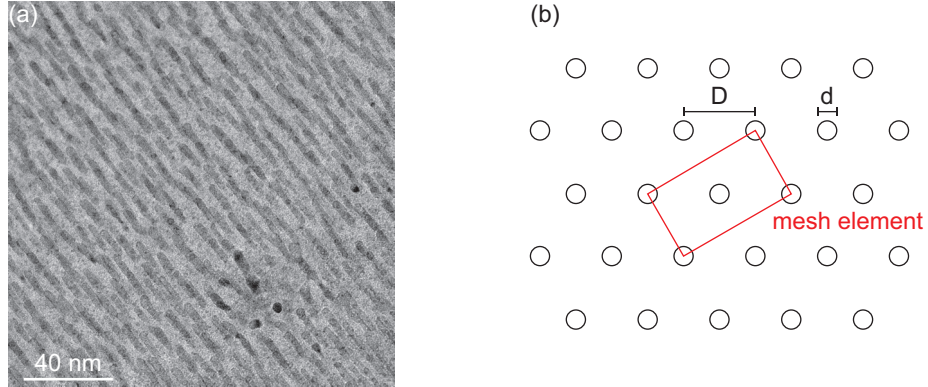


Figure 6.1 – (a) High-resolution transmission electron microscopy tilt view image of sample *s5*. (b) Schematics of a hexagonal lattice of hybrid nanowires in oxide matrix of diameter  $d$  and of interdistance  $D$ , the red cell shows the mesh element used in the finite-difference time-domain method simulation.

Sample *s5* was grown by two-step sequential pulsed laser deposition.  $\text{Co}_{0.8}\text{Ni}_{0.2}$  NWs of sample *s5* were deposited at  $830^\circ\text{C}$  according to the basic sequence  $[[n_{\text{SrTiO}_3} + n_{\text{NiO}}] + [n_{\text{SrTiO}_3} + n_{\text{CoO}}] \times 4] \times N$  with  $n_{\text{SrTiO}_3} = 18$ ,  $n_{\text{NiO}} = n_{\text{CoO}} = 9$  and  $N = 150$ . Au NWs were thereafter grown at  $750^\circ\text{C}$  according to the basic sequence  $[n_{\text{SrTiO}_3} + n_{\text{Au}}] \times N$  with  $n_{\text{SrTiO}_3} = 18$ ,  $n_{\text{Au}} = 6$  and  $N = 90$ . Fig. 6.1(a) shows the high-resolution transmission electron microscopy tilt view image of hybrid Au-CoNi-SrTiO<sub>3</sub> nanocomposite thin film *s5*. Hybrid nanowires in sample *s5* have the shape of cylinders, Au NWs and CoNi NWs are hardly differentiable from each other in Fig. 6.1(a). The diameter of the nanowires is  $\approx 3$  nm and they have a total length of  $t = 68 + 7$  nm (Table 5.2).

For the finite-difference time-domain method simulation, sample *s5* is modelled as a hexagonal lattice of Au- $\text{Co}_{0.8}\text{Ni}_{0.2}$  NWs in SrTiO<sub>3</sub> matrix (Fig. 6.1(b)). Parameters were taken from transmission electron microscopy images and x-ray diffraction. The diameter of the nanowires is  $d = 4$  nm and the interdistance is  $D = 12$  nm, that is equivalent to a volume fraction of 10%. The total thickness of the nanowires is  $t = 65 + 7$  nm. The mesh element is a square box sketched in red in Fig. 6.1(b). Optical constants of the SrTiO<sub>3</sub> substrate and the Au NWs were taken in the literature [78, 143], and that of  $\text{Co}_{0.8}\text{Ni}_{0.2}$  were defined as a linear combination of the optical constants of Co and Ni, taken in Ref. [144]. As the SrTiO<sub>3</sub> matrix is nonstoichiometric and oxygen-deficient, its optical constants were measured by ellipsometry from a SrTiO<sub>3</sub> thin film grown by pulsed laser deposition. Finite-difference time-domain method simulations presented in this work were conducted by Bruno Gallas from the *Institut des NanoSciences de Paris* (CNRS-Sorbonne Université).

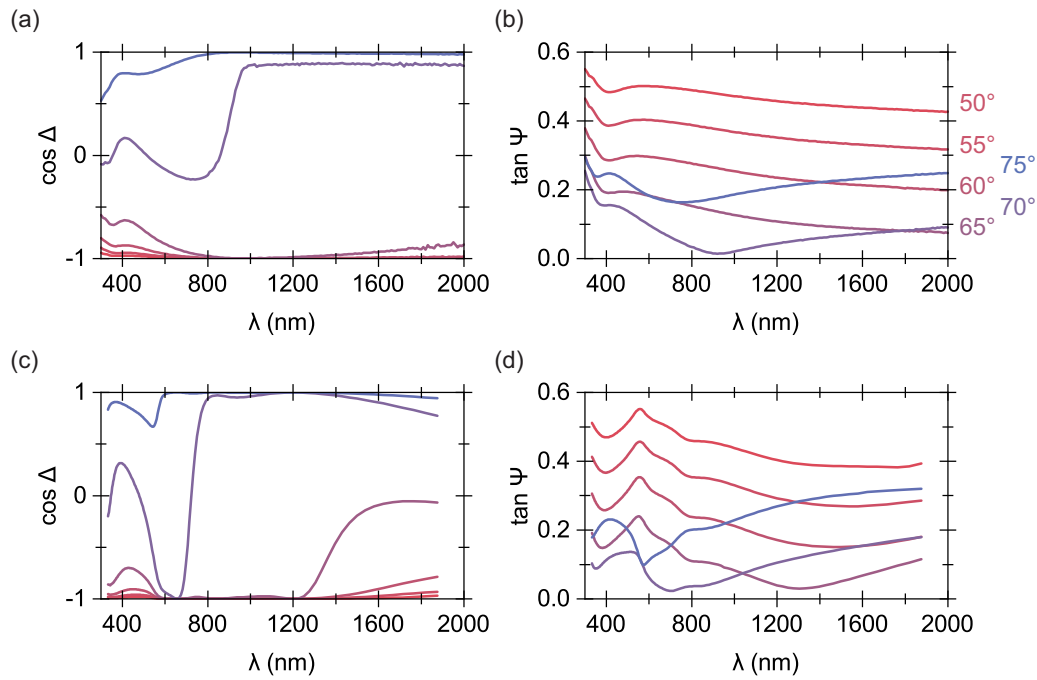


Figure 6.2 – (a)  $\cos \Delta$  and (b)  $\tan \Psi$  of sample *s5*, measured by ellipsometry for different angles of incidence. (c)  $\cos \Delta$  and (d)  $\tan \Psi$  of a hexagonal lattice of hybrid nanowires in oxide matrix of diameter 4 nm, interdistance 12 nm and thickness  $t = 65 + 7$  nm (Fig. 6.1(b)), simulated by finite-difference time-domain method.

The model used for the finite-difference time-domain method simulation is ideal. Indeed, nanowires in the model are homogeneously distributed perfect cylinders, which is not the case of the nanowires in sample *s5*. The relevance of the model can be tested by comparing simulation and experimental data. Sample *s5* was measured by ellipsometry. Fig. 6.2(a) shows the cosine of the phase difference  $\cos \Delta$  and Fig. 6.2(b) shows the ratio of amplitude  $\tan \Psi$ , as a function of the wavelength  $\lambda$  and the angle of incidence.  $\cos \Delta$  and  $\tan \Psi$  were then simulated by finite-difference time-domain method Fig. 6.2(c)(d). Even though simulated curves are not exactly identical to experimental measurements, same trends are seen in the simulated and experimental optical responses. It should however be noted that clear spectral features related to plasmonic excitation cannot be observed in the experimental values of  $\tan \Psi$ . This could be caused by an increased damping of plasmons due to the very small size of the Au NWs. In what follows, this simple and ideal model is used to calculate the absorption in nanocomposites.

### 6.2.2 Simulation of the absorption

Fig. 6.3 shows the ohmic loss in Au NWs of a hybrid Au-CoNi-SrTiO<sub>3</sub> nanocomposite thin film, simulated by finite-difference time-domain method for an angle of incidence of  $\theta = 60^\circ$ . Simulations were done for *p* and *s*-polarised light. As  $\theta$  is close to the Brewster angle of SrTiO<sub>3</sub>

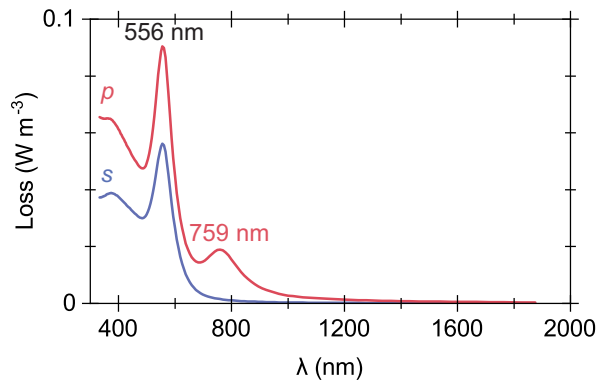


Figure 6.3 – Ohmic loss of Au NWs in hybrid Au-CoNi-SrTiO<sub>3</sub> nanocomposite thin films, simulated by finite-difference time-domain method. The angle of incidence is  $\theta = 60^\circ$  and the light is  $p$ -polarised (in red) or  $s$ -polarised (in blue).

$\theta_B = 67^\circ$ , absorption is stronger for  $p$ -polarised light than  $s$ -polarised light. Ohmic loss, which is related to the absorption of the nanoparticle, shows a single absorption band at 556 nm for  $s$ -polarised light, and two absorption bands at 556 nm and 759 nm for  $p$ -polarised light. The band at 556 nm is related to the transverse mode of the plasmonic resonance in Au NWs, whereas the band at 759 nm is related to the longitudinal mode. It should be noted that the latter can only be excited by  $p$ -polarised light, due to the geometry of the nanocomposite thin film.

Simulated ohmic loss in Au NWs shows that they sustain plasmonic resonances. Their effect on CoNi NWs can be studied by simulating the ohmic loss. A simulation was done for two cases, coated and uncoated Co<sub>0.8</sub>Ni<sub>0.2</sub> NWs in SrTiO<sub>3</sub> matrix. In both cases, nanowires were distributed homogeneously as in Fig. 6.1(b), and CoNi NWs were modelled with the same parameters. Fig. 6.4 shows the ohmic loss for CoNi NWs coated by Au NWs, plotted in blue and red, and for CoNi NWs, plotted in cyan and orange. Simulations were done for  $s$  and  $p$ -polarised light. As seen in Fig. 6.4(a), Au NWs do not seem to increase the ohmic loss in CoNi NWs when the incident light is  $s$ -polarised. A different situation is predicted for  $p$ -polarised light (Fig. 6.4(b)). The ohmic loss is indeed larger in coated CoNi NWs at  $\approx 800$  nm, equivalent to an increase of  $\approx 5\%$ . This value is low, possibly due to the size of the Au NWs. The absorption cross section of Au NWs is indeed proportional to their volume. Au NWs with larger volume could display stronger absorption, thus the increase of absorption in CoNi NWs could be much larger. On another note, the increase of absorption in real hybrid nanowires could be lower than that seen in the simulation, as defects in the material cause a broadening of the plasmonic resonance.

In this section, the absorption of hybrid nanocomposites was simulated by finite-difference time-domain method, using a simple model. The simulation of the optical absorption could be an useful tool for determining the optimal dimensions of future nanocomposites, and

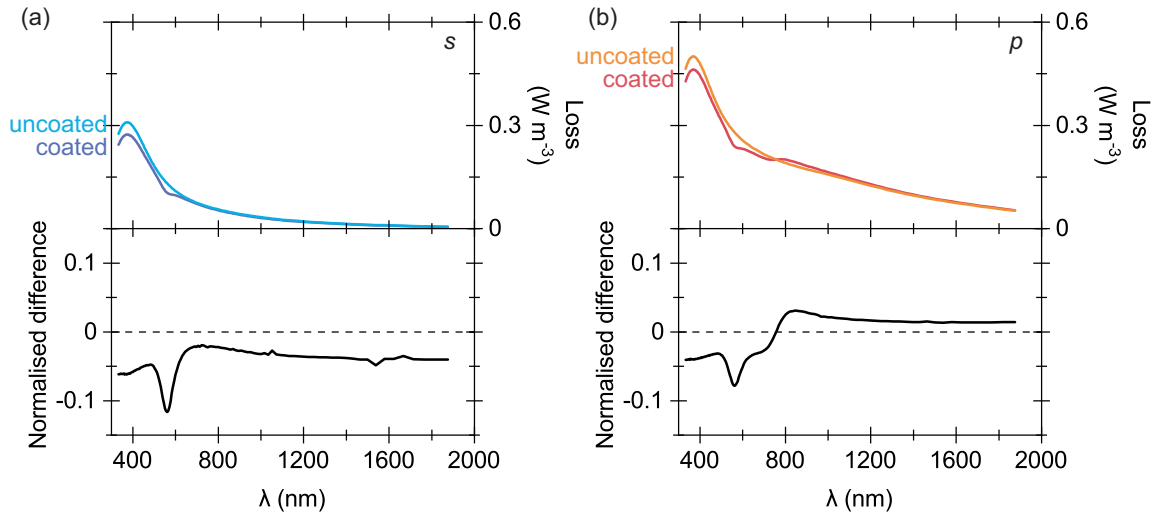


Figure 6.4 – Ohmic loss of  $\text{Co}_{0.8}\text{Ni}_{0.2}$  NWs, simulated by finite-difference time-domain method. The light is (a)  $s$  or (b)  $p$ -polarised. Ohmic loss of  $\text{Co}_{0.8}\text{Ni}_{0.2}$  NWs in hybrid Au- $\text{Co}_{0.8}\text{Ni}_{0.2}$ - $\text{SrTiO}_3$  nanocomposite thin films is plotted in blue and red, and of  $\text{Co}_{0.8}\text{Ni}_{0.2}$  NWs in  $\text{SrTiO}_3$  matrix is plotted in blue and red in cyan and orange. The difference between the ohmic loss in coated and uncoated  $\text{Co}_{0.8}\text{Ni}_{0.2}$  NWs is shown under the ohmic loss curves. For a positive difference, absorption is larger in coated nanoparticles.

should therefore be used as a guide before the growth of new samples. Though simulation predicts a negligible increase of the ohmic loss in hybrid nanocomposites, it still shows that plasmon-mediated amplification of the absorption in ferromagnetic nanoparticles is possible. For example, a solution to maximise the amplification is to increase the diameter and the length of the Au NWs, to make the plasmonic resonance stronger.

## 6.3 Magnetisation dynamics

### 6.3.1 Static magneto-optical Kerr effect

Increase of the absorption in hybrid nanocomposites presented in this work could play a weak and yet measurable role in photo-induced magnetisation dynamics. To study the role of Au NWs in the magnetisation dynamics of hybrid nanocomposites, demagnetisation experiments were conducted at the *Laboratoire d'optique appliquée* (CNRS-ENSTA) by pump-probe TRMOKE.

Two samples, sketched in Fig. 6.5(c), were studied. Sample  $t2$  is made of  $\text{Co}_{0.8}\text{Ni}_{0.2}$  NWs in  $\text{SrTiO}_3$  matrix, coated by a  $\text{Al}_2\text{O}_3$  thin layer to prevent oxidation of the nanowires, and sample  $s5$  of hybrid Au- $\text{Co}_{0.8}\text{Ni}_{0.2}$  NWs in  $\text{SrTiO}_3$  matrix. CoNi NWs were deposited under the same growth conditions in both samples. Out of plane  $M(H)$  curves of samples  $t2$  and  $s5$  (Fig. 6.5(a)(b)) were measured by polar magneto-optical Kerr effect at room temperature and  $\lambda = 632 \text{ nm}$ . These hystereses show that the samples can be probed by magneto-optical

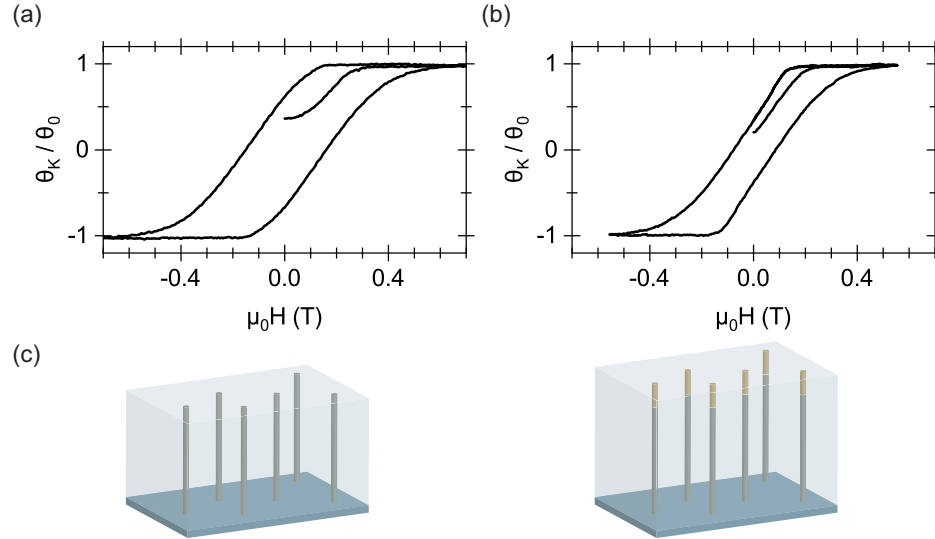


Figure 6.5 – Out of plane  $M(H)$  curves of samples (a)  $t2$  and (b)  $s5$ , measured by polar magneto-optical Kerr effect at room temperature. (c) Schematics of samples  $t2$  (left) and  $s5$  (right).

Kerr effect. The samples are in the blocked state above 300 K, with coercive field values  $\mu_0 H_c$  of 0.16 T and 0.08 T for samples  $t2$  and  $s5$ , respectively. Furthermore, a saturation field of  $\mu_0 H_s \approx 0.5$  T is measured in both samples.

### 6.3.2 Ultrafast demagnetisation

#### 6.3.2.1 General description

Kerr rotation variation  $\frac{\Delta\theta_K}{\theta_0}(t)$  curves (Fig. 6.6) of samples  $s5$  and  $t2$  were measured by TRMOKE, using a pump-probe set-up. Measurements were done between  $-2$  ps and  $20$  ps, with  $t = 0$  ps corresponding to the coincidence of the pump pulse and the probe pulse. Data were normalised by the average Kerr rotation signal  $\theta_0$  before  $t = 0$  ps. The pump was  $p$  or  $s$ -polarised, with incident fluences ranging from  $1.7$  mJ cm $^{-2}$  to  $19.8$  mJ cm $^{-2}$ . Protocols used for data measurement and treatment are explained in Paragraph 3.4.2.2.

The main features observed in the demagnetisation curves (Fig. 6.6) are:

- Sub-picosecond demagnetisation is observed in every measurement after pump-probe coincidence ( $t = 0$  ps) and  $\Delta\theta_K$  drops in less than 0.5 ps.
- Demagnetisation amplitude scales as pump fluence. Demagnetisation is larger as  $F$  increases.
- For a given pump fluence  $F$ , the magnetisation drop is larger for the  $p$ -polarised than the  $s$ -polarised pump in both samples.
- After the initial demagnetisation, magnetisation relaxes back to its initial state, which spans in a slower timescale of several picoseconds.
- Remagnetisation depends on pump fluence. It is slower for high fluences.

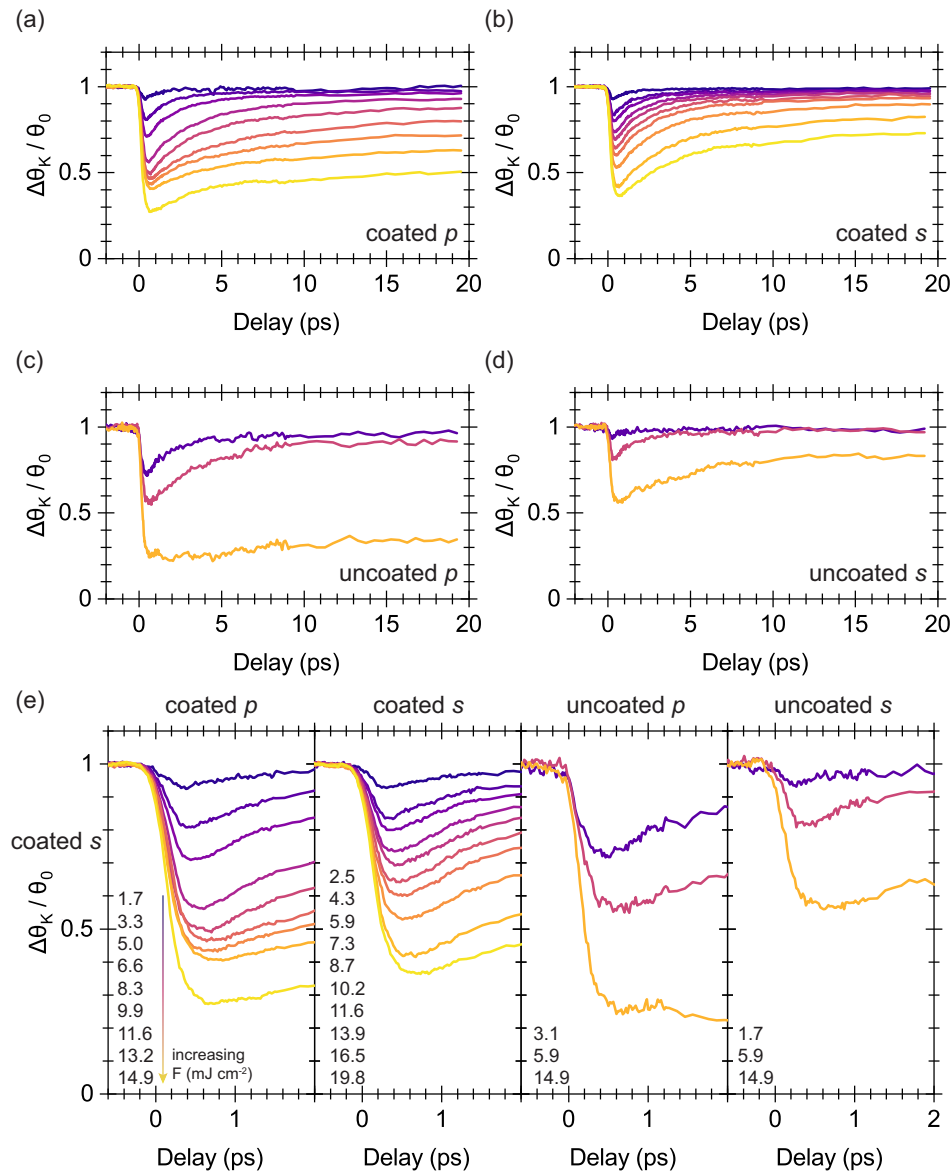


Figure 6.6 –  $\frac{\Delta\theta_K}{\theta_0}(t)$  curves of (a) sample s5 (coated) for a  $p$ -polarised and a (b)  $s$ -polarised pump, of (c) sample t2 (uncoated) for a  $p$ -polarised and a (d)  $s$ -polarised pump. Demagnetisation curves were measured by a pump-probe magneto-optical Kerr effect set-up for different fluences  $F$ . (e) Close-up from  $-0.6$  ps to 2 ps.  $t = 0$  ps corresponds to the coincidence of the pump pulse and the probe pulse.

— At first glance, no difference in demagnetisation process is observed in samples  $s5$  and  $t2$ .

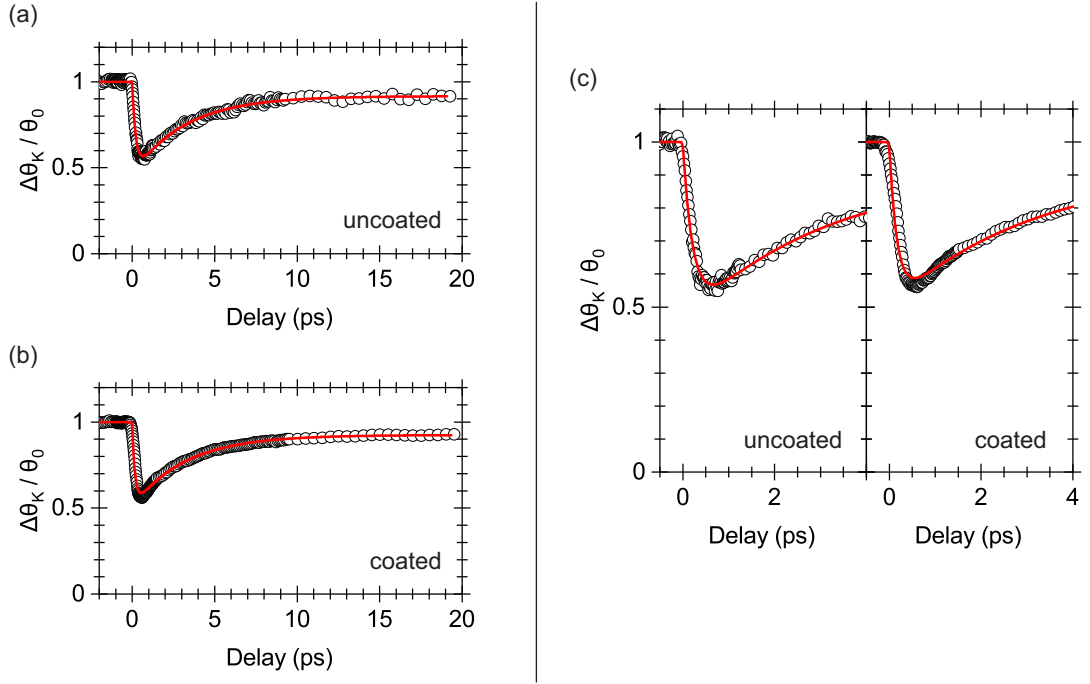


Figure 6.7 –  $\frac{\Delta\theta_K}{\theta_0}(t)$  demagnetisation curves of (a) samples  $t2$  and (b)  $s5$  for  $p$ -polarised pump pulses and an incident fluence of  $F = 5.9 \text{ mJ cm}^{-2}$ . (c) Close-up from  $-0.5 \text{ ps}$  to  $4 \text{ ps}$ . Experimental data (scatter) were fitted using Eq. 6.1 (line).

A more quantitative insight of magnetisation dynamics could be obtained by fitting the data. The fit function presented in this thesis is phenomenological and is composed of two terms. The first term is a bi-exponential function, in which the two exponentials denote the demagnetisation and remagnetisation processes. The bi-exponential function is convoluted by a second term, which is a gaussian function, to account for the time resolution of the experiment. This fit function is expressed as [145, 146]

$$\frac{\Delta\theta_K}{\theta_0}(t) = G(\sigma, t) * \left\{ 1 - A \left( 1 - e^{-t/\tau_{\text{demag}}} \right) \left( a + (1 - a) e^{-t/\tau_{\text{relax}}} \right) H(t) \right\} \quad (6.1)$$

where  $G(\sigma, t)$  is the gaussian function and  $H(t)$  is the Heaviside step function.  $A$  and  $a$  are phenomenological constants related to the magnetisation drop and recovery, respectively.  $\tau_{\text{demag}}$  is the demagnetisation time constant and  $\tau_{\text{relax}}$  is the relaxation time constant. Parameter  $\sigma$  is linked to the width of the laser pulse. The full width at half maximum of the pulse at the output of the laser is  $\text{FWHM} = 35 \text{ fs}$ , corresponding to a standard deviation of  $\sigma_{\text{out}} = \frac{\text{FWHM}}{2\sqrt{2\ln 2}} = 15 \text{ fs}$ . The width of the pulse is caused by the temporal resolution of the laser, as well as a convolution of the probe and pump pulses. The standard deviation is thus given from the definition of the

convolution of two gaussian functions and reads  $\sigma = \sqrt{\sigma_{\text{probe}}^2 + \sigma_{\text{pump}}^2}$ . A standard deviation of  $\sigma = 21$  fs is found if  $\sigma_{\text{probe}} = \sigma_{\text{pump}}$  is assumed.

Examples of curve fit are shown in Fig. 6.7. Experimental curves are plotted as scatters, and the fit result as a line. The fit matches experimental data of sample *t2*. On the other hand, it is less reliable for sample *s5*. The initial demagnetisation modelled by the fit function is faster than the measured one, and its amplitude is too low. The fit function cannot furthermore model the curve break at  $t = 1.5$  ps, measured in sample *s5*. This could point to more complex magnetisation dynamics. A more refined fit function should be built by adding additional terms to consider these complicated magnetisation dynamics. Though a solution to fit the data has not been found, a qualitative description of the demagnetisation curves is still possible and could provide information on the time evolution of magnetisation.

### 6.3.2.2 Initial demagnetisation

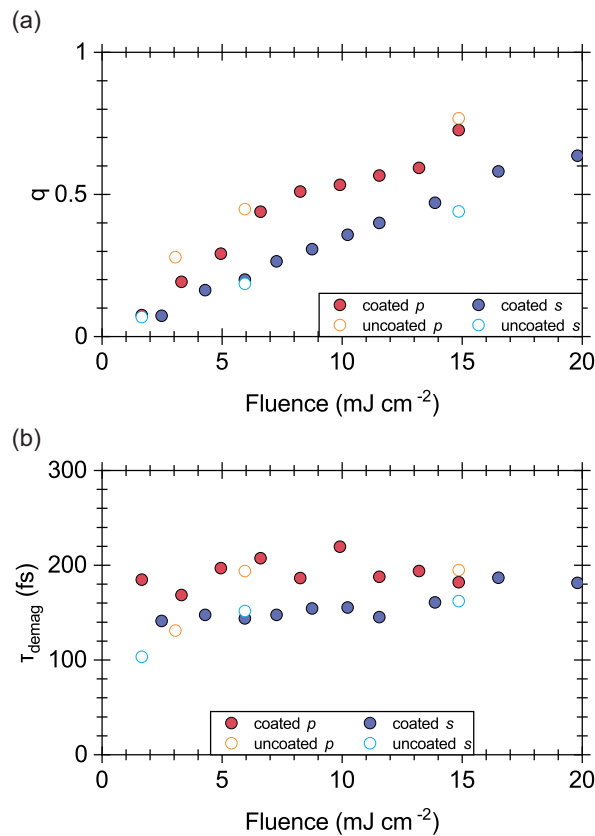


Figure 6.8 – (a) Demagnetisation amplitude  $q$  and (b) demagnetisation time constant  $\tau_{\text{demag}}$  as a function of the pump fluence  $F$ , read on Fig. 6.6.

Characteristic quantities related to sub-picosecond demagnetisation can be derived from Fig. 6.6. These quantities are the demagnetisation amplitude  $q$  and the demagnetisation time

constant  $\tau_{\text{demag}}$ .  $q$  is directly read from the curves.  $\tau_{\text{demag}}$  is deduced by measuring the delay at a magnetisation drop of  $1 - 1/e$  (or  $\approx 63.2\%$ ), as per the definition of an exponential decay.

$q$  and  $\tau_{\text{demag}}$  are presented as a function of  $F$  in Fig. 6.8. As seen in Fig. 6.8(a), demagnetisation amplitude  $q$  depends linearly on the pump fluence  $F$ .  $q$  increases as  $F$  is higher. For a given fluence, demagnetisation amplitude is furthermore larger for the  $p$ -polarised than the  $s$ -polarised pump. Besides, no difference in the magnetisation drop  $q$  in samples  $t2$  and  $s5$ . Fig. 6.8(b) shows the  $1 - 1/e$  demagnetisation time constant  $\tau_{\text{demag}}$  as a function of  $F$ .  $\tau_{\text{demag}}$  does not depend on the fluence, whether the pump is  $p$  or  $s$ -polarised. Mean demagnetisation time constant values of  $\langle \tau_{\text{demag}} \rangle = 190 \pm 20$  fs and  $\langle \tau_{\text{demag}} \rangle = 160 \pm 20$  fs are measured for a  $p$  and a  $s$ -polarised pump respectively.

A larger magnetisation quench  $q$  is measured for a  $p$ -polarised pump, indicating that the system absorbs more energy from  $p$ -polarised light. An explanation for this larger energy absorption could lie in the optical absorption in CoNi NWs. As previously seen in Fig. 6.4, absorption in CoNi NWs is larger for  $p$ -polarised light. At  $\lambda = 800$  nm and for an angle of incidence of  $\theta = 60^\circ$ , CoNi NWs absorb approximately four times more  $p$ -polarised light than  $s$ -polarised light. Demagnetisation experiments were conducted at an incidence angle of  $45^\circ$ , and simulations at  $\theta = 45^\circ$  should thus be conducted to quantify the absorption in CoNi NWs and possibly understand the difference in demagnetisation amplitude between the measurements using a  $p$  and a  $s$ -polarised pump.

Magnetisation quench is similar in samples  $t2$  and  $s5$  for the same fluences. Due to the size of the dataset of sample  $t2$ , a direct comparison between coated and uncoated samples would however be unreliable. Xu et al. experimentally measured and simulated the demagnetisation amplitude  $q$  in Py thin films coated by Au nanorods [37]. A linear dependence of  $q$  to the pump fluence was measured in uncoated magnetic thin films. This linear dependence was not found in coated Py film. It is divergent and the demagnetisation amplitude is much more amplified at higher fluences due to the plasmonic resonance.  $q$  dependence to the fluence  $F$  is linear in Au-CoNi-SrTiO<sub>3</sub> nanocomposite thin films. The demagnetisation amplitude in hybrid nanocomposites and in uncoated nanocomposites could be similar. Au NWs in sample  $s5$  thus could have no influence on the magnetisation drop.

Concerning demagnetisation time constant  $\tau_{\text{demag}}$ , experimental values of  $\tau_{\text{demag}} = 260$  fs were reported for Co thin films [147], and  $\tau_{\text{demag}} = 160$  fs and  $130$  fs for Ni thin films [147, 148].  $\tau_{\text{demag}}$  scales with the elemental magnetic moment and with the sign of the exchange interaction. A work by Radu and co-workers in magnetic thin films showed that  $\tau_{\text{demag}}$  is proportional to the magnetic moment per atom  $\mu$  by a factor of  $90 \pm 20$  fs  $\mu_B^{-1}$  [149]. This factor is purely experimental, and could be reliable for thin films only. Thus,  $\tau_{\text{demag}}$  values deduced from this factor must be interpreted with caution. Orbital and spin magnetic moments,  $m_l$  and  $m_s$ , of bulk Co and Ni tabulated in the literature are  $m_l^{\text{Co}} = 0.16 \mu_B$ ,  $m_s^{\text{Co}} = 1.6 \mu_B$ ,  $m_l^{\text{Ni}} = 0.058 \mu_B$  and  $m_s^{\text{Ni}} = 0.58 \mu_B$  [150, 151]. If one assumes that the magnetic moment per atom of the Co <sub>$x$</sub> Ni <sub>$1-x$</sub>  is a linear combination, that is  $\mu = xm^{\text{Co}} + (1-x)m^{\text{Ni}}$  with  $m = m_l + m_s$ ,

then the magnetic moment per atom of  $\text{Co}_{0.8}\text{Ni}_{0.2}$  is  $\mu = 1.54 \mu_B$ . Weng and co-workers studied the magnetic moment per atom by x-ray circular dichroism in  $\text{Co}_{0.8}\text{Ni}_{0.2}$  NWs and measured a value of  $\mu = 1.45 \mu_B$  [96]. The magnetic moment per atom deduced from tabulated bulk values gives a demagnetisation time in the order of  $\tau_{\text{demag}} = 138 \pm 20$  fs. A value in the order of  $\tau_{\text{demag}} = 131 \pm 20$  fs is calculated from experimental  $\mu$  values.  $\tau_{\text{demag}}$  values in Au-CoNi-SrTiO<sub>3</sub> nanocomposite thin films ( $\langle \tau_{\text{demag}} \rangle = 190 \pm 20$  fs and  $\langle \tau_{\text{demag}} \rangle = 160 \pm 20$  fs) are of the same order as those reported in thin films. They are also of the same order as the values calculated using the factor from Ref. [149]. Initial demagnetisation in nanocomposites and magnetic thin films thus could be similar.

### 6.3.2.3 Remagnetisation

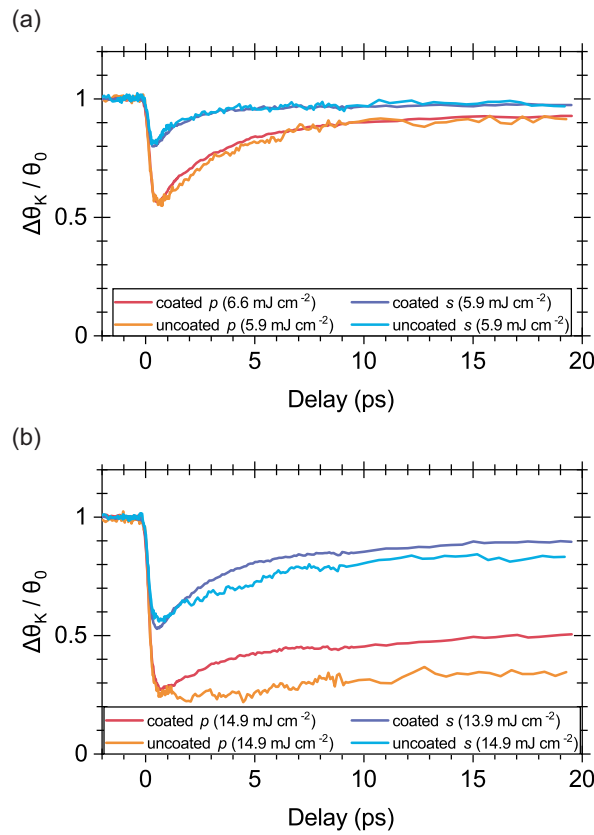


Figure 6.9 –  $\frac{\Delta\theta_K}{\theta_0}(t)$  curves of samples *s5* (coated) and *t2* (uncoated) for a *p* and a *s*-polarised pump, at (a) low and (b) high fluences.  $t = 0$  ps corresponds to the coincidence of the pump pulse and the probe pulse.

Fig. 6.9 shows the demagnetisation curves of samples *t2* and *s5* for similar pump fluences. Magnetisation recovery is slower for a *p*-polarised pump in both samples. For low fluences and a *p*-polarised pump, remagnetisation is similar in coated and uncoated samples. This same

situation is observed in the *s*-polarised measurements. A striking difference in remagnetisation is observed for high fluences. For the same pump polarisation, one notices that the curves of samples *t2* and *s5* split after  $\approx 1.5$  ps, and that two distinct remagnetisation processes are measured. For a *p*-polarised pump, magnetisation recovers by 34 % at  $t = 20$  ps in sample *s5*. On the other hand, magnetisation recovery in sample *t2* is limited, being of 15 % at  $t = 20$  ps. A lesser effect is observed for *s*-polarised measurements, with magnetisation recoveries at  $t = 20$  ps of 78 % and 62 % in coated and uncoated samples, respectively.

A slower magnetisation recovery is measured for a *p*-polarised pump. A system takes more time to reach equilibrium if more energy is absorbed. This situation is thus consistent with the fact that the thin films absorb more energy from *p*-polarised pulses. For low fluences, the remagnetisation process is similar in samples *t2* and *s5*. A clear difference is however measured for high fluences, where magnetisation recovers faster in sample *s5* than in sample *t2*. As discussed previously, magnetisation quench in samples *t2* and *s5* is similar for the same fluences. A comparable quantity of energy is thus absorbed by samples *t2* and *s5*. A faster remagnetisation in sample *s5* cannot therefore be interpreted as a larger quantity of absorbed energy. One explanation could be related to energy dissipation, as the Au-CoNi interface in sample *s5* could provide an additional channel of energy dissipation. Au NWs could thus play a role in dissipating the energy of Co<sub>0.8</sub>Ni<sub>0.2</sub> NWs. Interestingly, the difference in remagnetisation time is furthermore more significative as the fluence is high.

## 6.4 Conclusion

This chapter reported the preliminary study of magneto-optical properties in nanocomposite thin film samples. Two samples were extensively studied to provide an insight into the effects of Au NWs on the magnetisation dynamics of ferromagnetic nanocomposites. Optical properties simulated by finite-difference time-domain method of nanocomposite thin films were reported. Simulated ohmic loss in Au NWs of a hybrid Au-CoNi-SrTiO<sub>3</sub> nanocomposite thin film was presented. Two absorption bands were predicted in visible and near-infrared wavelengths and are related to the transverse and longitudinal modes of the plasmonic resonance. Absorption was then studied in CoNi NWs. No plasmon-induced increase of absorption in CoNi NWs was found when the incident light is *s*-polarised. On the other hand, *p*-polarised ohmic loss in CoNi NWs showed an increase by  $\approx 5$  % at  $\approx 800$  nm in the case of hybrid nanocomposites. Thus, finite-difference time-domain method simulations predict an increase of absorption in hybrid nanocomposites, though negligible.

$M(H)$  curves were measured by static magneto-optical Kerr effect in samples *t2* and *s5*. The samples are in the blocked state at room temperature, with a coercive field  $H_c$  of 0.16 T and 0.08 T for samples *t2* and *s5* respectively. Besides,  $M(H)$  curves proved the recovery of a magneto-optical Kerr signal. Magnetisation dynamics were measured by TRMOKE in samples *t2* and *s5*. Magnetisation drops in less than 0.5 ps after pump-probe coincidence and then

recovers partially. Magnetisation quench  $q$  is proportional to the pump fluence and larger for a  $p$ -polarised pump, possibly due to a larger optical absorption.  $q$  values in samples  $t2$  and  $s5$  are comparable for similar fluences. Demagnetisation time constant  $\tau_{\text{demag}}$  was not affected by the pump fluence.  $\langle\tau_{\text{demag}}\rangle$  values of  $190 \pm 20$  fs and  $160 \pm 20$  fs were measured for a  $p$ -polarised and a  $s$ -polarised pump respectively in sample  $s5$ .  $\langle\tau_{\text{demag}}\rangle$  values presented in this work are comparable to values reported in the literature for Co and Ni thin films. Thus, initial demagnetisation could be identical in thin films and nanocomposites. A striking difference was seen in the remagnetisation of samples  $s5$  and  $t2$ . The system could relax to equilibrium faster in coated samples. An interpretation could be that the Au-CoNi interface helps the dissipation of energy. This effect is furthermore more pronounced for high fluences.



## CONCLUSION

7.1 Conclusion . . . . .	117
7.2 Perspectives . . . . .	120

## 7.1 Conclusion

This thesis reports the growth and the experimental study of hybrid nanocomposite thin films. The intention was to study a relatively new class of nanostructures, vertically aligned nanocomposites. Novel magneto-optical effects have been reported in hybrid systems [33–39]. Hybrid vertically aligned nanocomposites thus could provide a promising line of research for magneto-optical studies, due to the possibility of tuning magnetic and optical properties through structure.

Au-SrTiO<sub>3</sub> NWs were grown by sequential pulsed laser deposition. The effect of the growth temperature on crystal quality was studied. Samples were thus deposited at different temperatures. High-resolution transmission electron microscopy proved the self-assembly of Au NWs in SrTiO<sub>3</sub> matrix on SrTiO<sub>3</sub> substrate. A mean diameter of the Au NWs of  $\approx 7$  nm was measured in electron microscopy images. Epitaxy was studied by x-ray diffraction, which showed that Au NWs are less polycrystalline at 550 °C, than at 650 °C. SrTiO<sub>3</sub> matrix crystal order is however higher at 650 °C. A preferential cube-on-cube epitaxy between Au and SrTiO<sub>3</sub> is measured in the thin film grown at an intermediate temperature of 600 °C. Optical properties of Au-SrTiO<sub>3</sub> nanocomposite thin films were studied by Gans theory, transmission spectroscopy and ellipsometry. Gans theory predicts two absorption bands, in the visible and the near-infrared wavelengths, related to the transverse and longitudinal modes of the plasmonic resonance, respectively. Au-SrTiO<sub>3</sub> nanocomposite thin films were measured by transmission spectroscopy and ellipsometry, proving that Au NWs sustain plasmonic resonances.

Au-Co<sub>0.8</sub>Ni<sub>0.2</sub>-SrTiO<sub>3</sub> nanocomposite thin films were deposited by two-step sequential pulsed laser deposition. Growth of hybrid nanocomposite thin films was proved by HRTEM. A mean diameter of the hybrid nanocomposites of  $\approx 3$  nm was measured. HAADF-STEM and EDXS proved phase separation of Au and Co<sub>0.8</sub>Ni<sub>0.2</sub> in hybrid nanocomposites. Au shows a preferential nucleation at the top of the CoNi NWs, as 80 % of them are coated. Reciprocal space mappings of hybrid nanocomposite thin films were measured at the SixS beamline of synchrotron SOLEIL, allowing the study of epitaxy in hybrid samples. Au NWs have an in plane texture, and CoNi NWs have a cube-on-cube structure with the SrTiO<sub>3</sub> matrix. Out of plane mappings show that the Co<sub>0.8</sub>Ni<sub>0.2</sub> peak is shifted from the bulk value, pointing

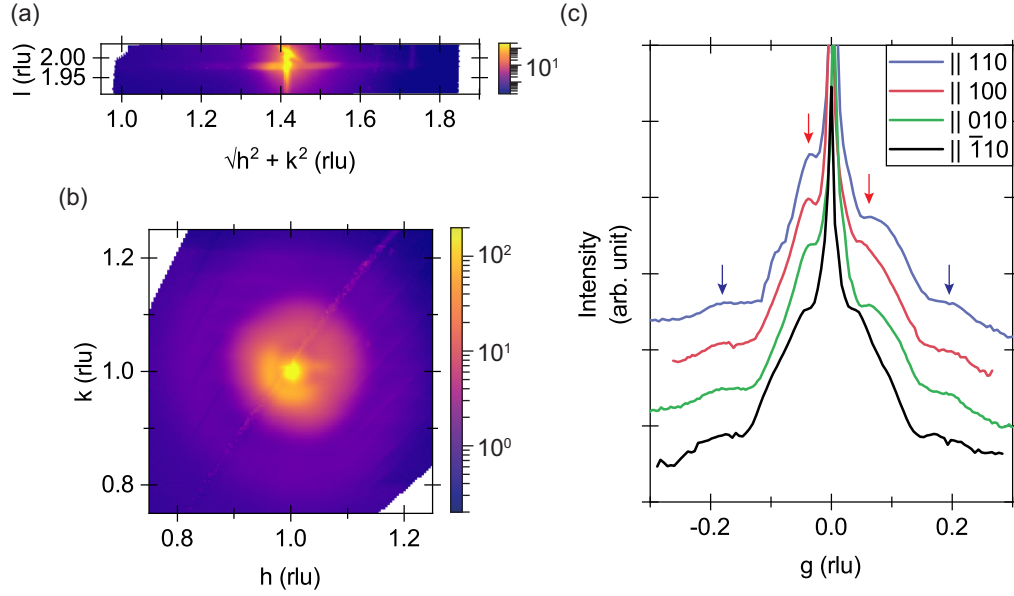


Figure 7.1 – Reciprocal space mappings and profiles of the 112 SrTiO<sub>3</sub> spot of sample *s6*. (a) Out of plane and (b) in plane reciprocal space mappings. (c) In plane profiles in the [110] (blue), [100] (red), [010] (green) and  $\bar{1}10$  (black) directions (log<sub>10</sub> scale). The first and second scattering rings are marked by a red and a blue arrow, respectively.

to an axial strain  $\epsilon_{zz}$  of 5% in CoNi NWs, caused by the epitaxy induced by the matrix. Off-Bragg scattering was measured in hybrid nanocomposite thin films by grazing incidence x-ray diffraction. As seen in Fig. 7.1, two scattering rings are observed around the matrix Bragg reflection. At Bragg condition of the host matrix, nanowires appear as holes for the incident x-ray, thus they can be modelled by a form factor. Information were extracted from the calculation of the form factor, such as the interdistance  $D$ , its variance  $\sigma$  and the diameter  $d$  of the nanowires. These values are consistent with HRTEM.

Magnetic properties were studied by VSM. An anisotropic magnetic response was measured, with an easy axis of magnetisation along the nanowires. A huge typical coercive field  $\mu_0 H_c$  of  $\approx 1$  T at 10 K was reported at 10 K. Coercive field at 0 K  $\mu_0 H_c$ , and blocking temperature  $T_b$  were extracted from  $\mu_0 H_c(T)$  curves by a fit using Sharrock's thermal reduction law.  $T_b$  values range from 203 K to 352 K. Activation lengths  $l^*$  were deduced from  $T_b$  values and compared to the Bloch domain wall widths  $\delta$ . Reversal initiates with the nucleation of a Bloch domain wall, as  $l^* \approx \delta$ . After nucleation, it then proceeds by propagation of the domain wall through the nanowire. Reversal is thus inhomogeneous and localised.  $\mu_0 H_c$  values were systematically higher than the magnetostatic anisotropy field  $\mu_0 H_a^{\text{ms}}$ , which indicates that another source of anisotropy is contributing positively to the magnetic anisotropy, that is the magnetoelastic anisotropy. The huge axial strain  $\epsilon_{zz} \approx 5\%$  deduced from reciprocal space mappings should be related to the anisotropy enhancement. As seen in Fig. 7.2, magnetoelastic anisotropy is a

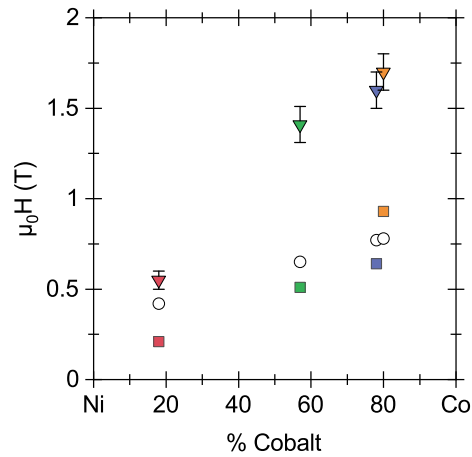


Figure 7.2 – Comparison between the out of plane coercive field  $\mu_0 H_c^{(0)}$  (squares), the in plane saturation field  $\mu_0 H_s^{IP}$  (triangles) and the magnetostatic anisotropy field  $\mu_0 H_a^{ms}$  (circles) in function of the content of Co (reproduced from [96]).

predominant source of anisotropy in  $\text{Co}_{0.8}\text{Ni}_{0.2}$  NWs for Co contents above 80 %. Experimental in plane saturation field  $\mu_0 H_s^{IP}$  was however found to be much lower than the anisotropy field  $\mu_0 H_a^{ms+me}$  due to possible local anisotropy inhomogeneity. A micromagnetic model was used to compute the inhomogeneity. An inhomogeneity ranging from 81 % to 90 % of the value of  $K_{me}$  was found. The perturbation could be related to a strain inhomogeneity in the nanowires, caused by defects. As reported in Ref. [60], a rotation of the (111) planes was found in highly strained  $\text{Co}_x\text{Ni}_{1-x}$  NWs, creating stacking faults. Therefore, this rotation mechanism could explain the anisotropy inhomogeneity, and thus localisation of the reversal and loss of coercive field.

A preliminary study of magneto-optical properties of nanocomposite thin films was reported. Optical properties were simulated by finite-difference time-domain method. Simulated ohmic loss of Au NWs in hybrid nanocomposite thin films showed two absorption bands, caused by plasmonic resonances. Optical absorption of  $\text{Co}_{0.8}\text{Ni}_{0.2}$  NWs was then simulated. An increase of absorption in coated  $\text{Co}_{0.8}\text{Ni}_{0.2}$  NWs of  $\approx 5\%$  at  $\approx 800$  nm is predicted for  $p$ -polarised light. Magnetisation dynamics were measured by pump-probe time-resolved magneto-optical Kerr effect at *Laboratoire d'optique appliquée*. Sub-picosecond demagnetisation and magnetisation recovery is observed in nanocomposite thin films. Demagnetisation amplitude  $q$  depends linearly to the pump fluence, and is larger for a  $p$ -polarised pump, possibly because of an increased optical absorption.  $q$  is comparable in coated and uncoated samples.  $\langle \tau_{\text{demag}} \rangle$  values of  $190 \pm 20$  fs and  $160 \pm 20$  fs were measured for a  $p$ -polarised and a  $s$ -polarised pump respectively in the coated sample. Values of the same order are reported in the literature for Co and Ni thin films. Therefore, initial demagnetisation could be identical in thin films and nanocomposites. Remagnetisation processes in coated and uncoated samples are however very

different. Magnetisation recovery is faster in the coated sample, possibly due to an additional energy dissipation channel caused by the Au-CoNi interface.

## 7.2 Perspectives

Magnetisation quench was reported to be comparable in hybrid nanocomposites and CoNi NWs. Au NWs could thus have a negligible role in the demagnetisation of hybrid nanocomposites presented in this thesis. As it turns out, a work by Ikemiya et al. in Ag-Co nanocomposites reports that magnetisation quench is larger as the Ag content increases, thus as the absorption increases due to a stronger plasmonic resonance [38]. An amplification of demagnetisation in hybrid nanocomposites is therefore possible. On the other, simulation shows that absorption increase is negligible in hybrid nanocomposites presented in this work. An effect of Au NWs in hybrid nanocomposite thin films could be observed if the plasmonic resonance was stronger. One way is to grow larger Au NWs, to sustain stronger plasmonic resonances. Absorption cross section, a quantity related to the plasmonic resonance, indeed scales as the volume of the particle. Consequently, larger Au NWs would absorb more energy that could be injected in the magnetic system and thus increase the magnetisation quench.

This thesis proves the possibility to measure ultrafast demagnetisation in nanocomposites with good signal-to-noise ratio. This preliminary report of magnetisation dynamics in Au-Co<sub>0.8</sub>Ni<sub>0.2</sub>-SrTiO<sub>3</sub> thin films paves the way for further ultrafast demagnetisation studies. For example, the effect of diameter, length, or more broadly the size of the nanocomposites on demagnetisation and remagnetisation processes could be investigated.

Demagnetisation by a spin-flip scattering mechanism induces a transfer of angular momentum from the spins to the lattice. This ultrafast Einstein-de Haas effect was reported by Dornes et al. in Fe thin films [152]. The experiment was carried out by time-resolved x-ray diffraction. After pumping the sample, they were able to measure transverse strain waves related to demagnetisation. Concerning nanowires, the ultrafast Einstein-de Haas effect may involve different transient transverse vibrational modes, depending on the direction of the initial magnetisation (i.e. if  $\vec{M}$  is parallel or perpendicular to the long axis). Then, it would be interesting to investigate demagnetisation of in plane magnetised vertically aligned nanocomposites, and check whether the out of plane-in plane asymmetry has an influence on the timescale and the amplitude of the magnetisation quenching.

Regarding the study of hybrid Au-CoNi NWs, the work by Bergeard and co-workers should be cited. This work focuses on sub-picosecond demagnetisation induced by noble Cu films. They studied the magnetisation dynamics of Cu/(Co/Pt) multilayer films using a back-probe set-up [153]. The thickness of the Cu film varied from 0 nm to 300 nm. Demagnetisation was measured for Cu thicknesses as large as 300 nm. Photons cannot penetrate the Cu film that deep and directly interact with the Co/Pt multilayer film. Bergeard et al. furthermore observed a time delay in the initial demagnetisation induced by the Cu film. This induced

delay is proportional to the Cu film thickness. This experiment shows that indirect laser-induced demagnetisation is possible thanks to hot electron injection by the Cu film. Thus, an interesting perspective would be to study hybrid nanocomposite thin films by back-probe set-up. Here, similarly to Cu film, Au NWs could generate and transport hot electrons. In turn, these hot electrons would be injected in the  $\text{Co}_{0.8}\text{Ni}_{0.2}$  NWs, causing loss of magnetisation. Thus, such demagnetisation would rely on indirect laser excitation. Is indirect laser-induced demagnetisation possible in Au- $\text{Co}_{0.8}\text{Ni}_{0.2}$ - $\text{SrTiO}_3$  thin film?

As discussed in the previous paragraph, exciting studies on electron injection could be carried out. The work of Bergeard et al. shows that the magnetisation of a material can be quenched by injection of hot electrons generated and transported by a noble metal film. A converse experiment could be designed. The magnetic material could be pumped and the noble metal film probed. Melnikov and co-workers studied Au/Fe/MgO thin films by second harmonic generation [154]. The sample was pumped by the back, exciting hot electrons in the Fe thin film, and probed by the front. Thanks to this set-up, Melnikov et al. detected a spin current of spin-polarised hot electrons at the surface of the Au film. A direct observation by spin-resolved photoelectron spectroscopy of spin polarisation by spin injection was reported by Bühlmann and co-workers [155]. Au/Fe/MgO thin films, of Au thickness ranging from 5 nm to 20 nm, were studied by pumping the back and probing the Au film, in the same spirit as the work of Melnikov and co-workers. A injection of spin current, caused by demagnetisation of the Fe film, was detected in the Au film. Bühlmann et al. furthermore measured an increase of spin polarisation in less than 200 fs. One could imagine similar experiments in hybrid nanocomposite thin films. By demagnetising  $\text{Co}_{0.8}\text{Ni}_{0.2}$  NWs, would it be possible to detect spin polarisation in Au NWs by time-resolved magneto-optical Kerr effect?

An exciting perspective, though rather far-off, would be the study of magnetisation dynamics in ferrimagnetic nanowires. Stanciu et al. reported all-optical switching in a ferrimagnetic GdFeCo thin film [32]. By inverse Faraday effect, they were able to switch magnetic order by a circularly polarised pulsed laser. This switching was furthermore related to the helicity of the circularly polarised pulse. All-optical magnetic switching in nanocomposite thin films would besides lead to tremendous applications in magnetic recording. Magnetic switching in nanocomposites has not been reported in the literature yet, and as a matter of fact would need intensive research. Consequently, growth of ferrimagnetic nanocomposites must be studied first, which means that sensible material choices and suitable conditions of deposition must be found.



## BIBLIOGRAPHY

- [1] E. A. Dobisz, Z. Z. Bandic, T.-W. Wu and T. Albrecht. « Patterned Media: Nanofabrication Challenges of Future Disk Drives ». In: *Proc. of the IEEE* 96.11 (2008), pp. 1836–1846. doi: 10.1109/JPROC.2008.2007600.
- [2] A. Moser, K. Takano, D. T. Margulies, M. Albrecht, Y. Sonobe, Y. Ikeda, S. Sun and E. E. Fullerton. « Magnetic recording: advancing into the future ». In: *J. Phys. D: Appl. Phys.* 19.35 (2002), R157–R167. doi: 10.1088/0022-3727/35/19/201.
- [3] G. Albuquerque, S. Hernandez, M. T. Kief, D. Mauri and L. Wang. « HDD Reader Technology Roadmap to an Areal Density of 4 Tbps and Beyond ». In: *IEEE Trans. Magn.* 58.2 (2022), pp. 1–10. doi: 10.1109/TMAG.2021.3081042.
- [4] S. Granz, J. Jury, C. Rea, G. Ju, J.-U. Thiele, T. Rausch and E. C. Gage. « Areal Density Comparison Between Conventional, Shingled, and Interlaced Heat-Assisted Magnetic Recording with Multiple Sensor Magnetic Recording ». In: *IEEE Trans. Magn.* 55.3 (2019), pp. 1–3. doi: 10.1109/TMAG.2018.2869046.
- [5] G. Scheunert, O. Heinonen, R. Hardeman, A. Lapicki, M. Gubbins and R. M. Bowman. « A review of high magnetic moment thin films for microscale and nanotechnology applications ». In: *Appl. Phys. Rev.* 3.1 (2016), p. 011301. doi: 10.1063/1.4941311.
- [6] H. J. Richter. « Recent advances in the recording physics of thin-film media ». In: *J. Phys. D: Appl. Phys.* 32.21 (1999), R147–R168. doi: 10.1088/0022-3727/32/21/201.
- [7] R. Wood. « Current Perspectives: Perpendicular Recording ». In: *J. Magn. Magn. Mater.* 321.6 (2009), pp. 555–561. doi: 10.1016/j.jmmm.2008.07.027.
- [8] H. J. Richter. « The transition from longitudinal to perpendicular recording ». In: *J. Phys. D: Appl. Phys.* 40.9 (2007), R149–R177. doi: 10.1088/0022-3727/40/9/r01.
- [9] D. Weller and A. Moser. « Thermal effect limits in ultrahigh-density magnetic recording ». In: *IEEE Trans. Magn.* 35.6 (1999), pp. 4423–4439. doi: 10.1109/20.809134.
- [10] W. A. Challener, C. Peng, A. V. Itagi, D. Karns, W. Peng, Y. Peng, X. Yang, X. Zhu, N. J. Gokemeijer, Y.-T. Hsia, G. Ju, R. E. Rottmayer, M. A. Seigler and E. C. Gage. « Heat-assisted magnetic recording by a near-field transducer with efficient optical energy transfer ». In: *Nat. Photonics* 3 (4 2009), pp. 220–224. doi: 10.1038/nphoton.2009.26.
- [11] M. H. Kryder, E. C. Gage, T. W. McDaniel, W. A. Challener, R. E. Rottmayer, G. Ju, Y.-T. Hsia and M. F. Erden. « Heat Assisted Magnetic Recording ». In: *Proc. IEEE* 96.11 (2008), pp. 1810–1835. doi: 10.1109/JPROC.2008.2004315.

- [12] N. Zhou, X. Xu, A. T. Hammack, B. C. Stipe, K. Gao, W. Scholz and E. C. Gage. « Plasmonic near-field transducer for heat-assisted magnetic recording ». In: *Nanophotonics* 3.3 (2014), pp. 141–155. doi: 10.1515/nanoph-2014-0001.
- [13] E. Beaurepaire, J.-C. Merle, A. Daunois and J.-Y. Bigot. « Ultrafast Spin Dynamics in Ferromagnetic Nickel ». In: *Phys. Rev. Lett.* 76 (22 1996), pp. 4250–4253. doi: 10.1515/nanoph-2014-0001.
- [14] J. Stöhr and H. C. Siegmann. *Magnetism: From Fundamentals to Nanoscale Dynamics*. Springer, 2006.
- [15] T. Kampfrath, R. G. Ulbrich, F. Leuenberger, M. Münzenberg, B. Sass and W. Felsch. « Ultrafast magneto-optical response of iron thin films ». In: *Phys. Rev. B* 65 (10 2002), p. 104429. doi: 10.1103/PhysRevB.65.104429.
- [16] A. Comin, M. Rossi, C. Mozzati, F. Parmigiani and G. P. Banfi. « Femtosecond dynamics of Co thin films on Si support ». In: *Solid State Commun.* 129.4 (2004), pp. 227–231. doi: 10.1016/j.ssc.2003.10.012.
- [17] E. Beaurepaire, M. Maret, V. Halté, J.-C. Merle, A. Daunois and J.-Y. Bigot. « Spin dynamics in CoPt<sub>3</sub> alloy films: A magnetic phase transition in the femtosecond time scale ». In: *Phys. Rev. B* 58 (18 1998), pp. 12134–12137. doi: 10.1103/PhysRevB.58.12134.
- [18] H.-S. Rhie, H. A. Dürr and W. Eberhardt. « Femtosecond Electron and Spin Dynamics in Ni/W(110) Films ». In: *Phys. Rev. Lett.* 90 (24 2003), p. 247201. doi: 10.1103/PhysRevLett.90.247201.
- [19] M. Cinchetti, M. Sánchez Albaneda, D. Hoffmann, T. Roth, J.-P. Wüstenberg, M. Krauß, O. Andreyev, H. C. Schneider, M. Bauer and M. Aeschlimann. « Spin-Flip Processes and Ultrafast Magnetization Dynamics in Co: Unifying the Microscopic and Macroscopic View of Femtosecond Magnetism ». In: *Phys. Rev. Lett.* 97 (17 2006), p. 177201. doi: 10.1103/PhysRevLett.97.177201.
- [20] A. Melnikov, H. Prima-Garcia, M. Lisowski, T. Gießel, R. Weber, R. Schmidt, C. Gahl, N. M. Bulgakova, U. Bovensiepen and M. Weinelt. « Nonequilibrium Magnetization Dynamics of Gadolinium Studied by Magnetic Linear Dichroism in Time-Resolved 4f Core-Level Photoemission ». In: *Phys. Rev. Lett.* 100 (10 2006), p. 107202. doi: 10.1103/PhysRevLett.100.107202.
- [21] C. Stamm, T. Kachel, N. Pontius, R. Mitzner, T. Quast, K. Holldack, S. Khan, C. Lupulescu, E. F. Aziz, M. Wietstruk, H. A. Dürr and W. Eberhardt. « Femtosecond modification of electron localization and transfer of angular momentum in nickel ». In: *Nature Mater.* 6 (10 2007), pp. 740–743. doi: 10.1038/nmat1985.

- [22] P. W. Granitzka, E. Jal, L. Le Guyader, M. Savoini, D. J. Higley, T. Liu, Z. Chen, T. Chase, H. Ohldag, G. L. Dakovski, W. F. Schlotter, S. Carron, M. C. Hoffman, A. X. Gray, P. Shafer, E. Arenholz, O. Hellwig, V. Mehta, Y. K. Takahashi, J. Wang, E. E. Fullerton, J. Stöhr, A. H. Reid and H. A. Dürr. « Magnetic Switching in Granular FePt Layers Promoted by Near-Field Laser Enhancement ». In: *Nano Lett.* 17 (4 2017), pp. 2426–2432. doi: 10.1021/acs.nanolett.7b00052.
- [23] B. Koopmans. « Time-resolved Kerr-effect and Spin Dynamics in Itinerant Ferromagnets ». In: *Handbook of Magnetism and Advanced Magnetic Materials*. Wiley, 2007.
- [24] I. Razdolski, A. Alekhin, U. Martens, D. Bürstel, D. Diesing, M. Münzenberg, U. Bovensiepen and A. Melnikov. « Analysis of the time-resolved magneto-optical Kerr effect for ultrafast magnetization dynamics in ferromagnetic thin films ». In: *J. Phys. Condens. Matter* 29.17 (2017), p. 174002. doi: 10.1088/1361-648x/aa63c6.
- [25] J. Hohlfeld, S.-S. Wellershoff, J. Güdde, U. Conrad, V. Jähnke and E. Matthias. « Electron and lattice dynamics following optical excitation of metals ». In: *Chem. Phys.* 251.1 (2000), pp. 237–258. doi: 10.1016/S0301-0104(99)00330-4.
- [26] B. Koopmans, J. J. M. Ruigrok, F. Dalla Longa and W. J. M. de Jonge. « Unifying Ultrafast Magnetization Dynamics ». In: *Phys. Rev. Lett.* 95 (26 2005), p. 267207. doi: 10.1103/PhysRevLett.95.267207.
- [27] M. Battiato, K. Carva and P. M. Oppeneer. « Superdiffusive Spin Transport as a Mechanism of Ultrafast Demagnetization ». In: *Phys. Rev. Lett.* 105 (2 2010), p. 027203. doi: 10.1103/PhysRevLett.105.027203.
- [28] E. Terrier, Y. Liu, B. P. Pichon, S. Bégin-Colin and V. Halté. « Ultrafast demagnetization in Fe<sub>3</sub>O<sub>4</sub> and  $\gamma$ -Fe<sub>2</sub>O<sub>3</sub> nanoparticles: the role of enhanced antiferromagnetic exchange interaction ». In: *J. Phys. D: Appl. Phys.* 49.50 (2016), p. 505001. doi: 10.1088/0022-3727/49/50/505001.
- [29] A. H. Reid, X. Shen, P. Maldonado, T. Chase, E. Jal, P. W. Granitzka, K. Carva, R. K. Li, J. Li, L. Wu, T. Vecchione, T. Liu, Z. Chen, D. J. Higley, N. Hartmann, R. Coffee, J. Wu, G. L. Dakovski, W. F. Schlotter, H. Ohldag, Y. K. Takahashi, V. Mehta, O. Hellwig, A. Fry, Y. Zhu, J. Cao, E. E. Fullerton, J. Stöhr, P. M. Oppeneer, X. J. Wang and H. A. Dürr. « Beyond a phenomenological description of magnetostriction ». In: *Nat. Commun.* 9 (1 2018), p. 388. doi: 10.1038/s41467-017-02730-7.
- [30] A. Kirilyuk, A. V. Kimel and T. Rasing. « Ultrafast optical manipulation of magnetic order ». In: *Rev. Mod. Phys.* 82 (3 2010), pp. 2431–2784. doi: 10.1103/RevModPhys.82.2731.
- [31] P. Scheid, Q. Remy, S. Lebègue, G. Malinowski and S. Mangin. « Light induced ultrafast magnetization dynamics in metallic compounds ». In: *J. Magn. Magn. Mater.* 560 (2022), p. 169596. doi: 10.1016/j.jmmm.2022.169596.

- [32] C. D. Stanciu, F. Hansteen, A. V. Kimel, A. Kirilyuk, A. Tsukamoto, A. Itoh and T. Rasing. « All-Optical Magnetic Recording with Circularly Polarized Light ». In: *Phys. Rev. Lett.* 99 (4 2007), p. 047601. doi: 10.1103/PhysRevLett.99.047601.
- [33] J. B. González-Díaz, A. García-Martín, J. M. García-Martín, A. Cebollada, G. Armelles, B. Sepúlveda, Y. Alaverdyan and M. Käll. « Plasmonic Au/Co/Au Nanosandwiches with Enhanced Magneto-optical Activity ». In: *Small* 4.2 (2008), pp. 202–205. doi: 10.1002/smll.200700594.
- [34] E. Moncada-Villa, O. N. Oliveira and J. R. Mejía-Salazar. « Uniaxial  $\epsilon$ -near-zero for giant enhancement of the transverse magneto-optical Kerr effect ». In: *Phys. Rev. B* 102 (16 2020), p. 165304. doi: 10.1103/PhysRevB.102.165304.
- [35] L. Wang, C. Clavero, Z. Huba, K. J. Carroll, E. E. Carpenter, D. Gu and R. A. Lukaszew. « Plasmonics and Enhanced Magneto-Optics in Core-Shell Co-Ag Nanoparticles ». In: *Nano Lett.* 11 (3 2011), pp. 1237–1240. doi: 10.1021/nl1042243.
- [36] M. Pancaldi, N. Leo and P. Vavassori. « Selective and fast plasmon-assisted photo-heating of nanomagnets ». In: *Nanoscale* 11 (16 2019), pp. 7656–7666. doi: 10.1039/C9NR01628G.
- [37] H. Xu, G. Hajisalem, G. M. Steeves, R. Gordon and B. C. Choi. « Nanorod Surface Plasmon Enhancement of Laser-Induced Ultrafast Demagnetization ». In: *Sci. Rep.* 5 (1 2019), pp. 2045–2322. doi: 10.1038/srep15933.
- [38] K. Ikemiya, K. Konishi, E. Fujii, T. Kogure, M. Kuwata-Gonokami and T. Hasegawa. « Self-assembly and plasmon-enhanced ultrafast magnetization of Ag-Co hybrid nanoparticles ». In: *Opt. Mater. Express* 4 (2014), pp. 1564–1573. doi: 10.1364/OME.4.001564.
- [39] T.-M. Liu, T. Wang, A. H. Reid, M. Savoini, X. Wu, B. Koene, P. Granitzka, C. E. Graves, D. J. Higley, Z. Chen, G. Razinskas, M. Hantschmann, A. Scherz, J. Stöhr, A. Tsukamoto, B. Hecht, A. V. Kimel, A. Kirilyuk, T. Rasing and H. A. Dürr. « Nanoscale Confinement of All-Optical Magnetic Switching in TbFeCo; Competition with Nanoscale Heterogeneity ». In: *Nano Lett.* 15 (10 2015), pp. 6862–6868. doi: 10.1021/acs.nanolett.5b02743.
- [40] X. Sun, J. L. MacManus-Driscoll and H. Wang. « Spontaneous Ordering of Oxide-Oxide Epitaxial Vertically Aligned Nanocomposite Thin Films ». In: *Annu. Rev. Mater. Res.* 50.1 (2020), pp. 229–253. doi: 10.1146/annurev-matsci-091719-112806.
- [41] M. Hennes, V. Schuler, X. Weng, J. Buchwald, D. Demaille, Y. Zheng and F. Vidal. « Growth of vertically aligned nanowires in metal-oxide nanocomposites: kinetic Monte-Carlo modeling versus experiments ». In: *Nanoscale* 10 (16 2013), pp. 7666–7675. doi: 10.1039/C7NR08974K.

- [42] M. Hennes, D. Demaille, G. Patriarche, T. Tran, Y. Zheng and F. Vidal. « Strain, magnetic anisotropy, and composition modulation in hybrid metal-oxide vertically assembled nanocomposites ». In: *MRS Bull.* 46 (2 2021), pp. 136–141. DOI: 10.1557/s43577-021-00029-z.
- [43] Q. Zhan, R. Yu, S. P. Crane, H. Zheng, C. Kisielowski and R. Ramesh. « Structure and interface chemistry of perovskite-spinel nanocomposite thin films ». In: *Appl. Phys. Lett.* 89.17 (2006), p. 172902. DOI: 10.1063/1.2364692.
- [44] B. Zhu, G. Schusteritsch, P. Lu, J. L. MacManus-Driscoll and C. J. Pickard. « Determining interface structures in vertically aligned nanocomposite films ». In: *APL Mater.* 6.7 (2019), p. 061105. DOI: 10.1063/1.5099204.
- [45] Y. Ni and A. G. Khachatryan. « From chessboard tweed to chessboard nanowire structure during pseudospinodal decomposition ». In: *Nature Mater.* 8 (5 2009), pp. 410–414. DOI: 10.1038/nmat2431.
- [46] Z. J. Wang. « Approaches to enhance low-field magnetoresistance effect at room temperature of self-assembled manganite nanocomposite films via microstructure design ». In: *MRS Bull.* 46 (2 2021), pp. 131–135. DOI: 10.1557/s43577-021-00031-5.
- [47] A. Chen, W. Zhang, F. Khatkhatay, Q. Su, C.-F. Tsai, L. Chen, Q. X. Jia, J. L. MacManus-Driscoll and H. Wang. « Magnetotransport properties of quasi-one-dimensionally channeled vertically aligned heteroepitaxial nanomazes ». In: *Appl. Phys. Lett.* 102.9 (2013), p. 093114. DOI: 10.1063/1.4794899.
- [48] X. Sun, Q. Li, J. Huang, J. Jian, P. Lu, X. Zhang, J. L. MacManus-Driscoll and H. Wang. « Strain and property tuning of the 3D framed epitaxial nanocomposite thin films via interlayer thickness variation ». In: *J. Appl. Phys.* 125.8 (2019), p. 082530. DOI: 10.1063/1.5053705.
- [49] S. Kawasaki, R. Takahashi, T. Yamamoto, M. Kobayashi, H. Kumigashira, J. Yoshinobu, F. Komori, A. Kudo and M. Lippmaa. « Photoelectrochemical water splitting enhanced by self-assembled metal nanopillars embedded in an oxide semiconductor photoelectrode ». In: *Nat. Commun.* 7 (1 2016), p. 11818. DOI: 10.1038/ncomms11818.
- [50] M. Lippmaa, S. Kawasaki, R. Takahashi and T. Yamamoto. « Nanopillar composite electrodes for solar-driven water splitting ». In: *MRS Bull.* 46 (2 2021), pp. 142–151. DOI: 10.1557/s43577-021-00030-6.
- [51] R. Wu, A. Kursumovic, X. Gao, C. Yun, M. E. Vickers, H. Wang, S. Cho and J. L. MacManus-Driscoll. « Design of a Vertical Composite Thin Film System with Ultralow Leakage To Yield Large Converse Magnetoelectric Effect ». In: *ACS Appl. Mater. Interfaces* 10.21 (2018), pp. 18237–18245. DOI: 10.1021/acsami.8b03837.

- [52] J. Gao, X. Wu, Q. Li, S. Du, F. Huang, L. Liang, H. Zhang, F. Zhuge, H. Cao and Y. Song. « Template-Free Growth of Well-Ordered Silver Nano Forest/Ceramic Metamaterial Films with Tunable Optical Responses ». In: *Adv. Mater.* 29.16 (2017), p. 1605324. doi: 10.1002/adma.201605324.
- [53] T. C. Kim, S. Ojha, G. Tian, S. H. Lee, H. K. Jung, J. W. Choi, L. Kornblum, F. J. Walker, C. H. Ahn, C. A. Ross and D. H. Kim. « Self-assembled multiferroic epitaxial BiFeO<sub>3</sub>–CoFe<sub>2</sub>O<sub>4</sub> nanocomposite thin films grown by RF magnetron sputtering ». In: *J. Mater. Chem. C* 6 (20 2018), pp. 5552–5561. doi: 10.1039/C8TC01192C.
- [54] V. Vega, T. Böhnert, S. Martens, M. Waleczek, J. M. Montero-Moreno, D. Görlitz, V. M. Prida and K. Nielsch. « Tuning the magnetic anisotropy of Co-Ni nanowires: comparison between single nanowires and nanowire arrays in hard-anodic aluminum oxide membranes ». In: *Nanotechnology* 23.46 (2012), p. 465709. doi: 10.1088/0957-4484/23/46/465709.
- [55] K. Nielsch and B. J. H. Stadler. « Template-based Synthesis and Characterization of High-density Ferromagnetic Nanowire Arrays ». In: *Handbook of Magnetism and Advanced Magnetic Materials*. Wiley, 2007.
- [56] X. Wang, J. Jian, H. Wang, J. Liu, Y. Pachaury, P. Lu, B. X. Rutherford, X. Gao, X. Xu, A. El-Azab, X. Zhang and H. Wang. « Nitride-Oxide-Metal Heterostructure with Self-Assembled Core–Shell Nanopillar Arrays: Effect of Ordering on Magneto-Optical Properties ». In: *Small* 17.5 (2021), p. 2007222. doi: 10.1002/smll.202007222.
- [57] J. Huang, X. L. Phuah, L. M. McClintock, P. Padmanabhan, K. S. N. Vikrant, H. Wang, D. Zhang, H. Wang, P. Lu, X. Gao, X. Sun, X. Xu, R. Edwin García, H.-T. Chen, X. Zhang and H. Wang. « Core-shell metallic alloy nanopillars-in-dielectric hybrid metamaterials with magneto-plasmonic coupling ». In: *Mater. Today* 51 (2021), pp. 39–47. doi: 10.1016/j.mattod.2021.10.024.
- [58] M. Hennes, X. Weng, E. Fonda, B. Gallas, G. Patriarche, D. Demaille, Y. Zheng and F. Vidal. « Phase separation and surface segregation in Co-Au-SrTiO<sub>3</sub> thin films: Self-assembly of bilayered epitaxial nanocolumnar composites ». In: *Phys. Rev. Materials* 3 (3 2019), p. 035002. doi: 10.1103/PhysRevMaterials.3.035002.
- [59] A. Chen and Q. Jia. « A pathway to desired functionalities in vertically aligned nanocomposites and related architectures ». In: *MRS Bull.* 46 (2 2021), pp. 115–122. doi: 10.1557/s43577-021-00032-4.
- [60] X. Weng, M. Hennes, T. Tran, N. Casaretto, D. Demaille, F. Vidal and Y. Zheng. « Orientation and lattice matching of CoNi nanowires embedded in SrTiO<sub>3</sub>: unveiling novel strain relaxation mechanisms in vertically aligned nanocomposites ». In: *CrystEngComm* 22 (28 2020), pp. 4730–4739. doi: 10.1039/D0CE00574F.

- [61] A. H. Morrish. *The Physical Principles of Magnetism*. Wiley, 1965.
- [62] R. C. O'Handley. *Modern Magnetic Materials: Principles and Applications*. Wiley, 2000.
- [63] J. A. Osborn. « Demagnetizing Factors of the General Ellipsoid ». In: *Phys. Rev.* 67.11-12 (1945), pp. 351–357. DOI: 10.1103/physrev.67.351.
- [64] A. P. Guimarães. *Principles of Nanomagnetism*. Springer, 2009.
- [65] D. Sellmyer and R. Skomski. *Advanced Magnetic Nanostructures*. Springer, 2006.
- [66] D. M. Paige, B. Szpunar and B. K. Tanner. « The magnetocrystalline anisotropy of cobalt ». In: *J. Magn. Magn. Mater.* 44.3 (1984), pp. 239–248. DOI: 10.1016/0304-8853(84)90248-8.
- [67] R. Skomski. *Simple Models of Magnetism*. Oxford University Press, 2008.
- [68] E. Tatsumoto, T. Okamoto, N. Iwata and Y. Kadena. « Temperature Dependence of the Magnetocrystalline Anisotropy Constants K1 and K2 of Nickel ». In: *J. Phys. Soc. Jpn.* 20.8 (1965), pp. 1541–1542. DOI: 10.1143/JPSJ.20.1541.
- [69] C. Kittel. « Physical Theory of Ferromagnetic Domains ». In: *Rev. Mod. Phys.* 21 (4 1949), pp. 541–583. DOI: 10.1103/RevModPhys.21.541.
- [70] E. C. Stoner and E. P. Wohlfarth. « A mechanism of magnetic hysteresis in heterogeneous alloys ». In: *Philos. Trans. Royal Soc. A* 240.826 (1948), pp. 599–642. DOI: 10.1098/rsta.1948.0007.
- [71] D. J. Sellmyer, M. Zheng and R. Skomski. « Magnetism of Fe, Co and Ni nanowires in self-assembled arrays ». In: *J. Phys. Condens. Matter* 13.25 (2001), R433–R460. DOI: 10.1088/0953-8984/13/25/201.
- [72] R. Skomski. « Nanomagnetism ». In: *J. Phys. Condens. Mat.* 15.20 (2003), R841–R896. DOI: 10.1088/0953-8984/15/20/202.
- [73] R. Skomski, H. Zeng, M. Zheng and D. J. Sellmyer. « Magnetic localization in transition-metal nanowires ». In: *Phys. Rev. B* 62 (6 2000), pp. 3900–3904. DOI: 10.1103/PhysRevB.62.3900.
- [74] W. F. Brown. « Thermal Fluctuations of a Single-Domain Particle ». In: *Phys. Rev.* 130.5 (1963), pp. 1677–1686. DOI: 10.1103/PhysRev.130.1677.
- [75] R. Skomski, D. Leslie-Pelecky, R. D. Kirby, A. Kashyap and D. J. Sellmyer. « Coercivity of disordered nanostructures ». In: *Scr. Mater.* 48.7 (2003), pp. 857–862. DOI: 10.1016/S1359-6462(02)00622-X.
- [76] M. P. Sharrock. « Time dependence of switching fields in magnetic recording media (invited) ». In: *J. Appl. Phys.* 76.10 (1994), pp. 6413–6418. DOI: 10.1063/1.358282.
- [77] G. Baffou. *Thermoplasmonics: Heating Metal Nanoparticles Using Light*. Cambridge University Press, 2017.

- [78] P. B. Johnson and R. W. Christy. « Optical Constants of the Noble Metals ». In: *Phys. Rev. B* 6 (12 1972), pp. 4370–4379. DOI: 10.1103/PhysRevB.6.4370.
- [79] C. F. Bohren and D. R. Huffman. *Absorption and Scattering of Light by Small Particles*. Wiley, 1998.
- [80] J. Olson, S. Dominguez-Medina, A. Hoggard, L.-Y. Wang, W.-S. Chang and S. Link. « Optical characterization of single plasmonic nanoparticles ». In: *Chem. Soc. Rev.* 44 (1 2015), pp. 40–57. DOI: 10.1039/C4CS00131A.
- [81] E. Stefan Kooij and B. Poelsema. « Shape and size effects in the optical properties of metallic nanorods ». In: *Phys. Chem. Chem. Phys.* 8 (28 2006), pp. 3349–3357. DOI: 10.1039/B518389H.
- [82] D. Dijkkamp, T. Venkatesan, X. D. Wu, S. A. Shaheen, N. Jisrawi, Y. H. Min-Lee, W. L. McLean and M. Croft. « Preparation of Y-Ba-Cu oxide superconductor thin films using pulsed laser evaporation from high  $T_c$  bulk material ». In: *Appl. Phys. Lett.* 51.8 (1987), pp. 619–621. DOI: 10.1063/1.98366.
- [83] R. Eason. *Pulsed Laser Deposition of Thin Films*. Wiley, 2006.
- [84] J. D. Ferguson, G. Arikan, D. S. Dale, A. R. Woll and J. D. Brock. « Measurements of Surface Diffusivity and Coarsening during Pulsed Laser Deposition ». In: *Phys. Rev. Lett.* 103 (25 2009), p. 256103. DOI: 10.1103/PhysRevLett.103.256103.
- [85] E. Tarsa, E. Hachfeld, F. Quinlan, J. Speck and M. Eddy. « Growth-related stress and surface morphology in homoepitaxial SrTiO<sub>3</sub> films ». In: *Appl. Phys. Lett.* 68.4 (1996), pp. 490–492. DOI: 10.1063/1.116376.
- [86] V. Schuler. « Nanofils ferromagnétiques auto-assemblés en matrice d'oxyde: croissance, épitaxie verticale et propriétés magnétiques ». PhD thesis. Université Pierre-et-Marie-Curie (Paris 6), 2015. URL: <http://www.theses.fr/2015PA066263>.
- [87] D. B. Williams and B. Carter. *Transmission Electron Microscopy: A Textbook for Materials Science*. 2nd. Springer, 2009.
- [88] B. Carter and D. B. Williams. *Transmission Electron Microscopy: Diffraction, Imaging and Spectrometry*. 1st. Springer International Publishing, 2016.
- [89] G. Bassett, J. W. Menter, D. W. Pashley and F. P. Bowden. « Moiré patterns on electron micrographs, and their application to the study of dislocations in metals ». In: *Proc. R. Soc. Lond. A* 246.1246 (1958), pp. 345–368. DOI: 10.1098/rspa.1958.0144.
- [90] B. D. Cullity. *Elements of X-ray Diffraction*. Addison-Wesley, 1956.
- [91] O. Robach, Y. Garreau, K. Aïd and M. B. Véron-Jolliot. « Corrections for surface X-ray diffraction measurements using the Z-axis geometry: finite size effects in direct and reciprocal space ». In: *J. Appl. Cryst.* 33.4 (2000), pp. 1006–1018. DOI: 10.1107/S0021889800004696.

- [92] A. J. Ying, C. E. Murray and I. C. Noyan. « A rigorous comparison of X-ray diffraction thickness measurement techniques using silicon-on-insulator thin films ». In: *J. Appl. Cryst.* 42.3 (2009), pp. 401–410. DOI: 10.1107/S0021889809006888.
- [93] J. Daillant and A. Gibaud. *X-ray and Neutron Reflectivity: Principles and Applications*. Springer, 2009.
- [94] K. Légaré, V. Chardonnet, I. Bermúdez Macias, M. Hennes, R. Delaunay, P. Lassonde, F. Légaré, G. Lambert, E. Jal and B. Vodungbo. « Analytic description and optimization of magneto-optical Kerr setups with photoelastic modulation ». In: *Rev. Sci. Instrum.* 93.7 (2022), p. 073001. DOI: 10.1063/5.0088610.
- [95] X. Weng. « Epitaxial  $\text{Co}_x\text{Ni}_{1-x}$  nanowires in  $\text{SrTiO}_3$  matrix: growth, structure and control of magnetic anisotropy ». PhD thesis. Sorbonne Université, 2019. URL: <http://www.theses.fr/2019SORUS418>.
- [96] X. Weng, M. Hennes, A. Juhin, P. Saintavit, B. Gobaut, E. Otero, F. Choueikani, P. Ohresser, T. Tran, D. Hrabovsky, D. Demaille, Y. Zheng and F. Vidal. « Strain-engineering of magnetic anisotropy in  $\text{Co}_x\text{Ni}_{1-x}$ - $\text{SrTiO}_3/\text{SrTiO}_3(001)$  vertically assembled nanocomposites ». In: *Phys. Rev. Materials* 6 (4 2022), p. 046001. DOI: 10.1103/PhysRevMaterials.6.046001.
- [97] T. B. Massalski, H. Okamoto, P. R. Subramanian and L. Kacprzak. *Binary Alloy Phase Diagrams*. 2nd. Vol. 1. ASM International, 1990.
- [98] D. J. Groenendijk and S. Gariglio. « Sequential pulsed laser deposition of homoepitaxial  $\text{SrTiO}_3$  thin films ». In: *J. Appl. Phys.* 120.22 (2016), p. 225307. DOI: 10.1063/1.4971865.
- [99] M. Ohring. *The Materials Science of Thin Films*. Academic Press, 1991.
- [100] S. Toshimasa, N. Yuji and F. Masayuki. « Defect structure in homoepitaxial non-stoichiometric strontium titanate thin films ». In: *Philos. Mag. A* 80.3 (2000), pp. 621–637. DOI: 10.1080/01418610008212072.
- [101] T. Ohnishi, K. Shibuya, T. Yamamoto and M. Lippmaa. « Defects and transport in complex oxide thin films ». In: *J. Appl. Phys.* 103.10 (2008), p. 103703. DOI: 10.1063/1.2921972.
- [102] C. M. Brooks, L. Fitting-Kourkoutis, T. Heeg, J. Schubert, D. A. Muller and D. G. Schlom. « Growth of homoepitaxial  $\text{SrTiO}_3$  thin films by molecular-beam epitaxy ». In: *Appl. Phys. Lett.* 94.16 (2009), p. 162905. DOI: 10.1063/1.3117365.
- [103] H. Arwin. « Dielectric function of a 200 nm Au thin film ». unpublished.
- [104] Y. Deng, Y. L. Du, M. S. Zhang, J. H. Han and Z. Yin. « Nonlinear optical properties in  $\text{SrTiO}_3$  thin films by pulsed laser deposition ». In: *Solid State Commun.* 135.4 (2005), pp. 221–225. DOI: 10.1016/j.ssc.2005.04.031.

- [105] P. K. Jain, S. Eustis and M. A. El-Sayed. « Plasmon Coupling in Nanorod Assemblies: Optical Absorption, Discrete Dipole Approximation Simulation, and Exciton-Coupling Model ». In: *J. Phys. Chem. B* 110.37 (2006), pp. 18243–18253. doi: 10.1021/jp063879z.
- [106] T. Nishizawa and K. Ishida. « The Co (Cobalt) system ». In: *Bull. Alloy Phase Diagr.* 4.4 (1983), pp. 387–390. doi: 10.1007/BF02868089.
- [107] F. Vidal, Y. Zheng, P. Schio, F. J. Bonilla, M. Barturen, J. Milano, D. Demaille, E. Fonda, A. J. A. de Oliveira and V. H. Etgens. « Mechanism of Localization of the Magnetization Reversal in 3 nm Wide Co Nanowires ». In: *Phys. Rev. Lett.* 109 (11 2012), p. 117205. doi: 10.1103/PhysRevLett.109.117205.
- [108] F. J. Bonilla, A. Novikova, F. Vidal, Y. Zheng, E. Fonda, D. Demaille, V. Schuler, A. Coati, A. Vlad, Y. Garreau, M. Sauvage Simkin, Y. Dumont, S. Hidki and V. Etgens. « Combinatorial Growth and Anisotropy Control of Self-Assembled Epitaxial Ultrathin Alloy Nanowires ». In: *ACS Nano* 7.5 (2013), pp. 4022–4029. doi: 10.1021/nn4000308.
- [109] T. Nishizawa and K. Ishida. « The Co-Ni (Cobalt-Nickel) system ». In: *Bull. Alloy Phase Diagr.* 4.4 (1983), pp. 390–395. doi: 10.1007/BF02868090.
- [110] V. Schuler, J. Milano, A. Coati, A. Vlad, M. Sauvage-Simkin, Y. Garreau, D. Demaille, S. Hidki, A. Novikova, E. Fonda, Y. Zheng and F. Vidal. « Growth and magnetic properties of vertically aligned epitaxial CoNi nanowires in (Sr, Ba)TiO<sub>3</sub> with diameters in the 1.8-6 nm range ». In: *Nanotechnology* 27 (2016), p. 495601. doi: 10.1088/0957-4484/27/49/495601.
- [111] J.-P. Palomares-Baez, E. Panizon and R. Ferrando. « Nanoscale Effects on Phase Separation ». In: *Nano Lett.* 17.9 (2017), pp. 5394–5401. doi: 10.1021/acs.nanolett.7b01994.
- [112] B. Predel. *Au-Ni, Landolt-Börnstein, Group IV Physical Chemistry*. Vol. 5A. Springer, 1991.
- [113] S. Bogatyrenko, A. Kryshnal, A. Minenkov and A. Kruk. « Miscibility gap narrowing on the phase diagram of AuNi nanoparticles ». In: *Scr. Mater.* 170 (2019), pp. 57–61. doi: 10.1016/j.scriptamat.2019.05.023.
- [114] G. Radtke, M. Hennes, M. Bugnet, Q. M. Ramasse, X. Weng, D. Demaille, B. Gobaut, P. Ohresser, E. Otero, F. Choueikani, A. Juhin, P. Saintavit, Y. Zheng and F. Vidal. « Atomic-Scale Study of Metal–Oxide Interfaces and Magnetoelastic Coupling in Self-Assembled Epitaxial Vertically Aligned Magnetic Nanocomposites ». In: *Adv. Mater. Interfaces* 6.17 (2019), p. 1900549. doi: 10.1002/admi.201900549.
- [115] A. Taylor. « Lattice Parameter of Binary Nickel-Cobalt Alloys ». In: *J. Inst. Met.* 77 (1950), p. 585.
- [116] W. B. Pearson and L. T. Thompson. « The lattice spacings of nickel solid solutions ». In: *Can. J. Phys.* 35.4 (1957), pp. 349–357. doi: 10.1139/p57-040.

- [117] M. Hnilička and L. Karmazin. « New lattice parameter study of Ni-Co alloys with respect to ordering in Ni<sub>3</sub>Co ». In: *Scr. Metall.* 8.8 (1974), pp. 1029–1032. DOI: 10.1016/0036-9748(74)90404-9.
- [118] T. Li, A. J. Senesi and B. Lee. « Small Angle X-ray Scattering for Nanoparticle Research ». In: *Chem. Rev.* 116.18 (2016), pp. 11128–11180. DOI: 10.1021/acs.chemrev.5b00690.
- [119] W. S. Wong, T. Sands and N. W. Cheung. « Damage-free separation of GaN thin films from sapphire substrates ». In: *Appl. Phys. Lett.* 72.5 (1998), pp. 599–601. DOI: 10.1063/1.120816.
- [120] Y. Bourlier, B. Bérini, M. Frégnaux, A. Fouchet, D. Aureau and Y. Dumont. « Transfer of Epitaxial SrTiO<sub>3</sub> Nanothick Layers Using Water-Soluble Sacrificial Perovskite Oxides ». In: *ACS Appl. Mater. Interfaces* 12.7 (2020), pp. 8466–8474. DOI: 10.1021/acsami.9b21047.
- [121] R. Takahashi and M. Lippmaa. « Sacrificial Water-Soluble BaO Layer for Fabricating Free-Standing Piezoelectric Membranes ». In: *ACS Appl. Mater. Interfaces* 12.22 (2020), pp. 25042–25049. DOI: 10.1021/acsami.0c05830.
- [122] G. Renaud, R. Lazzari and F. Leroy. « Probing surface and interface morphology with Grazing Incidence Small Angle X-Ray Scattering ». In: *Surf. Sci. Rep.* 64.8 (2009), pp. 255–380. DOI: 10.1016/j.surfrep.2009.07.002.
- [123] R. Lazzari. « *IsGISAXS*: a program for grazing-incidence small-angle X-ray scattering analysis of supported islands ». In: *J. Appl. Cryst.* 35.4 (2002), pp. 406–421. DOI: 10.1107/S0021889802006088.
- [124] T. Tran, X. Weng, M. Hennes, D. Demaille, A. Coati, A. Vlad, Y. Garreau, M. Sauvage-Simkin, M. Sacchi, F. Vidal and Y. Zheng. « Spatial correlation of embedded nanowires probed by X-ray off-Bragg scattering of the host matrix ». In: *J. Appl. Crystallogr.* 54.4 (2021), pp. 1173–1178. DOI: 10.1107/S1600576721006579.
- [125] D. Buttard, D. Bellet, G. Dolino and T. Baumbach. « X-ray diffuse scattering of p-type porous silicon ». In: *J. Appl. Phys.* 91.5 (2002), pp. 2742–2752. DOI: 10.1063/1.1429791.
- [126] V. I. Punegov, A. A. Lomov and K. D. Shcherbachev. « Characterization of InP porous layer by high-resolution X-ray diffraction ». In: *Phys. Status Solidi A* 204.8 (2007), pp. 2620–2625. DOI: 10.1002/pssa.200675689.
- [127] R. Hosemann and S. N. Bagchi. « The interference theory of ideal paracrystals ». In: *Acta Cryst.* 5.5 (1952), pp. 612–614. DOI: 10.1107/S0365110X52001702.
- [128] A. Guinier. *X-ray Diffraction in Crystals, Imperfect Crystals, and Amorphous Bodies*. Dover, 1963.
- [129] R. Hosemann and S. N. Bagchi. *Direct Analysis of Diffraction by Matter*. North-Holland, 1962.

- [130] J. L. Eads and R. P. Millane. « Diffraction by the ideal paracrystal ». In: *Acta Crystallogr. A* 57.5 (2001), pp. 507–517. DOI: 10.1107/S0108767301006341.
- [131] S. Kadowaki and M. Takahashi. « Magnetocrystalline Anisotropy of Nickel-Cobalt Alloys ». In: *J. Phys. Soc. Jpn.* 38.6 (1975), pp. 1612–1619. DOI: 10.1143/JPSJ.38.1612.
- [132] R. C. Hall. « Single Crystal Anisotropy and Magnetostriction Constants of Several Ferromagnetic Materials Including Alloys of NiFe, SiFe, AlFe, CoNi, and CoFe ». In: *J. Appl. Phys.* 30.6 (1959), pp. 816–819. DOI: 10.1063/1.1735247.
- [133] H. J. Leamy and H. Warlimont. « The Elastic Behaviour of Ni-Co Alloys ». In: *Phys. Status Solidi B* 37.2 (1970), pp. 523–534. DOI: 10.1002/pssb.19700370203.
- [134] X. Weng, M. Hennes, D. Hrabovsky, D. Demaille, F. Vidal and Y. Zheng. « Magnetoelastic effects and random magnetic anisotropy in highly strained ultrathin Ni nanowires epitaxied in a SrTiO<sub>3</sub> matrix ». In: *J. Magn. Magn. Mater.* 501 (2020), p. 166375. DOI: 10.1016/j.jmmm.2019.166375.
- [135] K. O'Grady and H. Laidler. « The limits to magnetic recording-media considerations ». In: *J. Magn. Magn. Mater.* 200.1 (1999), pp. 616–633. DOI: 10.1016/S0304-8853(99)00499-0.
- [136] T. Ono, H. Miyajima, K. Shigeto, K. Mibu, N. Hosoito and T. Shinjo. « Propagation of a Magnetic Domain Wall in a Submicrometer Magnetic Wire ». In: *Science* 294.5413 (1999), pp. 436–470. DOI: 10.1126/science.284.5413.468.
- [137] G. S. D. Beach, C. Nistor, C. Knutson, M. Tsoi and J. L. Erskine. « Dynamics of field-driven domain-wall propagation in ferromagnetic nanowires ». In: *Nature Mater.* 4 (10 2005), pp. 741–744. DOI: 10.1038/nmat1477.
- [138] R. Lavín, J. C. Denardin, J. Escrig, D. Altbir, A. Cortés and H. Gómez. « Angular dependence of magnetic properties in Ni nanowire arrays ». In: *J. Appl. Phys.* 106.10 (2009), p. 103903. DOI: 10.1063/1.3257242.
- [139] L. G. Vivas, M. Vazquez, J. Escrig, S. Allende, D. Altbir, D. C. Leitao and J. P. Araujo. « Magnetic anisotropy in CoNi nanowire arrays: Analytical calculations and experiments ». In: *Phys. Rev. B* 85 (3 2012), p. 035439. DOI: 10.1103/PhysRevB.85.035439.
- [140] H. Kronmüller. « Theory of Nucleation Fields in Inhomogeneous Ferromagnets ». In: *Phys. Status Solidi B* 144.1 (1987), pp. 385–396. DOI: 10.1002/pssb.2221440134.
- [141] P. Bruno. « Geometrically Constrained Magnetic Wall ». In: *Phys. Rev. Lett.* 83 (12 1999), pp. 2425–2428. DOI: 10.1103/PhysRevLett.83.2425.
- [142] A. Encinas-Oropesa, M. Demand, L. Piraux, I. Huynen and U. Ebels. « Dipolar interactions in arrays of nickel nanowires studied by ferromagnetic resonance ». In: *Phys. Rev. B* 63 (10 2001), p. 104415. DOI: 10.1103/PhysRevB.63.104415.
- [143] E. D. Palik. *Handbook of Optical Constants of Solids*. Academic Press, 1997.

- [144] P. B. Johnson and R. W. Christy. « Optical constants of transition metals: Ti, V, Cr, Mn, Fe, Co, Ni, and Pd ». In: *Phys. Rev. B* 9 (12 1974), pp. 5056–5070. DOI: 10.1103/PhysRevB.9.5056.
- [145] M. Hennes, G. Lambert, V. Chardonnet, R. Delaunay, G. S. Chiuzbăian, E. Jal and B. Vodungbo. « Element-selective analysis of ultrafast demagnetization in Co/Pt multilayers exhibiting large perpendicular magnetic anisotropy ». In: *Appl. Phys. Lett.* 120.7 (2022), p. 072408. DOI: 10.1063/5.0080275.
- [146] K. Yamamoto, S. E. Moussaoui, Y. Hirata, S. Yamamoto, Y. Kubota, S. Owada, M. Yabashi, T. Seki, K. Takanashi, I. Matsuda and H. Wadati. « Element-selectively tracking ultrafast demagnetization process in Co/Pt multilayer thin films by the resonant magneto-optical Kerr effect ». In: *Appl. Phys. Lett.* 116.17 (2020), p. 172406. DOI: 10.1063/5.0005393.
- [147] B. Koopmans, G. Malinowski, F. Dalla Longa, D. Steiauf, M. Fähnle, T. Roth, M. Cinchetti and M. Aeschlimann. « Explaining the paradoxical diversity of ultrafast laser-induced demagnetization ». In: *Nature Mater.* 9 (3 2010), pp. 259–265. DOI: 10.1038/nmat2593.
- [148] C. Stamm, N. Pontius, T. Kachel, M. Wietstruk and H. A. Dürr. « Femtosecond x-ray absorption spectroscopy of spin and orbital angular momentum in photoexcited Ni films during ultrafast demagnetization ». In: *Phys. Rev. B* 81 (10 2010), p. 104425. DOI: 10.1103/PhysRevB.81.104425.
- [149] I. Radu, C. Stamm, A. Eschenlohr, F. Radu, R. Abrudan, K. Vahaplar, T. Kachel, N. Pontius, R. Mitzner, K. Holldack, A. Föhlich, T. A. Ostler, J. H. Mentink, R. F. L. Evans, R. W. Chantrell, A. Tsukamoto, A. Itoh, A. Kirilyuk, A. V. Kimel and T. Rasing. « Ultrafast and Distinct Spin Dynamics in Magnetic Alloys ». In: *Spin* 5.3 (2015), p. 1550004. DOI: 10.1142/S2010324715500046.
- [150] O. Hjortstam, J. Trygg, J. M. Wills, B. Johansson and O. Eriksson. « Calculated spin and orbital moments in the surfaces of the 3d metals Fe, Co, and Ni and their overlayers on Cu(001) ». In: *Phys. Rev. B* 53 (14 1996), pp. 9204–9213. DOI: 10.1103/PhysRevB.53.9204.
- [151] I. M. L. Billas, A. Châtelain and W. A. de Heer. « Magnetism from the Atom to the Bulk in Iron, Cobalt, and Nickel Clusters ». In: *Science* 265.5179 (1994), pp. 1682–1684. DOI: 10.1126/science.265.5179.1682.
- [152] C. Dornes, Y. Acremann, M. Savoini, M. Kubli, M. J. Neugebauer, E. Abreu, L. Huber, G. Lantz, C. A. F. Vaz, H. Lemke, E. M. Bothschafter, M. Porer, V. Esposito, L. Rettig, M. Buzzi, A. Alberca, Y. W. Windsor, P. Beaud, U. Staub, D. Zhu, S. Song, J. M. Glowia and S. L. Johnson. « The ultrafast Einstein–de Haas effect ». In: *Nature* 565 (7738 2019), pp. 209–212. DOI: 10.1038/s41586-018-0822-7.

- [153] N. Bergeard, M. Hehn, S. Mangin, G. Lengaigne, F. Montaigne, M. L. M. Laliou, B. Koopmans and G. Malinowski. « Hot-Electron-Induced Ultrafast Demagnetization in Co/Pt Multilayers ». In: *Phys. Rev. Lett.* 117 (14 2016), p. 147203. doi: 10.1103/PhysRevLett.117.147203.
- [154] A. Melnikov, I. Razdolski, T. O. Wehling, E. T. Papaioannou, V. Roddatis, P. Fumagalli, O. Aktsipetrov, A. I. Lichtenstein and U. Bovensiepen. « Ultrafast Transport of Laser-Excited Spin-Polarized Carriers in Au/Fe/MgO(001) ». In: *Phys. Rev. Lett.* 107 (7 2011), p. 076601. doi: 10.1103/PhysRevLett.107.076601.
- [155] K. Bühlmann, G. Saerens, A. Vaterlaus and Y. Acremann. « Detection of femtosecond spin injection into a thin gold layer by time and spin resolved photoemission ». In: *Sci. Rep.* 10 (1 2020), p. 12632. doi: 10.1038/s41598-020-69477-y.